Dissertation

submitted to the

COMBINED FACULTY OF MATHEMATICS, ENGINEERING
AND NATURAL SCIENCES

of

HEIDELBERG UNIVERSITY, GERMANY

for the degree of
Doctor of Natural Sciences

put forward by
Eva-Marie Metz
born in Marburg, Germany

Oral examination: 02.07.2025

Deciphering Terrestrial Carbon Cycle Processes in Southern Hemispheric Semiarid Regions

Referees:

Prof. Dr. André Butz

Prof. Dr. Norbert Frank

Abstract

The land carbon sink partly mitigates climate change by taking up one third of the anthropogenic fossil fuel CO_2 emissions every year. Semiarid ecosystems contribute significantly to the interannual dynamics of the land sink. However, state-of-the-art land-atmosphere CO_2 flux estimates by in situ measurement-based atmospheric inversions and dynamic global vegetation models (DGVMs) show large uncertainties for semiarid regions in the Southern Hemisphere. This cumulative thesis demonstrates the potential of satellite data to improve regional CO_2 flux estimates in the Southern Hemisphere and to be used as an atmospheric constraint to evaluate DGVMs. CO_2 fluxes based on the Greenhouse Gases Observing Satellite (GOSAT) for 2009 - 2018 are evaluated in three study regions in Australia, southern Africa, and South America. Vegetation processes driving the flux dynamics are identified by using DGVMs that align well with the GOSAT-based fluxes. We find that ecosystem respiration responding to soil moisture and soil rewetting drives seasonal and interannual variability in the carbon cycle in semiarid regions. This work calls for improving the representation of soil rewetting processes in DGVMs to accurately model the carbon dynamics in semiarid regions and thereby reduce uncertainties of the global carbon budget and enable more accurate projections of climate-carbon feedbacks.

Zusammenfassung

Die terrestrische Kohlenstoffsenke verlangsamt den Klimawandel, indem sie ein Drittel der menschengemachten fossilen CO_2 Emissionen aufnimmt. Semiaride Ökosysteme tragen signifikant zu der Jahr-zu-Jahr Variabilität der Kohlenstoffsenke bei. Etablierte Methoden zur Abschätzung der CO_2 Flüsse wie beispielsweise atmosphärische Inversionen mit in situ Messungen oder globale Vegetationsmodelle (DGVMs) weisen hohe Unsicherheiten in semiariden Regionen der Südhemisphäre auf. Die vorliegende kumulative Doktorarbeit zeigt das Potential von Satellitendaten, die subkontinentalen CO_2-Flussabschätzungen zu verbessern und als Auswahlkriterium in der Analyse von DGVMs genutzt zu werden. CO_2 Flüsse, die auf Messungen des Greenhouse Gases Observing Satellite (GOSAT) basieren, werden für 2009-2018 in drei Regionen in Australien, dem südlichen Afrika und Süd-Amerika analysiert. Die Vegetationsprozesse, die die Flussdynamiken antreiben, werden mithilfe von DGVMs identifiziert, die mit den GOSAT basierten Flüssen übereinstimmen. Die Resultate zeigen, dass die auf Bodenwiederbefeuchtung reagierende Respiration der Ökosysteme die saisonale und Jahr-zu-Jahr Variabilität der Kohlenstoffflüsse in semiariden Regionen antreibt. Die vorliegende Arbeit fordert eine Verbesserung der Repräsentation von der Wiederbefeuchtung von Böden in DGVMs, um die Genauigkeit der modellierten Kohlenstoffflüsse in semiariden Gebieten zu verbessern und damit die Unsicherheiten in den Abschätzungen der globalen Kohlenstoffsenken und -quellen zu reduzieren und eine präzisere Prognose der Rückkopplung von Klima und Kohlenstoffkreislauf zu ermöglichen.

Contents

1. Introduction

Orbiting the Earth at a couple of hundred of kilometers height, satellites started to measure CO_2 concentrations in our Earth's atmosphere more than two decades ago (Pan et al., 2021). Their measurements provide us with global insights into the state of our atmosphere, such as the recent rise in CO_2 concentrations driven by human-made emissions. At the same time, they also allow us to estimate the increasing amount of atmospheric CO_2 taken up by the land ecosystems (Basu et al., 2013; Peiro et al., 2022; Byrne et al., 2023), which together with the CO_2 uptake into the ocean slows climate change (Friedlingstein et al., 2025). The future development of these sinks is debated as large uncertainties in our sink estimates and in our knowledge about the CO_2 exchange processes and their response to changing climate conditions exist (Raupach et al., 2014; Crisp et al., 2022; Gruber et al., 2023). The sparsity of ground-based measurements, which is especially prominent in the Southern Hemisphere, is one large source of uncertainty. Satellites provide the potential to overcome these limitations. As they also measure in remote regions, they can complement the sparse network of ground-based measurements and can help us improve our understanding of the global carbon cycle and its response to climate change (Sellers et al., 2018; Palmer et al., 2019; Byrne et al., 2020; Villalobos et al., 2020; Chen et al., 2021).

In this cumulative thesis, we use satellite CO_2 measurements of the Greenhouse Gas Observing Satellite (GOSAT) to investigate the terrestrial carbon cycle and its seasonal and interannual variability in three regions in the Southern Hemisphere (Figure 1.1): Australia with New Zealand (Metz et al., 2023, 2025b), southern Africa (south of 10°S, Metz et al., 2025a) and the temperate parts of South America as defined by the Transcom modeling project (see, e.g., Jacobson et al. (2023a)), further called the 'South American Temperate' region (Vardag et al., 2025).

This introduction chapter outlines the fundamentals of the global carbon cycle, including a description of ecosystem CO_2 fluxes between land and atmosphere in Section 1.1. Section 1.2 presents the available data sources of CO_2 concentration and flux measurements. The concept of atmospheric inversions is introduced in Section 1.3. Section 1.4 describes the used CO_2 flux datasets from dynamic global vegetation models (DGVMs). Finally, a short overview of the methods utilized, and the publications included in this thesis are displayed in Sections 1.5 and 1.6, respectively.

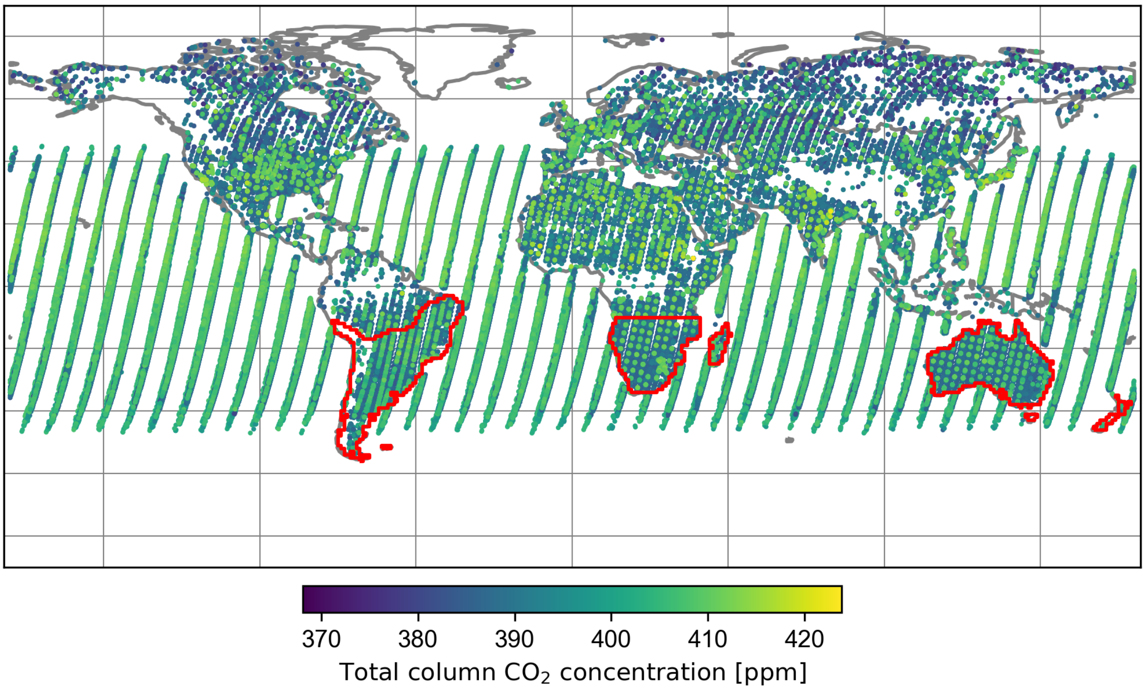

Figure 1.1.: GOSAT total column CO_2 concentration measurements from 2009 to 2019. The study regions, Australia, southern Africa, and the South American Temperate region (from east to west) are edged in red.

1.1. The Global Carbon Cycle

With CO_2 emissions from fossil fuel combustion and land-use change amounting to more than 10 GtC per year, humans are continuously increasing the CO_2 concentrations in the Earth's atmosphere. This causes a global temperature increase, which leads to significant changes in the climate of the Earth (Friedlingstein et al., 2025). Land ecosystems and oceans absorb approximately half of human-made CO_2 emissions every year, thus dampening the rise in atmospheric CO_2 concentrations (Friedlingstein et al., 2025). Despite steadily increasing emissions, the land and ocean sinks also increase keeping the absorbed fraction approximately constant (Bennedsen et al., 2019). The increase in these natural carbon sinks is believed to be driven by a growing amount of global vegetation biomass on land and by acidification of the oceans (Keenan and Williams, 2018; IPCC, 2023). Despite their importance, our knowledge about how climate change impacts the ocean and land sinks is still insufficient, and large uncertainties exist in predictions of the future sink development under a changing climate (Le Quéré et al., 2018; Bastos et al., 2020). It is debated whether and to what extent the natural carbon sinks can keep pace with the anthropogenic fossil fuel emissions in future (Raupach et al., 2014; Crisp et al., 2022; Gruber et al., 2023). Changes in the ocean overturning rate and reduced chemical capacity are expected (Raupach et al., 2014) and increasing respiration emissions exceeding the CO_2 uptake by vegetation growth were found (Bond-Lamberty et al., 2018). Therefore, research to improve our process understanding of the interaction of natural carbon sinks and climate is crucial to reliably predict future climate change.

1.1.1. The Land Sink

In its assessment reports published every 5-7 years, the Intergovernmental Panel on Climate Change (IPCC) summarizes the best estimates for anthropogenic CO_2 emissions and natural carbon sinks. The Global Carbon Budget Project (e.g. Friedlingstein et al., 2025) follows the IPCC methodology to estimate these so-called global carbon budgets annually to "develop a comprehensive, policy-relevant understanding of the global carbon cycle" (Global Carbon Project, 2003). The annual report presents estimates for the amount of CO_2 released by burning fossil fuels and land-use change. Additionally, it reports estimates of the counterbalancing amount of CO_2 taken up by the ocean and land sinks, and the CO_2 remaining in the atmosphere. Figure 1.2a, published in the most recent Global Carbon Budget report, displays the annual carbon emissions and the individual sinks over the last two centuries. The annual uptake of carbon into the land sink accounts for 30% of the total carbon sink (land + ocean + atmosphere, Friedlingstein et al., 2025).

In contrast to the rather smooth increase in the ocean sink, land fluxes exhibit strong interannual variability. This variability is reflected in the fluctuations of the atmospheric sink, that is, in the variability of the annual atmospheric CO_2 growth rate, which can vary substantially from one year to the next (see Figure 1.2b). The interannual variability of the terrestrial carbon sink is driven by climate variability (Zeng et al., 2005; Liu et al., 2017; Pan et al., 2020; Humphrey et al., 2021; Wang et al., 2022a; Liu et al., 2024a), as temperature and precipitation heavily influence ecosystem dynamics, such as vegetation growth (see Section 1.1.3). Climate modes like the El Niño Southern Oscillation phenomenon vary climatic conditions in recurrent patterns and show large correlations with the size of the terrestrial carbon sink (Zeng et al., 2005; Liu et al., 2024a). So-called El Niño years, which lead to warmer and drier conditions globally, usually cause higher atmospheric growth rates (16% in the period 1959 - 2021, Liu et al. (2024a)). In contrast, the cooler and wetter conditions in La Niña years reduce the growth rate by 9% (1959-2021, Liu et al., 2024a). Extraordinary anomalies like the La Niña year 2011, can lead to enhanced vegetation growth reducing the atmospheric growth rate anomalies by -0.5 ppm/year (Liu et al., 2024a). Changes in the carbon sink in response to climate anomalies provide an exceptional opportunity to study the influence of climatic changes on terrestrial ecosystems.

The carbon emissions and the estimated total carbon sink (sum of ocean and land sink and atmospheric growth) in Figure 1.2a do not balance perfectly. The

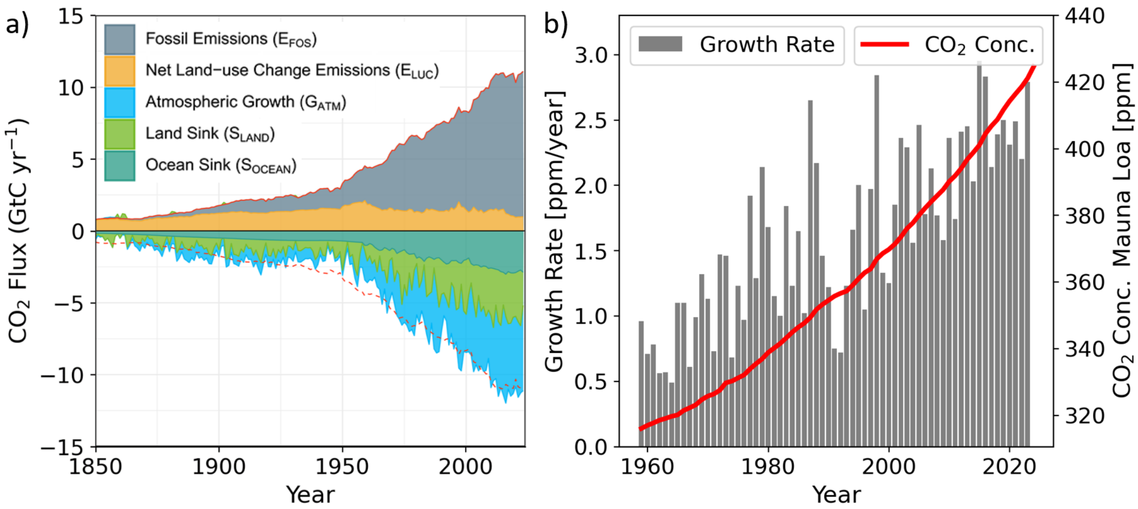

Figure 1.2.: The annual CO_2 fluxes of the global carbon cycle. Panel a) shows the development of the flux components over the last 170 years in gigatons carbon per year. The fossil and land-use change CO_2 emissions are partly taken up by the ocean and the land sink and partly remain in the atmosphere. The total emissions are mirrored as red dashed line to illustrate the budget imbalance. Panel b) shows the CO_2 concentrations measured locally at the Mauna Loa observatory as annual averages (red line) and the annual atmospheric CO_2 growth rate based on global CO_2 concentration measurements (grey bars).
Panel a) is taken with modifications from Friedlingstein et al. (2025, © Author(s) 2025, https://creativecommons.org/licenses/by/4.0/). Panel b) is based on global CO_2 growth rates and annual average CO_2 concentration measurements at Mauna Loa provided by NOAA (2024).

gap between emissions and total sink is called 'budget imbalance' and reflects our imperfect knowledge of the carbon cycle. It shows large year-to-year changes and is proposed to be mainly caused by errors in the estimation of the land and ocean sink (Le Quéré et al., 2018). The budget imbalance points towards the limitations of our current datasets' accuracy and towards deficits in our process understanding in land-atmosphere CO_2 exchange (Bastos et al., 2020). The uncertainties in carbon flux estimates become even larger when looking at smaller scales (Bastos et al., 2020). Therefore, regional-level analyses are important to identify sources of errors in the global flux estimates (Le Quéré et al., 2018) by improving our knowledge about the mechanisms and regions driving the development of the natural carbon sinks under climate change (Ballantyne et al., 2012).

1.1.2. Ecosystem Fluxes in the Land-Atmosphere CO_2 Exchange

The net exchange of CO_2 between ecosystems and atmosphere is called net biome productivity (NBP) and results from the interplay of much larger biospheric gross fluxes (see Figure 1.3). On the one hand, vegetation absorbs CO_2 through photosyn-

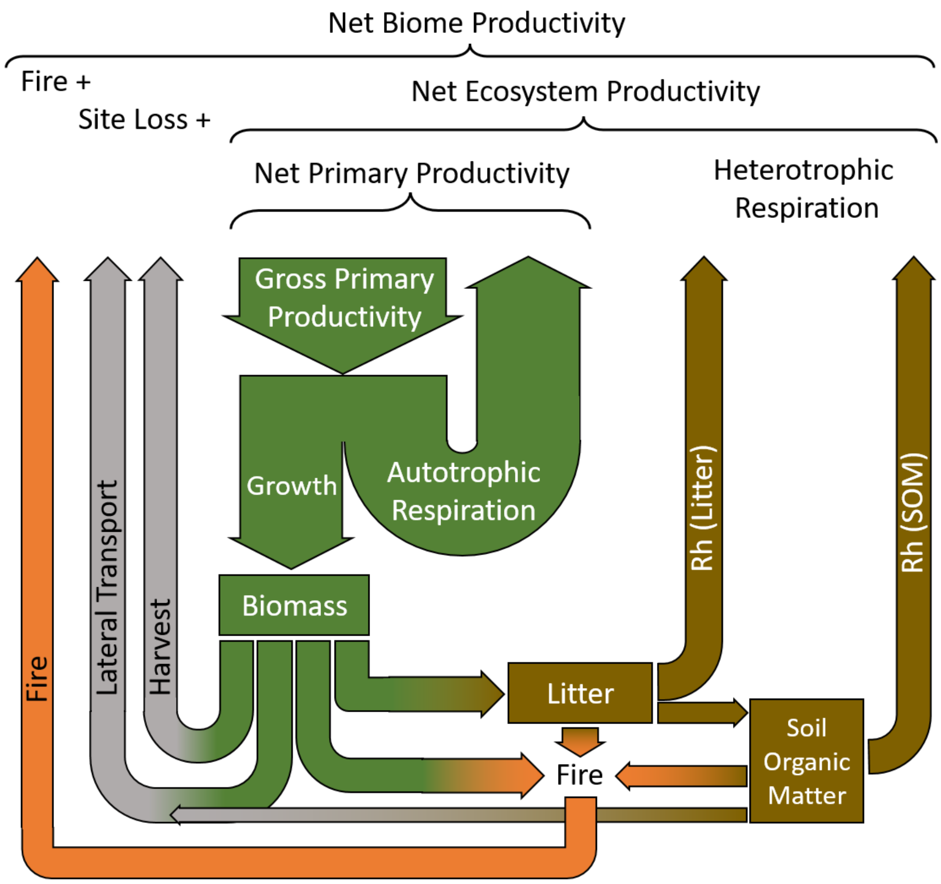

Figure 1.3.: Ecosystem fluxes. The different components in the carbon exchange of an ecosystem are given based on Schulze (2006) and Keenan and Williams (2018).

thesis and uses it to build up biomass. This flux, called gross primary productivity (GPP), is more than ten times larger than the human fossil fuel emissions (Friedlingstein et al., 2025). On the other hand, there is a release of CO_2 stored in vegetation and soils by autotrophic and heterotrophic respiration. Autotrophic respiration (Ra) is caused by growth and maintenance respiration when the plants' metabolism converts formerly stored carbon compounds into energy while releasing CO_2 (Keenan and Williams, 2018). Heterotrophic respiration (Rh) is produced by microbes respiring carbon stored in dead biomass, soils, and soil water. Both respiratory fluxes originate above and below ground. Emissions from Ra occur not only in the biomass above ground, such as leaf and stems, but also in the roots below ground. Emissions by the decomposition of organic matter occur in dead wood and heart-rots above ground (Harmon et al., 2011), but also in soil organic matter and soil litter. The sum of Ra and Rh, called total ecosystem respiration (TER), nearly offsets GPP. The sum of all respiratory fluxes below ground is called soil respiration (Bond-Lamberty et al., 2024). Soil respiration is assumed to constitute the largest component of TER (Law et al., 2002; Bond-Lamberty et al., 2024) and its temporal patterns are similar to TER (Barba et al., 2018).

The net ecosystem exchange (NEE) is the residual of balancing TER and GPP and is defined as:

$$NEE = -NEP = \overbrace{Rh + \underbrace{Ra - GPP}_{\text{-NPP}}}^{\text{TER}} \tag{1.1}$$

with NPP being the net primary productivity, the plant uptake of CO_2 which is used for long-term biomass growth. Net ecosystem productivity (NEP) is defined with opposite sign of NEE (Keenan and Williams, 2018). Photosynthesis and respiration dominate the circulation of carbon between ecosystems and their surroundings. Additionally, there are smaller contributions of CO_2 emissions by fires and other disturbance fluxes ('*other*') such as harvest, land-use change, non-CO_2 carbon emissions, and lateral transport through terrestrial-aquatic carbon transfer (Keenan and Williams, 2018). The resulting net exchange between land and atmosphere, NBP, is given by

$$NBP = NEE + fire + other. \tag{1.2}$$

1.1.3. Environmental Drivers of Ecosystem Fluxes

The terrestrial carbon gross fluxes and, with that, also the resulting net fluxes have a natural variability driven by environmental conditions. Photosynthesis and therefore GPP depends directly on the input of photosynthetically active radiation. Furthermore, temperature and precipitation impact GPP (Baldocchi et al., 2016). For example, there is an optimal leaf temperature for photosynthesis, water is essential for plant growth, and sub- or supra-optimal air moisture conditions lead to plant stomata closure (Way et al., 2021). Hence, water-stress conditions and high temperatures can limit GPP. The specific temperature and precipitation dependencies of GPP differ for individual species. Finally, also the ambient CO_2 concentration impacts GPP. Based on the Calvin-Benson cycle mechanisms for carbon fixation, one could assume that elevated CO_2 concentrations cause a larger biospheric carbon sink, but the net effect of climate change on the terrestrial carbon sink is debated (Way et al., 2021).

Also TER and its components, Ra and Rh, are impacted by climate and environmental conditions. Recent photosynthetic carbon uptake is the main driver of Ra (Unger et al., 2012). For this reason, Ra is indirectly affected by soil moisture through the dependence of GPP on water availability. Rh is directly affected by temperature, as the kinetics of the enzymatic reactions are temperature-dependent (Davidson et al., 2006). This so-called intrinsic temperature dependence (Davidson et al., 2006) is often described by the Q_{10} law, which quantifies how much a reaction rate increases with a 10°C temperature rise (Bond-Lamberty et al., 2024). However, temperature is not the only driver of Rh, but environmental conditions such as substrate supply, desiccation stress, and the amount of root and microbial biomass also impact Rh (Davidson and Janssens, 2006). Desiccation stress is directly caused by the decline in water availability and also the substrate supply depends on soil water as a transport medium (Moyano et al., 2013), making soil moisture an important driver of Rh. The impact of different soil moisture levels on Rh is visualized in Figure 1.4.

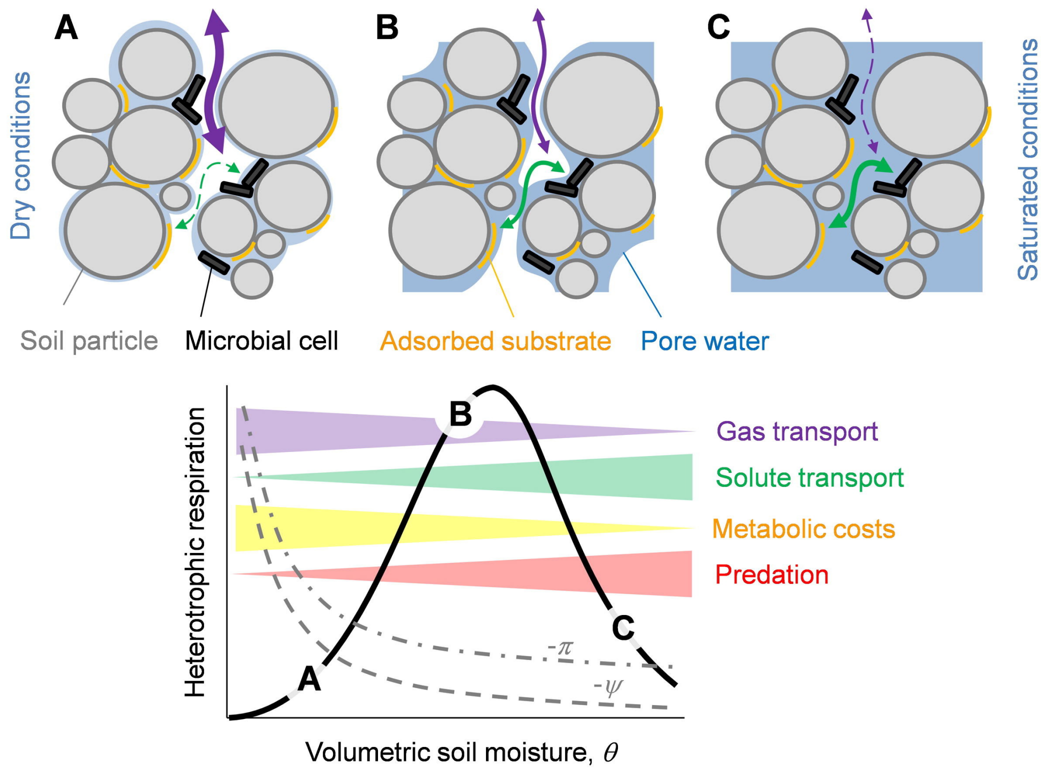

Figure 1.4.: Illustration of the soil moisture impact on heterotrophic respiration. The top panels depict the interaction of microbial cells and organic substrate in soil pores for different soil moisture conditions (dry to saturated conditions from left to right). The bottom panel shows the schematic trajectory of Rh in dependence on soil moisture. Furthermore, the extent of gas transport, solute transport, metabolic cost, and predation pressure on microorganisms is indicated dependent on the soil moisture. Ψ is the soil water potential and π is the cell osmotic potential under which a stable turgor pressure can be maintained. Reprinted from Moyano et al. (2013), with permission from Elsevier.

In the case of suboptimal soil moisture conditions (Figure 1.4A), the transport of substrate to soil microbe communities is hampered. Furthermore, microbes are exposed to osmotic stress, which increases the metabolic cost to maintain osmotic equilibrium with the surrounding (Davidson et al., 2006; Schimel et al., 2007; Moyano et al., 2013). Both conditions strongly limit Rh. However, also high soil water levels (Figure 1.4C) can hamper Rh. The water in the soil pores hinders oxygen diffusion and only anaerobic decomposition, which is generally slower, can take place (Davidson and Janssens, 2006). Hence, Rh can be limited by sub- and supraoptimal soil moisture levels and maximizes under intermediate soil moisture conditions (Figure 1.4B).

1.1.4. Semiarid Regions

Dryland ecosystems cover 41% of the global land surface (Bastos et al., 2022). They are characterized by precipitation being lower than the amount of evaporation during most of the year (Wang et al., 2022b). This exposes the ecosystems to water-stress and extensive drought conditions. In semiarid parts of the drylands, there is still a sufficient amount of precipitation in the wet season so that substantial vegetation can grow (Bastos et al., 2022). Given the sensitivity of vegetation growth and ecosystem respiration to water availability and temperature described in the previous section, carbon flux dynamics in semiarid regions are largely driven by precipitation and temperature dynamics. Due to their high sensitivity to climate and their large spatial extent (see Figure 1.5) semiarid regions have a large potential impact on the dynamics of the global carbon sink.

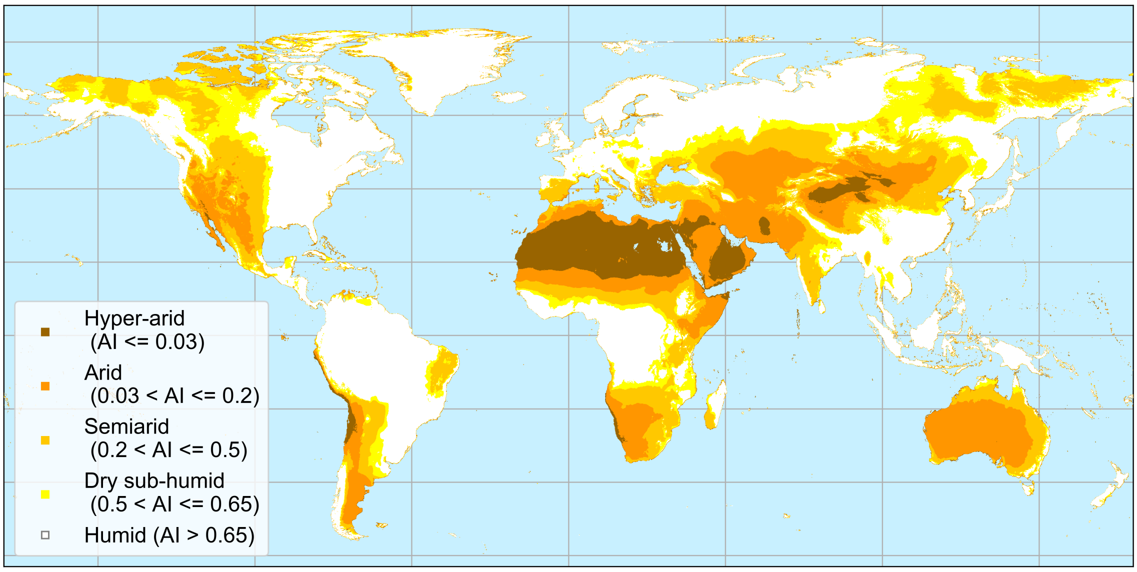

Figure 1.5.: Map of global drylands. The distribution of our world's drylands is given for different aridity classes. The aridity classes are based on the aridity index (AI) following the guidelines of the United Nations Environment Program (Middleton and Thomas, 1993). The figure is created with data of the Global Aridity Index and Potential Evapotranspiration Climate Database v3 (Zomer and Trabucco, 2019; Zomer et al., 2022).

The relation of precipitation and potential evapotranspiration is often used to define the extent of semiarid regions. Exact definitions vary, e.g. Frater et al. (2009) define areas with precipitation below evapotranspiration during seven to nine months to be semiarid. Others use the aridity index (AI) defined as the ratio of precipitation and potential evapotranspiration (Feng and Fu, 2013; Wang et al., 2022b; Feldman et al., 2024b) following the guidelines of the United Nations Environment Program (Middleton and Thomas, 1993). The guidelines distinguish between hyper-arid ($AI <= 0.03$), arid ($0.03 < AI <= 0.2$), semiarid ($0.2 < AI <= 0.5$), dry sub-humid

(0.5 < AI <= 0.65), and humid (0.65 < AI) regions. As shown in Figure 1.5, large areas in the Southern Hemisphere are drylands. The Australian continent is dominated by arid and semiarid ecosystems. Southern hemispheric Africa and South America are also partly covered by arid and semiarid regions. We use a simplified definition for semiarid regions similar to Frater et al. (2009) taking into account the seasonality of precipitation. We identify regions with a distinct drought phase by selecting areas with marginal precipitation in at least four consecutive months. These conditions are given in the whole southern Africa region and in large parts of Australia (see Figure S3 in Metz et al., 2023) and the South American Temperate region (see Figure 3 in Vardag et al., 2025)

Dry conditions hamper the growth of larger trees and closed vegetation, so that savannas, grass-, and shrublands are the dominant vegetation types in drylands (Bastos et al., 2022). In Australia, the arid and semiarid regions are sparsely vegetated and mainly covered by savannas (Haverd et al., 2013). Similarly, the southern African vegetation is mainly grasses, shrubs, and savannas and is highly water-limited in its growth (Williams et al., 2008). In South America, the drylands in the Andes, southern Argentina and the easternmost semiarid region are mainly covered by forests, other woodlands, grasslands, or barren land (FAO, 2019).

In all three regions, a distinct drought season characterizes the local climate. In addition to the large seasonal variability, year-to-year fluctuations are also high, causing large variability in ecosystem dynamics on seasonal and interannual time scales (Williams et al., 2007; Teckentrup et al., 2021; Villalobos et al., 2022; Ernst et al., 2024). For example, in 2011 Australia experienced persistent wet conditions caused by an interplay of multiple climate modes. This led to strong vegetation growth and an exceptionally large Australian carbon sink, which contributed around 60% to the global terrestrial carbon sink anomaly in this year (Poulter et al., 2014; Detmers et al., 2015).

Recent findings suggest a prominent role of semiarid ecosystems in driving global carbon flux variability and trends (Poulter et al., 2014; Ahlström et al., 2015) due to the strong impacts of precipitation and water availability on semiarid vegetation (Haverd et al., 2017; Piao et al., 2020). As shown in Figure 1.6, semiarid regions have been found to be the ecosystems which impact the trend and variability of the global terrestrial carbon sink most.

The dominant processes for carbon uptake and emission in semiarid regions are, however, not completely understood and state-of-the-art vegetation models struggle to accurately represent the carbon fluxes (MacBean et al., 2021; Wang et al., 2022b). For example, vegetation models have difficulties estimating the interannual variability of carbon fluxes in semiarid regions (MacBean et al., 2021; Teckentrup et al., 2021) and modeling the response of carbon fluxes to water availability correctly (MacBean

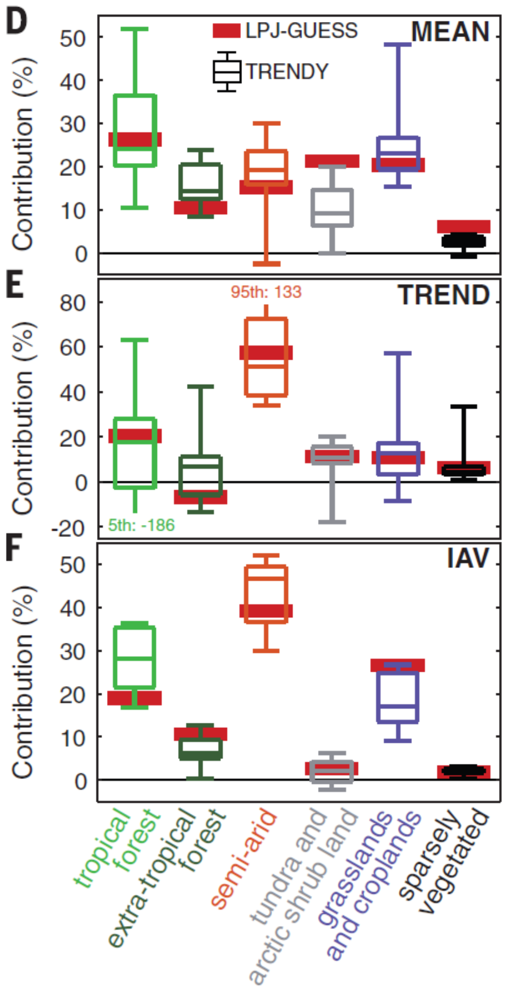

Figure 1.6.: Contributions of global ecosystems to the mean global terrestrial carbon sink, its trend and interannual variability (IAV). The contribution of different land ecosystems to the mean (top panel, D), trend (middle panel, E), and IAV (bottom panel, F) of global NBP is given. The contributions are estimated using the biogeochemical dynamic global vegetation model LPJ-GUESS (red marker line) and the TRENDY ensemble of vegetation models (boxplot). From Ahlström et al. (2015). Reprinted with permission from AAAS.

et al., 2021; Wang et al., 2022b). Uncertainties also remain in our knowledge about driver attribution for semiarid carbon fluxes. Disentangling the effect of precipitation and temperature is challenging (Meng et al., 2024; Wang et al., 2022a,b) and the impact of the temporal distribution of precipitation, e.g. its seasonality or pulse events of precipitation, on semiarid ecosystems remains uncertain (Wang et al., 2022b; Feldman et al., 2024a).

The Birch Effect

Precipitation pulses can have a large impact on carbon fluxes in semiarid regions (Huxman et al., 2004). In arid and semiarid ecosystems, plant growth and respiration are strongly reduced during the drought phase as a large fraction of species are dormant. The first rain events at the beginning of the rainy season induce the reactivation of these species. Thereby, plants and soil microbes react differently to precipitation events. Most plants need to develop a substantial canopy before being able to take up carbon via photosynthesis (Huxman et al., 2004). In addition, frequent or large rain events are necessary so that water reaches deeper soil layers where the plant roots are located (Huxman et al., 2004). Moreover, persistent humidity in the air is needed to avoid stomata closure, which inhibits photosynthesis (Way et al., 2021).

Soil respiration, however, can increase rapidly after precipitation events, as increasing soil moisture immediately increases microbial activity and decomposition (Austin et al., 2004). Moreover, even small precipitation pulses can affect biochemical processes driven by microbial communities close to the surface (Austin et al., 2004). This difference in the responses of photosynthesis and respiration causes dry ecosystems to act as an immediate carbon source at the onset of the rainy season. The onset of carbon assimilation by plant growth is delayed, but then increasingly dominates the CO_2 exchange. This causes the ecosystems to be an effective sink in the growth period.

Soil respiration pulses caused by the immediate microbial response to soil rewetting events are known under the term 'Birch Effect' (Birch, 1964; Jarvis et al., 2007; Casals et al., 2011; Unger et al., 2012). These pulses show strong nonlinear dynamics (Fan et al., 2015). In addition to the direct dependence of microbial activity on soil moisture, other effects that amplify CO_2 release into the atmosphere are described in literature. Firstly, percolating water fills pore spaces which have formerly been filled with high concentrations of CO_2 accumulating from soil respiration during drought phases (Huxman et al., 2004). This leads to an immediate release of this CO_2 into the atmosphere. Secondly, percolating water transports carbon into the soils and soil re-wetting can break soil structures and liberate formerly inaccessible labile carbon, both leading to enhanced substrate availability (Manzoni et al., 2014; Fan et al., 2015). Due to these effects, soil respiration pulses in rewetting cycles emit a larger amount of CO_2 than constantly moist soils (Singh et al., 2023).

1.2. Satellite and In Situ Measurements

In this thesis, different measurement datasets are used to analyze the carbon cycle and vegetation CO_2 exchange processes in the study regions. We use satellite and in situ measurements of atmospheric CO_2 and flux tower measurements of local CO_2 fluxes. Furthermore, we take solar-induced fluorescence (SIF) measurements as a proxy for GPP.

1.2.1. CO_2 Concentration Measurements

The dynamics of CO_2 in our atmosphere can be directly assessed by measuring atmospheric CO_2 concentrations. We use local in situ CO_2 measurements and satellite total column CO_2 measurements.

In situ CO_2 measurements

Numerous laboratories and institutions around the world maintain local atmospheric greenhouse gas observations, such as CO_2 mole fraction measurements (Masarie et al., 2014). Since 1996 the GLOBALVIEW data product exists which, maintained by the National Oceanic and Atmospheric Administration (NOAA), collects the measurements of various laboratories. The data product and its extension within the Observation Package (ObsPack) framework is created for the scientific community (Masarie et al., 2014). The datasets include different types of atmospheric CO_2 mole fraction measurements, i.e., in situ or flask measurements from ships, aircraft, towers, or surface platforms (Masarie et al., 2014). The measurements have a high quality with a measurement accuracy of at least 0.1 ppm (Hall et al., 2021). They are provided by different institutions, including NOAA, the Commonwealth Scientific and Industrial Research Organisation (CSIRO), and the Integrated Carbon Observation System (ICOS) (Jacobson et al., 2023a). Figure 1.7 shows the locations, types and maintaining institutions of the measurement sites. In the following, these local CO_2 mole fraction measurements will be referred to as 'in situ measurements'.

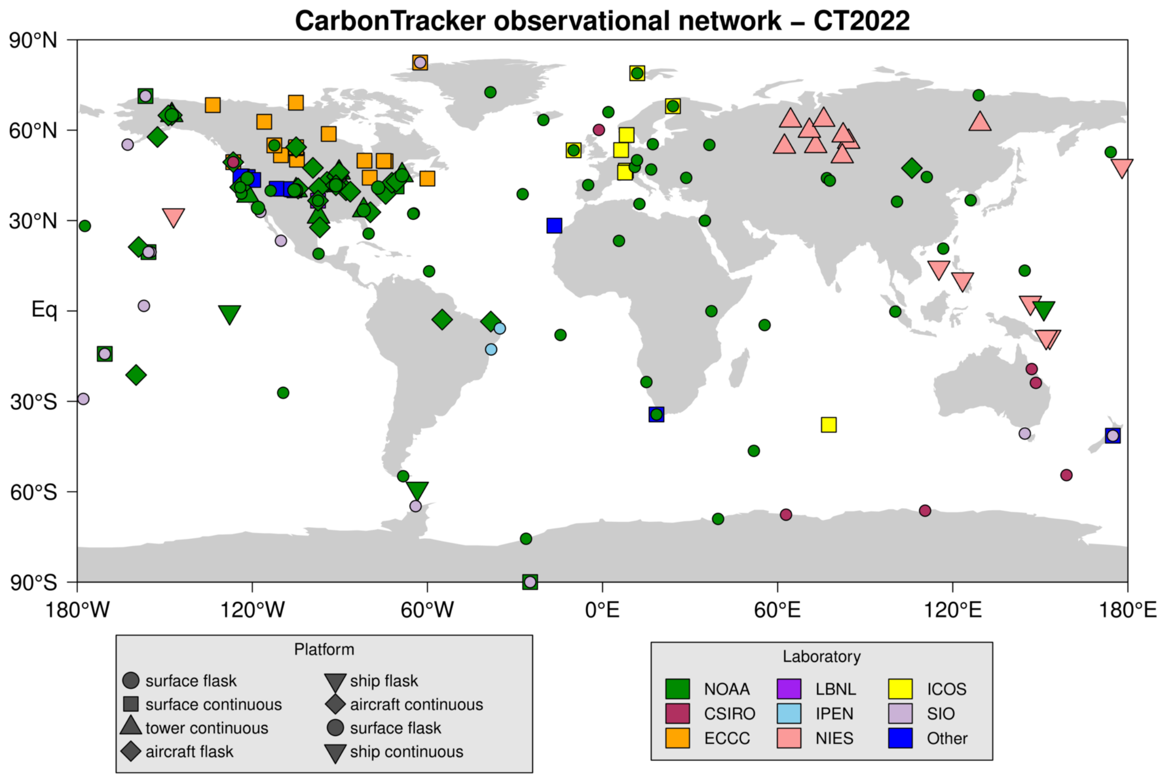

Figure 1.7.: Observational network of CO_2 concentration measurements as used in CarbonTracker CT2022. Figure provided by NOAA Global Monitoring Laboratory, Boulder, Colorado, USA (https://gml.noaa.gov) and taken from Jacobson et al. (2023a).

Satellites

For more than 20 years, satellites have been measuring CO_2 concentrations from space (Pan et al., 2021). With the launch of GOSAT in 2009, CO_2 columns with high sensitivity to near-surface concentrations started to be measured to observe CO_2 sources and sinks (Basu et al., 2013; Pan et al., 2021). Other satellite projects followed, such as the Orbiting Carbon Observatory-2 (OCO-2) in 2014, increasing the spatial resolution of CO_2 measurements (Pan et al., 2021). Both satellites, GOSAT and OCO-2, measure sunlight scattered back from the Earth's surface. The measured spectra in the near infrared range contain CO_2 absorption signals. These signals can be used to infer column averaged dry air CO_2 mole fractions (XCO_2) along the light path column. To do so, retrieval algorithms that model the measurement of the sunlight and the radiative transfer through the atmosphere are used to inversely estimate the amount of CO_2 in the air column (Rodgers, 2000). In the present dissertation, GOSAT XCO_2 data generated with the RemoTeC radiative transfer and retrieval algorithm version 2.4.0 (Butz et al., 2011; Butz, 2022) and with the NASA Atmospheric CO_2 Observations from Space (ACOS) algorithm version 9 (Taylor et al., 2022) are used. The two retrievals differ in the implementation of the inverse framework and in the data preparation. For example, they differ in the used optimization methods, the handling of surface pressure, and the micro-physical aerosol properties. Furthermore, they apply different bias corrections on the XCO_2 values retrieved from the measured spectra, and RemoTeC uses a stricter filtering of the data. These methodological differences can lead to differences in the retrieved XCO_2 data even though both retrievals use the same GOSAT measurement spectra. OCO-2 XCO_2 data used in this thesis are only retrieved with the ACOS algorithm version 10r and version 11.1r (OCO-2 Science Team et al., 2020; OCO-2/OCO-3 Science Team et al., 2022; Jacobs et al., 2024). GOSAT and OCO-2 differ in the amount and characteristics of the measurements. Both fly in a sun-synchronous orbit covering the Earth within three (GOSAT) and 16 (OCO-2) days. GOSAT has a sub-satellite field of view of about 10 km x 10 km, which is larger than for OCO-2 (1.3 km x 2.3 km). Furthermore, OCO-2 measures 50 times more frequently than GOSAT (Crisp, 2008; Suto et al., 2021).

Satellites measure CO_2 in the whole air column through which the measured sunlight passes. In contrast to that, in situ measurements are point samples which are mostly taken close to the surface. Furthermore, satellites cannot provide the same high precision as in situ measurements. GOSAT has a single measurement precision between 1.5 ppm (ACOS) and 1.9 ppm (RemoTeC) (Buchwitz et al., 2017; Taylor et al., 2022) and a seasonal and regional systematic error of 0.5 ppm and 0.6 ppm, respectively (RemoTeC) (Buchwitz et al., 2017). Additional challenges, for example, cloud coverage, aerosols in the atmosphere, high solar zenith angles, and changing surface albedo, pose problems in inferring valid CO_2 concentrations from satellite measurements (Butz et al., 2011; Basu et al., 2013; Guerlet et al., 2013). Multiple validation and filter steps need to be applied to allow reliable records of satellite XCO_2 measurements (Butz et al., 2011; Basu et al., 2013; Guerlet et al., 2013). This leads to a reduced amount of satellite measurements over the cloudy tropics, high latitudes and high-altitude regions. This is clearly visible in Figure 1.1, which shows all GOSAT XCO_2 measurements from 2009 to 2019 inferred by the RemoTeC retrieval. In the following, the term satellite measurements refers to the retrieved XCO_2 values and not to the initially measured absorption spectra.

1.2.2. Local CO_2 Flux Measurements

To gain insight into the local land-atmosphere exchange of CO_2 in response to temperature and soil moisture, we make use of local CO_2 flux measurements by eddy covariance systems. The eddy covariance technique allows direct and continuous measurements of surface fluxes of tracers such as CO_2 (Aubinet et al., 2012; Pastorello et al., 2020). The measurement technique is used at numerous measurement sites around the world. Measurement devices are mounted at different heights on tower constructions (Pastorello et al., 2020). The measurement sites will be referred to as flux towers in the following. By measuring vertical wind velocities and CO_2 concentration variations with high frequency (ten measurements per second), turbulent CO_2 fluxes between biosphere and atmosphere can be derived for half-hour intervals (Aubinet et al., 2012). The area which influences the measurement is called the footprint and can extend up to hundreds of meters around the tower, depending on the wind situation (Pastorello et al., 2020). In addition to trace gas fluxes, flux towers usually measure energy and water exchange between land surface and atmosphere. Furthermore, other environmental parameters like air and soil temperature and soil moisture are also recorded.

There are multiple regional flux tower networks, for example the OzFlux network for Australia and New Zealand (Beringer et al., 2016, 2022) or AmeriFlux for North and South America (Novick et al., 2018). The FLUXNET initiative (Baldocchi et al., 2001) collects and provides the station data of the regional networks centrally. Most but not all stations of the regional networks are included in this global database. In this thesis, we use the AmeriFlux and FLUXNET stations in the South American Temperate region and southern Africa. The OzFlux network sites are particularly important as they play a central role in Metz et al. (2025b) in addition to being used in Metz et al. (2023).

The OzFlux network

The OzFlux network was established in the year 2001 in Australia and New Zealand. The following short introduction is based on the network website (`https://www.ozflux.org.au/`) and a review article by Beringer et al. (2022). There are more than 50 flux tower sites in the OzFlux network (see Figure 1.8) with 29 sites being currently active. The stations cover a broad range of ecosystems and climate conditions. Most of the stations are located in semiarid or arid regions with a low amount of annual precipitation and a distinct drought season. However, there are also stations with high annual rainfall of up to 5700 mm per year that enable the growth of tropical forests at these sites.

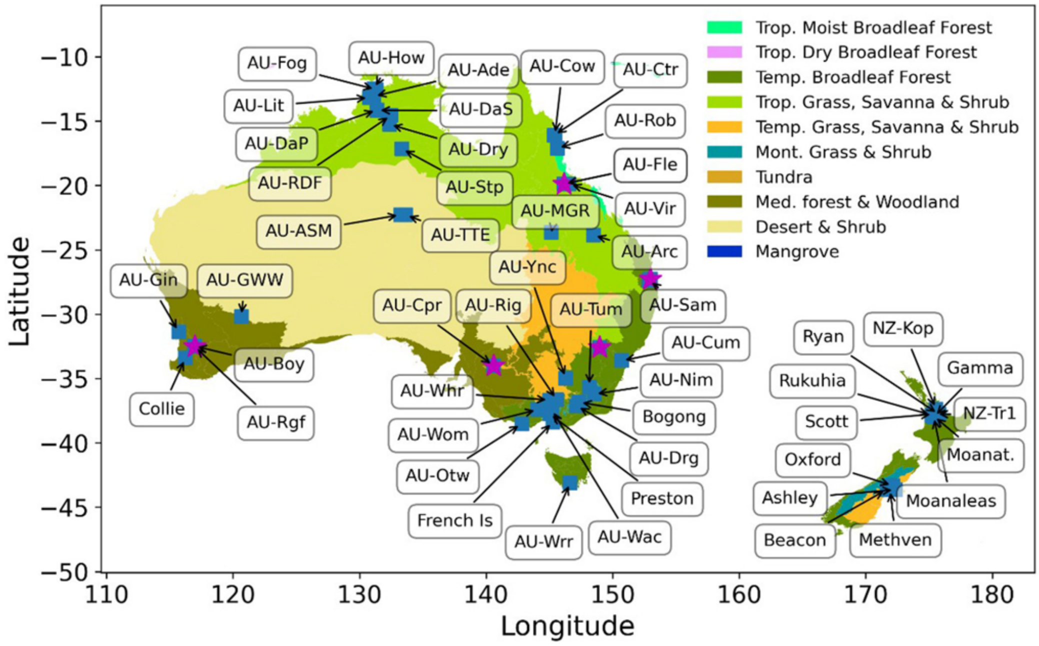

Figure 1.8.: The OzFlux network in Australia and New Zealand. The flux tower stations are given with the corresponding FLUXNET name if possible. The background map shows the different ecosystems in Australia and New Zealand. The Figure is taken without modifications from Beringer et al. (2022, © 2022 The Authors. https://creativecommons.org/licenses/by/4.0/).

In our analyses, we only include the OzFlux stations located in Australia. We use half-hourly measurements of net CO_2 flux (NEE), soil temperature, and soil moisture. Soil moisture and soil temperature are measured close to the surface at a depth of 5 cm to 10 cm. We only use stations with at least one year of measurements. We calculate daily nighttime NEE averages as a proxy for TER as done in previous studies (Mahecha et al., 2010; Barba et al., 2018; Pastorello et al., 2020; Meng et al., 2024). This approach assumes that photosynthesis and, therefore, GPP can only take place with sufficient sunlight. Hence, GPP is close to zero during night, so that the measured night fluxes only consist of TER.

1.2.3. SIF: Solar-Induced Fluorescence

We use SIF measurements in our analyses. SIF emerges during the photosynthesis process. Parts of the photosynthetically active radiation (PAR) absorbed by chlorophyll in plant leafs is not used in the light reactions of photosynthesis, but get dissipated as fluorescence (Meroni et al., 2009; Joiner et al., 2018) as shown in Figure 1.9. The emitted fluorescence is in the red and near-infrared spectral ranges and can be measured by satellites (Frankenberg et al., 2011; Joiner et al., 2018). SIF is found to be proportional to GPP in biome-scale analyses with monthly time resolution (Zhang et al., 2016a,b; Joiner et al., 2018; Sun et al., 2018; Pierrat et al., 2022). Hence, SIF can be used as a proxy for GPP (Li et al., 2018). We use SIF measurements of the GOME-2 satellite (Joiner et al., 2023) to access the seasonal timing of biomass build-up.

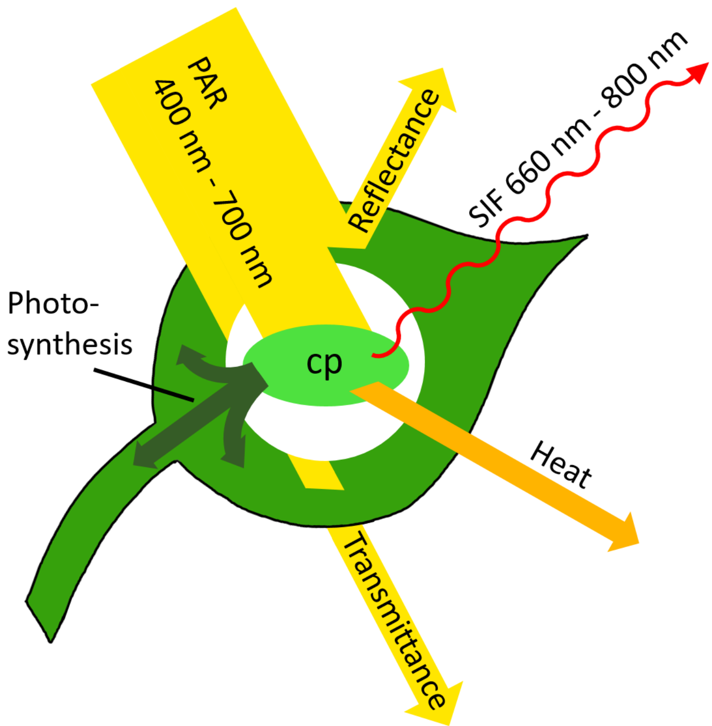

Figure 1.9.: Light absorption and emissions in leafs. PAR gets partly absorbed by chlorophyll in the chloroplast (cp) of the plant cells. The chlorophyll molecules return from their exited states to their ground states by driving photosynthesis, releasing energy as heat, or re-emitting the light as chlorophyll fluorescence (SIF).

1.3. Top-down Estimates of Carbon Fluxes by Atmospheric Inversions

CO_2 concentration measurements can be fed into atmospheric inversion systems to infer land-atmosphere fluxes based on the concentration measurements (e.g., Rödenbeck et al. (2003); Peters et al. (2007); Basu et al. (2013); Chandra et al. (2022)). Many atmospheric inversion systems are based on Bayesian optimization techniques (Chevallier et al., 2006; Byrne et al., 2023). The systems optimize surface fluxes transported forward through the atmosphere to agree best with concentration measurements within the given transport and measurement uncertainties. At the same time, the systems prevent the fluxes from deviating too far from assumed prior fluxes within the given prior uncertainties (Rodgers, 2000).

1.3.1. Bayesian Inversion

The Bayesian optimization technique is based on Bayes' theorem which formulates the probability for a state $\mathbf{x}$ (in this context a vector of CO_2 fluxes) given a set of (CO_2 concentration) measurements $\mathbf{y}$ (Rodgers, 2000):

$$P(\mathbf{x}|\mathbf{y}) = \frac{P(\mathbf{y}|\mathbf{x})P(\mathbf{x})}{P(\mathbf{y})}. \tag{1.3}$$

Thereby, $P(\mathbf{y}|\mathbf{x})$ is the probability of measurements given a certain state. $P(\mathbf{x})$ and $P(\mathbf{y})$ describe the probabilities of the measurements and the state given their uncertainties, respectively. The state $\mathbf{x}$ and the measurements $\mathbf{y}$ in an atmospheric inversion are connected by an atmospheric transport model. For chemically inert gases, such as CO_2, the atmospheric transport can be described by a linear function of the fluxes with the atmospheric transport operator matrix $\mathbf{H}$:

$$\mathbf{y} = \mathbf{H}\mathbf{x} + \epsilon_{\mathbf{y}}. \tag{1.4}$$

By assuming a Gaussian distribution of the measurement errors $\epsilon_{\mathbf{y}}$ and the flux uncertainties, the probabilities can be described by a normal distribution using the mean of the measurements as $\overline{\mathbf{y}} = \mathbf{H}\mathbf{x}$ and prior knowledge of the state $\mathbf{x}_a$ (Rodgers, 2000):

$$P(\mathbf{y}|\mathbf{x}) = \frac{1}{\sqrt{(2\pi)^m|\mathbf{R}|}}\exp\left(-\frac{1}{2}(\mathbf{y}-\mathbf{H}\mathbf{x})^T\mathbf{R}^{-1}(\mathbf{y}-\mathbf{H}\mathbf{x})\right) \tag{1.5}$$

and

$$P(\mathbf{x}) = \frac{1}{\sqrt{(2\pi)^n|\mathbf{B}|}}\exp\left(-\frac{1}{2}(\mathbf{x}_a-\mathbf{x})^T\mathbf{B}^{-1}(\mathbf{x}_a-\mathbf{x})\right). \tag{1.6}$$

The covariance matrices $\mathbf{R}$ and $\mathbf{B}$ are symmetric with the variances of the measurements and of the prior fluxes on the respective diagonals. The covariances of the measurements (and prior fluxes) are on the off-diagonals of $\mathbf{R}$ (and $\mathbf{B}$) and are given by

$$cov_{i,j} = \sigma_i\sigma_j corr_{i,j} \tag{1.7}$$

pairwise for the measurements $\mathrm{y_i}$ and $\mathrm{y_j}$ (and prior fluxes $\mathrm{x_i}$ and $\mathrm{x_j}$) with their correlation $corr$ and individual standard deviation σ. By inserting Equation 1.5 and 1.6 in Equation 1.3, and by combining all normalization factors including P($\mathbf{y}$) in one factor C, we get the following:

$$P(\mathbf{x}|\mathbf{y}) = C * \exp\left(-\frac{1}{2}(\mathbf{y}-\mathbf{Hx})^T\mathbf{R}^{-1}(\mathbf{y}-\mathbf{Hx}) - \frac{1}{2}(\mathbf{x}_a-\mathbf{x})^T\mathbf{B}^{-1}(\mathbf{x}_a-\mathbf{x})\right). \quad (1.8)$$

The most likely set of fluxes given a measurement can now be obtained by maximizing Equation 1.8. This equals minimizing its exponent, which can be handled like a cost function J with

$$J = \frac{1}{2}(\mathbf{y}-\mathbf{Hx})^T\mathbf{R}^{-1}(\mathbf{y}-\mathbf{Hx}) + \frac{1}{2}(\mathbf{x}_a-\mathbf{x})^T\mathbf{B}^{-1}(\mathbf{x}_a-\mathbf{x}). \quad (1.9)$$

Hence, the land-atmosphere fluxes $\mathbf{x}$ are optimized taking into account the measurements $\mathbf{y}$, the prior fluxes $\mathbf{x}_a$, the atmospheric transport model $\mathbf{H}$, the uncertainties of atmospheric transport and measurements $\mathbf{R}$, and the uncertainties associated with prior fluxes $\mathbf{B}$. The choice of the prior fluxes, the transport model, and the associated uncertainties vary among inversions. At the end of Section 1.3.2, the configurations of the TM5 four-dimensional variational inversion system (TM5-4DVar, Basu et al., 2013) are described in more detail.

Evaluating the result of an inversion

Having a look at Equation 1.9, we can see that the availability of measurements and the choice of the uncertainties in the covariance matrices determine the weighting of the measurement and the prior information in the inversion. An inverse problem can be highly underconstrained, meaning that there are considerably fewer independent measurements than independent state vector elements. In this case, the inversion heavily relies on the prior for those fluxes that are not connected to measurements via atmospheric transport (or prior flux correlations). Furthermore, high measurement uncertainties in combination with comparably small prior flux uncertainties also put more weight on the second part of the cost function J. Therefore, also in this case, the posterior fluxes will strongly resemble the prior fluxes. For this reason, posterior fluxes that align closely with the prior fluxes can indicate a sparse availability of measurements or a weak weighting of the measurement information in the inversion by using large measurement uncertainties compared to the prior uncertainties. However, also if prior fluxes already capture the 'true' state of the atmosphere well, there will be a good agreement of prior and posterior fluxes, as the measurements agree well with the prior fluxes and do not induce any changes.

Different metrics exist to quantitatively evaluate the information content provided by the measurements in an inversion. Using the exact analytical solution of Equation 1.9 given by

$$\hat{\mathbf{x}} = \mathbf{x}_a + (\mathbf{H}^T\mathbf{R}^{-1}\mathbf{H} + \mathbf{B}^{-1})^{-1}\ \mathbf{H}^T\mathbf{R}^{-1}\ (\mathbf{y} - \mathbf{H}\mathbf{x}_a) \tag{1.10}$$

with the optimized posterior state $\hat{\mathbf{x}}$ (see Rodgers, 2000), the corresponding posterior covariances can be calculated as

$$\mathbf{S}_{\hat{\mathbf{x}}} = (\mathbf{H}^T\mathbf{R}^{-1}\mathbf{H} + \mathbf{B}^{-1})^{-1}. \tag{1.11}$$

Comparing the posterior covariances to the prior covariances can give some indication about the information content. Another useful metric is the Averaging Kernel $\mathbf{A}$ (Rodgers, 2000) with

$$\mathbf{A} = (\mathbf{H}^T\mathbf{R}^{-1}\mathbf{H} + \mathbf{B}^{-1})^{-1}\ \mathbf{H}^T\mathbf{R}^{-1}\mathbf{H}. \tag{1.12}$$

Using $\mathbf{A}$ and the unity matrix $\mathbf{I}$ and neglecting the measurement error $\epsilon_{\mathbf{y}}$, the posterior state can be expressed as

$$\hat{\mathbf{x}} = \mathbf{A}\mathbf{x} + (\mathbf{I}-\mathbf{A})\mathbf{x}_a. \tag{1.13}$$

This expression shows that $\mathbf{A}$ can be used as a measure of how much the inversion can reveal about the true state and how much it only reproduces the given prior knowledge. Hence, $\mathbf{A}$ can be a useful metric to evaluate the results of an inversion.

However, the matrix multiplication and matrix inversion needed in Equation 1.10 and 1.11 are becoming increasingly computationally costly with increasing dimensions of the inverse problem (Yadav and Michalak, 2013). For inversion setups with large state vectors and a large number of measurements (as given in global atmospheric inversions) the exact analytical solution cannot be calculated and iterative approaches to find the minimum of Equation 1.9 are used. Doing so, the posterior covariance matrix and metrics such as the averaging kernel can only be approximated.

1.3.2. Global GOSAT Inversion with TM5-4DVar

We use the atmospheric inversion system TM5-4DVar to estimate global CO_2 fluxes based on CO_2 concentration measurements. We assimilate GOSAT CO_2 concentration measurements together with in situ CO_2 concentration measurements from the GlobalView+ 5.0 and NRT 5.0 dataset provided by NOAA (Carbontracker Team, 2019; Cooperative Global Atmospheric Data Integration Project, 2019). The following description of the TM5-4DVar setup is based on Basu et al. (2013), if not stated otherwise.

As indicated by its name, the inversion system uses the global chemistry Transport Model, version 5 (TM5) and a Four-Dimensional Variational Data Assimilation

(4DVar) inversion scheme based on a Bayesian optimization technique to optimize land-atmosphere fluxes on a weekly 3°x2° resolution (Metz et al., 2023). The 4DVar inversion scheme seeks to minimize the cost function J given in Equation 1.9 using an adjoint model to estimate the gradient of J. It iteratively optimizes the state in the three spatial dimensions also considering its temporal development.

The optimized net surface flux is internally split up into ocean, biosphere, fire, and anthropogenic fossil fuel fluxes. As anthropogenic fluxes have much smaller uncertainties compared to biogenic and ocean fluxes (Friedlingstein et al., 2025), they are assumed to be correctly represented by the prior fluxes and are therefore not optimized. While the ocean fluxes can be separated spatially from the other fluxes, the fire and biosphere fluxes cannot be distinguished and are optimized jointly. The inversion uses climatological prior fluxes, namely fire emissions of the Quick Fire Emission Database (QFED, Darmenov and Da Silva (2015)) and fossil fuel emissions of the Open-source Data Inventory for Anthropogenic CO_2 (ODIAC, Oda and Maksyutov, 2011; Oda et al., 2018). More details about the prior fluxes used can be found in Weir et al. (2020). The priors for ocean, biosphere, and fire fluxes are taken as mean seasonal cycle from 2000 to 2019 with a year-specific scaling to match the annual global atmospheric CO_2 growth rate. A daily cycle is imposed on the biospheric fluxes.

The entries in the prior flux covariance matrix **B** are calculated as

$$cov(x_{r_1,t_1}, x_{r_2,t_2}) = \sigma_{r_1,t_1}\sigma_{r_2,t_2}C_r(r_1,r_2)C_t(t_1,t_2) \tag{1.14}$$

with the uncertainty $\sigma_{r,t}$ of each individual prior flux $x_{r,t}$ at position r and time t on the diagonal and correlated uncertainties on the off-diagonals with exponentially decaying correlation functions over space and time (C_r and C_t). The uncertainties of the individual prior fluxes are fractions (0.84 over land, 0.6 over ocean) of the absolute prior fluxes themselves with a fixed minimum value to avoid zero uncertainties.

TM5-4DVar uses daily averages of in situ measurements. For that, only measurements during four hours in the afternoon for low altitudes or during four hours after midnight for mountain stations are averaged. In these times, the footprint of the stations is assumed to be the largest, as the planetary boundary layer is at its highest (afternoon) and its lowest height (night). Satellite measurements are individually assimilated in the inversion. The errors of the satellite measurements can be correlated, for example, due to atmospheric transport uncertainties or retrieval uncertainties. TM5-4DVar accounts for these correlations by inflating the errors of the satellite measurements. The inflation factor depends on the proximity of the surrounding measurements. Errors of clustered measurements are inflated more so that these measurements are weighted less. The observations are then assumed to be independent, so that the measurement covariance matrix **R** is diagonal. Taking into account the measurement errors σ_{obs} and the uncertainties of the modeled atmospheric transport σ_{mod} the entry at the i-th position on the diagonal is

$$\mathbf{R}_{ii} = \sigma^2_{obs,i} + \sigma^2_{mod,i}. \tag{1.15}$$

Thereby, σ_{mod} is calculated as the standard deviation of the CO_2 mixing ratios in the grid cells around the measurement. In Basu et al. (2013), with a 6°x4° spatial resolution, the mean errors for the in situ measurements are 3 ppm (σ_{mod}) and 2.5 ppm (σ_{obs}) and for satellite measurements 0.05 ppm (σ_{mod}) and 3.6 ppm (σ_{obs}). The high σ_{obs} for in situ measurements, compared to the single measurement error of 0.1 ppm, reflects the variability of the CO_2 concentrations during the four-hour averaging window.

As already mentioned above, for global inversions as performed with TM5-4DVar, the exact solution of the inverse problem cannot be calculated, and an iterative approach is used to find the minimum of the cost function (see Basu et al. (2013) for more details). For this reason, the posterior covariances and metrics such as the averaging kernel can only be approximated and are not reported because of the large associated uncertainties.

In our studies, we use three inversion configurations: Two inversions assimilating in situ measurements together with GOSAT/RemoTeC and GOSAT/ACOS individually (in the following called 'TM5-4DVar/RemoTeC+IS' and 'TM5-4DVar/ACOS+IS', respectively) and one inversion with in situ measurements only ('TM5-4DVar/IS'). The mean of 'TM5-4DVar/RemoTeC+IS' and 'TM5-4DVar/ACOS+IS' will be referred to as 'TM5-4DVar/GOSAT+IS' in the following. The different inversion runs allow us to analyze the impact of the different measurement datasets on the optimized fluxes. Next to TM5-4DVar/IS, we also use the in situ measurement-based atmospheric inversions CarbonTracker (Peters et al., 2007; Jacobson et al., 2023b) and CAMS (Chevallier et al., 2005, 2010, 2019). Both provide CO_2 fluxes for the whole time period from 2009 to 2018. In the following, we will refer to these atmospheric inversions (including TM5-4DVar/IS) as 'in-situ-only inversions'.

1.3.3. OCO-2 MIP: The Orbiting Carbon Observatory-2 Model Intercomparison Project

In the Orbiting Carbon Observatory-2 model intercomparison project (OCO-2 MIP), 14 different atmospheric inversion modeling groups collaborate with the aim of analyzing the effect of assimilating OCO-2 XCO_2 measurements in different atmospheric inversions (Byrne et al., 2023). Within the project, different measurement configurations using in situ measurements and land or ocean OCO-2 measurements, and combinations of these, are used to conduct different inversion experiments. In the publications presented in this thesis, we use the inversion experiment with in situ measurements only (in the following called 'MIP/IS') and the experiment with in situ measurements together with land and ocean OCO-2 measurements (in the following called 'MIP/OCO-2+IS'). For both inversion experiments, OCO-2 MIP provides fluxes only from 2015 on. The 14 different atmospheric inversion systems use the same fossil fuel prior fluxes but differ in the other assumed prior fluxes, their used transport models and inversion systems. More details on the individual models are given in Table 1 in Byrne et al. (2023). With the different models and measurement configurations, the project aims at quantifying the impact of transport model errors, inversion setups, measurement setups, and retrieval errors on the optimized CO_2 fluxes. Like TM5-4DVar, the other OCO-2 MIP models can also only report a total land flux, as fire and biosphere fluxes cannot be separated in the inversions. Next to the optimized land-atmosphere fluxes of the different experiments, the OCO-2 MIP project also provides the individual prior fluxes used in the models. Furthermore, 5% of the OCO-2 measurements are withheld for validation purposes. By transporting their optimized fluxes forward in time, the model groups calculate XCO_2 values at the location of these OCO-2 measurements ('OCO-2 cosamples'). The prior fluxes and the OCO-2 cosamples are used in the publications of this thesis (Metz et al., 2023, 2025a) for evaluation purposes.

1.4. Bottom-up Carbon Flux Estimates

The atmospheric inversions described in Section 1.3 provide estimates of the net CO_2 exchange between land and atmosphere. However, they cannot partition the net flux into its components (e.g. GPP and TER, see Figure 1.3). Bottom-up approaches do not only provide net fluxes, but also model the individual vegetation gross fluxes. By comparing the top-down fluxes provided by the atmospheric inversions with bottom-up model estimates, we can analyze the vegetation processes driving the net flux dynamics. We make use of flux datasets from two different bottom-up approaches: DGVMs and FLUXCOM. Both are described in more detail in the following.

1.4.1. Dynamic Global Vegetation Models

We use CO_2 flux datasets of DGVMs which are included in the "trends and drivers of the regional-scale terrestrial sources and sinks of carbon dioxide" (TRENDY, version 9, Le Quéré et al., 2013) intercomparison project. The aim of the project is to provide global land CO_2 flux estimates for the annual global carbon budget estimated by the Global Carbon Project (e.g. Friedlingstein et al., 2025). We use the 18

DGVMs in TRENDY version 9, which provide monthly CO_2 fluxes: CABLE-POP, CLASSIC, CLM5.0, DLEM, IBIS, ISAM, ISBA-CTRIP, JSBACH, JULES-ES-1p0, LPJ, LPX-Bern, OCN, ORCHIDEE, ORCHIDEE-CNP, ORCHIDEEv3, SDGVM, VISIT, and YIBs. The models simulate global vegetation and soil carbon dynamics and are driven by a common set of meteorological input data, CO_2 concentrations, and land-use data (Le Quéré et al., 2013; Friedlingstein et al., 2020). They parameterize the individual processes driving the CO_2 exchange (e.g., respiration given the ambient temperature, water availability, and biomass), which allows the models to provide output for NEE, GPP, TER, and its components Ra and Rh. Most of the models also give NBP and fewer models consider and provide fire and land-use change fluxes. More details about the models are given in Bastos et al. (2020, Table 1) and Friedlingstein et al. (2025, Table S1).

Initially, the individual models have been designed with a focus on different ecosystems and regions (Seiler et al., 2022). For this reason, the models differ in the considered processes and assumed environmental conditions, e.g., they use different spatial distribution of vegetation types (Friedlingstein et al., 2020; Teckentrup et al., 2021). Furthermore, the models differ largely in the parameterization of processes. The response of vegetation fluxes to the onset of the rainy season plays a major role in the results of this thesis. In the following, a short overview of the GPP and TER response parameterizations is given. The focus is thereby on the most important TRENDY models for this thesis, namely JSBACH (Delire et al., 2020), OCN (Zaehle et al., 2010), LPJ (Poulter et al., 2011), CABLE-POP (Haverd et al., 2018), CLASSIC (Melton et al., 2020), ORCHIDEE (Krinner et al., 2005), ORCHIDEEv3 (Vuichard et al., 2019), and YIBs (Yue and Unger, 2015). The characteristics of the models are discussed in more detail in the given references. For the modeling of GPP, TRENDY models use plant functional types (PFTs) to classify plants into groups with similar traits. The models differ in the spatial distribution and in the parameterizations of growth dynamics assumed for individual PFTs (Seiler et al., 2022). Most models have drought-impacted PFTs, such as grasslands and shrublands. The growth of these plants largely depends on sufficient accumulation of soil moisture in the rooting zone (JSBACH, OCN, LPJ, CLASSIC, ORCHIDEE, ORCHIDEEv3, and CABLE-POP). Various other drivers of GPP are possible, such as the accumulation of warm days, so-called 'growing degree days' (LPJ) or the development of sufficient leaf area (OCN) needed for the growing season to start. These parameterizations can lead to a delayed increase in GPP with respect to the start of the rainy season. The respiration component Rh depends on temperature alone (YIBs), or temperature in combination with precipitation (JSBACH) or soil moisture (LPJ, CLASSIC, ORCHIDEEv3, CABLE-POP, and ORCHIDEE). Short-term (days to months in contrast to years) Rh dynamics are commonly driven by litter respiration with short turn-over times.

Therefore, soil moisture in the upper soil layers is more important for short-term Rh dynamics than deeper soil layer moisture. The exact functional parameterization of the soil moisture dependence of Rh varies from a simple steadily increasing dependence (LPJ) to more complex parabolic functions with an optimal soil moisture range (CABLE-POP).

Due to the different parameterizations and processes implemented in the models, the models' output fluxes can vary largely. Friedlingstein et al. (2020) and Seiler et al. (2022) show that TRENDY models in general perform better for certain parameters than for others. They find that TRENDY models have a higher skill in modeling surface runoff than vegetation biomass and GPP. The lowest skill scores and the largest deviations are reported for the modeled leaf area index, NEE, and below all soil organic carbon.

1.4.2. FLUXCOM and GFED

The second bottom-up dataset we use is the FLUXCOM dataset (Jung et al., 2020). FLUXCOM upscales local eddy covariance tower CO_2 flux measurements to global scale by using machine learning models combined with Moderate Resolution Imaging Spectroradiometer (MODIS, Justice et al., 2002) satellite remote sensing data (Tramontana et al., 2016; Jung et al., 2020). In total 224 flux measurement towers of the FLUXNET dataset are used (Tramontana et al., 2016). Only eight of the towers are in the study regions of this thesis (four in Australia, three in southern Africa, and one in the South American Temperate region). Nine different machine learning algorithms are trained and used to predict NEE, GPP, and TER fluxes globally with a spatial resolution of 0.08° x 0.08° and a temporal resolution of eight days. The final dataset is the ensemble mean of the nine flux estimates. We use the FLUXCOM NEE dataset version 1 (setup RS_V006) as described in Jung et al. (2020).

To compare the NEE estimate of FLUXCOM with the NBP estimates of the atmospheric inversions and TRENDY models, we add fire emissions to FLUXCOM. To do so, we use CO_2 emissions provided by the Global Fire Emission Database (GFED, van der Werf et al., 2017). GFED uses the burned area and the active fire product of MODIS (Giglio et al., 2013) combined with biomass estimates of the Carnegie-Ames-Stanford-Approach biogeochemical model (CASA model) and biome-specific emission factors to estimate fire CO_2 emissions (van der Werf et al., 2017).

1.5. Analyzing Carbon Flux Dynamics by Combining Top-down and Bottom-up Estimates

This section provides an overview of the methodological workflow used in the publications presented in this thesis. In Section 1.5.1 to Section 1.5.4 the methods used in Metz et al. (2023), Metz et al. (2025a), and Vardag et al. (2025) are outlined. Section 1.5.4 also describes the analysis workflow in Metz et al. (2025b). A schematic illustration of the methods used is given in Figure 1.10. Details on the individual analysis steps can be found in the corresponding publication and its supplemental material.

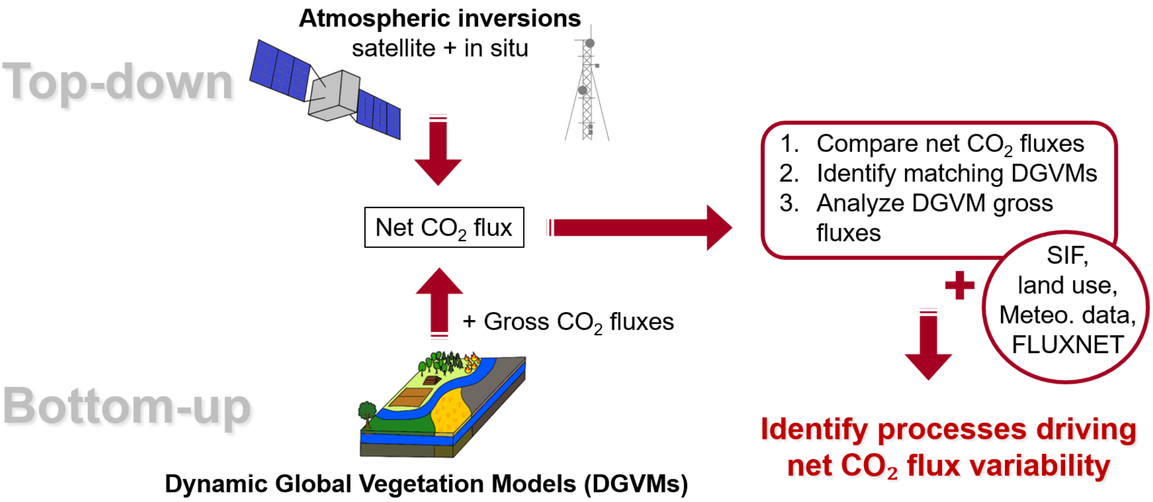

Figure 1.10.: Schematic illustration of the used methods. The top-down net CO_2 flux estimates of atmospheric inversions based on satellite and in situ measurements are compared with bottom-up net CO_2 flux estimates by DGVMs. The DGVMs estimating fluxes which align well with the top-down estimates are selected. Their modeled gross fluxes are used for further analysis of the vegetation processes driving the net CO_2 exchange. SIF measurements are used to further evaluate the DGVMs and to analyze the seasonality in vegetation biomass buildup. Land use data and meteorological data are utilized to examine the impact of land cover and climate conditions on the fluxes. Finally local CO_2 flux measurements serve to analyze local flux variability in response to local temperature and soil moisture dynamics.

1.5.1. Regional Analysis of Satellite XCO_2 Measurements

For our analyses we use GOSAT XCO_2 measurements retrieved with ACOS and RemoTeC (see Section 1.2.1). Before using the satellite measurements in an atmospheric inversion, we examine their robustness in the region of interest. We are especially interested in the following questions:

How does the sampling of the satellite measurements impact the continental signal?

GOSAT overpasses are around 12:50 local time with a return time of three days (Suto et al., 2021). However, clouds and aerosols in the atmosphere can prevent reliable measurements. The sampling of a region can, therefore, be inhomogeneous in space and time. When analyzing the regional CO_2 concentration variability, it is important to verify whether the entire analyzed region drives the signal or whether the region is temporally inhomogeneously sampled. In Figure 1.1, for example, one can see that the measurement density is lower over the Andes in the South American Temperate region and in the north of the southern Africa regions towards the equator. Such sampling assessments can provide important information for the later analyses of satellite-based atmospheric inversion fluxes and are included in the supplement of Metz et al. (2023, Figure S4) and Metz et al. (2025a, Figure A5 and A6).

Are there systematic features in the seasonal or interannual variability of the CO_2 concentrations?

To access the variability in CO_2 concentrations over the region of interest more easily, we detrend the data by subtracting the background of increasing global CO_2 concentrations from the GOSAT measurements. As background, we assume linearly increasing global CO_2 concentrations and use the annual growth rates of CO_2 concentrations provided by NOAA (NOAA, 2024, see Figure 1.11). The remaining XCO_2 signal is then dominated by the regional seasonal variability of CO_2 concentrations. In the given example of detrended monthly averaged GOSAT XCO_2 in Figure 1.11, we can directly see that the concentrations are the highest at the end of each year. Moreover, CO_2 concentrations are especially low in 2011 and 2017 over southern Africa.

How do the GOSAT measurements compare with other CO_2 concentration measurements?

In addition to GOSAT, XCO_2 can be obtained from other satellites and ground-based total column measurements. By comparing the two GOSAT XCO_2 retrievals (ACOS and RemoTeC) with each other and with measurements of other devices, the robustness of the found signal can be assessed. Next to the OCO-2 satellite, which started measuring five years later than GOSAT, there are ground-based stations of the Total Carbon Column Observing Network (TCCON, Wunch et al., 2011) and the Collaborative Carbon Column Observing Network (COCCON, Frey et al., 2019) that perform total column measurements of CO_2. When comparing GOSAT XCO_2 with these measurements, one needs to be aware of the different temporal and spatial mea-

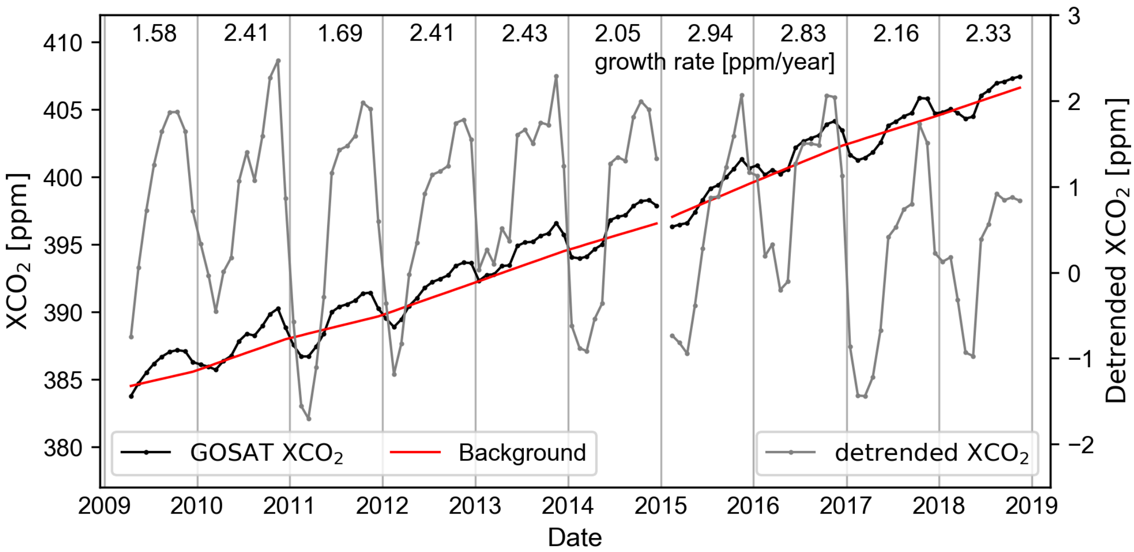

Figure 1.11.: Detrending monthly and regionally averaged XCO_2. The linearly increasing global atmospheric CO_2 concentration background (red line with left y-axis) is calculated using the growth rates reported by NOAA (2024) given on top. The background is subtracted from the total monthly mean XCO_2 (black) over southern Africa to obtain the detrended XCO_2 in grey.

surement sampling. TCCON and COCCON stations are at certain fixed locations, and overpasses of GOSAT need to be selected to accurately perform a measurement comparison. OCO-2 has a slightly different ground track and a different sampling than GOSAT. Moreover, also the ACOS and RemoTeC datasets differ in the included GOSAT measurements, as both retrievals apply different filter criteria. Hence, also when comparing different satellite datasets, a cosampling by only selecting co-located measurements is needed. For example, a discussion of the effect of cosampling is included in Metz et al. (2025a) in Figure A1.

1.5.2. Flux Estimates Based on Satellite and In Situ CO_2 Data

As described in Section 1.3.2, we assimilate GOSAT XCO_2 (not detrended) and in situ measurements in the atmospheric inversion TM5-4DVar. By comparing the different measurement configurations (TM5-4DVar/GOSAT+IS, TM5-4DVar/IS, TM5-4DVar/prior) we can evaluate the impact of the different measurement types on the estimated CO_2 fluxes. If the estimated fluxes closely follow the prior fluxes, this can indicate that they are only weakly constraint by the atmospheric concentration measurements. Either because only few measurements exist in the respective region or because the inversion weights the prior fluxes more strongly than the measurements (see Section 1.3.1).

To verify the consistency of our flux estimates and findings, we compare our estimated fluxes with those provided by the OCO-2 MIP ensemble. Firstly, we assess how well the TM5-4DVar inversions align with the OCO-2 MIP. Specifically, we compare TM5-4DVar/IS with MIP/IS estimates and we evaluate how well TM5-4DVar/GOSAT+IS aligns with MIP/OCO-2+IS. Secondly, we verify that our findings regarding the information content of the used measurement types (satellite and in situ) as described above, also hold true for OCO-2 MIP. To do so, we analyze whether the estimated fluxes of the satellite inversions differ significantly from those of the in-situ-only inversions and the prior fluxes, i.e. we analyze whether the differences between satellite-based inversion fluxes, in-situ-only inversion fluxes, and the prior fluxes are larger than the spreads within the individual inversion groups. If this is the case, we can see that the two measurement types provide (different) information on the regional carbon fluxes.

For our analyses, we average the fluxes regionally and monthly. Even though TM5-4DVar optimizes the fluxes on finer scale of weekly, 2° latitude x 3° longitude, the fluxes on this resolution are highly underconstrained due to the comparably sparse measurement density. The allocation of the high-resolution fluxes is, therefore, highly uncertain. Only by averaging the fluxes spatially and temporally, a sufficient amount of measurements is available to constrain the fluxes.

To assess the fraction of CO_2 exchange between land and atmosphere, which is only caused by vegetation processes (that is, NEE), we subtract GFED fire emissions (Section 1.4.2) from TM5-4DVar/GOSAT+IS. We thereby neglect the 'other' disturbance fluxes in Equation 1.2, i.e. we assume that land-use change and lateral fluxes are of minor importance for the seasonal and interannual variability in the regional carbon cycle compared to GPP, Ra, and Rh. We test this assumption and find that estimates of riverine fluxes and land-use change fluxes are smaller than 1%-2% of the monthly gross fluxes (GPP, Ra, and Rh) for our study regions (see Appendix B.1). Thus, we do not expect a substantial impact of riverine fluxes and land-use change fluxes on the seasonal and interannual variability in CO_2 fluxes in our study regions, and neglecting the 'other' disturbance fluxes is a valid assumption for our analyses.

To summarize, by comparing the optimized fluxes of the different inversion setups, we aim at identifying which measurement types can provide information about the carbon cycle in our regions of interest. By choosing the inversion setup which uses the most measurement information instead of mainly relying on prior information, we improve the carbon flux estimates in the study regions. We can then use these flux estimates for further analyses.

1.5.3. Flux Estimates by DGVMs

The DGVMs in the TRENDY ensemble do not only model the net fluxes between atmosphere and land, but also model the underlying vegetation fluxes like GPP and

TER. Furthermore, their estimates are derived by simulating individual vegetation processes such as photosynthesis given the environmental conditions. Hence, they inform not only on the carbon exchange fluxes, but also provide information on the processes driving the net carbon exchange. However, as most of the models are originally developed for different regions, the TRENDY models largely differ in the modeled processes and their specific implementation. This results in substantially varying model estimates of the fluxes in specific regions, which often do not agree in magnitude, seasonal timing, and interannual variability as found in Teckentrup et al. (2021), Metz et al. (2023), Metz et al. (2025a), Vardag et al. (2025), and Foster et al. (2024). Hence, regional CO_2 flux estimates of the TRENDY ensemble have large uncertainties.

We use our TM5-4DVar/GOSAT+IS fluxes and GOME-2 SIF measurements as atmospheric constraints on the NBP, NEE, and GPP fluxes, respectively. By selecting only the TRENDY models that align best with the atmospheric constraints, we identify those models that most accurately capture the carbon dynamics in the respective region. The selected models can then be used to further analyze the gross fluxes driving the net exchange between land and atmosphere. Taking into account climatic conditions and knowledge about the implemented processes in the selected TRENDY models, the vegetation processes driving the carbon flux variability can be identified. In doing so, we combine the advantages of the top-down and bottom-up approaches. We use our measurement-based fluxes which most accurately represent the true atmospheric conditions and use the consistent vegetation models to analyze the underlying vegetation fluxes and identify driving processes and climatic drivers.

1.5.4. Local Flux Measurements Can Help to Track Down Vegetation Processes

In the publications of this thesis we use flux tower measurements of the FLUXNET and OzFlux network. Flux towers measure the CO_2 fluxes between surface and atmosphere and environmental conditions such as soil moisture and temperature every 30 minutes (see Section 1.2.2).

In the first three publications, we use flux tower measurements to verify our hypothesis that the Birch effect takes place in our study regions. The flux tower measurements have the disadvantage of not being representative for the whole study regions as they only inform about fluxes in their vicinity. Hence, they cannot be used to constrain a continent's carbon budget. This is especially the case in the South American Temperate region and southern Africa, where only one and three flux towers are located in the semiarid areas of each region, respectively. However, the local scale of the measurements also has advantages. The measurements are representative of the local vegetation exchange processes and do not average over multiple exchange processes in different areas as our regional flux estimates do. Furthermore, flux towers provide high temporal resolution flux measurements compared to the atmospheric inversion and TRENDY fluxes. We use daily averages of the CO_2 flux, soil moisture, and temperature measurements. By doing so, we can observe the immediate response of the local CO_2 fluxes to precipitation, soil moisture, and temperature changes. While this does not imply that the observed effects take place in the entire study region, we can prove the existence of certain responses occurring at least at the flux tower locations in semiarid regions.

In Metz et al. (2025b) we use 40 OzFlux flux towers to investigate the response of TER to soil moisture in Australia. We perform linear regressions of the daily averages of measured TER and soil moisture and use the estimated slopes as a measure of the sensitivity of TER to soil moisture. The flux towers cover a broad range of climatic conditions and ecosystems in Australia (see Figure 1.8). This enables us to analyze the direct response of TER to soil moisture in different aridity regimes. Furthermore, we compare the found sensitivities to those calculated with daily resolved modeled CO_2 fluxes of the vegetation model LPJ at the individual flux tower locations. In doing so, the flux tower measurements provide the opportunity to assess the performance of vegetation models with respect to the implementations of certain parameters.

1.6. Overview of Publications

The aim of the present thesis is to evaluate the potential of satellite data to improve CO_2 flux estimates in semiarid regions in the Southern Hemisphere and to analyze the seasonal and interannual variability of these fluxes to better understand the climatic drivers of the carbon cycle in these remote regions. The thesis is composed of three peer-reviewed publications and one unpublished manuscript. In the following, short summaries of the publications and the manuscript are given.

Publication 1

The first publication (Metz et al., 2023) investigates the dynamics in satellite-based CO_2 fluxes and total column concentrations in Australia. We find large CO_2 emissions at the end of the year, which largely control the interannual variability in the Australian CO_2 fluxes. In situ measurement-based atmospheric inversions and the ensemble mean of TRENDY vegetation models fail in capturing these carbon flux dynamics accurately. By identifying a subset of vegetation models that reproduce the end of the year emissions, we find that they are caused by a dephasing of Rh and GPP at the beginning of the rainy season in the semiarid regions of Australia. Rewetting conditions are the main driver of the early increase in Rh compared to GPP. The findings indicate a relevant contribution of the formerly only locally known Birch effect to the continental-scale CO_2 emissions.

This publication shows that satellite measurements can provide the basis for observing CO_2 flux dynamics and pinpointing individual CO_2 exchange processes in remote regions. We therewith improve the accuracy of CO_2 flux estimates and provide specific recommendations on how to improve vegetation models for Australia.

Publication 2

In the second publication (Metz et al., 2025a), we use the GOSAT-based CO_2 fluxes to analyze the southern African carbon cycle. We compare GOSAT-based and OCO-2-based CO_2 fluxes. A good agreement was found for those MIP/OCO-2+IS models that put sufficient weight on the used OCO-2 measurements. Furthermore, we find a large spread in the CO_2 fluxes modeled by TRENDY models. By using the satellite-based CO_2 fluxes and GOME-2 SIF measurements as atmospheric constraints on the TRENDY NBP, NEE, and GPP fluxes, respectively, we can identify three vegetation models that capture well the carbon dynamics in southern Africa. Using the subset of vegetation models, we find a dephasing of Rh and GPP at the start of the rainy season that shapes the seasonal cycle of carbon fluxes. The interannual variability of the CO_2 fluxes is, however, driven by GPP.

This study emphasizes the advantages of using satellite-based atmospheric constraints to reduce the uncertainty in carbon flux estimates in southern Africa and to further track down the processes driving the variability in CO_2 fluxes. This publication shows that the methods used in Metz et al. (2023) can be applied to other regions with a sparse in situ measurement coverage. It reveals the impact of soil rewetting-driven Rh on the seasonal cycle of semiarid CO_2 fluxes in southern Africa.

Publication 3

In this publication (Vardag et al., 2025) the CO_2 flux variability in the South American Temperate region is investigated. We find large discrepancies in CO_2 flux estimates of models within the TRENDY project. We can identify two TRENDY models that align well with GOSAT-based CO_2 fluxes. Using this subset of vegetation models, we can pinpoint the semiarid region in the east to drive the seasonality of the CO_2 fluxes in the whole study region. We find a clear dephasing of Rh and GPP in this eastern semiarid area, which drives the seasonality in CO_2 fluxes. Local flux measurements show the existence of the Birch effect in this region and suggest the importance of the effect on a regional scale in the South American Temperate region.

This study underlines the importance of accurately modeling the impact of soil rewetting on soil respiration in semiarid regions. Together with Metz et al. (2023) and Metz et al. (2025a), it shows the advantages of satellite data and the importance of Rh emission dynamics in the semiarid regions in the Southern Hemisphere.

Publication 4

In this submitted manuscript (Metz et al., 2025b), we analyze the sensitivity of TER to soil moisture by using measurements of 40 OzFlux flux towers in Australia. We find the highest sensitivities at semiarid measurement sites. In contrast to that, TER measured at humid stations does not show a significant dependence on soil moisture. We compare these findings with TER dynamics modeled by the vegetation model LPJ. In agreement with the OzFlux measurements, the modeled TER sensitivities at dry stations are high. However, LPJ also shows significant sensitivities at humid stations, which is in contrast to the OzFlux results. Our findings indicate that the response of Rh to soil moisture implemented in LPJ needs to be reduced for high soil moisture levels. Furthermore, we suggest that a closer evaluation of soil moisture dynamics in LPJ is required. Both can help to enable LPJ to capture the carbon flux dynamics in the different aridity regimes in Australia more accurately.

This study deepens the findings of Metz et al. (2023) with respect to possible improvements of vegetation models for Australian CO_2 flux estimations. The study provides specific recommendations for LPJ to improve the TER response to soil moisture in different aridity regimes in Australia.

2. Publications

This chapter displays the publications included in this thesis. Due to licensing reasons for Metz et al. (2023), the manuscript version ”accepted for publication”, instead of the finally published one, is reproduced here. The second and third publications are included as published in *Biogeosciences* and *Geophysical Research Letters*, respectively, without any changes. The last publication is included as an unpublished manuscript submitted to *Environmental Research Letters*.

The first publication, Metz et al. (2023), is published with the following Copyright: Please find more information about the license for the reuse of the publication here: `https://www.science.org/do/10.5555/science-journals-editorial-policies/full/standardandusgovtlicensetopublish_2024-1733323122573.pdf`. The second publication (Metz et al., 2025a) and the third publication (Vardag et al., 2025) are distributed under the Creative Commons Attribution 4.0 license (https://creativecommons.org/licenses/by/4.0/).

The first Section 2.1 summarizes the author contributions of the individual publications. It is followed by the publications in the following order: Metz et al. (2023) in Section 2.2, Metz et al. (2025a) in Section 2.3, Vardag et al. (2025) in Section 2.4, and finally the manuscript of Metz et al. (2025b) in Section 2.5. The publications have not been used in other dissertations.

2.1. General Information and Author Contributions

Publication 1

Soil Respiration–driven CO_2 Pulses Dominate Australia's Flux Variability

Published on March 31st, 2023 in *Science*

`https://www.science.org/doi/epdf/10.1126/science.add7833`

Author list: Eva-Marie Metz, Sanam N. Vardag, Sourish Basu, Martin Jung, Bernhard Ahrens, Tarek El-Madany, Stephen Sitch, Vivek K. Arora, Peter R. Briggs, Pierre Friedlingstein, Daniel S. Goll, Atul K. Jain, Etsushi Kato, Danica Lombardozzi, Julia E. M. S. Nabel, Benjamin Poulter, Roland Séférian, Hanqin Tian, Andrew Wiltshire, Wenping Yuan, Xu Yue, Sönke Zaehle, Nicholas M. Deutscher, David W. T. Griffith, André Butz

Author contributions: I am the main author of the publication. I conducted the complete data analyses and visualization of the data. Together with André Butz and Sanam Vardag, I developed the applied analysis methods and conceptualization. The paper was written jointly by André Butz, Sanam Vardag, Martin Jung, Sourish Basu, and me.

Publication 2

Seasonal and Interannual Variability in CO_2 Fluxes in Southern Africa Seen by GOSAT

Published on January 30th, 2025 in *Biogeoscience*

https://doi.org/10.5194/bg-22-555-2025

Author list: Eva-Marie Metz, Sanam N. Vardag, Sourish Basu, Martin Jung, André Butz

Author contributions: I am the main author of the publication. I analyzed and visualized the data. Together with André Butz and Sanam Vardag, I developed the applied analysis methods and conceptualization. I wrote the first draft which was then finalized with the feedback of André Butz, Sanam Vardag, Martin Jung and Sourish Basu.

Publication 3

CO_2 Release during Soil Rewetting Shapes the Seasonal Carbon Dynamics in South American Temperate Region

Published on April 22nd, 2025 in *Geophysical Research Letters*

https://doi.org/10.1029/2024GL111725

Author list: Sanam Noreen Vardag, Eva-Marie Metz, Lukas Artelt, Sourish Basu, André Butz

Author contributions: I am an important contributor to this publication. I together with Lukas Artelt did the data analyses and visualization. The basis of the analyses scripts have been written by me and further developed and adapted by Lukas Artelt. Together with André Butz and Sanam Vardag, I developed the applied analysis methods and conceptualization. Sanam Vardag wrote the first draft, which got finalized with the feedback of me and the other co-authors.

Publication 4: Manuscript draft

Responses of Terrestrial Ecosystem Respiration to Soil Moisture Across Australia's Aridity Regimes

Submitted to *Environmental Research Letters*

Author list: Eva-Marie Metz, Sanam N. Vardag, Andrew F. Feldman, Benjamin Poulter, Thomas Colligan, Brenden J. Fischer-Femal, André Butz

Author contributions: I am the main author of the publication. I analyzed and visualized the data. The development of the applied analysis methods and the conceptualization was carried out by me together with André Butz, Sanam Vardag, Andrew Feldman, and Benjamin Poulter. I wrote the first draft, which was then finalized with the feedback of all co-authors.

2.2. Publication 1: Soil Respiration–driven CO_2 Pulses Dominate Australia's Flux Variability

Eva-Marie Metz, Sanam N. Vardag, Sourish Basu, Martin Jung, Bernhard Ahrens, Tarek El-Madany, Stephen Sitch, Vivek K. Arora, Peter R. Briggs, Pierre Friedlingstein, Daniel S. Goll, Atul K. Jain, Etsushi Kato, Danica Lombardozzi, Julia E. M. S. Nabel, Benjamin Poulter, Roland Séférian, Hanqin Tian, Andrew Wiltshire, Wenping Yuan, Xu Yue, Sönke Zaehle, Nicholas M. Deutscher, David W. T. Griffith, André Butz

From

Metz, E.-M., Vardag, S. N., Basu, S., Jung, M., Ahrens, B., El-Madany, T., Sitch, S., Arora, V. K., Briggs, P. R., Friedlingstein, P., Goll, D. S., Jain, A. K., Kato, E., Lombardozzi, D., Nabel, Julia E. M. S., Poulter, B., Séférian, R., Tian, H., Wiltshire, A., Yuan, W., Yue, X., Zaehle, S., Deutscher, N. M., Griffith, D. W. T., and Butz, A.: Soil respiration-driven CO2 pulses dominate Australia's flux variability, Science, 379, 1332–1335, https://doi.org/10.1126/science.add7833, 2023.

Please note that references 50-130 of the supplemental materials are already given in the reference list of the main manuscript. For this reason, they are not given again with the supplementary materials as stated in the original Supplementary Materials list in the accepted manuscript.

Title: Soil-respiration driven CO_2 pulses dominate Australia's flux variability

Authors: Eva-Marie Metz[1*], Sanam N. Vardag[1,2], Sourish Basu[3,4], Martin Jung[5], Bernhard Ahrens[5], Tarek El-Madany[5], Stephen Sitch[6], Vivek K. Arora[7], Peter R. Briggs[8], Pierre Friedlingstein[9,10], Daniel S. Goll[11], Atul K. Jain[12], Etsushi Kato[13], Danica Lombardozzi[14], Julia E.M.S. Nabel[5,15], Benjamin Poulter[16], Roland Séférian[17], Hanqin Tian[18], Andrew Wiltshire[19], Wenping Yuan[20], Xu Yue[21], Sönke Zaehle[5], Nicholas M. Deutscher[22], David W.T. Griffith[22] and André Butz[1,2,23*]

Affiliations:

[1]Institute of Environmental Physics, Heidelberg University; Im Neuenheimer Feld 229, Heidelberg, 69120, Germany.

[2]Heidelberg Center for the Environment (HCE), Heidelberg University; Im Neuenheimer Feld, 130.1, Heidelberg, 69120, Germany.

[3]Goddard Space Flight Center, NASA; 8800 Greenbelt Rd, Greenbelt, 20771, Maryland, USA.

[4]Earth System Science Interdisciplinary Center, University of Maryland; 5825 University Research Court, Suite 4001, College Park, 20740, Maryland, USA.

[5]Max Planck Institute for Biogeochemistry; Hans-Knöll-Straße 10, Jena, 07745, Germany.

[6]College of Life and Environmental Sciences, University of Exeter; North Park Road, Exeter, EX4 4RJ, Devon, UK.

[7]Canadian Centre for Climate Modelling and Analysis, Environment and Climate Change Canada; 200-2474 Arbutus Road, Victoria, B.C., V8N 1V9, Canada.

[8]Climate Science Centre, CSIRO Oceans and Atmosphere; Canberra, ACT 2601, Australia.

[9]College of Engineering, Mathematics and Physical Sciences, University of Exeter; Exeter EX4 4QF, United Kingdom.

[10]Laboratoire de Météorologie Dynamique, Institut Pierre-Simon Laplace, CNRS-ENS-UPMC-X, Département de Géosciences, Ecole Normale Supérieure; 24 rue Lhomond, 75005 Paris, France.

[11]Université Paris Saclay, CEA-CNRS-UVSQ, LSCE/IPSL; Gif sur Yvette, France.

[12]Department of Atmospheric Sciences, University of Illinois; Urbana, IL 61801, USA.

[13]Institute of Applied Energy; Tokyo 105-0003, Japan.

[14]Climate and Global Dynamics Laboratory, National Center for Atmospheric Research; 1850 Table Mesa Drive Boulder, CO 80305, USA

[15]Max Planck Institute for Meteorology; Bundesstr. 53, 20146 Hamburg, Germany.

[16]Biospheric Sciences Laboratory, Goddard Space Flight Center, NASA; Greenbelt, 20771, Maryland, USA.

[17]CNRM, Université de Toulouse, Météo-France, CNRS; Toulouse, France.

[18]Schiller Institute for Integrated Science and Society, Department of Earth and Environmental Sciences, Boston College, Chestnut Hill, MA 02467, USA

[19]Met Office Hadley Centre; FitzRoy Road, Exeter EX1 3PB, UK.

[20]School of Atmospheric Sciences, Southern Marine Science and Engineering Guangdong Laboratory (Zhuhai), Sun Yat-sen University; Zhuhai 519082, China.

[21]Jiangsu Key Laboratory of Atmospheric Environment Monitoring and Pollution Control, Jiangsu Collaborative Innovation Center of Atmospheric Environment and Equipment Technology, School of Environmental Science and Engineering, Nanjing University of Information Science & Technology (NUIST), Nanjing 210044, China

[22]Centre for Atmospheric Chemistry, School of Earth, Atmospheric and Life Sciences, University of Wollongong; Wollongong, NSW, 2522, Australia

[23]Interdisciplinary Center for Scientific Computing (IWR), Heidelberg University; Im Neuenheimer Feld, 205, Heidelberg, 69120, Germany.

*Corresponding author. Email: eva-marie.metz@iup.uni-heidelberg.de, andre.butz@iup.uni-heidelberg.de

Abstract: The Australian continent contributes substantially to the year-to-year variability of the global terrestrial carbon dioxide (CO_2) sink. However, the scarcity of in-situ observations in remote areas prevents deciphering the processes that force the CO_2 flux variability. Here, examining atmospheric CO_2 measurements from satellites in the period 2009-2018, we find recurrent end-of-dry-season CO_2 pulses over the Australian continent. These pulses largely control the year-to-year variability of Australia's CO_2 balance, due to 2-3 times higher seasonal variations compared to previous top-down inversions and bottom-up estimates. The pulses occur shortly after the onset of rainfall and are driven by enhanced soil-respiration preceding photosynthetic uptake in Australia’s semi-arid regions. The suggested continental-scale relevance of soil-rewetting processes has large implications for our understanding and modelling of global climate-carbon cycle feedbacks.

One Sentence Summary: Satellite CO_2 measurements find large CO_2 pulses over Australia attributable to rewetting of seasonally dry soils.

Terrestrial ecosystems drive the seasonal and year-to-year variability of the global carbon dioxide (CO_2) sink (*1*). Previous research identified semi-arid regions as hotspots of global CO_2 balance inter-annual variability (*2–5*) due to their large sensitivity of photosynthetic carbon uptake to fluctuations in water availability (*6, 7*). The Australian continent is primarily covered with semi-arid ecosystems and experiences large variations in rainfall. This makes Australia particularly relevant for the variability in the global carbon cycle (*8–13*), contributing up to 60% to yearly anomalies of the global terrestrial CO_2 sink (*2*).

However, current approaches for attributing global CO_2 sink variations to certain regions and mechanisms are highly uncertain, which limits our ability to model climate-carbon cycle feedbacks and project future climate (*14, 15*). Global process-based ecosystem models underestimate observed CO_2 flux variability across semi-arid sites due to the complexity of carbon-water cycle interactions and the diversity of ecosystem responses to water fluctuations (*16, 17*). The same holds true for machine learning based models trained on local carbon flux observations (*18, 19*), which is due to the scarcity of available flux measurements in low-latitude semi-arid regions (*20*) as well as due to the inability to represent potentially important non-instantaneous carry-over effects (*21*). Atmospheric transport inversions based on in-situ measurements of airborne CO_2 also suffer from the scarcity of observations in remote areas and thus the inversions cannot reliably attribute CO_2 flux variability to specific regions, despite growing monitoring capacities (*22, 23*). However, recent satellite observations of atmospheric column CO_2 deliver data where ground-based in-situ concentration measurements and carbon flux networks are sparse and thus, satellite CO_2 data can fill important gaps and provide new constraints on regional scale patterns and processes (*8, 24–28*).

Here, using satellite observations of atmospheric CO_2 concentrations from the Greenhouse Gases Observing Satellite (GOSAT) for the period 2009 to 2018, we identify a net CO_2 pulse to the atmosphere that occurs over Australia at the end of the dry season in most years with variable magnitude. We show that this pattern appears to dominate the seasonal and year-to-year variations of Australia's CO_2 balance for that period, while it is not evident in traditional atmospheric inversions using in-situ measurements only, in the FLUXCOM machine learning based extrapolations of in-situ flux measurements (18, 20), and most process-based ecosystem models of the TRENDY initiative (29). The few process-based TRENDY models that reproduce the CO_2 pulse pattern qualitatively suggest that it is caused by rapid respiratory carbon release with the onset of the rainy season while the increase in photosynthetic carbon uptake lags behind. This observed process is consistent with the phenomenon of respiration pulses after rewetting events discussed in the context of the "Birch effect" (*30, 31*). Such pulses have been described extensively in local studies of water-limited systems (*32*) but their large-scale relevance remained unknown.

Atmospheric CO_2 peak over Australia

The Greenhouse Gases Observing Satellite (GOSAT) has been delivering global measurements of the column-average dry-air mole fractions ("concentrations") of atmospheric CO_2 since its launch in 2009 (*33*). After subtracting the secular trend (*34*), the record of GOSAT concentrations for the period 2009-2018 (Fig. 1) reveals a seasonal pattern above Australia with CO_2 draw-down in March, April, May (MAM) and a CO_2 peak of variable magnitude at the end of the dry season in October, November, December (OND). These patterns are consistent among two retrievals independently applied to GOSAT (GOSAT/RemoTeC (*35*) and GOSAT/ACOS (*36*), Table S1) and they are present in CO_2 concentrations measured by the Orbiting Carbon Observatory (OCO-2 (*37, 38*), period 2015 to 2018, Table S1) as well as in ground-based data of the Total Carbon Column Observing Network (*39*) (Fig. S1 and S2).

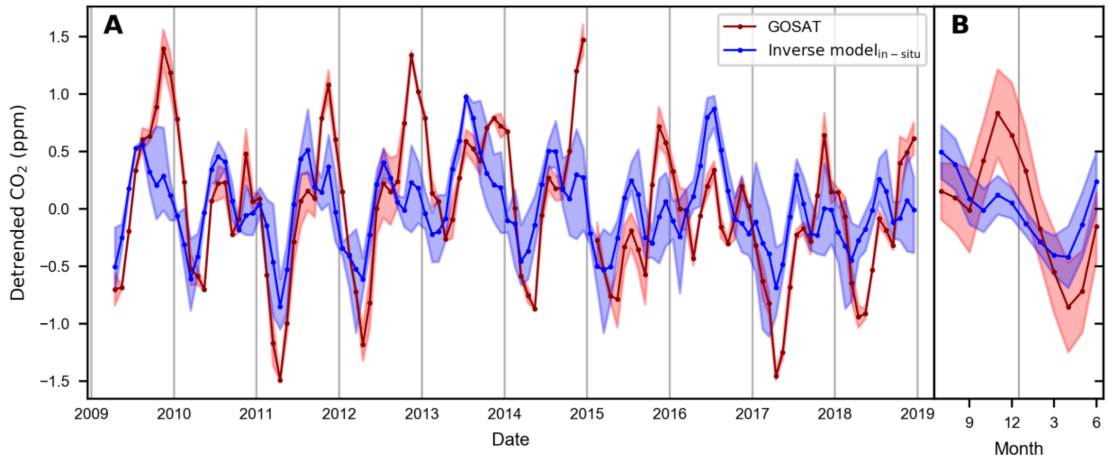

Fig. 1. Detrended CO_2 concentrations over Australia from satellite and models. (A) Detrended column-average dry-air mole fractions of CO_2 measured by GOSAT (red) and simulated by inverse models assimilating in-situ ground-based measurements (blue). Data are monthly averages for Australia. Red shading indicates the range of the GOSAT/RemoTeC and GOSAT/ACOS algorithms. Blue shading indicates the range of the CarbonTracker, CAMS, and TM5-4DVAR inverse models. **(B)** Mean and standard deviation (shading) over the period 2009 to 2018.

In contrast, the atmospheric column CO_2 concentrations simulated by three inverse atmospheric transport models (CarbonTracker CT2019B (*40*), CAMS (*41*), TM5-4DVAR (*42*)) underestimate the CO_2 draw-down in MAM and lack the CO_2 pulses in OND (Fig. 1). Driven by atmospheric winds, these transport models deliver concentration fields that are optimally compatible with in-situ measured CO_2 concentrations and the a priori biogenic, oceanic, fire and fossil CO_2 surface-atmosphere fluxes (*34*). However, due to their sparsity in and around Australia (see Fig. S3 compared to Fig. S4), the in-situ measurements provide only marginal constraints on the regional flux balance. Thus, the discrepancy between CO_2 concentrations from GOSAT and traditional in-situ based atmospheric inversions hints at the existence of a carbon release mechanism in Australian ecosystems that has remained undetected by the existing in-situ CO_2 monitoring system.

Australian top-down and bottom-up fluxes

To improve on the surface flux estimates for Australia, we feed the GOSAT CO_2 concentrations into one of the atmospheric inverse models (TM5-4DVAR) together with the in-situ CO_2 measurements. We find indeed that the recurring end-of-dry-season CO_2 concentration peaks are attributed to a carbon release pattern originating from land ecosystems, which is not present in the inversions when assimilating in-situ CO_2 data alone (Fig. 2A and Fig. S5).

Our new estimates of Australia's carbon balance variability based on assimilating GOSAT together with in-situ data show a nearly doubled peak-to-peak amplitude of the seasonal cycle (175±40 TgC/month, mean ± standard deviation over the 2009 to 2018 period, July-to-June peak-to-peak amplitude) compared to the in-situ-only inversions (88±13 TgC/month). Moreover, the end-of-dry-season CO_2 pulses found by the GOSAT inversions imply a more than 4-fold greater year-to-year variability of the annual CO_2 fluxes (0.207 PgC/a, standard deviation over the 2010 to 2018 period) than for the in-situ-only inversions (0.039 PgC/a) (Fig. S6 and Table S2). Fluxes obtained by assimilating OCO-2 together with in-situ data for the period 2015 to 2018 show the same end-of-dry-season pulses and agree well with the fluxes of the GOSAT inversion (see Fig. S7).

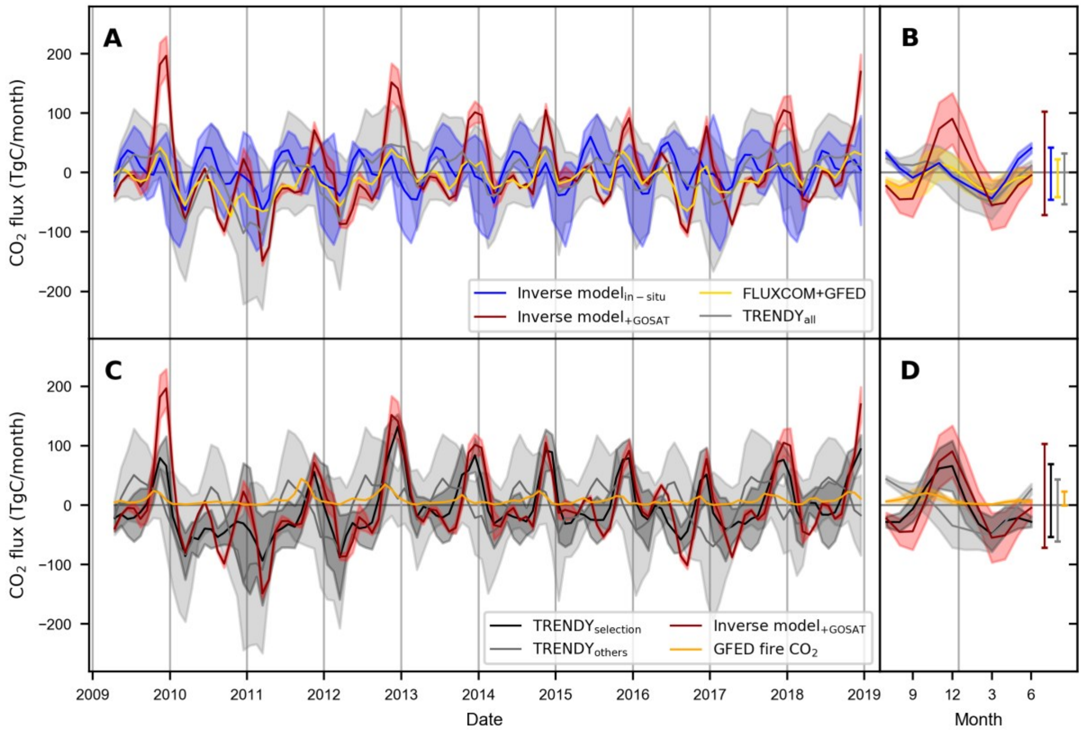

Fig. 2. Australian net CO_2 fluxes. (A) Top-down estimates of the net monthly Australian carbon fluxes inferred by in-situ CO_2 measurements based inverse models (blue) and by TM5-4DVAR assimilating in-situ measurements together with GOSAT observations (red), compared to bottom-up FLUXCOM+GFED NBP (yellow) and the TRENDY ensemble mean NBP (grey). Shading indicates the range among the various top-down data streams (in-situ based CarbonTracker, CAMS, and TM5-4DVAR in blue, TM5-4DVAR$_{+GOSAT/RemoTeC}$ and TM5-4DVAR$_{+GOSAT/ACOS}$ in red) and the standard deviation among the TRENDY ensemble (grey). **(C)** NBP of a subgroup of TRENDY models (black) compared to the other models (grey), to the GOSAT inversions (red, same as in (A)) and to GFED fire emissions (orange). Shading as in (A). **(B)** and **(D)** Mean and standard deviation (shading) over the period 2009 to 2018 and the mean peak-to-peak seasonal cycle amplitudes (bars). Positive fluxes correspond to carbon emissions into the atmosphere.

To understand the origin of the CO_2 pulses, we compare to bottom-up estimates from machine learning (FLUXCOM (*18, 20*)) and 18 process-based dynamic global vegetation models (DGVMs) from the TRENDY (v9) ensemble (*42*). Those also provide the component fluxes of gross primary productivity (GPP) and terrestrial ecosystem respiration (TER) enabling the attribution to variations in photosynthetic carbon uptake and respiratory carbon release. We further include fire emissions (FIRE) from the Global Fire Emission Database (GFED) as a potential factor for explaining the pattern. To compare to the top-down inversions, we calculate net biome production (NBP = TER + FIRE - GPP) by adding fire emissions from GFED to net ecosystem exchange (NEE = TER – GPP) from FLUXCOM. That is, positive fluxes correspond to carbon emissions into the atmosphere. For TRENDY, NBP is taken directly from the simulations of the DGVMs. We find that FLUXCOM+GFED derived NBP lacks the end-of-dry-season CO_2 pulses (Fig. 2A) and its seasonal amplitude (64±16 TgC/month) underestimates the one found by the GOSAT inversions by a factor of 3. This could be explained by the sparsity of Australian flux tower data in the training of the FLUXCOM machine learning models (only 4 of 224 sites lie in Australia, see Fig. S3) causing extrapolation errors (*18*), and by known weaknesses in representing certain fluctuations in response to water availability (*19*) or "memory" effects due to non-accounted carbon pool dynamics (*43*). Our analysis further suggests that local and transported fire emissions might contribute at the beginning of the carbon pulses but cannot explain their magnitude and duration (Fig. 2B and Fig. S8).

The ensemble of TRENDY NBP simulations shows a large inter-model spread and also no end-of-dry-season CO_2 pulses on average (Fig. 2A) causing a seasonal amplitude (85±20 TgC/month) which is about half of that of the GOSAT inversions. However, the dry season pulses are present in a subset of five of the TRENDY DGVMs (Fig. 2B and Table S1, 'Characteristics of TRENDY$_{selection}$' in *34*). For this subset, the timing, the duration and the magnitude (except for the year 2009) of the pulses and their seasonal amplitude (123±31 TgC/month) are closer to the pulses found by the GOSAT inversions. This finding suggests that the CO_2 pulses can be explained by ecosystem processes shaping the phasing of photosynthesis and respiration.

Phasing of respiration and photosynthesis

We find that the subset of DGVMs which are in good agreement with the GOSAT inversions reveals a distinctly different seasonal timing of GPP and TER than the other DGVMs. For the selected subset, the CO_2 pulses are driven by TER, which increases rapidly at the onset of the rainy season while GPP takes up only a few weeks later (Fig. 3A). The pulses originate mainly from an early increase of soil-respiration in semi-arid regions (Fig. S9, Fig. S10A). For the other DGMVs, TER and GPP show a mostly synchronous phasing throughout the year yielding no CO_2 pulses (Fig. 3B and Fig. S10B). The precipitation records for the semi-arid regions of Australia (Fig. 3C, Fig. S3) suggest that the soil-respiration driven pulses shown by the GOSAT inversions and the selected TRENDY models are weaker or do not occur in years with anomalously strong precipitation during the dry period (Austral winter) such as in the La Nina years 2010 and 2016. This implies that the observed pulses are conditional on rewetting of dry soils and that it is through the strength of the pulses that climatic conditions have control on Australia's annual CO_2 balance (Fig. S6)

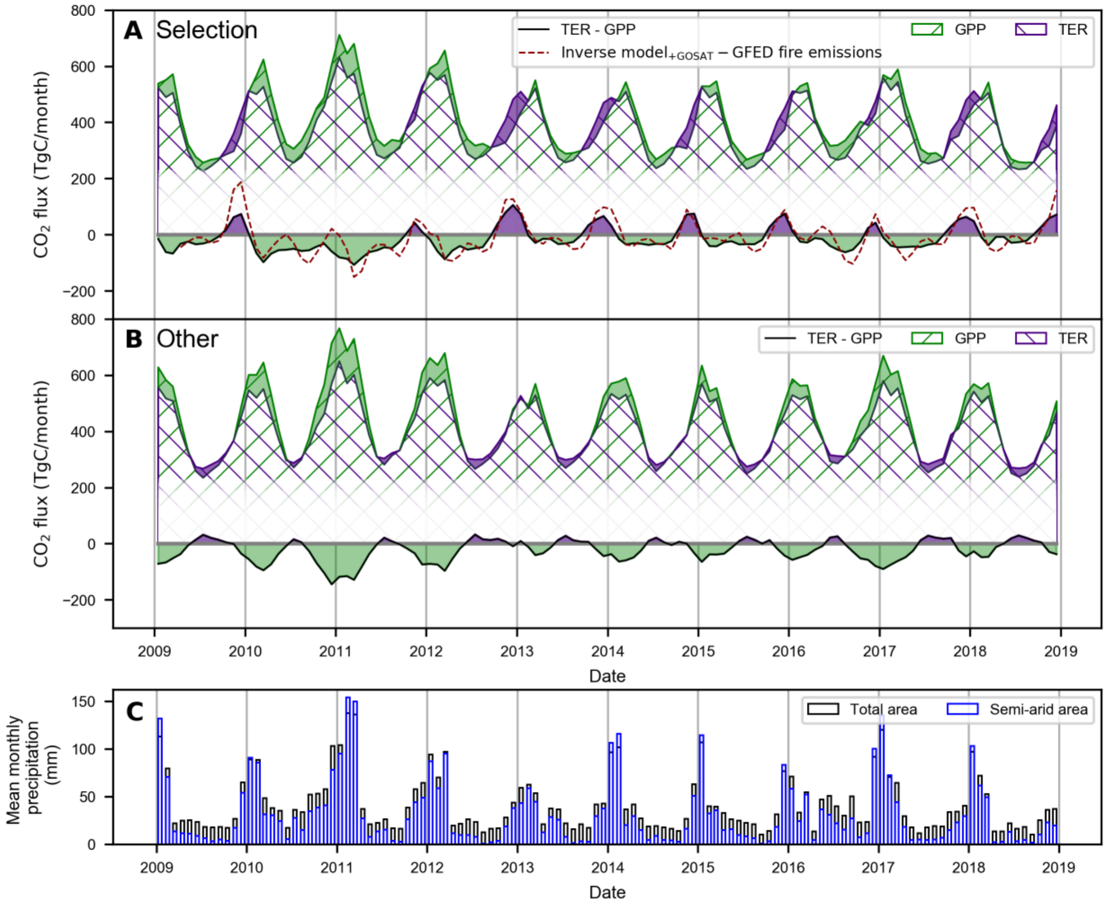

Fig. 3. Seasonal timing of gross carbon fluxes among TRENDY models. (A) Gross primary production (GPP, green) and total respiration (TER, purple) for Australia for the selection of TRENDY DGVMs that replicate the end-of-dry-season CO_2 pulses. The difference of TER and GPP is given in black in the lower part together with GOSAT-based inversion where GFED fire emissions are subtracted (dashed red). **(B)** Same as panel a but for the other TRENDY models that do not replicate the end-of-dry-season CO_2 pulses. **(C)** Mean monthly precipitation over the entire Australian region (black) and the semi-arid part (see Fig. S3) of Australia (blue).

The detected continental-scale CO_2 pulses are consistent with site-level observations of dryland ecosystems which show an asynchronous response of respiration and photosynthesis to precipitation pulses (*44*). The rapid response of microbial respiration to rewetting events, is known as “Birch effect” and has been described in the literature of specific sites in some semi-arid regions for many decades (*30–32*). After being dormant in the dry period, soil microbes are activated by the moisture supply from rainfall. Benefitting from warm soils, accumulated and readily available substrate gets respired quickly going along with rapid growth of microbial populations. These dynamics of soil microbial processes cause respiration CO_2 pulses with rewetting of dry soils which are evident in Australian flux tower data (Fig. S11 and S12). Photodegradation of surface litter (*45*) and the death of microorganisms during the dry period (*46, 47*) may lead to the accumulation of easily decomposable substrate available to microorganisms at the onset of rain. It remains an open question whether the respiration pulses are mainly driven by substrates accumulated during the dry period and to what extent they are fueled by mobilization and decomposition of physically protected carbon (*47*). These processes are not represented explicitly or in detail in the TRENDY DGVMs and thus, the DGVMs cannot resolve how the site-level mechanisms scale up to the continental-scale effect observed here. Nonetheless, a selection of models effectively captures the continental-scale CO_2 pulses by a fast response of respiration and a delayed response of photosynthesis to the onset of the rainy season. This highlights the importance of subtle differences in effective parameterizations of respiration and photosynthesis to moisture fluctuations. Associated uncertainties affect the skill of the models to represent the carbon cycle of semi-arid ecosystems.

Our study demonstrates that the soil-respiration driven CO_2 pulses over Australia following the end of the dry season are of large-scale relevance and appear to dominate the variability of the continent’s carbon balance. The GOSAT inversions have shed light on a blind spot of previous top-down and bottom-up approaches for quantifying and attributing CO_2 flux variability. This is important since Australia's semi-arid regions contribute largely to the IAV of the global terrestrial carbon sink and since it is the ecosystem response to the phasing of dry and wet periods that drives the seasonal mechanism behind the large IAV. Thus, our study calls for revisiting the contributions of global semi-arid systems to CO_2 balance variations and for assessing implications for our ability to model climate-carbon feedbacks in semi-arid regions. Only a few of the global vegetation models are able to reproduce the observed CO_2 pulses which suggests that only their respective parameterizations are able to represent the sensitivity of the underlying mechanism to changes in climatic conditions and thus, to accurately project semi-arid carbon flux variability under a changing climate. Considering the large uncertainties associated with modeling climate-carbon feedbacks (*14,15,48*), our findings may contribute continental-scale mechanistic understanding that can help reduce these uncertainties for dryland ecosystems which are found particularly sensitive to climate change (*49*).

References and Notes

1. P. Friedlingstein, M. O'sullivan, M. W. Jones, R. M. Andrew, J. Hauck, A. Olsen, G. P. Peters, W. Peters, J. Pongratz, S. Sitch, C. Le Quéré, J. G. Canadell, P. Ciais, R. B. Jackson, S. Alin, Aragão, Luiz E. O. C., A. Arneth, V. Arora, N. R. Bates, M. Becker, A. Benoit-Cattin, H. C. Bittig, L. Bopp, S. Bultan, N. Chandra, F. Chevallier, L. P. Chini, W. Evans, L. Florentie, P. M. Forster, T. Gasser, M. Gehlen, D. Gilfillan, T. Gkritzalis, L. Gregor, N. Gruber, I. Harris, K. Hartung, V. Haverd, R. A. Houghton, T. Ilyina, A. K. Jain, E. Joetzjer, K. Kadono, E. Kato, V. Kitidis, J. I. Korsbakken, P. Landschützer, N. Lefèvre, A. Lenton, S. Lienert, Z. Liu, D. Lombardozzi, G. Marland, N. Metzl, D. R. Munro, Nabel, Julia E. M. S., S.-I. Nakaoka, Y. Niwa, K. O'Brien, T. Ono, P. I. Palmer, D. Pierrot, B. Poulter, L. Resplandy, E. Robertson, C. Rödenbeck, J. Schwinger, R. Séférian, I. Skjelvan, A. J. P. Smith, A. J. Sutton, T. Tanhua, P. P. Tans, H. Tian, B. Tilbrook, G. van der Werf, N. Vuichard, A. P. Walker, R. Wanninkhof, A. J. Watson, D. Willis, A. J. Wiltshire, W. Yuan, X. Yue, S. Zaehle, Global Carbon Budget 2020. *Earth Syst. Sci. Data*. **12**, 3269–3340 (2020), doi:10.5194/essd-12-3269-2020.

2. B. Poulter, D. Frank, P. Ciais, R. B. Myneni, N. Andela, J. Bi, G. Broquet, J. G. Canadell, F. Chevallier, Y. Y. Liu, S. W. Running, S. Sitch, G. R. van der Werf, Contribution of semi-arid ecosystems to interannual variability of the global carbon cycle. *Nature*. **509**, 600–603 (2014), doi:10.1038/nature13376.

3. A. Ahlström, M. R. Raupach, G. Schurgers, B. Smith, A. Arneth, M. Jung, M. Reichstein, J. G. Canadell, P. Friedlingstein, A. K. Jain, others, The dominant role of semi-arid ecosystems in the trend and variability of the land CO_2 sink. *Science*. **348**, 895–899 (2015).

4. M. Jung, M. Reichstein, C. R. Schwalm, C. Huntingford, S. Sitch, A. Ahlström, A. Arneth, G. Camps-Valls, P. Ciais, P. Friedlingstein, F. Gans, K. Ichii, A. K. Jain, E. Kato, D. Papale, B. Poulter, B. Raduly, C. Rödenbeck, G. Tramontana, N. Viovy, Y.-P. Wang, U. Weber, S. Zaehle, N. Zeng, Compensatory water effects link yearly global land CO_2 sink changes to temperature. *Nature*. **541**, 516–520 (2017), doi:10.1038/nature20780.

5. V. Humphrey, A. Berg, P. Ciais, P. Gentine, M. Jung, M. Reichstein, S. I. Seneviratne, C. Frankenberg, Soil moisture-atmosphere feedback dominates land carbon uptake variability. *Nature*. **592**, 65–69 (2021).

6. S. Piao, X. Wang, K. Wang, X. Li, A. Bastos, J. G. Canadell, P. Ciais, P. Friedlingstein, S. Sitch, Interannual variation of terrestrial carbon cycle: Issues and perspectives. *Glob Change Biol*. **26**, 300–318 (2020), doi:10.1111/gcb.14884.

7. V. Haverd, A. Ahlström, B. Smith, J. G. Canadell, Carbon cycle responses of semi-arid ecosystems to positive asymmetry in rainfall. *Glob Change Biol*. **23**, 793–800 (2017), doi:10.1111/gcb.13412.

8. R. G. Detmers, O. Hasekamp, I. Aben, S. Houweling, T. T. Leeuwen, A. Butz, J. Landgraf, P. Köhler, L. Guanter, B. Poulter, Anomalous carbon uptake in Australia as seen by GOSAT. *Geophys. Res. Lett.* **42**, 8177–8184 (2015), doi:10.1002/2015GL065161.

9. X. Ma, A. Huete, J. Cleverly, D. Eamus, F. Chevallier, J. Joiner, B. Poulter, Y. Zhang, L. Guanter, W. Meyer, Z. Xie, G. Ponce-Campos, Drought rapidly diminishes the large net CO_2 uptake in 2011 over semi-arid Australia. *Sci. Rep.* **6**, 37747 (2016), doi:10.1038/srep37747.

10. J. Cleverly, D. Eamus, Q. Luo, N. Restrepo Coupe, N. Kljun, X. Ma, C. Ewenz, L. Li, Q. Yu, A. Huete, The importance of interacting climate modes on Australia's contribution to global carbon cycle extremes. *Sci. Rep.* **6**, 23113 (2016), doi:10.1038/srep23113.

11. Z. Xie, A. Huete, J. Cleverly, S. Phinn, E. McDonald-Madden, Y. Cao, F. Qin, Multi-climate mode interactions drive hydrological and vegetation responses to hydroclimatic extremes in Australia. *Remote Sensing of Environment*. **231**, 111270 (2019), doi:10.1016/j.rse.2019.111270.

12. A. Bastos, M. O'Sullivan, P. Ciais, D. Makowski, S. Sitch, P. Friedlingstein, F. Chevallier, C. Rödenbeck, J. Pongratz, I. T. Luijkx, others, Sources of uncertainty in regional and global terrestrial CO_2 exchange estimates. *Global Biogeochemical Cycles*. **34**, e2019GB006393 (2020).

13. L. Teckentrup, M. G. de Kauwe, A. J. Pitman, D. S. Goll, V. Haverd, A. K. Jain, E. Joetzjer, E. Kato, S. Lienert, D. Lombardozzi, others, Assessing the representation of the Australian carbon cycle in global vegetation models. *Biogeosciences*. **18**, 5639–5668 (2021).

14. P. M. Cox, C. Huntingford, M. S. Williamson, Emergent constraint on equilibrium climate sensitivity from global temperature variability. *Nature*. **553**, 319–322 (2018), doi:10.1038/nature25450.

15. S. Wenzel, P. M. Cox, V. Eyring, P. Friedlingstein, Projected land photosynthesis constrained by changes in the seasonal cycle of atmospheric CO_2. *Nature*. **538**, 499–501 (2016), doi:10.1038/nature19772.

16. D. L. Hoover, A. A. Pfennigwerth, M. C. Duniway, Drought resistance and resilience: The role of soil moisture–plant interactions and legacies in a dryland ecosystem. *J. Ecol. (Journal of Ecology)*. **109**, 3280–3294 (2021), doi:10.1111/1365-2745.13681.

17. N. MacBean, R. L. Scott, J. A. Biederman, P. Peylin, T. Kolb, M. E. Litvak, P. Krishnan, T. P. Meyers, V. K. Arora, V. Bastrikov, D. Goll, D. L. Lombardozzi, Nabel, Julia E. M. S., J. Pongratz, S. Sitch, A. P. Walker, S. Zaehle, D. J. P. Moore, Dynamic global vegetation models underestimate net CO_2 flux mean and inter-annual variability in dryland ecosystems. *Environ. Res. Lett.* **16**, 94023 (2021), doi:10.1088/1748-9326/ac1a38.

18. G. Tramontana, M. Jung, C. R. Schwalm, K. Ichii, G. Camps-Valls, B. Ráduly, M. Reichstein, M. A. Arain, A. Cescatti, G. Kiely, others, Predicting carbon dioxide and energy fluxes across global FLUXNET sites with regression algorithms. *Biogeosciences*. **13**, 4291–4313 (2016).

19. P. Bodesheim, M. Jung, F. Gans, M. D. Mahecha, M. Reichstein, Upscaled diurnal cycles of land–atmosphere fluxes: a new global half-hourly data product. *Earth Syst. Sci. Data*. **10**, 1327–1365 (2018), doi:10.5194/essd-10-1327-2018.

20. M. Jung, C. Schwalm, M. Migliavacca, S. Walther, G. Camps-Valls, S. Koirala, P. Anthoni, S. Besnard, P. Bodesheim, N. Carvalhais, others, Scaling carbon fluxes from eddy covariance sites to globe: synthesis and evaluation of the FLUXCOM approach. *Biogeosciences*. **17**, 1343–1365 (2020).

21. S. Sippel, M. Reichstein, X. Ma, M. D. Mahecha, H. Lange, M. Flach, D. Frank, Drought, Heat, and the Carbon Cycle: a Review. *Curr. Clim. Change Rep.* **4**, 266–286 (2018), doi:10.1007/s40641-018-0103-4.

22. J. Beringer, L. B. Hutley, I. McHugh, S. K. Arndt, D. Campbell, H. A. Cleugh, J. Cleverly, V. Resco de Dios, D. Eamus, B. Evans, C. Ewenz, P. Grace, A. Griebel, V. Haverd, N. Hinko-Najera, A. Huete, P. Isaac, K. Kanniah, R. Leuning, M. J. Liddell, C. Macfarlane, W. Meyer, C. Moore, E. Pendall, A. Phillips, R. L. Phillips, S. M. Prober, N. Restrepo-Coupe, S. Rutledge, I. Schroder, R. Silberstein, P. Southall, M. S. Yee, N. J. Tapper, E. van Gorsel, C. Vote, J. Walker, T. Wardlaw, An introduction to the Australian and New Zealand flux tower network –OzFlux. *Biogeosciences*. **13**, 5895–5916 (2016), doi:10.5194/bg-13-5895-2016.

23. J. Cleverly, D. Eamus, W. Edwards, M. Grant, M. J. Grundy, A. Held, M. Karan, A. J. Lowe, S. M. Prober, B. Sparrow, B. Morris, TERN, Australia's land observatory: addressing the global challenge of forecasting ecosystem responses to climate variability and change. *Environ. Res. Lett.* **14**, 95004 (2019), doi:10.1088/1748-9326/ab33cb.

24. P. J. Sellers, D. S. Schimel, B. Moore, J. Liu, A. Eldering, Observing carbon cycle–climate feedbacks from space. *Proc. Natl. Acad. Sci. USA*. **115**, 7860–7868 (2018), doi:10.1073/pnas.1716613115.

25. P. I. Palmer, L. Feng, D. Baker, F. Chevallier, H. Bösch, P. Somkuti, Net carbon emissions from African biosphere dominate pan-tropical atmospheric CO_2 signal. *Nature communications*. **10**, 1–9 (2019).

26. B. Byrne, J. Liu, M. Lee, I. Baker, K. W. Bowman, N. M. Deutscher, D. G. Feist, D. W. T. Griffith, L. T. Iraci, M. Kiel, J. S. Kimball, C. E. Miller, I. Morino, N. C. Parazoo, C. Petri, C. M. Roehl, M. K. Sha, K. Strong, V. A. Velazco, P. O. Wennberg, D. Wunch, Improved Constraints on Northern Extratropical CO_2 Fluxes Obtained by Combining Surface-Based and Space-Based Atmospheric CO_2 Measurements. *J. Geophys. Res. Atmos.* **125** (2020), doi:10.1029/2019JD032029.

27. Z. Chen, D. N. Huntzinger, J. Liu, S. Piao, X. Wang, S. Sitch, P. Friedlingstein, P. Anthoni, A. Arneth, V. Bastrikov, D. S. Goll, V. Haverd, A. K. Jain, E. Joetzjer, E. Kato, S. Lienert, D. L. Lombardozzi, P. C. McGuire, J. R. Melton, Nabel, Julia E M S, J. Pongratz, B. Poulter, H. Tian, A. J. Wiltshire, S. Zaehle, S. M. Miller, Five years of variability in the global carbon cycle: comparing an estimate from the Orbiting Carbon Observatory-2 and process-based models. *Environ. Res. Lett.* **16**, 54041 (2021), doi:10.1088/1748-9326/abfac1.

28. Y. Villalobos, P. Rayner, S. Thomas, J. Silver, The potential of Orbiting Carbon Observatory-2 data to reduce the uncertainties in CO_2 surface fluxes over Australia using a variational assimilation scheme. *Atmos. Chem. Phys.* **20**, 8473–8500 (2020), doi:10.5194/acp-20-8473-2020.

29. S. Sitch, P. Friedlingstein, N. Gruber, S. D. Jones, G. Murray-Tortarolo, A. Ahlström, S. C. Doney, H. Graven, C. Heinze, C. Huntingford, S. Levis, P. E. Levy, M. Lomas, B. Poulter, N. Viovy, S. Zaehle, N. Zeng, A. Arneth, G. Bonan, L. Bopp, J. G. Canadell, F. Chevallier, P. Ciais, R. Ellis, M. Gloor, P. Peylin, S. L. Piao, C. Le Quéré, B. Smith, Z. Zhu, R. Myneni, Recent trends and drivers of regional sources and sinks of carbon dioxide. *Biogeosciences*. **12**, 653–679 (2015), doi:10.5194/bg-12-653-2015.

30. H. F. Birch, Mineralisation of plant nitrogen following alternate wet and dry conditions. *Plant Soil*. **20**, 43–49 (1964), doi:10.1007/bf01378096.

31. P. Jarvis, A. Rey, C. Petsikos, L. Wingate, M. Rayment, J. Pereira, J. Banza, J. David, F. Miglietta, M. Borghetti, G. Manca, R. Valentini, Drying and wetting of Mediterranean soils stimulates decomposition and carbon dioxide emission: the "Birch effect". *Tree Physiol. (Tree Physiology)*. **27**, 929–940 (2007), doi:10.1093/treephys/27.7.929.

32. P. Casals, L. Lopez-Sangil, A. Carrara, C. Gimeno, S. Nogués, Autotrophic and heterotrophic contributions to short-term soil CO_2 efflux following simulated summer precipitation pulses in a Mediterranean dehesa. *Global Biogeochem. Cycles*. **25**, n/a-n/a (2011), doi:10.1029/2010GB003973.

33. A. Kuze, H. Suto, K. Shiomi, S. Kawakami, M. Tanaka, Y. Ueda, A. Deguchi, J. Yoshida, Y. Yamamoto, F. Kataoka, T. E. Taylor, H. L. Buijs, Update on GOSAT TANSO-FTS

performance, operations, and data products after more than 6 years in space. *Atmos. Meas. Tech.* **9**, 2445–2461 (2016), doi:10.5194/amt-9-2445-2016.

34. *Materials and methods are available as supplementary materials at the Science website*.

35. A. Butz, S. Guerlet, O. Hasekamp, D. Schepers, A. Galli, I. Aben, C. Frankenberg, J.-M. Hartmann, H. Tran, A. Kuze, G. Keppel-Aleks, G. Toon, D. Wunch, P. Wennberg, N. Deutscher, D. Griffith, R. Macatangay, J. Messerschmidt, J. Notholt, T. Warneke, Toward accurate CO_2 and CH_4 observations from GOSAT. *Geophys. Res. Lett.* **38**, n/a-n/a (2011), doi:10.1029/2011GL047888.

36. T. E. Taylor, C. W. O'Dell, D. Crisp, A. Kuze, H. Lindqvist, P. O. Wennberg, A. Chatterjee, M. Gunson, A. Eldering, B. Fisher, M. Kiel, R. R. Nelson, A. Merrelli, G. Osterman, F. Chevallier, P. I. Palmer, L. Feng, N. M. Deutscher, M. K. Dubey, D. G. Feist, O. E. García, D. W. T. Griffith, F. Hase, L. T. Iraci, R. Kivi, C. Liu, M. de Mazière, I. Morino, J. Notholt, Y.-S. Oh, H. Ohyama, D. F. Pollard, M. Rettinger, M. Schneider, C. M. Roehl, M. K. Sha, K. Shiomi, K. Strong, R. Sussmann, Y. Té, V. A. Velazco, M. Vrekoussis, T. Warneke, D. Wunch, An 11-year record of XCO_2 estimates derived from GOSAT measurements using the NASA ACOS version 9 retrieval algorithm. *Earth Syst. Sci. Data*. **14**, 325–360 (2022), doi:10.5194/essd-14-325-2022.

37. A. Eldering, P. O. Wennberg, D. Crisp, D. S. Schimel, M. R. Gunson, A. Chatterjee, J. Liu, F. M. Schwandner, Y. Sun, C. W. O'Dell, C. Frankenberg, T. Taylor, B. Fisher, G. B. Osterman, D. Wunch, J. Hakkarainen, J. Tamminen, B. Weir, The Orbiting Carbon Observatory-2 early science investigations of regional carbon dioxide fluxes. *Science*. **358**, eaam5745 (2017), doi:10.1126/science.aam5745.

38. Y. Villalobos, P. J. Rayner, J. D. Silver, S. Thomas, V. Haverd, J. Knauer, Z. M. Loh, N. M. Deutscher, D. W. T. Griffith, D. F. Pollard, Interannual variability in the Australian carbon cycle over 2015–2019, based on assimilation of OCO-2 satellite data. *Atmospheric Chemistry and Physics Discussions*, 1–57 (2022), doi:10.5194/acp-2022-15.

39. D. Wunch, G. C. Toon, J.-F. L. Blavier, R. A. Washenfelder, J. Notholt, B. J. Connor, D. W. T. Griffith, V. Sherlock, P. O. Wennberg, The Total Carbon Column Observing Network. *Phil. Trans. R. Soc. A.* **369**, 2087–2112 (2011), doi:10.1098/rsta.2010.0240.

40. W. Peters, A. R. Jacobson, C. Sweeney, A. E. Andrews, T. J. Conway, K. Masarie, J. B. Miller, L. M. P. Bruhwiler, G. Pétron, A. I. Hirsch, D. E. J. Worthy, G. R. van der Werf, J. T. Randerson, P. O. Wennberg, M. C. Krol, P. P. Tans, An atmospheric perspective on North American carbon dioxide exchange: CarbonTracker. *Proc. Natl. Acad. Sci. USA*. **104**, 18925–18930 (2007), doi:10.1073/pnas.0708986104.

41. F. Chevallier, P. Ciais, T. J. Conway, T. Aalto, B. E. Anderson, P. Bousquet, E. G. Brunke, L. Ciattaglia, Y. Esaki, M. Fröhlich, CO_2 surface fluxes at grid point scale estimated from a global 21 year reanalysis of atmospheric measurements. *J. Geophys. Res. Atmos.* **115** (2010).

42. S. Basu, S. Guerlet, A. Butz, S. Houweling, O. Hasekamp, I. Aben, P. Krummel, P. Steele, R. Langenfelds, M. Torn, S. Biraud, B. Stephens, A. Andrews, D. Worthy, Global CO_2 fluxes

estimated from GOSAT retrievals of total column CO_2. *Atmos. Chem. Phys.* **13**, 8695–8717 (2013), doi:10.5194/acp-13-8695-2013.

43. S. Besnard, N. Carvalhais, M. A. Arain, A. Black, B. Brede, N. Buchmann, J. Chen, J. G. P. W. Clevers, L. P. Dutrieux, F. Gans, M. Herold, M. Jung, Y. Kosugi, A. Knohl, B. E. Law, E. Paul-Limoges, A. Lohila, L. Merbold, O. Roupsard, R. Valentini, S. Wolf, X. Zhang, M. Reichstein, Memory effects of climate and vegetation affecting net ecosystem CO_2 fluxes in global forests. *PloS one*. **14**, e0211510 (2019), doi:10.1371/journal.pone.0211510.

44. T. E. Huxman, K. A. Snyder, D. Tissue, A. J. Leffler, K. Ogle, W. T. Pockman, D. R. Sandquist, D. L. Potts, S. Schwinning, Precipitation pulses and carbon fluxes in semiarid and arid ecosystems. *Oecologia*. **141**, 254–268 (2004).

45. F. E. Moyano, S. Manzoni, C. Chenu, Responses of soil heterotrophic respiration to moisture availability: An exploration of processes and models. *Soil Biology and Biochemistry*. **59**, 72–85 (2013), doi:10.1016/j.soilbio.2013.01.002.

46. W. BORKEN, E. MATZNER, Reappraisal of drying and wetting effects on C and N mineralization and fluxes in soils. *Glob Change Biol*. **15**, 808–824 (2009), doi:10.1111/j.1365-2486.2008.01681.x.

47. J. P. Schimel, Life in Dry Soils: Effects of Drought on Soil Microbial Communities and Processes. *Annu. Rev. Ecol. Evol. Syst.* **49**, 409–432 (2018), doi:10.1146/annurev-ecolsys-110617-062614.

48. V. K. Arora *et al.,* Carbon–concentration and carbon–climate feedbacks in CMIP6 models and their comparison to CMIP5 models. *Biogeosciences*. **17**, 4173–4222 (2020), doi:10.5194/bg-17-4173-2020.

49. X. Lian *et al.,* Multifaceted characteristics of dryland aridity changes in a warming world. *Nat Rev Earth Environ*. **2**, 232–250 (2021), doi:10.1038/s43017-021-00144-0.

50. K. R. Gurney, R. M. Law, A. S. Denning, P. J. Rayner, B. C. Pak, D. Baker, P. Bousquet, L. Bruhwiler, Y.-H. Chen, P. Ciais, I. Y. Fung, M. Heimann, J. John, T. Maki, S. Maksyutov, P. Peylin, M. Prather, S. Taguchi, Transcom 3 inversion intercomparison: Model mean results for the estimation of seasonal carbon sources and sinks. *Global Biogeochem. Cycles*. **18**, n/a-n/a (2004), doi:10.1029/2003GB002111.

51. OCO-2 Science Team, Michael Gunson, Annmarie Eldering, ACOS GOSAT/TANSO-FTS Level 2 Full Physics Standard Product, V9r, Greenbelt, MD, USA, Goddard Earth Sciences Data and Information Services Center (GES DISC, 2022), https://doi.org/10.5067/OSGTIL9OV0PN

52. OCO-2 Science Team, Michael Gunson, Annmarie Eldering, “OCO-2 Level 2 bias-corrected XCO_2 and other select fields from the full-physics retrieval aggregated as daily files, Retrospective processing V10r, Greenbelt, MD, USA, Goddard Earth Sciences Data and Information Services Center (GES DISC, 2022), https://doi.org/10.5067/E4E140XDMPO2.

53. A. R. Jacobson, K. N. Schuldt, J. B. Miller, T. Oda, P. Tans, A. Andrews *et al.*, CarbonTracker CT2019, NOAA Global Monitoring Laboratory (2020); https://www.esrl.noaa.gov/gmd/ccgg/carbontracker/CT2019B/.

54. F. Chevallier, R. J. Engelen, P. Peylin, The contribution of AIRS data to the estimation of CO_2 sources and sinks. *Geophys. Res. Lett.* **32**, L23801 (2005).

55. F. Chevallier, M. Remaud, C. W. O'Dell, D. Baker, P. Peylin, A. Cozic, Objective evaluation of surface- and satellite-driven carbon dioxide atmospheric inversions. *Atmos. Chem. Phys.* **19**, 14233–14251 (2019), doi:10.5194/acp-19-14233-2019.

56. K. A. Masarie, W. Peters, A. R. Jacobson, P. P. Tans, ObsPack: a framework for the preparation, delivery, and attribution of atmospheric greenhouse gas measurements. *Earth Syst. Sci. Data*. **6**, 375–384 (2014), doi:10.5194/essd-6-375-2014.

57. NOAA, *Global Monitoring Laboratory: Trends in Atmospheric Carbon Dioxide* (available at https://www.esrl.noaa.gov/gmd/ccgg/trends/gl_gr.html).

58. B. Byrne, D. F. Baker, S. Basu, M. Bertolacci, K. W. Bowman, D. Carroll, A. Chatterjee, F. Chevallier, P. Ciais, N. Cressie, D. Crisp, S. Crowell, F. Deng, Z. Deng, N. M. Deutscher, M. Dubey, S. Feng, O. García, D. W. T. Griffith, B. Herkommer, L. Hu, A. R. Jacobson, R. Janardanan, S. Jeong, M. S. Johnson, D. B. A. Jones, R. Kivi, J. Liu, Z. Liu, S. Maksyutov, J. B. Miller, S. M. Miller, I. Morino, J. Notholt, T. Oda, C. W. O'Dell, Y.-S. Oh, H. Ohyama, P. K. Patra, H. Peiro, C. Petri, S. Philip, D. F. Pollard, B. Poulter, M. Remaud, A. Schuh, M. K. Sha, K. Shiomi, K. Strong, C. Sweeney, Y. Té, H. Tian, V. A. Velazco, M. Vrekoussis, T. Warneke, J. R. Worden, D. Wunch, Y. Yao, J. Yun, A. Zammit-Mangion, N. Zeng, National CO_2 budgets (2015–2020) inferred from atmospheric CO 2 observations in support of the Global Stocktake. *Earth System Science Data Discussions.* 1-59 (2022), https://doi.org/10.5194/essd-2022-213.

59. S. Crowell, D. Baker, A. Schuh, S. Basu, A. R. Jacobson, F. Chevallier, J. Liu, F. Deng, L. Feng, K. McKain, A. Chatterjee, J. B. Miller, B. B. Stephens, A. Eldering, D. Crisp, D. Schimel, R. Nassar, C. W. O'Dell, T. Oda, C. Sweeney, P. I. Palmer, D. B. A. Jones, The 2015–2016 carbon cycle as seen from OCO-2 and the global in situ network. *Atmos. Chem. Phys.* **19**, 9797–9831 (2019), doi:10.5194/acp-19-9797-2019.

60. H. Peiro, S. Crowell, A. Schuh, D. F. Baker, C. O'Dell, A. R. Jacobson, F. Chevallier, J. Liu, A. Eldering, D. Crisp, F. Deng, B. Weir, S. Basu, M. S. Johnson, S. Philip, I. Baker, Four years of global carbon cycle observed from the Orbiting Carbon Observatory 2 (OCO-2) version 9 and in situ data and comparison to OCO-2 version 7. *Atmos. Chem. Phys.* **22**, 1097–1130 (2022), doi:10.5194/acp-22-1097-2022.

61. A. S. Darmenov, A. da Silva, "The Quick Fire Emissions Dataset (QFED): Documentation of versions 2.1, 2.2 and 2.4" in Technical Report Series on Global Modeling and Data Assimilation, Volume 38 (R. D. Koster, 2015).

62. T. Oda, S. Maksyutov, A very high-resolution (1 km×1 km) global fossil fuel CO_2 emission inventory derived using a point source database and satellite observations of nighttime lights. *Atmos. Chem. Phys.* **11**, 543–556 (2011), doi:10.5194/acp-11-543-2011.

63. T. Oda, S. Maksyutov, R. J. Andres, The Open-source Data Inventory for Anthropogenic Carbon dioxide (CO_2), version 2016 (ODIAC2016): A global, monthly fossil-fuel CO_2 gridded emission data product for tracer transport simulations and surface flux inversions. *Earth Syst. Sci. Data*. **10**, 87–107 (2018), doi:10.5194/essd-10-87-2018.

64. B. Weir, L. E. Ott, G. J. Collatz, S. R. Kawa, B. Poulter, A. Chatterjee, T. Oda, S. Pawson, Bias-correcting carbon fluxes derived from land-surface satellite data for retrospective and near-real-time assimilation systems. *Atmos. Chem. Phys.* **21**, 9609–9628 (2021), doi:10.5194/acp-21-9609-2021.

65. G. R. van der Werf, J. T. Randerson, L. Giglio, T. T. van Leeuwen, Y. Chen, B. M. Rogers, M. Mu, M. J. E. van Marle, D. C. Morton, G. J. COLLATZ, R. J. Yokelson, P. S. Kasibhatla, Global fire emissions estimates during 1997–2016. *Earth Syst. Sci. Data*. **9**, 697–720 (2017), doi:10.5194/essd-9-697-2017.

66. J. Muñoz Sabater, ERA5-Land monthly averaged data from 1981 to present. *Copernicus Climate Change Service (C3S) Climate Data Store (CDS)*, Accessed on 20.12.2021 (2019), doi:10.24381/cds.68d2bb3.

67. J. Muñoz Sabater, ERA5-Land monthly averaged data from 1981 to present. *Copernicus Climate Change Service (C3S) Climate Data Store (CDS)*, Accessed on 20.12.2021 (2021), doi:10.24381/cds.68d2bb3.

68. C. H. Reick, V. Gayler, D. Goll, S. Hagemann, M. Heidkamp, J. E. M. S. Nabel, T. Raddatz, E. Roeckner, R. Schnur, S. Wilkenskjeld, "JSBACH 3 - The land component of the MPI Earth System Model: documentation of version 3.2". (2021).

69. J. R. Melton, V. K. Arora, E. Wisernig-Cojoc, C. Seiler, M. Fortier, E. Chan, L. Teckentrup, CLASSIC v1.0: the open-source community successor to the Canadian Land Surface Scheme (CLASS) and the Canadian Terrestrial Ecosystem Model (CTEM) – Part 1: Model framework and site-level performance. *Geosci. Model Dev.* **13**, 2825–2850 (2020), doi:10.5194/gmd-13-2825-2020.

70. B. Poulter, P. Ciais, E. Hodson, H. Lischke, F. Maignan, S. Plummer, N. E. Zimmermann, Plant functional type mapping for earth system models. *Geosci. Model Dev.* **4**, 993–1010 (2011), doi:10.5194/gmd-4-993-2011.

71. X. Yue, N. Unger, The Yale Interactive terrestrial Biosphere model version 1.0: description, evaluation and implementation into NASA GISS ModelE2. *Geosci. Model Dev.* **8**, 2399–2417 (2015), doi:10.5194/gmd-8-2399-2015.

72. S. Zaehle, A. D. Friend, P. Friedlingstein, F. Dentener, P. Peylin, M. Schulz, Carbon and nitrogen cycle dynamics in the O-CN land surface model: 2. Role of the nitrogen cycle in the historical terrestrial carbon balance. *Global Biogeochem. Cycles*. **24**, n/a-n/a (2010), doi:10.1029/2009GB003522.

73. J. R. Melton, R. K. Shrestha, V. K. Arora, The influence of soils on heterotrophic respiration exerts a strong control on net ecosystem productivity in seasonally dry Amazonian forests. *Biogeosciences*. **12.4,** 1151-1168 (2015), doi:10.5194/bg-12-1151-2015.

74. J. Beringer, Adelaide River OzFlux tower site OzFlux, Australian and New Zealand Flux Research and Monitoring (2013); http://hdl.handle.net/102.100.100/14228.

75. J. Cleverly, Alice Springs Mulga OzFlux site OzFlux, Australian and New Zealand Flux Research and Monitoring (2011); http://hdl.handle.net/102.100.100/14217.

76. I. Schroder, Arcturus Emerald OzFlux tower site OzFlux, Australian and New Zealand Flux Research and Monitoring (2014); http://hdl.handle.net/102.100.100/14249.

77. J. Laubach, Ashley Dene Research Station OzFlux, Australian and New Zealand Flux Research and Monitoring (2019); http://hdl.handle.net/102.100.100/78604.

78. J. Laubach, Beacon Farm OzFlux, Australian and New Zealand Flux Research and Monitoring (2016); http://hdl.handle.net/102.100.100/26730.

79. J. Beringer, Boyagin OzFlux tower site OzFlux, Australian and New Zealand Flux Research and Monitoring (2017); http://hdl.handle.net/102.100.100/61760.

80. Calperum Tech, Calperum Chowilla OzFlux tower site OzFlux, Australian and New Zealand Flux Research and Monitoring (2013); http://hdl.handle.net/102.100.100/14236.

81. M. Liddell, Cape Tribulation OzFlux tower site OzFlux, Australian and New Zealand Flux Research and Monitoring (2013); http://hdl.handle.net/102.100.100/14242.

82. J. Beringer, Collie OzFlux, Australian and New Zealand Flux Research and Monitoring (2018); http://hdl.handle.net/102.100.100/70007.

83. M. Liddell, Cow Bay OzFlux tower site OzFlux, Australian and New Zealand Flux Research and Monitoring (2013); http://hdl.handle.net/102.100.100/14244.

84. A. Griebel, CumberlandPlain Melaleuca OzFlux, Australian and New Zealand Flux Research and Monitoring (2019); http://hdl.handle.net/102.100.100/77413.

85. E. Pendall, Cumberland Plain OzFlux Tower Site OzFlux, Australian and New Zealand Flux Research and Monitoring (2015); http://hdl.handle.net/102.100.100/25164.

86. J. Beringer, Daly Pasture OzFlux tower site OzFlux, Australian and New Zealand Flux Research and Monitoring (2013); http://hdl.handle.net/102.100.100/14238.

87. P. Isaac, Daly Regrowth OzFlux tower site_old_20131128 OzFlux, Australian and New Zealand Flux Research and Monitoring (2010); http://hdl.handle.net/102.100.100/14215.

88. J. Beringer, Daly Uncleared OzFlux tower site OzFlux, Australian and New Zealand Flux Research and Monitoring (2013); http://hdl.handle.net/102.100.100/14239.

89. R. Simpson, Dargo High Plains OzFlux Tower Site OzFlux, Australian and New Zealand Flux Research and Monitoring (2012); http://hdl.handle.net/102.100.100/14221.

90. M. Silva, Digby Plantation OzFlux, Australian and New Zealand Flux Research and Monitoring (2022) local: MONa66b5e42-b7b8-47b9-8338-86a0ee0c6881.

91. J. Beringer, Dry River OzFlux tower site OzFlux, Australian and New Zealand Flux Research and Monitoring (2013); http://hdl.handle.net/102.100.100/14229.

92. M. Silva, Gatum Pasture OzFlux, Australian and New Zealand Flux Research and Monitoring (2022) local: MON34708884-3e7d-4c5a-ba8c-1597e1ff867d.

93. R. Silberstein, Gingin OzFlux, Australian and New Zealand Flux Research and Monitoring (2015); http://hdl.handle.net/102.100.100/22677.

94. C. Macfarlane, Great Western Woodlands OzFlux, Australian and New Zealand Flux Research and Monitoring (2013); http://hdl.handle.net/102.100.100/14226.

95. J. Beringer, Howard Springs OzFlux tower site OzFlux, Australian and New Zealand Flux Research and Monitoring (2013); http://hdl.handle.net/102.100.100/14234.

96. J. Beringer, Howard Springs Understory OzFlux tower site OzFlux, Australian and New Zealand Flux Research and Monitoring (2013); http://hdl.handle.net/102.100.100/14240.

97. J. Beringer, Litchfield OzFlux tower site OzFlux, Australian and New Zealand Flux Research and Monitoring (2015); http://hdl.handle.net/102.100.100/25690.

98. P. Grace, Longreach Mitchell Grass Rangelands OzFlux tower site OzFlux, Australian and New Zealand Flux Research and Monitoring (2019); http://hdl.handle.net/102.100.100/100147.

99. R. Simpson, Nimmo High Plains OzFlux Tower Site OzFlux, Australian and New Zealand Flux Research and Monitoring (2012); http://hdl.handle.net/102.100.100/14220.

100. E. vanGorsel, Otway OzFlux tower site OzFlux, Australian and New Zealand Flux Research and Monitoring (2012); http://hdl.handle.net/102.100.100/14222.

101. J. Beringer, Red Dirt Melon Farm OzFlux tower site OzFlux, Australian and New Zealand Flux Research and Monitoring (2014); http://hdl.handle.net/102.100.100/14245.

102. J. Beringer, Ridgefield OzFlux tower site OzFlux, Australian and New Zealand Flux Research and Monitoring (2016); http://hdl.handle.net/102.100.100/33951.

103. J. Beringer, Riggs Creek OzFlux tower site OzFlux, Australian and New Zealand Flux Research and Monitoring (2014); http://hdl.handle.net/102.100.100/14246.

104. M. Liddell, Robson Creek OzFlux tower site OzFlux, Australian and New Zealand Flux Research and Monitoring (2013); http://hdl.handle.net/102.100.100/14243.

105. D. Rowlings, Samford Ecological Research Facility OzFlux tower site OzFlux, Australian and New Zealand Flux Research and Monitoring (2011); http://hdl.handle.net/102.100.100/14219.

106. J. Beringer, Sturt Plains OzFlux tower site OzFlux, Australian and New Zealand Flux Research and Monitoring (2013); http://hdl.handle.net/102.100.100/14230.

107. J. Cleverly, Ti Tree East OzFlux Site OzFlux, Australian and New Zealand Flux Research and Monitoring (2013); http://hdl.handle.net/102.100.100/14225.

108. W. Woodgate, Tumbarumba OzFlux tower site OzFlux, Australian and New Zealand Flux Research and Monitoring (2013); http://hdl.handle.net/102.100.100/14241.

109. J. Beringer, Wallaby Creek OzFlux tower site OzFlux, Australian and New Zealand Flux Research and Monitoring (2013); http://hdl.handle.net/102.100.100/14231.

110. A. Phillips, Warra OzFlux tower site OzFlux, Australian and New Zealand Flux Research and Monitoring (2015); http://hdl.handle.net/102.100.100/22566.

111. J. Beringer, Whroo OzFlux tower site OzFlux, Australian and New Zealand Flux Research and Monitoring (2013); http://hdl.handle.net/102.100.100/14232.

112. S. Arndt, Wombat State Forest OzFlux-tower site OzFlux, Australian and New Zealand Flux Research and Monitoring (2013); http://hdl.handle.net/102.100.100/14237.

113. J. Beringer Yanco JAXA OzFlux tower site OzFlux, Australian and New Zealand Flux Research and Monitoring (2013); http://hdl.handle.net/102.100.100/14235.

114. D. W. Griffith, N. M. Deutscher, V. A. Velazco, P. O. Wennberg, Y. Yavin, G. Keppel-Aleks, R. A. Washenfelder, G. C. Toon, J.-F. Blavier, C. Paton-Walsh, N. B. Jones, G. C. Kettlewell, B. J. Connor, R. C. Macatangay, C. Roehl, M. Ryczek, J. Glowacki, T. Culgan, G. W. Bryant, TCCON data from Darwin (AU), Release GGG2014.R0, CaltechDATA (2014); https://doi.org/10.14291/tccon.ggg2014.darwin01.R0/1149290.

115. Griffith, D. W. T., Velazco, V. A., Deutscher, N. M., Paton-Walsh, C., Jones, N. B., Wilson, S. R., Macatangay, R. C., Kettlewell, G. C., Buchholz, R. R., & Riggenbach, M. O., TCCON data from Wollongong (AU), Release GGG2014.R0, CaltechDATA (2014); https://doi.org/10.14291/tccon.ggg2014.wollongong01.R0/1149291.

116. F. Di Giuseppe, S. Rémy, F. Pappenberger, F. Wetterhall, *Combining fire radiative power observations with the fire weather index improves the estimation of fire emissions* (2017).

117. C. Wiedinmyer, S. K. Akagi, R. J. Yokelson, L. K. Emmons, J. A. Al-Saadi, J. J. Orlando, A. J. Soja, The Fire INventory from NCAR (FINN) – a high resolution global model to estimate the emissions from open burning. *Geosci. Model Dev.* **4**, 625–641 (2011), doi:10.5194/gmdd-3-2439-2010.

118. D. S. Goll, E. Joetzjer, M. Huang, P. Ciais, Low Phosphorus Availability Decreases Susceptibility of Tropical Primary Productivity to Droughts. *Geophys. Res. Lett.* **45**, 8231–8240 (2018), doi:10.1029/2018GL077736.

119. G. Krinner, N. Viovy, N. de Noblet-Ducoudré, J. Ogée, J. Polcher, P. Friedlingstein, P. Ciais, S. Sitch, I. C. Prentice, A dynamic global vegetation model for studies of the coupled atmosphere-biosphere system. *Global Biogeochem. Cycles*. **19** (2005), doi:10.1029/2003GB002199.

120. N. Vuichard, P. Messina, S. Luyssaert, B. Guenet, S. Zaehle, J. Ghattas, V. Bastrikov, P. Peylin, Accounting for carbon and nitrogen interactions in the global terrestrial ecosystem model ORCHIDEE (trunk version, rev 4999): multi-scale evaluation of gross primary production. *Geosci. Model Dev.* **12**, 4751–4779 (2019), doi:10.5194/gmd-12-4751-2019.

121. V. Haverd, B. Smith, L. Nieradzik, P. R. Briggs, W. Woodgate, C. M. Trudinger, J. G. Canadell, M. Cuntz, A new version of the CABLE land surface model (Subversion revision r4601) incorporating land use and land cover change, woody vegetation demography, and a novel optimisation-based approach to plant coordination of photosynthesis. *Geosci. Model Dev.* **11**, 2995–3026 (2018), doi:10.5194/gmd-11-2995-2018.

122. D. M. Lawrence, R. A. Fisher, C. D. Koven, K. W. Oleson, S. C. Swenson, G. Bonan, N. Collier, B. Ghimire, L. Kampenhout, D. Kennedy, E. Kluzek, P. J. Lawrence, F. Li, H. Li, D. Lombardozzi, W. J. Riley, W. J. Sacks, M. Shi, M. Vertenstein, W. R. Wieder, C. Xu, A. A. Ali, A. M. Badger, G. Bisht, M. Broeke, M. A. Brunke, S. P. Burns, J. Buzan, M. Clark, A. Craig, K. Dahlin, B. Drewniak, J. B. Fisher, M. Flanner, A. M. Fox, P. Gentine, F. Hoffman, G. Keppel-Aleks, R. Knox, S. Kumar, J. Lenaerts, L. R. Leung, W. H. Lipscomb, Y. Lu, A. Pandey, J. D. Pelletier, J. Perket, J. T. Randerson, D. M. Ricciuto, B. M. Sanderson, A. Slater, Z. M. Subin, J. Tang, R. Q. Thomas, M. Val Martin, X. Zeng, The Community Land Model Version 5: Description of New Features, Benchmarking, and Impact of Forcing Uncertainty. *J. Adv. Model. Earth Syst.* **11**, 4245–4287 (2019), doi:10.1029/2018MS001583.

123. H. Tian, G. Chen, C. Lu, X. Xu, D. J. Hayes, W. Ren, S. Pan, D. N. Huntzinger, S. C. Wofsy, North American terrestrial CO_2 uptake largely offset by CH_4 and N_2O emissions: toward a full accounting of the greenhouse gas budget. *Climatic change*. **129**, 413–426 (2015), doi:10.1007/s10584-014-1072-9.

124. W. Yuan, D. Liu, W. Dong, S. Liu, G. Zhou, G. Yu, T. Zhao, J. Feng, Z. Ma, J. Chen, Y. Chen, S. Chen, S. Han, J. Huang, L. Li, H. Liu, S. Liu, M. Ma, Y. Wang, J. Xia, W. Xu, Q. Zhang, X. Zhao, L. Zhao, Multiyear precipitation reduction strongly decreases carbon uptake over northern China. *J. Geophys. Res. Biogeosci.* **119**, 881–896 (2014), doi:10.1002/2014JG002608.

125. P. Meiyappan, A. K. Jain, J. I. House, Increased influence of nitrogen limitation on CO_2 emissions from future land use and land use change. *Global Biogeochem. Cycles*. **29**, 1524–1548 (2015), doi:10.1002/2015GB005086.

126. C. Delire, R. Séférian, B. Decharme, R. Alkama, J.-C. Calvet, D. Carrer, A.-L. Gibelin, E. Joetzjer, X. Morel, M. Rocher, D. Tzanos, The Global Land Carbon Cycle Simulated With ISBA-CTRIP: Improvements Over the Last Decade. *J. Adv. Model. Earth Syst.* **12** (2020), doi:10.1029/2019MS001886.

127. A. A. Sellar, C. G. Jones, J. P. Mulcahy, Y. Tang, A. Yool, A. Wiltshire, F. M. O'connor, M. Stringer, R. Hill, J. Palmieri, others, UKESM1: Description and evaluation of the UK Earth System Model. *J. Adv. Model. Earth Syst.* **11**, 4513–4558 (2019).

128. S. Lienert, F. Joos, A Bayesian ensemble data assimilation to constrain model parameters and land-use carbon emissions. *Biogeosciences*. **15**, 2909–2930 (2018), doi:10.5194/bg-15-2909-2018.

129. A. P. Walker, T. Quaife, P. M. van Bodegom, M. G. de Kauwe, T. F. Keenan, J. Joiner, M. R. Lomas, N. MacBean, C. Xu, X. Yang, F. I. Woodward, The impact of alternative trait-scaling hypotheses for the maximum photosynthetic carboxylation rate (Vcmax) on global gross primary production. *The New phytologist*. **215**, 1370–1386 (2017), doi:10.1111/nph.14623.

130. E. Kato, T. Kinoshita, A. Ito, M. Kawamiya, Y. Yamagata, Evaluation of spatially explicit emission scenario of land-use change and biomass burning using a process-based biogeochemical model. *Journal of Land Use Science*. **8**, 104–122 (2013), doi:10.1080/1747423x.2011.628705.

Acknowledgments: We thank the Japanese Aerospace Exploration Agency, National Institute for Environmental Studies and the Ministry of Environment for the GOSAT data and their continuous support as part of the Joint Research Agreement. OCO-2 data were produced by the OCO-2 project at the Jet Propulsion Laboratory, California Institute of Technology, and obtained from the OCO-2 data archive maintained at the NASA Goddard Earth Science Data and Information Services Center. CarbonTracker CT2019B results are provided by NOAA ESRL, Boulder, Colorado, USA from the website at http://carbontracker.noaa.gov. We thank all TRENDY modelers for providing model output as part of the TRENDY v9 ensemble. The study has greatly benefited from discussions with Christian Frankenberg.

Author contributions:

AB, SNV, and EMM were involved in conceptualization and methodology. EMM conducted the formal analysis and the visualization under supervision of AB and SNV. AB, SNV, EMM, MJ, and SB wrote the original draft. SB performed the dedicated TM5-4DVar runs. SS, VKA, PRB, PF, DSG, AKJ, EK, JEMSN, BP, RS, HT, AW, WY, XY, SZ provided TRENDY data. NMD and DWTG provided TCCON data. All authors contributed to the editing and review of the manuscript.

Competing interests: Authors declare that they have no competing interests.

Data and materials availability: GOSAT/RemoTeC2.4.0 XCO2 data can be obtained from doi: 10.5281/zenodo.5886662 (last access: 2022-02-25). GOSAT/ACOS data is available at https://oco2.gesdisc.eosdis.nasa.gov/data/GOSAT_TANSO_Level2/ACOS_L2_Lite_FP.9r/ (last access: 2020-07-28). OCO-2 data is available at https://disc.gsfc.nasa.gov/datasets/OCO2_L2_Lite_FP_10r/summary (last access: 2020-11-01). TCCON data can be downloaded at https://data.caltech.edu/records/269 (last access: 2022-02-25). CarbonTracker CT2019B CO2 fluxes and concentrations can be downloaded from https://gml.noaa.gov/aftp/products/carbontracker/co2/CT2019B/fluxes/monthly/ (last access: 2021-02-19) and https://gml.noaa.gov/aftp/products/carbontracker/co2/CT2019B/molefractions/co2_total_monthly/ (last access: 2022-02.25) respectively. CAMS concentrations and fluxes can be found at datasets/data/cams-ghg-inversions/ (last access: 2021-10-07). GFAS emissions records are available at https://apps.ecmwf.int/datasets/data/cams-gfas/ (last access: 2020-11-13). CAMS and GFAS data were generated using Copernicus Atmosphere Service Information [2021] and neither the European Commission nor ECMWF is responsible for any use that may be made of the information it contains. GFED fire emissions are available at https://www.geo.vu.nl/~gwerf/GFED/GFED4/ (last access: 2020-07-10). FINN data were retrieved from the American National Center for Atmospheric Research https://www2.acom.ucar.edu/modeling/finn-fire-inventory-ncar (last access: 2020-11-18). The used OzFlux data can be downloaded from https://www.ozflux.org.au/ (last access: 2021-11-16). ERA5-land data records contain modified Copernicus Atmosphere Service Information [2021] available at the Climate Data Store https://cds.climate.copernicus.eu/cdsapp#!/dataset/reanalysis-era5-land-monthly-means (last access: 2021-12-20). This work used eddy covariance data collected by the TERN-OzFlux facility. OzFlux would like to acknowledge the financial support of the Australian Federal Government via the National Collaborative Research Infrastructure Scheme and the Education Investment Fund. OzFlux data is available at https://data.ozflux.org.au (last access: 2023-01-20). TRENDYv9 model output and FLUXCOM products are available at https://sites.exeter.ac.uk/trendy and http://fluxcom.org/CF-Download/, respectively. Datafiles S1, S2, and S3 in the supplement contain monthly TRENDY and FLUXCOM data as used here. Monthly TM5-4DVar data are available in datafile S1 and S4.

The code used in this study is available at github.

Supplementary Materials:

Materials and Methods

Figs. S1 to S12

Tables S1 to S2

References (*50-130*)

Data S1 to S4

Materials and Methods

Summary of observation and model data

The main characteristics of the observation and model data are listed in Table S1.

TRANSCOM region Australia

Our region of interest is 'Australia' as defined by the TRANSCOM-3 experiment (*50*) including the Australian continent and New Zealand. For the main analysis, concentration and flux data are averaged and aggregated, respectively, over a month or a year for the entire region. Satellite concentrations are only reported if averaging includes more than 10 data points. To avoid sampling effects on the coastline, all flux datasets are aggregated on a 1°×1° grid before applying the TRANSCOM region mask to aggregate over the entire region and one month. Grid cells with their centers inside the Australian region are counted to belong to the region. The only exceptions are the TM5-4DVAR fluxes, as they are already provided as monthly regional fluxes.

CO_2 concentrations

We primarily use GOSAT column-average dry-air mole fractions of CO_2 (Fig. 1), also denoted XCO_2, generated by operating the RemoTeC radiative transfer and retrieval algorithm (*8, 35*) on shortwave-infrared spectra of sunlight backscattered to GOSAT by the Earth's surface and atmosphere (called GOSAT/RemoTeC). The algorithm version employed here corresponds to the one used previously (*8*) with updates related to the quality filtering and to ancillary input data, in particular updated a priori gas concentrations. Furthermore, we also use GOSAT CO_2 records generated by the NASA Atmospheric CO_2 Observations from Space (ACOS) algorithm version 9r(Lite) (*51*) (called GOSAT/ACOS). Fig. S4 illustrates the measurement count over Australia for dry and rainy seasons.

To confirm robustness of the satellite data, we compare GOSAT CO_2 against records of the Orbiting Carbon Observatory-2 version 10 (OCO-2) (*52*) covering the time period 2014 to 2018 (Table S1 and Fig. 1). We further compare the satellite data to ground-based measurements of the column-average dry-air mole fractions reported by the Total Carbon Column Observing Network (TCCON) (*39*). Thereby, data of the two Australian stations Darwin and Wollongong are used (Table S1 and Fig. S2). Both stations are located near the coastline and neither are in the semi-arid regions (see Fig. S3). Therefore, the comparison to the continental GOSAT data suffers from limited representativeness.

Simulated CO_2 concentrations (Fig. 1) are taken from three inverse atmospheric transport models (Table S1) that estimate surface-atmosphere fluxes which are optimally compatible with atmospheric concentration measurements and prior flux knowledge: TM5 four-dimensional variational inversion system (TM5-4DVAR) (*42*), CarbonTracker (CT2019B) (40*, 53*), and the Copernicus Atmosphere Monitoring Service (CAMS) (*41, 54, 55*). Given the optimized fluxes, the transport model is run forward to produce simulated concentration fields. All three models assimilate ground-based in-situ CO_2 concentration measurements collected from the global monitoring networks (*56*). We use TM5-4DVAR for further analysis to assimilate the GOSAT/RemoTeC and GOSAT/ACOS data together with the in-situ observations.

For illustrating the seasonal concentration dynamics in Fig. 1, we remove the secular increase of CO_2 concentrations in the atmosphere by detrending the concentration data, i.e. we subtract the global atmospheric background assuming a piece-wise yearly linear increase according to the annual mean carbon dioxide growth rates (*GR*) reported by the National Oceanic and Atmospheric Administration (NOAA) based on globally averaged marine surface data (*57*). Thus, the background concentration for month *m* ([1,...,12]) and year *y* ([2009,...,2018]) reads:

$$BG_{y,m} = BG + \sum_{i=2009}^{y-1} (GR_i) + \frac{m}{12} GR_y \quad (1)$$

where BG is an overall offset determined by setting the mean of the detrended CO_2 concentrations to zero, the second term accumulates the growth since the start of the time series in the year 2009 until the start of year y, and the third term accounts for the fractional increase during the respective year y. We subtract the background individually for all CO_2 concentration data sets (satellite as well as simulation data). Note that detrending is only applied to concentration data used in Fig. 1 for illustration purposes, the inverse models assimilate whole CO_2 concentrations.

CO_2 top-down fluxes

The three inverse atmospheric models TM5-4DVAR, CarbonTracker, and CAMS, that provide simulated CO_2 concentration fields, also provide estimates of the surface-atmosphere fluxes compatible with ground-based in-situ CO_2 measurements (Fig. 2A). For further analysis, we use TM5-4DVAR to assimilate the GOSAT CO_2 data together with the ground-based in-situ observations (Fig. 2A and 2B). Fig. S5 compares the TM5-4DVAR flux estimates for the in-situ and GOSAT-based inversions to the a priori fluxes. The in-situ based fluxes show only small departures from the prior while the GOSAT-based inversion deviates substantially which hints at the additional information content unlocked by the satellite data. Furthermore, for the period 2014-2018, we examine carbon flux estimates from the OCO-2 Model Intercomparison Project (MIP) (*58-60*), that assimilate OCO-2 satellite data together with ground-based in-situ data (Fig. S7). Depending on whether GOSAT/RemoTeC, GOSAT/ACOS, or OCO-2 MIP data are used, we denote the respective flux estimates in the Extended Materials with InverseModel$_{\text{+GOSAT/RemoTeC/}}$, InverseModel$_{\text{+GOSAT/ACOS}}$,and InverseModel$_{\text{+OCO-2}}$. The models provide output in terms of the net CO_2 fluxes partitioned into biosphere, oceanic, fire, and fossil fluxes. TM5-4DVAR is configured to estimate weekly biosphere and oceanic fluxes on a regular 3°(longitude) × 2°(latitude) grid while fire and fossil emissions are imposed from the Quick Fire Emissions Dataset (QFED (*61*)) and the Open-source Data Inventory for Anthropogenic CO_2 (ODIAC (*62, 63*)), respectively. The construction of the prior oceanic, fire and biosphere fluxes are detailed elsewhere (*64*). We average the oceanic, biospheric and fire fluxes between 2000 and 2019 to create 20-year climatological land and ocean sinks. We then apply year-specific scaling on these sinks to match the observed annual atmospheric CO_2 growth given year-specific fossil CO_2 emissions. The prior fluxes thus constructed follow the atmospheric growth of CO_2 over two decades.

For all inversions, NBP is calculated as the sum of a posteriori biosphere fluxes and fire emissions. Positive fluxes correspond to carbon emissions into the atmosphere, negative fluxes indicate carbon uptake by the ecosystems. While all TM5-4DVAR data is already provided on the scale of TRANSCOM regions, CAMS and CarbonTracker fluxes are aggregated on a 1°x1° grid before applying the TRANSCOM region mask.

CO_2 bottom-up fluxes

FLUXCOM provides estimates of global bottom-up net ecosystem exchange (NEE) based on upscaling of local flux measurements. To this end, a machine learning approach uses the eddy covariance measurements by the FLUXNET tower network together with meteorological and satellite remote sensing data to deliver NEE globally at fine spatial resolution (*18, 20*). The FLUXCOM version, used here, only includes four stations of the Australian OzFlux network (Fig. S3). To calculate FLUXCOM compatible NBP (Fig. 2A), we take the sum of the remote sensing FLUXCOM ensemble and fire emissions from the Global Fire Emission Database (GFED) v4.1s (*65*). Fluxes due to land-use change are neglected.

The TRENDY model inter-comparison project collects various DGVMs and contributes to the Global Carbon Project (*1*). Here, we use 18 TRENDY version 9 models listed in Table S1. NBP, GPP and TER provided by the TRENDY DGVMs are aggregated on a 1°x1° grid before applying the TRANSCOM region mask. As the land-ocean masks among the TRENDY models differ, the continental NBP is taken as mean flux in units $\mu gCO_2m^{-2}s^{-1}$, then multiplied by the Australian region area to obtain total fluxes and converted to TgC/month. Most of the models provide NBP directly. For the models CABLE-POP and DLEM, not providing net fluxes, NBP is constructed from only GPP and TER, as both models do not provide FIRE fluxes. The subset of models showing the end-of-dry-season CO_2 pulses is termed TRENDY*selection*. The other subset of TRENDY models not showing the pulses are called TRENDY*others* (Fig. 2B, Fig. 3, Fig. S9, Fig. S10, and Table S1).

Figure 3C shows the timing of bottom-up NBP for correlations with monthly mean precipitation. The latter is taken from the European Centre for Medium Range Weather Forecasts (ECMWF) ERA5-land data product (*66, 67*). We average the ERA-5 data over entire Australia and the semi-arid parts (see Fig. S3) defined as all the 1°x1° grid cells with less than 22 mm of monthly mean precipitation during four consecutive months in the ten-year averaged annual cycle.

Characteristics of TRENDY*selection*

The model subset TRENDY*selection* consists of the five models JSBACH (*68*), CLASSIC (*69*), LPJ (*70*), YiBs (*71*), and OCN (*72*). They show characteristics that lead to a temporal shift, a dephasing, between the increase of respiration and GPP at the end of the dry season in semi-arid ecosystems. In all five models, GPP is either constrained by a drought dependent phenology for semi-arid plants (grass and shrublands) or dependent on a certain amount of moisture in the soil column. Except for YiBs, soil-respiration (heterotrophic respiration) is (co-)driven by soil moisture or precipitation. Large sensitivity of soil-respiration to upper soil moisture or precipitation causes respiration to increase early after a precipitation event. The GPP increase, however, is delayed because soil moisture needs to accumulate or, GPP is purely phenology driven.

JSBACH uses the soil carbon module YASSO, which drives soil-respiration by (15-days mean) precipitation. JSBACH has primarily C4 grasses and raingreen shrubs in Australia. GPP for both plant types in JSBACH depends on a soil moisture driven phenology. Thereby, sufficient soil moisture needs to be available in the upper soil layer (grasses) or the deeper root zone (shrubs) for the plants to grow. The need for soil moisture to accumulate leads to a delayed start of the growing season after the initial rainfalls, especially for raingreen shrubs. At the beginning of the growing season, plant respiration (autotrophic respiration) is implemented to exceed GPP (*68*).

In CLASSIC respiration as well as GPP are driven by soil moisture. Soil-respiration is constrained at both high and low moistures values in the soil. Thereby, the soil-respiration is separated into litter respiration driven by surface near soil moisture and soil carbon respiration driven by deeper soil moisture. The soil moisture controls of GPP are determined by soil moisture in the rooting zone. Hence, litter respiration starts immediately after precipitation events whereas soil moisture needs to accumulated and infiltrate the soils before GPP can start to increase (*69,73*).

LPJ assumes deciduous and evergreen plants in Australia. While GPP of some plant types is soil moisture driven, other plant types (deciduous plants) are driven by first January growing degree days. Soil respiration is limited by temperature and soil moisture. This may lead to lags between GPP and soil respiration (*70*).

YiBs includes a drought-dependent phenology for semi-arid plants, such as shrubland and grassland. Thereby, shrubland GPP in regions with mean soil temperatures greater than 12°C is driven by soil moisture in the whole soil column. Grassland GPP is additionally affected by temperature. The respiration in YiBs is mainly driven by temperature (*71*).

In OCN, GPP for grasses and raingreen plant functional types is dependent on the exceedance of a soil moisture threshold. Furthermore, for a substantial increase of GPP a sufficiently high leave area index (LAI) needs to develop, which is in turn driven by the daily available carbon. Both, the need of soil moisture to accumulate after the start of the rainy season and the necessary allocation of available carbon from below ground, leads to a time delay of the increase in GPP after the start of the rainy season. At the same time GPP starts to increase, plant respiration becomes activated, leading to an early season phase in which plant respiration exceeds GPP. Soil-respiration is driven by soil moisture in the whole soil column and in the upper soil layers. Due to the sensitivity to the upper soil layer moisture, soil-respiration can increase rapidly after a precipitation event (*72*).

Local OzFlux stations

In our analyses, we consider the following stations from the OzFlux network: Adelaide River (AU-Ade, *74*), Alice Springs Mulga (AU-ASM, *75*), Arcturus Emerald (*76*), Ashley Dene dry (NZ-And, *77*), Ashley Dene wet (NZ-Adw, *77*), Beacon Farm (NZ-BFm, *78*), Boyagin (AU-Boy, *79*), Calperum Chowilla (AU-Cpr, *80*), Cape Tribulation (AU-Ctr, *81*), Collie (AU-Col, *82*), Cow Bay (AU-Cow, *83*), Cumberland Plain Maleleuca (*84*), Cumberland Plain (AU-Cum, *85*), Daly Pasture (AU-DaP, *86*), Daly Regrowth (*87*), Daly Uncleared (AU-DaS, *88*), Dargo High Plains (AU-Drg, *89*), Digby Plantation (*90*), Dry River (AU-Dry, *91*), Gatum Pasture (*92*), Gingin (AU-Gin, *93*), Great Western Woodlands (AU-GWW, *94*), Howard Springs (AU-How, *95*), Howard Springs Understory (*96*), Lichtfield (AU-Lit, *97*), Longreach Mitchell Grass Rangelands (*98*), Nimmo High Plains (AU-Nim, *99*), Otway (AU-Otw, *100*), Red Dirt Melon Farm (*101*), Ridgefield (AU-Rgf, *102*), Riggs Creek (AU-Rig, *103*), Robson Creek (AU-Rob, *104*), Samford Ecological Research Facility (AU-Sam, *105*), Sturt Plains (AU-Stp, *106*), Ti Tree East (AU-TTE, *107*), Tumbarumba (AU-Tum, *108*), Wallaby Creek (AU-Wac, *109*), Warra (AU-Wrr, *110*), Whroo (AU-Whr, *111*), Wombat State Forest (AU-Wom, *112*), Yanco JAXA (AU-Ync, *113*).

We use the surface upward mole flux of carbon dioxide ('Fc'/'Fco2'), rainfall amount ('Precipitation'), and soil moisture content ('SWS') of the OzFlux L3 data and calculate daily aggregates. Only stations providing data for these three parameters were taken into account. To detect CO_2 emission pulses due to precipitation rewetting dry soils ('Birch effects'), we run filter statistics over the entire dataset. We identify local pulse events by 1) substantial precipitation (> 5 mm/d), 2) low soil moisture the day before precipitation (SWS in the lower 10% of the individual stations SWS range and SWS <7%), 3) and an increase in net CO_2 flux compared to the previous seven days. If the three filter criteria are met, we count a local Birch event for the respective station (red dots for the examples in Fig. S11). Then, for each month, we count the stations, which show at least one precipitation driven respiration pulse. This number is shown in Fig. S12 together with how many stations were active per month in total.

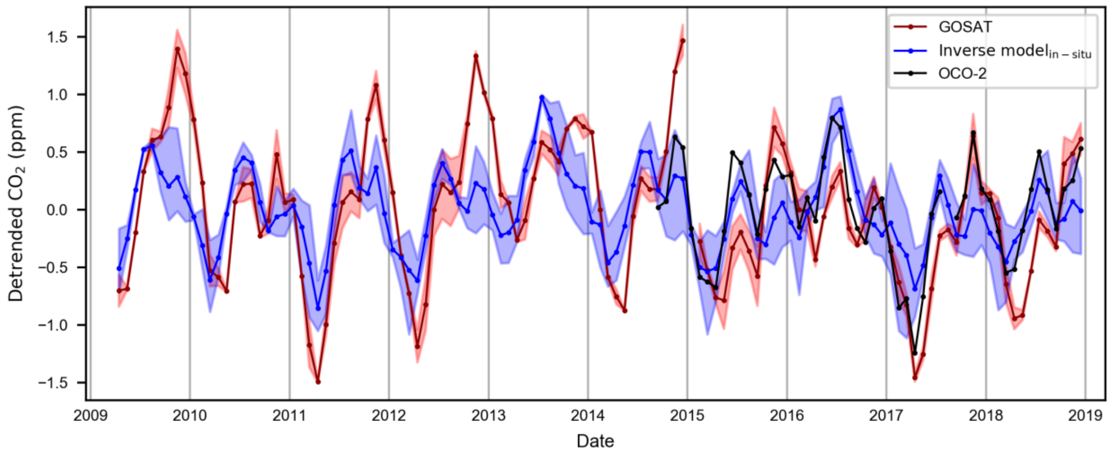

Fig. S1. Detrended CO_2 concentrations above Australia from GOSAT, OCO-2 and inverse models. Detrended monthly mean column-average dry-air mole fractions of CO_2 measured by GOSAT (red), OCO-2 (black, from 2014) and simulated by in-situ-driven inverse models (blue) averaged over continental Australia. Red shading indicates the range of the GOSAT/RemoTeC and GOSAT/ACOS algorithms. Blue shading indicates the range of the CarbonTracker, CAMS, and TM5-4DVAR inverse models.

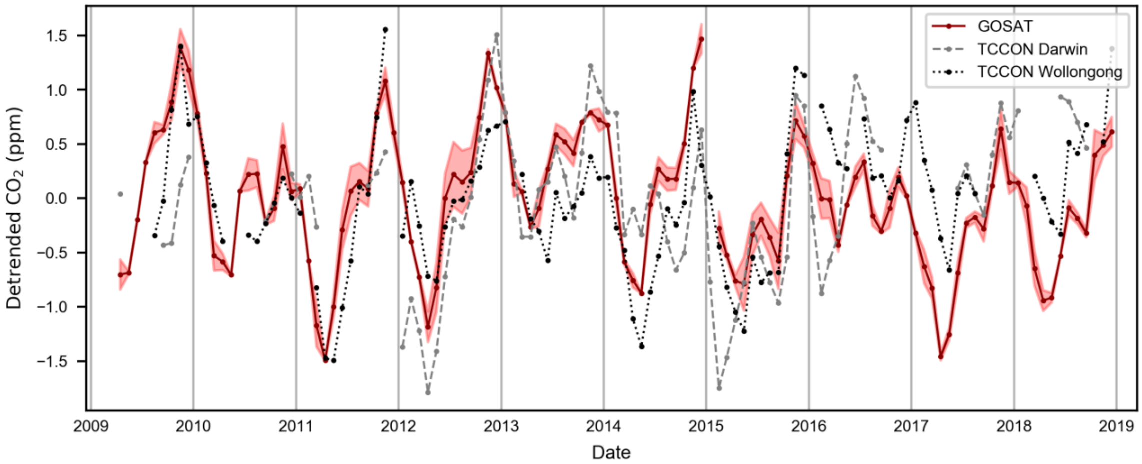

Fig. S2. Detrended CO_2 concentrations above Australia from satellite and TCCON stations. Detrended monthly mean column-average dry-air mole fractions of CO_2 measured by GOSAT (red) averaged over continental Australia and for individual TCCON stations (Darwin (*114*) in grey, Wollongong (*115*) in black). Red shading indicates the range of the GOSAT/RemoTeC and GOSAT/ACOS algorithms.

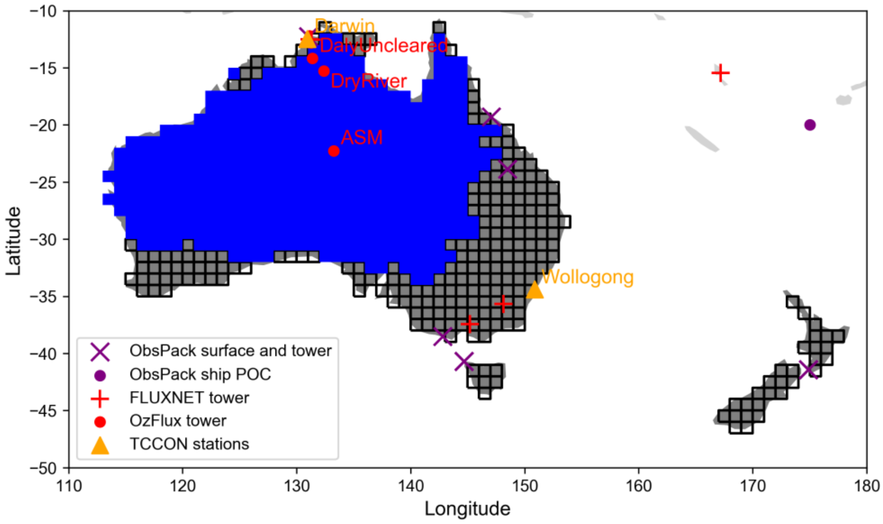

Fig. S3. TRANSCOM region and CO_2 measurement stations. The Australian regions of the TRANSCOM-3 intercomparison project is depicted in dark grey. The TRANSCOM region Australia includes Australia and New-Zealand and is divided in a semi-arid (blue) and not semi-arid part (black borders) on a 1°x1° grid. The CO_2 concentration measurement stations included in ObsPack (*56*) are shown in purple (crosses for surface and tower measurements, dot for Pacific Ocean Cruise (POC) measurements). These measurements are used by the inverse models. The eddy covariance flux measurement towers within FLUXNET and used by FLUXCOM are given as red crosses. The three OzFlux towers used in Fig. S11 are given as red dots with labels. The two TCCON stations are marked as yellow triangles with labels.

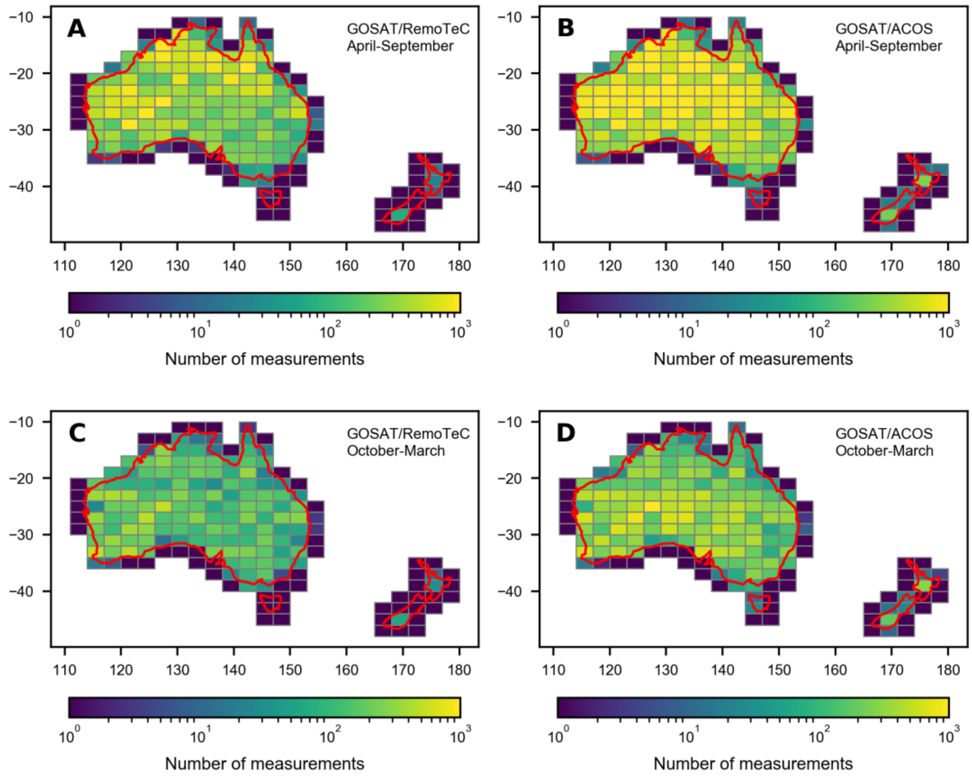

Fig. S4. Number and distribution of GOSAT CO_2 concentration data above Australia. **(A)** and **(C)** Total number of GOSAT/RemoTeC and **(B)** and **(D)** GOSAT/ACOS data from 2009 to 2018 per 3°x2° grid cell for **(A)** and **(B)** the dry months (April – September) and **(C)** and **(D)** the rainy season (October – March). The spatial data pattern results from the stripe-like GOSAT sampling procedure. The maximum number of measurements per 1°x1° grid cell is 1022 (A), 1843 (B), 536 (C), and 1028 (D). The radiative transfer treatment in RemoTeC requires stricter filtering of the GOSAT data and causes a reduced number of measurements in GOSAT/RemoTeC compared to GOSAT/ACOS.

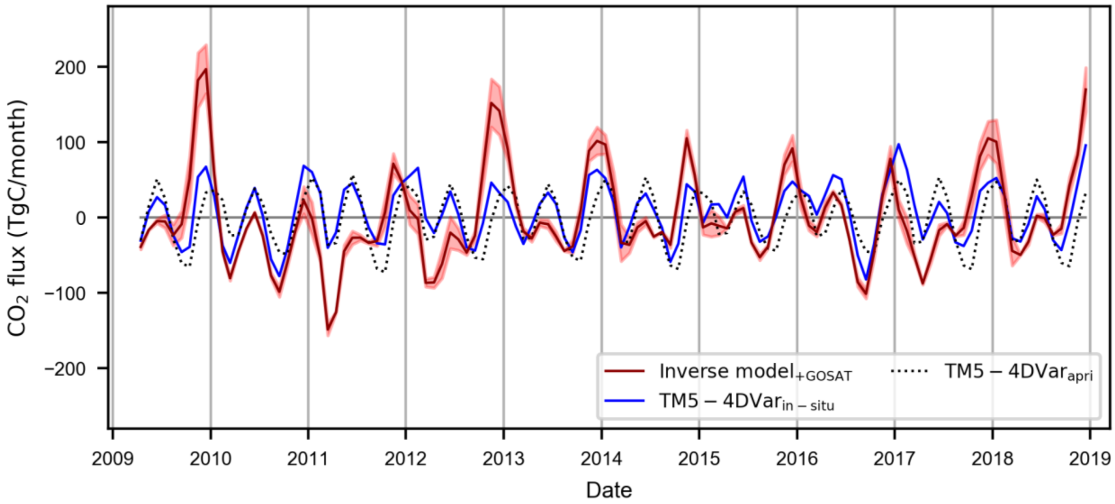

Fig. S5. Australian net CO_2 fluxes from TM5-4DVAR comparing in-situ based and GOSAT inversions with the a priori data. Like Fig. 2A, but highlighting the comparison to a priori fluxes. Top-down estimates of the net monthly Australian carbon fluxes inferred by TM5-4DVAR assimilating in-situ CO_2 measurements alone (blue) and together with GOSAT observations (red) compared to the prior fluxes used by TM5-4DVAR (black, dotted). Shading indicates the range among GOSAT/RemoTeC and GOSAT/ACOS.

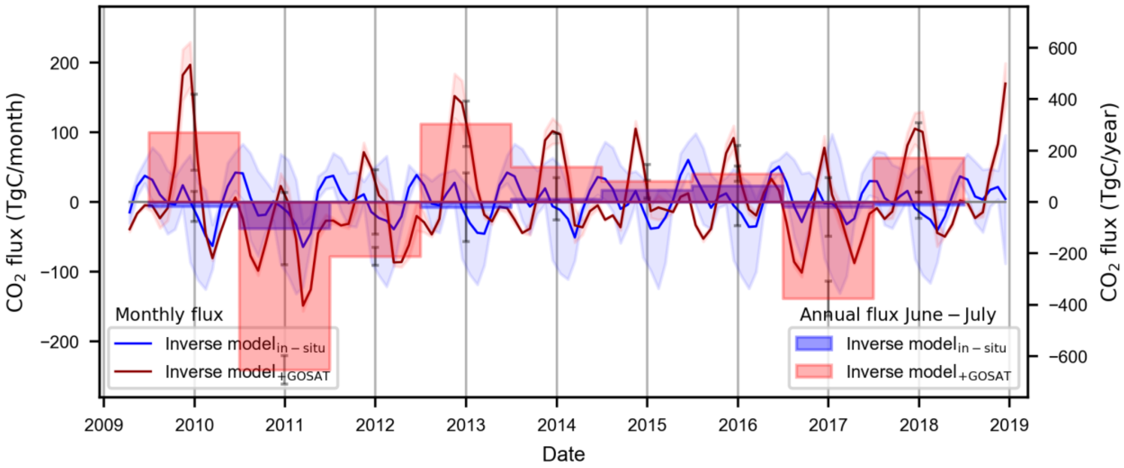

Fig. S6. Australian annual and monthly net CO_2 fluxes. Like Fig. 2A, but highlighting annual fluxes (July to June). Top-down estimates of the net Australian carbon fluxes inferred by inverse models assimilating in-situ CO2 measurements alone (blue), and inferred by TM5-4DVAR assimilating in-situ CO_2 together with GOSAT observations (red). Monthly CO_2 fluxes (lines) refer to the left-hand ordinate (TgC/month), annual CO_2 fluxes (bars) refer to the right-hand ordinate (units TgC/year). For the monthly fluxes, shading indicates the range among the various top-down data streams. For the annual fluxes (sum of monthly fluxes between July and June), the range among the data streams is indicated by the error bars.

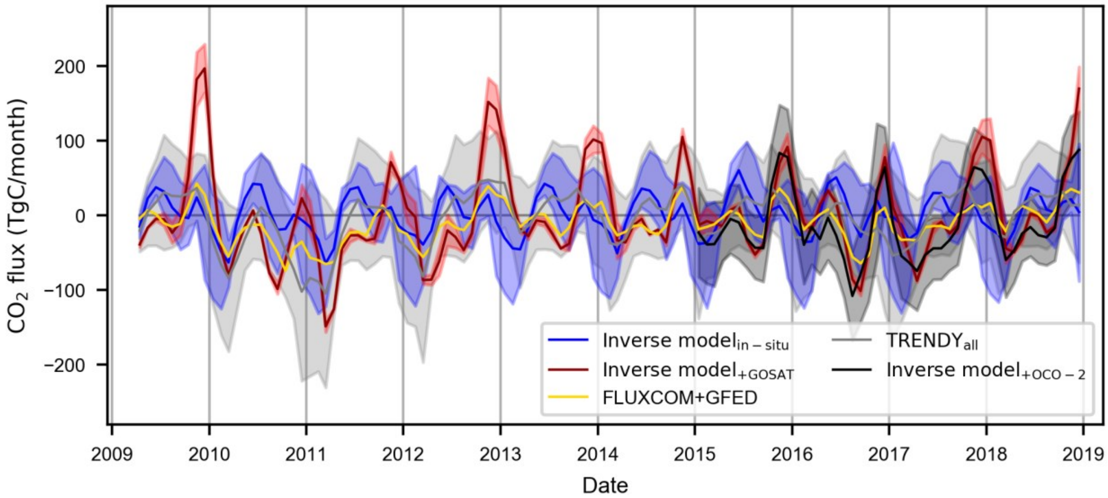

Fig. S7. Australian net CO_2 fluxes including estimates from the OCO-2 Model Intercomparison Project (MIP). Like Fig. 2A, but additionally with OCO-2 based fluxes for the period 2015-2018. Top-down estimates of the net monthly Australian carbon fluxes inferred by inverse models assimilating in-situ CO_2 measurements alone (blue), and inferred by TM5-4DVAR assimilating in-situ CO_2 together with GOSAT observations (red), compared to the ensemble-mean fluxes of the OCO-2 Model Intercomparison Project (MIP, black), bottom-up FLUXCOM+GFED NBP (yellow) and the TRENDY ensemble mean NBP (grey). Shading indicates the range among the various top-down data streams (blue, red) and the standard deviation among the TRENDY and MIP ensemble (light grey and dark grey).

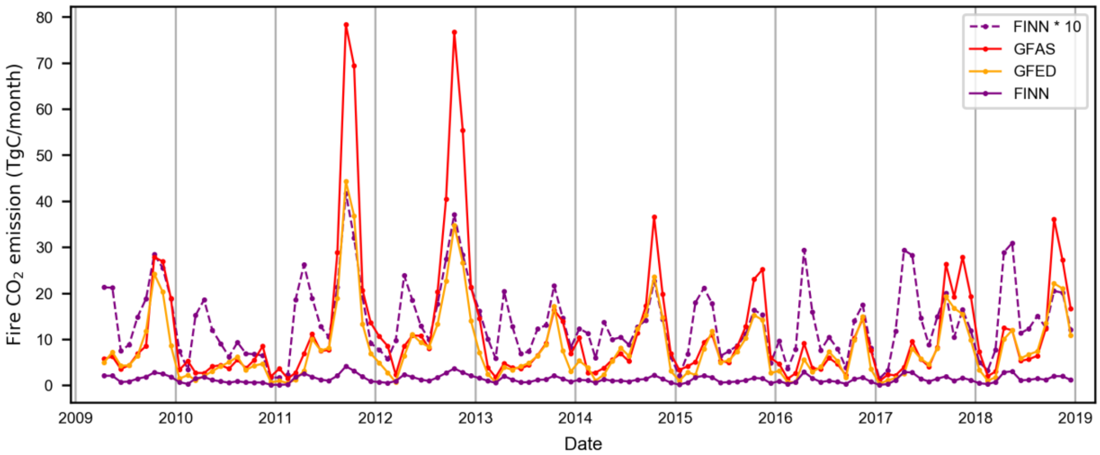

Fig. S8. CO_2 fire emissions in Australia. The monthly CO_2 fire emissions collected by three fire emission databases (GFED in orange, Global Fire Assimilation System (GFAS (*116*)) in red and the Fire INventory from NCAR (FINN (*117*)) in purple). The FINN fire emissions are additionally given amplified by a factor of ten to visualize their seasonal structure.

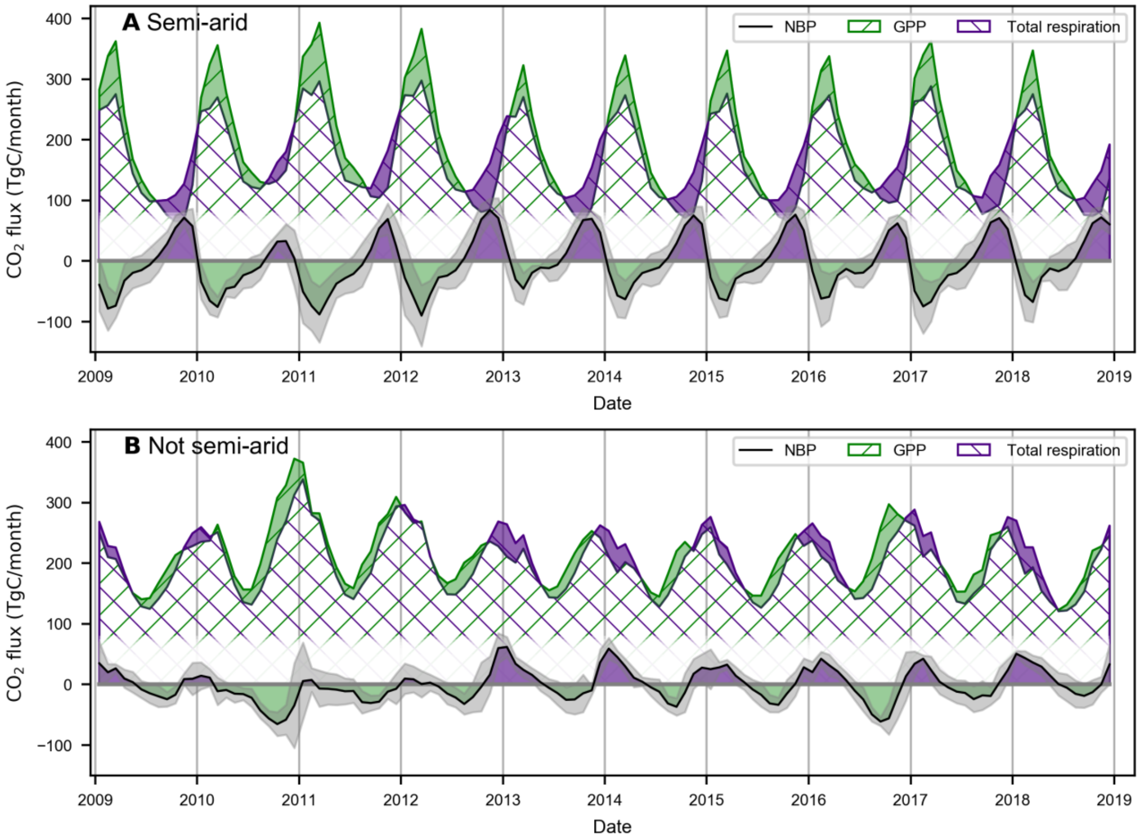

Fig. S9. Seasonal timing of gross carbon fluxes among the selected TRENDY models. **(A),** Gross primary production (GPP, green) and total respiration (violet) for the semi-arid parts of Australia (see map Fig. S3) for the selection of TRENDY DGVMs that replicate the end-of-dry-season CO_2 pulses. NBP is shown in black in the lower part (grey shading indicates the standard deviation among the model subset). **(B**), Same as panel (A) but for the parts of Australia which are not semi-arid.

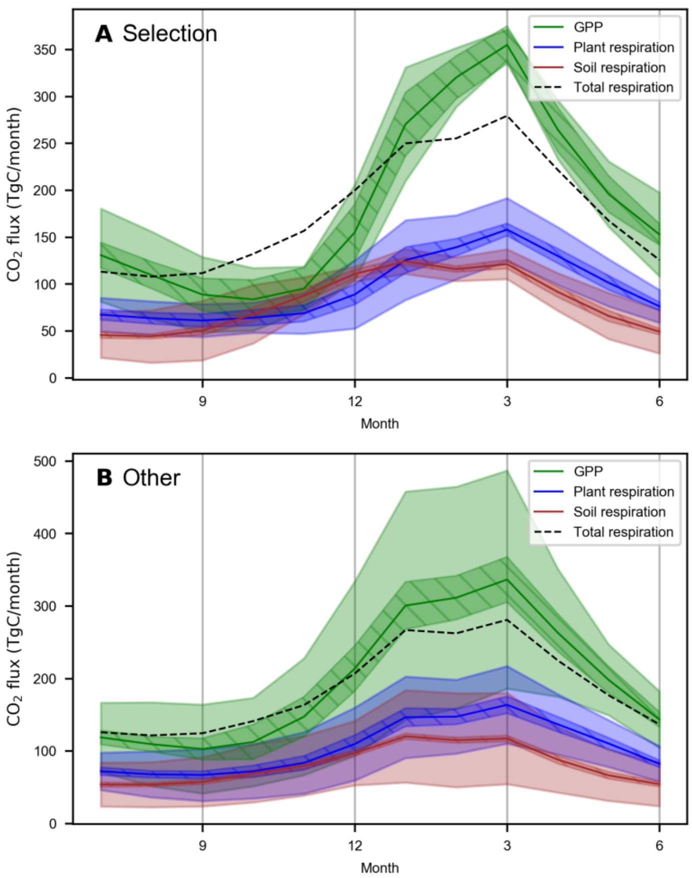

Fig. S10. Seasonal cycle of semi-arid carbon fluxes among the TRENDY models. (A) Gross primary production (GPP, green), plant respiration (blue), soil-respiration (brown) and total respiration (black dotted) for the semi-arid parts of Australia (see map Fig. S3) among the 5 selected TRENDY models that show end-of-dry-season CO_2 pulses. **(B)** Same as (A) but for the 13 TRENDY models that do not show the CO_2 pulses. The monthly fluxes are averaged over the period 2009 to 2018 and over the respective TRENDY subsets. The shadings indicate the standard deviations among the models (transparent) and among the period 2009 to 2018 (stripes pattern).

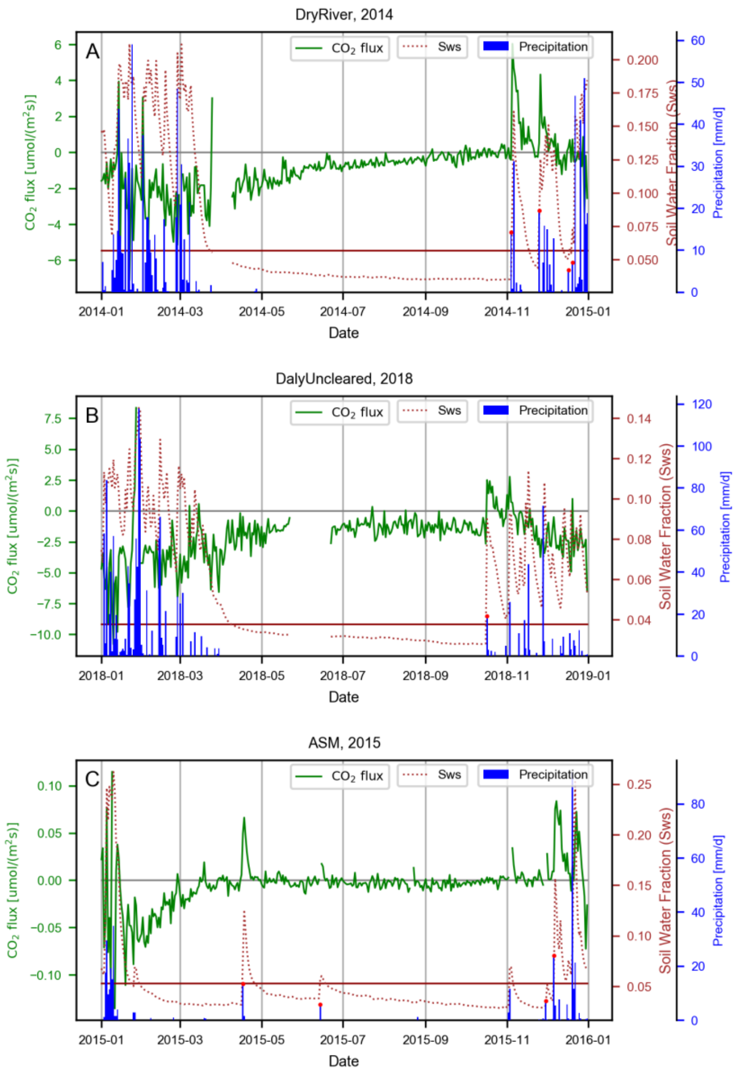

Fig. S11. Local data from OzFlux eddy covariance flux towers. (A)-(C) Daily mean net carbon fluxes (green), precipitation (blue) and soil moisture (red dashed) measured by OzFlux stations for periods illustrating local correlations between moisture supply and CO_2 fluxes. Red dots mark precipitation events which correlate with rewetting of previously dry soil and a subsequent CO_2 emission pulse (see Fig. S11 for the statistics among all OzFlux stations) (A) Station record Daly Uncleared (*88*). (B) Station record Dry River (*91*). (C) Station record Alice Springs Mulga (*75*) (ASM). The locations of the stations are given in Fig. S3.

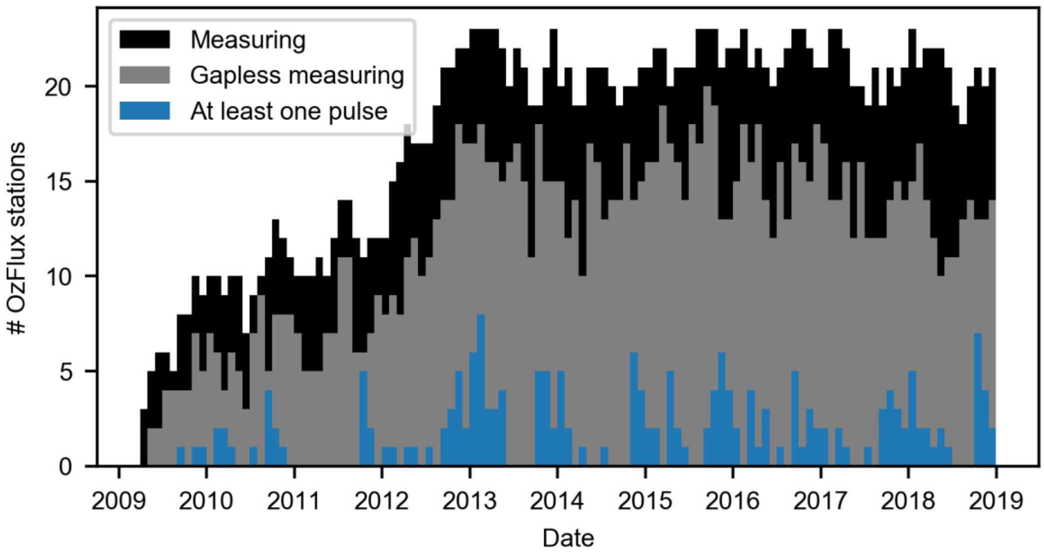

Fig. S12. Occurrence of local CO_2 pulses correlated with rewetting. Monthly count of OzFlux stations measuring at least one CO_2 emission pulse correlated with rewetting of dry soil (blue). Black and grey bars count the number of stations measuring at least for half of the month and the number of stations measuring without interruption in that month, respectively.

Table S1. Summary of datasets.

Description	**Dataset**	**Resolution**	**References**
GOSAT XCO$_2$	GOSAT/RemoTeC v2.4.0	10.5 km footprint	(*35*)
	GOSAT/ACOS v9r(Lite)	10.5 km footprint	(*36, 51*)
Validation XCO$_2$	OCO-2 v10r	1.3×2.3 km footprint	(*36, 52*)
	TCCON Darwin, Wollongong	local	(*39, 114, 115*)
Model XCO$_2$ based on in-situ data	TM5 − 4DVAR$_{in-situ}$	regional, monthly	(*42*)
	CarbonTracker CT2019B$_{in-situ}$	3°×2°, monthly	(*40, 53*)
	CAMS$_{in-situ}$ v20r2	3.7°×1.81°, monthly	(*41, 54, 55*)
Inverse Model$_{in-situ}$	TM5 − 4DVAR$_{in-situ}$	regional, monthly	(*42*)
	CarbonTracker CT2019B$_{in-situ}$	1°×1°, monthly	(*40, 53*)
	CAMS$_{in-situ}$ v20r2	3.7°×1.81°, monthly	(*41, 54, 55*)
Inverse Model$_{+GOSAT}$	TM5-4DVAR/RemoTeC	regional, monthly	(*42*)
	TM5-4DVAR/ACOS	regional, monthly	(*42*)
FLUXCOM	FLUXCOM NEE	0.08°×0.08°, 8-days	(*18, 20*)
+ GFED	GFED v4.1s	0.25°×0.25°, monthly	(*65*)
TRENDY$_{selection}$	JSBACH S3	1.86°x1.88° [1)]	(*68*)
	CLASSIC S3	2.80°x2.81° [1)]	(*69*)
	LPJ S3	0.5°x0.5° [1)]	(*70*)
	YIBs S3	1°x1° [1)]	(*71*)
	OCN S3	1°x1° [1)]	(*72*)
TRENDY$_{others}$	ORCHIDEE-CNP S3	2°x2° [1)]	(*118*)
	ORCHIDEE S3	0.5°x0.5° [1)]	(*119*)
	ORCHIDEEv3 S3	2°x2° [1)]	(*120*)
	CABLE-POP S3	1°x1° [1)]	(*121*)
	CLM5.0 S3	0.94°x1.25° [1)]	(*122*)
	DLEM S3	0.5°x0.5° [1)]	(*123*)
	IBIS S3	1°x1° [1)]	(*124*)
	ISAM S3	0.5°x0.5° [1)]	(*125*)
	ISBA-CTRIP S3	1°x1° [1)]	(*126*)
	JULES-ES-1.0 S3	1.25°x1.88° [1)]	(*127*)
	LPX-Bern S3	0.5°x0.5° [1)]	(*128*)
	SDGVM S3	1°x1° [1)]	(*129*)
	VISIT S3	0.5°x0.5° [1)]	(*130*)
precipitation	ERA5-land data total precipitation	1°×1°, monthly	(*66, 67*)

[1)] all TRENDY model data is provided in monthly temporal resolution

The main characteristics and references of the observation and model data are listed. Links to the data-sets are provided in the ’Availability of data and materials’ section.

Table S2. Seasonal and interannual variability of CO_2 flux datasets.

Ensembles	Mean Amplitude [TgC/month]	Relative Amplitude	Standard Deviation [TgC/month]	IAV [TgC/a]
Inv. Model$_{+GOSAT}$	174.53	1	40	207
Inv. Model$_{in-situ}$	87.64	0.50	13	39
TRENDY$_{all}$	85.40	0.49	20	210
TRENDY$_{selection}$	122.95	0.70	31	236
TRENDY$_{others}$	104.83	0.60	27	201
FLUXCOM+GFED	64.09	0.37	16	157
GFED	21.82	0.13	10	

July-to-June peak-to-peak amplitude of NBP (mean in TgC/month, relative w.r.t. the GOSAT inversions, standard deviation in TgC/month over the 2009 to 2018 period) and NBP interannual variations (IAV) (standard deviation in TgC/a over the 2010 to 2018 period) for the datasets used.

2.3. Publication 2: Seasonal and Interannual Variability in CO_2 Fluxes in Southern Africa Seen by GOSAT

Eva-Marie Metz, Sanam N. Vardag, Sourish Basu, Martin Jung, André Butz

From

Metz, E.-M., Vardag, S. N., Basu, S., Jung, M., and Butz, A.: Seasonal and interannual variability in CO_2 fluxes in southern Africa seen by GOSAT, Biogeoscience, 22, 555–584, https://doi.org/10.5194/bg-22-555-2025, 2025.

Biogeosciences, 22, 555–584, 2025
https://doi.org/10.5194/bg-22-555-2025

Biogeosciences
Open Access
Research article

Seasonal and interannual variability in CO_2 fluxes in southern Africa seen by GOSAT

Eva-Marie Metz[1], **Sanam Noreen Vardag**[1,2], **Sourish Basu**[3,4], **Martin Jung**[5], **and André Butz**[1,2,6]

[1]Institute of Environmental Physics, Heidelberg University, 69120 Heidelberg, Germany
[2]Heidelberg Center for the Environment (HCE), Heidelberg University, 69120 Heidelberg, Germany
[3]Goddard Space Flight Center, NASA, Greenbelt, MD 20771, USA
[4]Earth System Science Interdisciplinary Center, University of Maryland, College Park, MD 20740, USA
[5]Department of Biogeochemical Integration, Max Planck Institute for Biogeochemistry, 07745 Jena, Germany
[6]Interdisciplinary Center for Scientific Computing (IWR), Heidelberg University, 69120 Heidelberg, Germany

Correspondence: Eva-Marie Metz (eva-marie.metz@iup.uni-heidelberg.de)

Received: 26 June 2024 – Discussion started: 2 September 2024
Revised: 25 November 2024 – Accepted: 26 November 2024 – Published: 30 January 2025

Abstract. The interannual variability in the global carbon sink is heavily influenced by semiarid regions. Southern hemispheric Africa has large semiarid and arid regions. However, there is only a sparse coverage of in situ CO_2 measurements in the Southern Hemisphere. This leads to uncertainties in measurement-based carbon flux estimates for these regions. Furthermore, dynamic global vegetation models (DGVMs) show large inconsistencies in semiarid regions. Satellite CO_2 measurements offer a spatially extensive and independent source of information about the southern African carbon cycle.

We examine Greenhouse Gases Observing Satellite (GOSAT) CO_2 concentration measurements from 2009 to 2018 in southern Africa. We infer CO_2 land–atmosphere fluxes which are consistent with the GOSAT measurements using the TM5-4DVar atmospheric inversion system. We find systematic differences between atmospheric inversions performed on satellite observations versus inversions that assimilate only in situ measurements. This suggests limited measurement information content in the latter. We use the GOSAT-based fluxes and solar-induced fluorescence (SIF; a proxy for photosynthesis) as atmospheric constraints to select DGVMs of the TRENDYv9 ensemble which show compatible fluxes. The selected DGVMs allow for the study of the vegetation processes driving the southern African carbon cycle. By doing so, our satellite-based process analyses pinpoint photosynthetic uptake in the southern grasslands to be the main driver of the interannual variability in the southern African carbon fluxes, agreeing with former studies based on vegetation models alone. We find that the seasonal cycle, however, is substantially influenced by enhanced soil respiration due to soil rewetting at the beginning of the rainy season. The latter result emphasizes the importance of correctly representing the response of semiarid ecosystems to soil rewetting in DGVMs.

1 Introduction

The terrestrial carbon sink currently takes up nearly one-third of anthropogenic greenhouse gases and thereby mitigates climate change (Friedlingstein et al., 2023). The amount of CO_2 taken up by global ecosystems varies substantially from year to year. This interannual variability (IAV) reflects the response of ecosystem carbon uptake to varying climate conditions, such as temperature or precipitation fluctuations (Zeng et al., 2005; Zhang et al., 2018; Piao et al., 2020). Current vegetation models struggle to accurately reproduce the IAV of the terrestrial carbon sink, and an imbalance exists between the modeled and measured total global sink estimates (Friedlingstein et al., 2023). The imbalance is even stronger when examining carbon fluxes on smaller spatial scales (Bastos et al., 2020) and implies that there is still an insufficient understanding of the terrestrial processes driving land carbon exchange. A better understanding is needed to improve climate models and climate change predictions (Steiner, 2020).

Published by Copernicus Publications on behalf of the European Geosciences Union.

Semiarid regions contribute substantially to the IAV in the global terrestrial carbon sink. In these regions, precipitation and temperature fluctuations heavily impact the IAV in carbon fluxes (Poulter et al., 2014; Ahlström et al., 2015). Africa has large areas of semiarid and arid ecosystems (Williams et al., 2007) and contributes substantially to the global IAV (Williams et al., 2007; Valentini et al., 2014; Pan et al., 2020). However, in situ CO_2 measurements in Africa are very sparse, leading to large uncertainties in carbon flux estimates from atmospheric inversions and machine learning approaches (Valentini et al., 2014; Ernst et al., 2024). Dynamic global vegetation models (DGVMs) also show large inconsistencies amongst each other and tend to underestimate the interannual CO_2 flux variability in semiarid regions (MacBean et al., 2021).

Satellite CO_2 concentration measurements, for example, from the Greenhouse Gases Observing Satellite (GOSAT) measuring CO_2 concentrations since 2009 or the Orbiting Carbon Observatory-2 (OCO-2) launched in 2014, have much denser coverage compared with in situ measurements. Previous studies have found systematic differences between satellite-based CO_2 concentrations and fluxes in southern Africa and those based on in situ measurements (Mengistu and Mengistu Tsidu, 2020; Byrne et al., 2023). Byrne et al. (2023) attribute these differences mainly to the sparse coverage of in situ CO_2 measurements. The studies emphasize the potential of satellite-based atmospheric inversions to provide additional information and, therefore, more robust estimates of the carbon fluxes in southern Africa, which then enable research on processes driving the CO_2 exchange. Metz et al. (2023) demonstrate the potential of combining satellite-based CO_2 flux estimates with DGVMs in Australia to decipher soil respiration processes driving the Australian terrestrial CO_2 exchange at the continental scale.

Here, we investigate the decadal dataset of GOSAT CO_2 concentrations over southern Africa from 2009 to 2018. We run a global inversion with GOSAT and in situ measurements to infer GOSAT-satellite-based CO_2 exchange between the land and atmosphere and compare the results to those based on in situ measurements alone, to FLUXCOM products, and to the TRENDYv9 ensemble of DGVMs. By selecting a subset of DGVMs that match the satellite-based carbon fluxes, we analyze the underlying processes driving the IAV and seasonal variability in the southern African carbon cycle.

2 Data and methods

2.1 Study region

Our study region spans southern Africa south of 10° S including Madagascar (see Fig. 1). This region agrees with the region selection in Mengistu and Mengistu Tsidu (2020) and considers the different climatic conditions found on the African continent. North of the study region, Africa is influenced by the low-pressure system of the Intertropical Convergence Zone, leading to a tropical wet regime. In southern Africa, high-pressure cells lead to dry conditions and cause the existence of the Kalahari Desert (Mengistu and Mengistu Tsidu, 2020). Even though total annual precipitation is decreasing southwards, the whole region experiences distinct wet and dry seasons and is influenced strongly by the IAV in precipitation (Fan et al., 2015; Valentini et al., 2014). The study region is mainly covered by (woody) savannas, grassland, and shrubland (see Fig. 1).

The vegetation is mostly water limited in its growth (Williams et al., 2008) and exposed to large seasonal fires. The fire season starts in May in the western part of southern Africa and spreads eastwards to reach southern hemispheric Africa in September (Edwards et al., 2006). Fires on the whole African continent are the largest contributor to global fire carbon emissions, accounting for more than half of these emissions (van Marle et al., 2017; Shi et al., 2015; Valentini et al., 2014). They reduce the African carbon sink significantly (Lasslop et al., 2020). We subdivide the study region into a northern, savanna-dominated region and a southern grassland and shrubland region separated at 17° S, excluding Madagascar.

2.2 Total column CO_2 measurements

For our analyses, we use column-averaged dry-air mole fractions of CO_2 (XCO_2; referred to as CO_2 concentrations in the following) measured by the Greenhouse Gases Observing Satellite (GOSAT) over land in our study region. GOSAT was launched in 2009 and has a sub-satellite field of view of 10.5 km radius with a sparse sampling grid. We use GOSAT CO_2 concentration data generated by applying version 2.4.0 of the RemoTeC radiative transfer and retrieval algorithm (Butz, 2022), as used in Metz et al. (2023). The retrieval version covers the period from April 2009 to June 2019 and is based on the preceding RemoTeCv2.3.8, as used in Detmers et al. (2015). The major updates between versions 2.3.8 and 2.4.0 are stricter quality filtering in the latter and updated ancillary input data, especially for the prior gas concentrations used. Moreover, GOSAT CO_2 concentration data generated by version 9 of the NASA Atmospheric CO_2 Observations from Space (ACOS) algorithm (Lite), available for the period from April 2009 to June 2020, are used (Taylor et al., 2022). In the following, the datasets are called GOSAT/RemoTeC and GOSAT/ACOS (see Table A1 for more information about the datasets and the nomenclature used in this study). GOSAT/ACOS single measurements have a precision of 1.5 ppm and a mean bias of 0.2 ppm in validation against TCCON (Taylor et al., 2022). GOSAT/RemoTeC was found to have a similar precision of 1.9 ppm (Buchwitz et al., 2017) and, by construction, a mean bias of 0 ppm in comparison to TCCON after bias correction. GOSAT/RemoTeC was found to have regional and seasonal systematic errors of 0.6 and 0.5 ppm, respectively (Buchwitz et al., 2017).

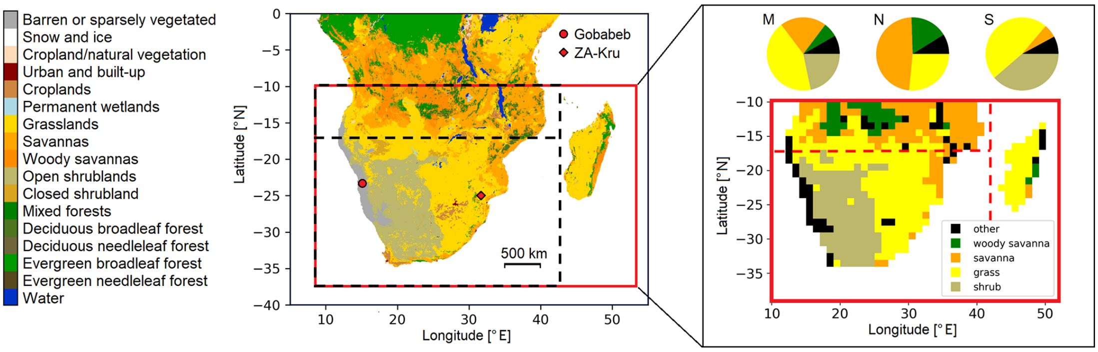

Figure 1. Study region southern Africa. The land cover in the study region is given based on MODIS (MCD12C1) data (Friedl and Sulla-Menashe, 2022). Additionally, the main region used for the analyses is depicted using a red box. In the inset map on the right-hand side, the land cover is aggregated into larger land cover classes and on a $1° \times 1°$ spatial resolution, which is used for most of the analyzed data. The main region, thereby, comprises 547 grid cells. The dashed boxes show the subdivision into a northern and a southern region. Madagascar is part of the main region, but it is excluded in the subdivision. The pie charts depict the share of the different land cover classes in the main study region (M), the northern subregion (N), and the southern subregion (S). The locations of the Gobabeb COCCON measurement site (Frey et al., 2021; Dubravica et al., 2021) and the flux tower in Kruger National Park (Archibald et al., 2009) are given as a red circle and red diamond, respectively.

For evaluation purposes, land glint and land nadir (LGLN) XCO_2 data (version 11.1r) measured by the Orbiting Carbon Observatory-2 (OCO-2) satellite are used (OCO-2/OCO-3 Science Team et al., 2022; Jacobs et al., 2024). OCO-2 was launched in 2014 and has a sub-satellite field of view of 1.3 km × 2.3 km. Furthermore, Collaborative Carbon Column Observing Network (COCCON) XCO_2 data from the Gobabeb station (Namibia; Frey et al., 2021; Dubravica et al., 2021) are taken for comparison. COCCON stations measure XCO_2 using a sun-viewing ground-based Fourier transform infrared spectrometer (Frey et al., 2019). We use the full dataset of COCCON measurements (i.e., we do not apply further filtering or co-sampling to GOSAT), as there are too few coinciding GOSAT measurements.

To examine the seasonal variability in CO_2 concentrations in the study region, the global background trend is subtracted from the total CO_2 measurements to obtain detrended CO_2 concentrations. For this, we assume a yearly linear increase in the global atmospheric CO_2 and use the annual mean CO_2 growth rate (GR) published by the National Oceanic and Atmospheric Administration (NOAA). The growth rates are based on globally averaged CO_2 concentration measurements of marine surface sites (NOAA, 2024); their calculation is further described in the main text and in Fig. A3 in Taylor et al. (2023) and in Pandey et al. (2024). The following equation describes the used background trend:

$$\mathrm{BG}_{y,m} = \mathrm{BG}_0 + \sum\nolimits_{i=2009}^{y-1} (\mathrm{GR}_i) + \frac{m}{12}\mathrm{GR}_y. \quad (1)$$

Thereby, the increase in the CO_2 concentrations in the previous years from 2009 onwards is described by the second part in the equation. The increase within the previous months in the respective year is given by the third part. Both are added to an overall offset BG_0 in 2009. This offset is estimated so that the mean of the detrended CO_2 concentrations over the whole time period is zero.

2.3 Fluxes

2.3.1 Top-down fluxes

Carbon fluxes can be obtained by assimilating measured CO_2 atmospheric concentrations in an atmospheric inversion. Atmospheric inversions typically build on Bayesian optimization (i.e., they optimize forward-transported CO_2 emissions such that these agree best with the observations within measurement and model uncertainties, while concurrently not deviating from the prior within given prior uncertainties). For our study, we use three atmospheric inversions based on in situ CO_2 measurements: the TM5 four-dimensional variational inversion system (TM5-4DVar; Basu et al., 2013), NOAA's modeling and assimilation system CarbonTracker (CT2022; Peters et al., 2007; Jacobson et al., 2023), and the Copernicus Atmosphere Monitoring Service (CAMS; Chevallier et al., 2005, 2010, 2019). The models estimate global CO_2 fluxes based on a set of in situ CO_2 measurements from global monitoring networks (Masarie et al., 2014). The models use different prior datasets. For example, for the biogenic CO_2 fluxes, TM5-4DVar and CarbonTracker build on different implementations of the Carnegie–Ames–Stanford approach (Randerson et al., 1996), as further described in Metz et al. (2023), Weir et al. (2021), and Jacobson et al. (2023), while CAMS uses biogenic fluxes of the ORCHIDEE model (Chevallier et al., 2019). Furthermore, the inversion systems use different transport models and inversion techniques. While TM5-4DVar and CarbonTracker use the TM5 transport model, CAMS uses the LMDZ global atmospheric transport model. TM5-4DVar and

CAMS make use of a 4DVar data assimilation, while CarbonTracker uses an ensemble Kalman filter. All three models use ECMWF ERA5 data as meteorological drivers. The output resolution is monthly at $3° \times 2°$ for TM5-4DVar and CarbonTracker2022 and monthly at $3.7° \times 1.81°$ for CAMS (see Table A1 for more details). The ensemble of the three models is referred to as "in-situ-only" inversions in the following, while TM5-4DVar based on in situ measurements is called "TM5-4DVar/IS".

In addition to in situ measurements, satellite CO_2 concentration measurements can be assimilated by atmospheric inversions. To this end, we use the TM5-4DVar model and assimilate GOSAT CO_2 concentration measurements over land and ocean as well as the in situ measurements. We use the individual total CO_2 concentration measurements; i.e., we do not apply any detrending or spatiotemporal averaging. Detrending and spatiotemporal averaging is only applied for visualization purposes to show the variability in the monthly CO_2 concentrations (Sect. 3.1). Depending on the specific GOSAT dataset used, we refer to these fluxes in the following as "TM5-4DVar/RemoTeC + IS", "TM5-4DVar/ACOS + IS", or (when using the mean of both) "TM5-4DVar/GOSAT + IS". More details about the TM5-4DVar settings can be found in Metz et al. (2023). For comparison, we also draw on data of the OCO-2 Model Intercomparison Project (MIP; Byrne et al., 2023) for the years from 2015 to 2018. Within the MIP, atmospheric inversions estimate carbon fluxes by assimilating OCO-2 satellite XCO_2 observations and in situ data. All MIP inversion models use the same fossil fuel emission dataset but differ with respect to the chosen datasets for all other prior fluxes (Byrne et al., 2023). We specifically make use of the LNLGIS (assimilation of OCO-2 LNLG observations and in situ measurements) and the IS (assimilation of in situ measurements only) experiment in the following, referred to as "MIP/OCO-2 + IS" and "MIP/IS", respectively. Like Byrne et al. (2023), we exclude the LoFI MIP model, as it uses a nontraditional inversion scheme differing from the MIP protocol. MIP/OCO + IS and MIP/IS provide fluxes with a monthly, $1° \times 1°$ resolution.

All inversions optimize for biogenic and oceanic fluxes but impose anthropogenic fossil fuel emissions and fire emissions. The sum of (imposed) fire and biogenic fluxes yields our net biome productivity (NBP) estimates. In this study, positive fluxes denote a release of CO_2 from land into the atmosphere. All fluxes are regridded to monthly, $1° \times 1°$ fluxes before performing the region selection.

By transporting the posterior fluxes after the optimization, atmospheric inversions can model posterior concentration fields, which can be interpolated to the time and location of the satellite measurements for comparison. This so-called co-sampling is used to eliminate sampling errors when comparing modeled concentrations to satellite measurements. We use the modeled and co-sampled posterior concentrations of the in-situ-only inversions introduced at the beginning of this section.

2.3.2 Bottom-up fluxes

We compare the top-down CO_2 fluxes to bottom-up flux datasets from DGVMs as collected by version 9 of the "Trends and drivers of the regional-scale terrestrial sources and sinks of carbon dioxide" (TRENDY; Le Quéré et al., 2013; Sitch et al., 2020) intercomparison project. The project was established to support the annual global carbon budget estimation conducted by the Global Carbon Project (e.g., Friedlingstein et al., 2020). These TRENDY models give vegetation CO_2 fluxes simulated using a harmonized set of meteorological input data and CO_2 concentrations (Le Quéré et al., 2013; Friedlingstein et al., 2020). We use the NBP, gross primary productivity (GPP), autotrophic respiration (RA), and heterotrophic respiration (RH) of 18 DGVMs (see Table A1 in the Appendix). We thereby use the following definition:

$$\begin{aligned} \mathrm{NBP} &= \mathrm{NEE} + \mathrm{fire} + \mathrm{fluc} = \mathrm{TER} - \mathrm{GPP} + \mathrm{fire} + \mathrm{fluc} \\ &= \mathrm{RH} - \mathrm{NPP} + \mathrm{fire} + \mathrm{fluc}, \end{aligned} \tag{2}$$

with the total ecosystem respiration (TER), calculated as the sum of RA and RH; the fire emissions (fire); the land use change fluxes (fluc); and the net primary productivity (NPP), calculated as the GPP minus the RA. Most of the TRENDY models provide NBP fluxes directly. In the case of the CABLE-POP and DLEM models, NBP is calculated as RH minus NPP, as both models do not provide fire and land use change fluxes. The spatial resolutions of the model output differ (see Table A1). Therefore, we aggregate fluxes on a monthly, $1° \times 1°$ grid before applying the region selection.

Additionally, we use version 1 (setup RS_V006) of the FLUXCOM net ecosystem exchange (NEE) product, as described in Jung et al. (2020). FLUXCOM uses machine learning models and meteorological data to upscale eddy-covariance tower CO_2 flux measurements to the global scale (Tramontana et al., 2016; Jung et al., 2020). To obtain an NBP estimate, we combine the NEE fluxes with fire CO_2 emissions provided by the Global Fire Emissions Database (GFED; van der Werf et al., 2017). FLUXCOM and GFED are provided as $0.08° \times 0.08°$, 8 d fluxes and $0.25° \times 0.25°$, daily fluxes, respectively, and are aggregated on a monthly, $1° \times 1°$ grid before applying the region selection.

2.4 Other datasets

To investigate the climatic conditions influencing the carbon fluxes, we use temperature, upper-layer soil moisture, and precipitation datasets of the European Centre for Medium-Range Weather Forecasts (ECMWF) ERA5-Land data product (Muñoz Sabater, 2019) with a monthly resolution on a $0.25° \times 0.25°$ spatial grid. ERA5 datasets are aggregated on a $1° \times 1°$ grid before performing the region selection. Furthermore, we use solar-induced fluorescence (SIF) measurements by the GOME-2 satellite from 2009 to January 2018 (Joiner et al., 2023). SIF is considered to be proportional to GPP on a monthly timescale and at a biome resolution (Sun et al., 2018; Joiner et al., 2018; Pierrat et al., 2022; Zhang et al., 2016a, b). It can, therefore, be used as a proxy for CO_2 uptake by photosynthesis (Li et al., 2018).

3 Results

3.1 Monthly CO_2 concentrations by atmospheric inversions

To access the seasonal and interannual dynamics in southern Africa, we detrend the monthly mean CO_2 concentrations following Eq. (1) (see Sect. 2.2). The remaining CO_2 enhancements for the study region are shown in Fig. 2. The GOSAT-measured CO_2 enhancements reveal a clear seasonal cycle with a minimum concentrations in the first half of the year and maximum concentrations in the second half of the year. This general seasonal timing is confirmed by the posterior concentrations of the in-situ-only inversions. However, yearly reoccurring differences between GOSAT and the in-situ-only based CO_2 enhancements from September to November are clearly visible. Thus, the spread between GOSAT/ACOS and GOSAT/RemoTeC (see also Fig. A1) is much smaller than their difference from and the spread among the in-situ-only inversions. The difference pattern between GOSAT and in-situ-only-based CO_2 concentrations has already been described by Mengistu and Mengistu Tsidu (2020) and has been shown by Taylor et al. (2022). Furthermore, especially in the second half of the year, different in-situ-only inversions are not consistent, as indicated by the large shading in Fig. 2a (see also the individual models in Fig. A2). Reasons for these discrepancies will be further analyzed in Sect. 3.3.

For comparison, we additionally use the OCO-2 satellite, which was launched in 2014, and 1 year of COCCON CO_2 column measurements in Namibia. Both datasets show a similar seasonal cycle to that seen by GOSAT; i.e., they show concentration maxima later in the year than the in-situ-only inversions (see Figs. A3 and A4). No other total column measurement sites – e.g., of the COCCON network or Total Carbon Column Observing Network (TCCON, Wunch et al., 2011) – with coinciding consecutive measurements for more than 1 year exist in the Southern Hemisphere for continental Africa, limiting the validation possibilities of satellite total column measurements in this region.

3.2 Southern African top-down and bottom-up CO_2 fluxes

Assimilating the GOSAT CO_2 concentration measurements in TM5-4DVar, we obtain GOSAT-based top-down fluxes at a monthly resolution for the study region (see Sect. 2.3.1). As for the concentrations, a clear seasonal cycle is visible (Fig. 3). From January to May, CO_2 is taken up by the land surface, with a maximum uptake around March. From June to December, CO_2 is released into the atmosphere and reaches a maximum flux in September to November. The number of GOSAT measurements (see Figs. A5 and A6) is variable throughout the year, with the smallest number occurring during the rainy season around December and January. This leads to larger uncertainties in the monthly mean satellite CO_2 concentrations and satellite-based fluxes during the transition from maximum to minimum concentrations and fluxes.

A similar timing of the seasonal cycle is also captured by the in-situ-only inversion fluxes (CAMS, CT2022, and TM5-4DVar/IS). However, the in-situ-only inversions' seasonal amplitude is smaller than for TM5-4DVar/GOSAT + IS. To analyze the differences found between TM5-4DVar/GOSAT + IS and the in-situ-only atmospheric inversions, we evaluate the information content provided by the measurements about the southern African carbon fluxes. To this end, we compare the TM5-4DVar fluxes (TM5-4DVar/IS and TM5-4DVar/GOSAT + IS) to the prior fluxes of the inversion model. From Fig. 4, it becomes clear that the in-situ-only fluxes (TM5-4DVar/IS) mainly follow the dynamics of the prior fluxes, whereas the GOSAT-based fluxes deviate significantly from the prior. This is expected, as the sparse coverage of in situ measurements in Africa (and the Southern Hemisphere in general) provides only little information about the African carbon fluxes. In contrast, satellites provide nearly global coverage of CO_2 measurements. Using these measurements in TM5-4DVar, new information about the southern African carbon fluxes can be obtained and may lead to a deviation of TM5-4DVar/GOSAT + IS from the prior. This finding also explains the differences among the three in-situ-only inversions (see shaded range of the in-situ-only inversions in Fig. 3). The inversions assume different prior fluxes, which they follow closely, as the information from the in situ data does not substantially inform the inversion.

When assimilating OCO-2 satellite measurements instead of GOSAT measurements, the MIP/OCO-2 + IS ensemble mean also shows a larger amplitude of the southern African carbon fluxes compared with in-situ-only inversions and MIP/IS (Fig. 5). However, the spread among the MIP/OCO-2 + IS models is large, especially during the maximum emissions from September to November. Some models show lower emissions similar to the in-situ-only inversions, whereas others agree with TM5-4DVar/GOSAT + IS. By analyzing the performance of the individual models in these 3 months, we find that three MIP/OCO-2 + IS models reproduce the OCO-2 measurements the best (see Fig. A7), indicating that the OCO-2 measurements were given a considerable weight in the inversion and, thus, that the optimized fluxes were informed by measurements (see Appendix A). At the same time, these three inversion models (Baker, CAMS,

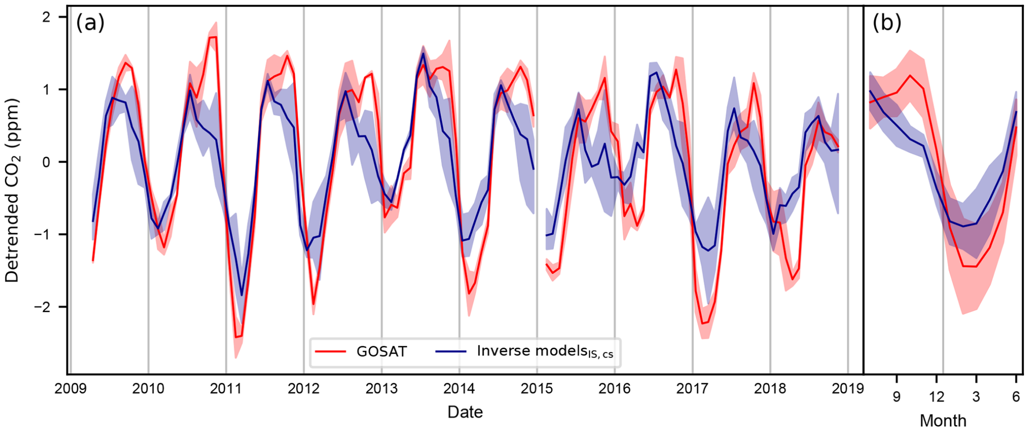

Figure 2. Monthly southern African detrended CO_2 concentrations. GOSAT-measured and detrended CO_2 concentrations are depicted in red. Modeled posterior CO_2 concentrations of three in-situ-only inversions are co-sampled (cs) on GOSAT and depicted as the mean (in blue). Panel **(a)** shows the monthly mean CO_2 concentrations. The shading indicates the range among the individual ensemble members (GOSAT/ACOS + IS and GOSAT/RemoTeC + IS in red; CT2022, CAMS, and TM5-4DVar/IS in blue). Panel **(b)** shows the mean seasonal cycle for 2009–2018, with the standard deviation over the years given as shading.

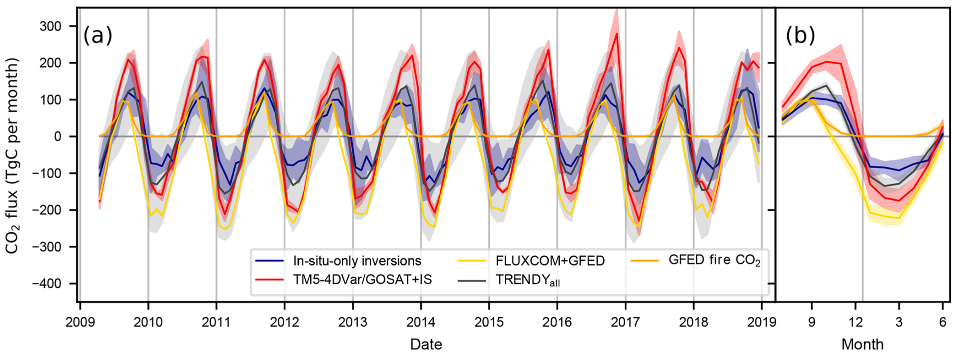

Figure 3. Top-down and bottom-up southern African net CO_2 fluxes. Panel **(a)** shows the mean monthly net CO_2 fluxes for the southern African region, while panel **(b)** shows the mean seasonal cycle of the fluxes over the 2009 to 2018 period. The TM5-4DVar/GOSAT + IS fluxes are given in red, whereas in-situ-only inversion fluxes are shown in blue. The mean over all TRENDY models is given in gray. GFED fire emissions are shown in orange, whereas they are displayed in combination with FLUXCOM NEE in yellow. The shading indicates the range over the GOSAT-based fluxes (TM5-4DVar/ACOS + IS and TM5-4DVar/RemoTeC + IS) and the in-situ-only inversion fluxes (CT2022, CAMS, and TM5-4DVar/IS) and the standard deviation over the TRENDY ensemble in panel **(a)**. In panel **(b)**, shading indicates the standard deviation over the years. Positive fluxes indicate emissions into the atmosphere. Negative fluxes correspond to an uptake of CO_2 into the land surface.

and TM5-4DVar/OCO-2 + IS) show the largest CO_2 emissions and agree best with TM5-4DVar/GOSAT + IS (see Figs. 5 and A7–A9). Still, their estimated emissions are slightly lower than those of TM5-4DVar/GOSAT + IS. When directly comparing the two TM5-4DVar inversions TM5-4DVar/GOSAT + IS and TM5-4DVar/OCO-2 + IS (Fig. 5), the latter has smaller emission values. This is most likely a result of the slightly smaller seasonal amplitude of the CO_2 concentrations measured by OCO-2 compared with GOSAT (see Fig. A3).

In conclusion, we find that satellite-based inversions, which are actually compatible with the satellite measurements, show larger carbon fluxes in southern Africa than in-situ-only inversions, which suffer from the limited information provided by the sparse in situ measurements for southern Africa. Our results support current studies (e.g., Basu et al., 2013; Sellers et al., 2018; He et al., 2023) reporting that satellite observations do inform atmospheric inversions well for flux estimates at subcontinental scales. Satellite CO_2 concentration measurements, therefore, provide a unique information source and are especially valuable in regions with sparse in situ measurement coverage. The already long record provided by GOSAT will be more and more complemented over time by the growing record of OCO-2 and future CO_2 sensors providing even more extensive measurements.

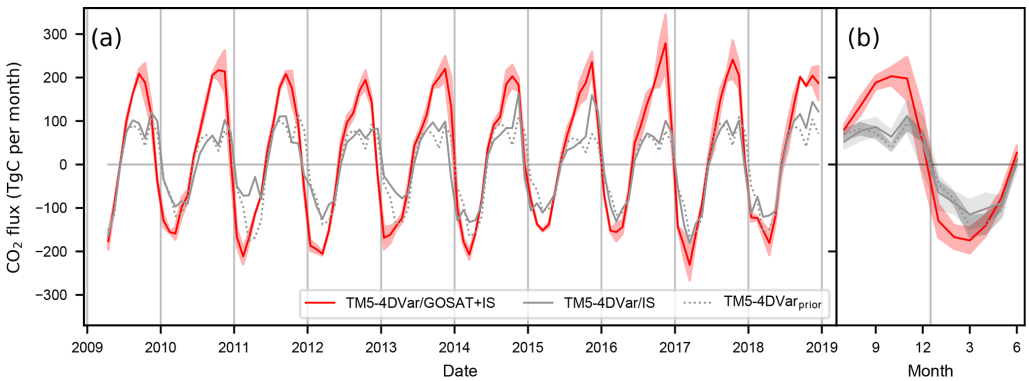

Figure 4. Top-down southern African net CO_2 fluxes from TM5-4DVar. In panel **(a)**, mean monthly net CO_2 fluxes for the southern African region from the TM5-4DVar prior (dotted gray line), the in-situ-only inversion TM5-4DVar/IS (solid gray line), and the TM5-4DVar/GOSAT + IS inversion (solid red line) are given. Red shading indicates the range of the TM5-4DVar/ACOS + IS and TM5-4DVar/RemoTeC + IS inversions. Panel **(b)** shows the mean seasonal cycle for 2009–2018, with the standard deviation over the years given as shading.

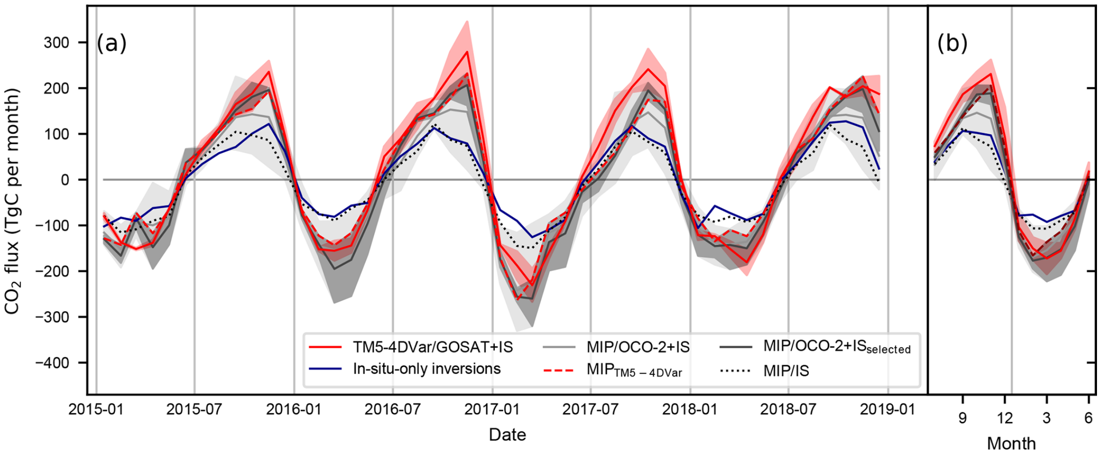

Figure 5. Top-down southern African net CO_2 fluxes from MIP. In panel **(a)**, mean monthly net CO_2 fluxes for the study region are given by TM5-4DVar/GOSAT + IS (solid red line), the MIP/OCO-2 + IS ensemble mean (solid gray line), the mean over three selected MIP models (CAMS, TM5-4DVar, and Baker; solid black line), and TM5-4DVar/OCO-2 + IS as part of the MIP ensemble (dashed red line). In-situ-only inversion fluxes are given as a solid blue line for the mean of CAMS, CT2022, and TM5-4DVar/IS, whereas they are given as a dotted black line from the MIP/IS ensemble. The shading indicates the range over the GOSAT fluxes (TM5-4DVar/ACOS + IS and TM5-4DVar/RemoTeC + IS), the MIP ensemble, and the three selected MIP models. Panel **(b)** gives the mean seasonal cycle from 2015 to 2018, with shading indicating the range over the MIP ensembles' models and the standard deviation of the TM5-4DVar/GOSAT + IS over the years.

Next to the in-situ-only inversion fluxes, we compare the TM5-4DVar/GOSAT + IS fluxes to FLUXCOM CO_2 fluxes. As FLUXCOM only provides NEE fluxes, we add GFED fire CO_2 emissions to obtain an NBP estimate. In Fig. 3, FLUXCOM + GFED only reaches positive monthly fluxes from June to September due to fire emissions occurring during that time. From October to May, it shows a net CO_2 uptake. While the timing of the maximum sink agrees well between FLUXCOM + GFED and the inversion fluxes, FLUXCOM + GFED shows a smaller amplitude and an earlier drop in emissions compared with TM5-4DVar/GOSAT + IS and in-situ-only inversion fluxes. The tendency of FLUXCOM to report a stronger carbon sink for the Southern Hemisphere compared with other datasets is described in Jung et al. (2020). It is expected that the sparsity of eddy-covariance towers in Africa or in similar ecosystems hampers the machine-learning-based approach of FLUXCOM for estimating CO_2 fluxes in the study area. Jung et al. (2020) described larger uncertainties due to representation errors in semiarid regions.

Finally, we compare the inversion results to the ensemble of process-based vegetation models of the TRENDYv9

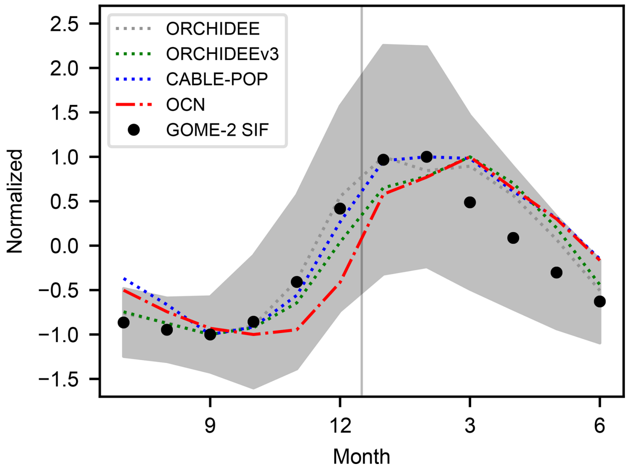

Figure 6. Seasonal cycle of SIF and selected TRENDY models. The normalized mean seasonal cycles of GOME-2 SIF (2009–January 2018), GPP from the three selected DGVMs (ORCHIDEE, ORCHIDEEv3, and CABLE-POP), and OCN GPP (2009–2018) are shown using solid black symbols, colored dotted lines, and a red dot-dash line, respectively. The spatial standard deviation over monthly GOME-2 SIF aggregated to $1° \times 1°$ is given as shading.

project. The mean of the DGVM ensemble in Fig. 3a shows a smaller amplitude than the GOSAT fluxes and compares with the in-situ-only inversion fluxes. However, as indicated by the large standard deviation, the models deviate substantially from each other. Foster et al. (2024) and Metz et al. (2023) observed a similar large spread among DGVMs for the North American temperate region and Australia, respectively. Both studies highlight the importance of performing a sub-selection of DGVMs agreeing well with atmospheric CO_2 measurements.

3.3 GOSAT and SIF atmospheric constraints on TRENDY models

Given the large spread of the TRENDY models, we select DGVMs according to their agreement with the GOSAT-based CO_2 fluxes and SIF. Thus, in a first step, we compare the monthly mean DGVM and TM5-4DVar/GOSAT + IS NBP and NEE fluxes based on the root-mean-square error (RMSE) of the monthly fluxes and the agreement in the seasonality. In a second step, only for the well-matching DGVMs, we additionally compare the GPP normalized mean seasonal cycle to the GOME SIF normalized mean seasonal cycle. Only models with a timing of the minimum and maximum GPP agreeing within ±1 month with the normalized SIF seasonal cycle are selected (see Fig. 6). This ensures the correct seasonal timing of the modeled GPP fluxes.

Based on these criteria, we select the ORCHIDEE (RMSE NBP: 60.2 TgC per month; RMSE NEE: 68.2 TgC per month), ORCHIDEEv3 (RMSE NBP 70.2 TgC per month; RMSE NEE: 56.2 TgC per month) and CABLE-POP (RMSE NBP: 78.2 TgC per month; RMSE NEE: 63.6 TgC per month) models. All other models, except for the model OCN, had already been excluded in the first step of the NBP and NEE comparison. OCN performs well in the NBP and NEE comparison but shows larger deviations in the SIF–GPP comparison (see Fig. 6). Therefore, it was excluded in the second selection step and is not included in the TRENDY selection. The exclusion of OCN underlines the importance of the SIF/GPP selection and demonstrates that a correct timing of the net CO_2 exchange fluxes does not necessarily imply the correctness of the modeled gross fluxes. In general, it is noteworthy that only 3 out of 18 TRENDY models pass our selection process. This again reveals the large uncertainties associated with the TRENDY ensemble estimate for semi-arid southern Africa.

The NBP mean over these three models is given in Fig. 7a and b. The models reproduce the timing and strength of the TM5-4DVar/GOSAT + IS NBP fluxes. Only at the beginning of the emission period around July to September are the TRENDY selection fluxes lower. Furthermore, the selection shows a significantly smaller sink in 2012 and a smaller source in 2016. Note that ORCHIDEE is part of the TRENDY selection and is also used by the in-situ-only inversion CAMS as prior flux assumption. This explains why CAMS best matches TM5-4DVar/GOSAT + IS CO_2 fluxes and GOSAT CO_2 concentrations (see Figs. A2 and A7, respectively).

Fire emissions contribute substantially to the seasonality in the southern African carbon fluxes. They largely explain the beginning of the emission period from July to September (see Fig. 3). Different fire emission data products differ significantly and suggest large uncertainties in the magnitude of the actual fire emissions in our study region (see Fig. A10). GFED, which we use for our analyses, shows the largest fire emissions but could even underestimate the actual emissions as suggested by current literature for southern hemispheric Africa (Ramo et al., 2021; van der Velde et al., 2024).

To exclude the influence of fire emission in the comparison, we analyze the monthly NEE fluxes of the TRENDY selection compared with the TM5-4DVar/GOSAT + IS NBP fluxes with GFED fire emissions subtracted. The subtraction of the fire emissions leads to a better agreement between both datasets, especially at the beginning of the emission period, suggesting that fire fluxes in the DGVMs do not agree with the GFED fire fluxes (see Fig. 7c and d). This goes along with the large uncertainties in DGVM fire fluxes reported previously (Bastos et al., 2020).

Figure 7c additionally shows the annual NEE fluxes (July–June) as bars. The absolute difference between TM5-4DVar/GOSAT + IS and TRENDY annual fluxes is large in some years. These differences are caused by a stronger sink at the beginning of 2012 and enhanced emissions at the end of 2013 and 2016 in TM5-4DVar/GOSAT + IS compared with TRENDY. However, while both datasets do not agree on the absolute value of annual fluxes in most of the years, they

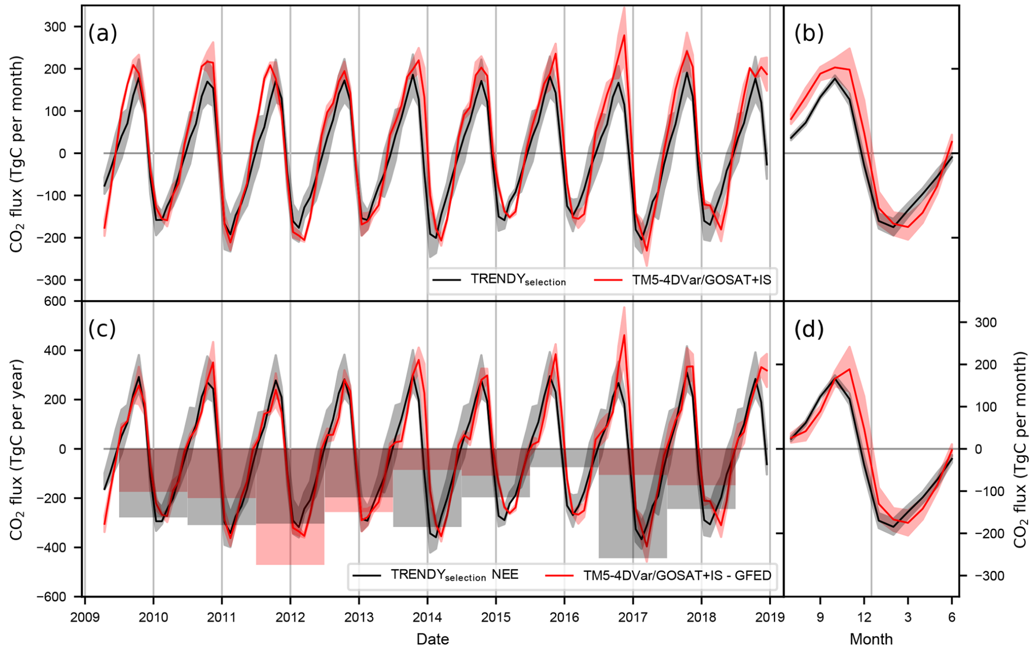

Figure 7. Annual and mean monthly NBP and NEE fluxes in southern Africa. The NBP fluxes from TM5-4DVar/GOSAT + IS (red) and selected TRENDY models (black) are given as mean monthly fluxes in panel **(a)** and as the mean seasonal cycle in panel **(b)**. Similar to that, panels **(c)** and **(d)** show the monthly NEE fluxes (GFED is subtracted from TM5-4DVar/GOSAT + IS). Additionally, the annual (July–June) NEE fluxes of the selected TRENDY models and TM5-4DVar/GOSAT + IS–GFED fluxes are given. The shading indicates the standard deviation over the TRENDY models and the range of TM5-4DVar/ACOS + IS and TM5-4DVar/RemoTeC + IS in panels **(a)** and **(c)** and the standard deviation of the monthly fluxes over the years in panels **(b)** and **(d)**.

show a similar IAV. Both datasets show a slightly stronger CO_2 uptake from 2010 to 2012. These years were strong and moderate La Niña years with enhanced rainfall in 2010 and 2011 in the study region compared with the long-term mean (see Fig. A11). Additionally, lower-than-average temperatures led to enhanced soil moisture near the surface in 2010–2011. The soil moisture declined in 2012 to reach the long-term average. In 2015 and 2016, the sink given by the GOSAT and TRENDY selection NEE fluxes is small. These 2 years were a weak and a strong El Niño year, respectively, with dry conditions and, in the case of 2016, exceptionally high temperatures (see Fig. A11). These findings agree well with the results of Pan et al. (2020), who highlighted the fact that temperature and precipitation extremes heavily impact African ecosystems and, therefore, play a key role in the African carbon fluxes.

To conclude, the monthly NEE and NBP fluxes and, to a lesser extent, the IAV in the selected TRENDY models agree well with TM5-4DVar/GOSAT + IS NEE and NBP, although the latter was not a criterion in the selection process of the TRENDY models. This suggests that the selected models indeed capture the carbon cycle dynamics, even on a decadal timescale. For this reason, we use the model selection for further investigations of the vegetation processes driving the southern African carbon cycle.

3.4 Seasonal and interannual variability in TRENDY gross fluxes

To investigate the vegetation dynamics shaping the seasonal cycle of the southern African CO_2 exchange, we use the selected TRENDY models to further split up the net ecosystem exchange fluxes into the gross fluxes NPP (GPP − RA) and RH. The gross and net fluxes are given as the mean seasonal cycle and annual anomalies in Fig. 8. In the mean seasonal cycle for the whole study region (Fig. 8a), we can see a clear difference in timing between RH and GPP − RA. Heterotrophic respiration increases early in September and October, while RA increases 1–2 months later along with GPP (see Fig. A12). The dephasing between RH and GPP − RA leads to a prolonged emission phase in the net CO_2 exchange. It takes place in the whole region and occurs in the savanna-dominated north (Fig. 8c) and in the grassland and shrublands in the south (Fig. 8e). The dephasing takes place in every year (see Fig. A13) and is present in all selected TRENDY models. It causes a mean CO_2 release of 494 TgC during the emission phase, which is about 17 % and 18 % of the annual total RH and GPP − RA, respectively. When looking at the monthly precipitation over the study region (see Fig. A14), one can identify a distinct drought phase occurring in the whole study region. The subsequent start of the rainy season in September and October temporally coincides with the early increase in RH. This finding resembles the results of Metz et al. (2023) in Australia: an increase in soil respiration with the beginning of the rainy season prior to the start of the growing season. Their study found soil respiration pulses resulting from the rewetting of soils to cause the continental-scale increase in soil respiration. Such soil respiration pulses at local arid sites are discussed in the context of the Birch effect (Birch, 1964; Jarvis et al., 2007), whereby the rewetting of the soil enables microbial populations to grow and to transform the carbon stored in the soils into CO_2 emissions. CO_2 is then released in substantial amounts within a short period of time. As in Metz et al. (2023), we find short-duration emission pulses in the daily flux record of a FLUXNET station in the study region. Exemplary annual records of the FLUXNET station in the Kruger National Park (Archibald et al., 2009) show CO_2 emission caused by precipitation pulses (see Fig. A15). This is also reported in Fan et al. (2015), who studied a 2-year measurement record of carbon fluxes in Kruger National Park in more detail. Their study found recurring respiration emission pulses due to precipitation events and attributed them to the Birch effect. The TM5-4DVar/GOSAT + IS fluxes indicate an even larger time lag between the increase in soil respiration and NPP in some years compared with TRENDY. A prolonged emission phase of an additional 1–2 months (see Fig. 7c) takes place in years with especially low soil moisture (2013, 2015, and 2016; see Fig. A11). This later drop in emissions could either be caused by a delayed start of the GPP rise in the growing season or enhanced soil respiration due to the drier conditions causing an enhanced accumulation of soil carbon during the years. It is not possible to investigate this further, as none of the TRENDY DGVMs captured the IAV in the timing of the emission phase.

It is noteworthy that large parts of the unselected “other” TRENDY models miss the dephasing between RH and GPP − RA. Their NBP estimates, therefore, do not agree with the emissions around October found by the satellite inversion. Implementing soil respiration due to rewetting more accurately in those models could improve their agreement with the satellite-based fluxes. Metz et al. (2023) found that the dephasing in the TRENDY models is most likely caused by a different response time of soil respiration and vegetation growth to precipitation; e.g., water needs to percolate into the deeper soil layers with plant roots to initiate plant growth, whereas heterotrophic respiration is driven by upper-soil-layer soil moisture or precipitation. The implementation of such a time lag between heterotrophic respiration and GPP seems to be a necessary but not a sufficient prerequisite to accurately capture the seasonal carbon flux variability in semiarid southern Africa. Our results call for studies on how to implement the response of ecosystems to soil rewetting more accurately to improve the consistency and accuracy of the TRENDY ensemble in semiarid regions.

Looking at the annual gross flux anomalies given by the TRENDY selection (Fig. 8b), we see that the IAV in NBP and NEE is mainly driven by GPP. Enhanced GPP from 2010 to 2012 leads to a constantly stronger uptake of CO_2. In 2017, a strongly enhanced GPP causes a large CO_2 sink. Reduced GPP in 2013, 2015, and 2016 results in positive NEE anomalies associated with a reduced NEE sink. RH only plays a minor role and mostly slightly counteracts the GPP anomalies. These findings agree with the studies of Ciais et al. (2009), Weber et al. (2009), and Williams et al. (2008), who identified GPP variability as a major source of African fluxes’ IAV. It is, however, in contrast to semiarid Australia, where Metz et al. (2023) found a large IAV in RH driven by precipitation anomalies during the dry season. The African study region, however, has a distinct and regular dry season every year (see Fig. A14), leading to a smaller influence of RH on the IAV. Note that GOSAT suggests a much smaller annual CO_2 sink in 2017. However, the discrepancy is mainly caused by a significant difference in the emissions in the second half of the year, while both datasets agree well with respect to the phase of carbon uptake (see Fig. 7c). Therefore, the TM5-4DVar/GOSAT + IS fluxes support the large GPP anomaly given by the TRENDY models but suggest stronger respiration or fire fluxes at the end of 2016.

Looking at the subregions (Fig. 8d and f), one can see that the sinks in 2010, 2011, and 2017 are mainly driven by the southern grassland region, where enhanced precipitation occurred during these years (see Fig. A11). The comparably large release in 2016 seems to be driven by the whole African region experiencing the highest annual temperatures and driest conditions within the 10-year study period. Therefore, the GPP IAV seems to be heavily impacted by precipitation variability. According to GFED (see Fig. A10), fire emissions play a minor role in impacting GPP and driving NBP anomalies. The variability in fire emissions is much lower than for NBP and GPP − RA. In the whole study region, the IAV (calculated as standard deviation over the years) in the GPP − RA and NBP fluxes is 97.7 and 94.1 $TgC\,yr^{-1}$, respectively. The IAV in GFED fire emissions is 27.3 $TgC\,yr^{-1}$, which is a similarly low value to the IAV in RH (27.1 $TgC\,yr^{-1}$). Furthermore, the annual fire emissions do not amplify the trend in the NBP anomalies. They were at a normal level during the large positive NBP anomaly in 2016. Higher-than-average fire emissions counteract the sink anomalies in 2011–2012, and only the slightly reduced fires in 2017 amplify the sink anomaly.

4 Conclusions

The sparsity of in situ CO_2 concentration and flux measurements results in large uncertainties in carbon flux estimates in the southern African region. We show that satellite measurements provide additional information, leading to an improvement in our knowledge about the southern African carbon

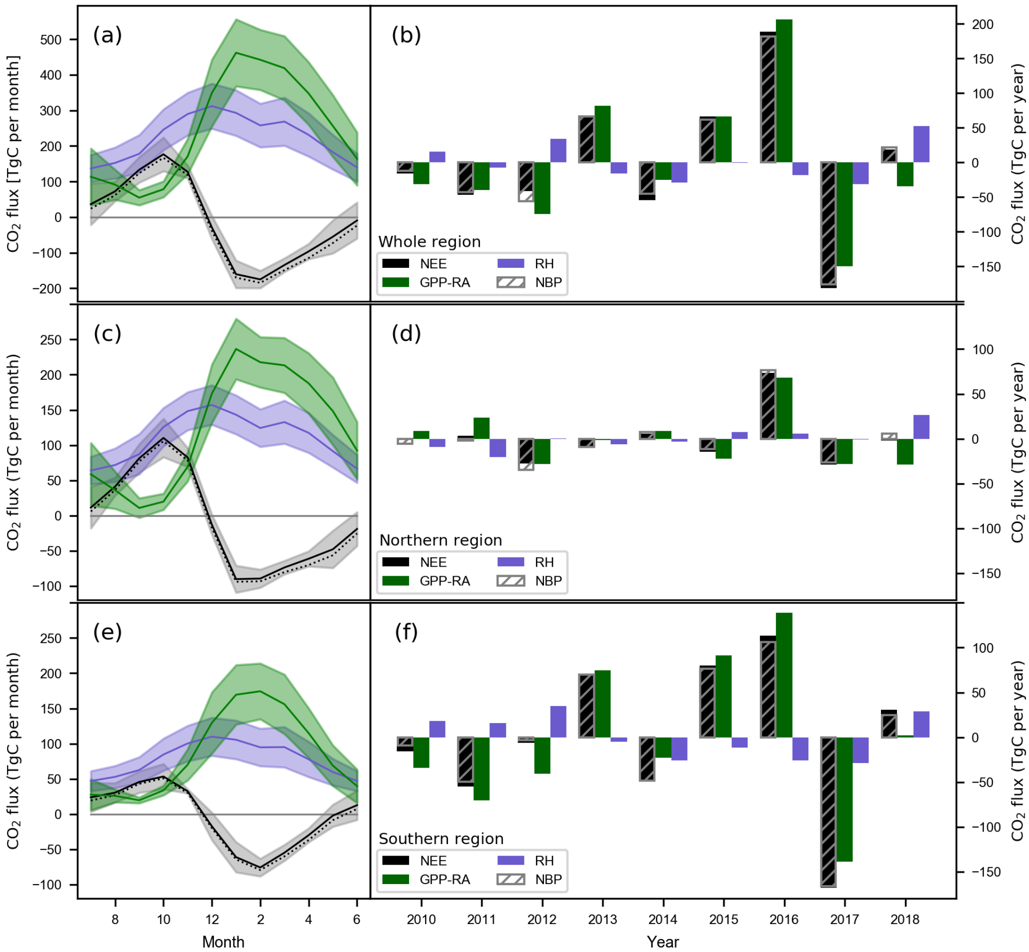

Figure 8. Annual and mean monthly CO_2 net and gross fluxes. The mean monthly fluxes **(a, c, e)** and annual (July–June) anomalies **(b, d, f)** of NEE, NBP, GPP − RA, and RH of the selected TRENDY models are given in black, gray (dotted), green, and blue, respectively. The fluxes are given for the whole study region **(a, b)**, the savanna-dominated northern region (north of 17° S; **c, d**), and the southern region with grassland and shrubland **(e, f)**. The annual anomalies are calculated by subtracting the individual long-term mean of the annual fluxes. Thus, a positive GPP anomaly denotes a reduced GPP and vice versa. The shading in panels **(a)**, **(c)**, and **(e)** indicates the standard deviation over the three selected models (ORCHIDEE, ORCHIDEEv3, and CABLE-POP).

cycle. Our study demonstrates that satellite-measurement-based atmospheric inversions and SIF can be used as atmospheric constraints for sub-selecting TRENDY DGVMs. This is necessary, as TRENDY flux estimates show a large spread in our study region.

Using the satellite-based selection of TRENDY DGVMs, we find that the IAV in NBP and NEE in southern Africa is driven by GPP variability. This supports findings by Ciais et al. (2009), Weber et al. (2009), and Williams et al. (2008) using individual vegetation models. The enhancements in annual GPP mainly originate in the grasslands and shrublands in the southern part of the study region and occur in years with an enhanced amount of precipitation. The seasonal variability in the southern African carbon fluxes is impacted by soil respiration dynamics, which are driven by the onset of the rainy season. Respiration pulses have been reported under the term of the Birch effect for arid Africa (Fan et al., 2015) and have been shown to be relevant at the continental scale in semiarid Australia (Metz et al., 2023). This enforces the relevance of rain-induced CO_2 emissions for the southern African region and for semiarid regions in general. Our results emphasize the importance of correctly representing the response of semiarid ecosystems to soil rewetting in DGVMs (e.g., different response times of RH and GPP), as this was found to be a prerequisite to accurately capture the seasonal carbon cycle dynamics.

Appendix A: The performance of the individual MIP models.

In Fig. 5, the ensemble mean of MIP/OCO-2 + IS shows lower emissions than TM5-4DVar/GOSAT + IS in the second half of the year. A selection of three models (Baker, TM5-4DVar, and CAMS), however, shows larger fluxes and agrees better with the GOSAT-based fluxes (see Sect. 3.2 and Fig. 5). Next to the OCO-2-informed posterior fluxes used for the analysis in the main text, the MIP/OCO-2 + IS dataset provides the prior fluxes used by the individual MIP models. Furthermore, 5 % of the OCO-2 measurements are withheld for validation purposes and modeled XCO_2 values co-sampled on the left-out measurements are provided for each model except CSU. The OCO-2 co-samples and the prior fluxes of the MIP models can be used to further evaluate the differences between the three selected models and the other MIP models.

In Fig. A7, the mismatch between XCO_2 modeled by the MIP and XCO_2 measured by OCO-2 is given for the months of the strongest emissions (September–November). The XCO_2 mismatch is the smallest for the three selected models, Baker, TM5-4DVar, and CAMS, which concurrently have the smallest mismatch to TM5-4DVar/GOSAT + IS. Hence, the models that reproduce the OCO-2 measurements best also agree best with the GOSAT-based CO_2 fluxes.

The differences between posterior and prior fluxes for the MIP models are given in Fig. A8. TM5-4DVar and Baker have the largest differences between the posterior and prior fluxes. Therefore, it is likely that, even though the prior fluxes of TM5-4DVar and Baker deviate strongly from the GOSAT-based fluxes (see Fig. A9), considerable weight was given to the OCO-2 measurements in the inversion. As a result, the posterior fluxes are closer to the GOSAT-based fluxes than to their prior fluxes (Fig. A8). As the CAMS prior already agrees reasonably well with TM5-4DVar/GOSAT + IS fluxes, no conclusion on the weights can be drawn here.

The other MIP models, which have lower emission fluxes, show larger mismatches to the OCO-2 XCO_2 measurements for September to November (Fig. A7). Although, for most of these models, assimilating OCO-2 increases the emission fluxes and reduces the difference to the GOSAT-based fluxes (see Figs. A8 and A9), the changes (i.e., the difference between posterior and prior fluxes) are small compared with TM5-4DVar and Baker (see Fig. A8). The larger mismatch to OCO-2 XCO_2 and the smaller posterior–prior flux differences seem to indicate that a smaller weight was given to the OCO-2 measurements compared with the selected MIP models.

In general, the GOSAT flux mismatch and the OCO-2 XCO_2 mismatch is larger in October and November than in September. This is most likely caused by the prior fluxes in September already being closer to the GOSAT-based fluxes than in the other 2 months (see Fig. A9b).

Table A1. Summary of the datasets. The main characteristics and references of the observation and model data are listed. Links to the datasets are provided in the "Data availability" section.

Description	Dataset	Resolution	References
GOSAT XCO_2	GOSAT/RemoTeC v2.4.0 GOSAT/ACOS v9r(Lite)	10.5 km footprint 10.5 km footprint	Butz et al. (2011); Butz (2022) Taylor et al. (2022); OCO-2 Science Team et al. (2019)
Validation XCO_2	OCO-2 v11r COCCON Gobabeb	1.3 km × 2.3 km footprint local	Jacobs et al. (2024); OCO-2/OCO-3 Science Team et al. (2022) Frey et al. (2021); Dubravica et al. (2021)
Model XCO_2 based on in situ data	TM5 − 4DVar/IS CarbonTracker CT2022 CAMS v21r1	3° × 2°, monthly 3° × 2°, monthly 3.7° × 1.81°, monthly	Basu et al. (2013) Peters et al. (2007); Jacobson et al. (2023) Chevallier et al. (2005, 2010, 2019); Copernicus Atmosphere Monitoring Service (2020)
In-situ-only inversions	TM5 − 4DVar/IS CarbonTracker CT2022 CAMS v20r1	3° × 2°, monthly 1° × 1°, monthly 3.7° × 1.81°, monthly	Basu et al. (2013) Peters et al. (2007); Jacobson et al. (2023) Chevallier et al. (2005, 2010, 2019); Copernicus Atmosphere Monitoring Service (2020)
TM5-4DVar/GOSAT + IS	TM5-4DVar/RemoTeC + IS and TM5-4DVar/ACOS + IS	3° × 2°, monthly	Basu et al. (2013)
TM5-4DVar/OCO-2 + IS	TM5-4DVar of MIP/LNLGIS	1° × 1°, monthly	Basu et al. (2013); Byrne et al. (2023); Baker et al. (2022)
MIP/OCO-2 + IS MIP/IS	MIP/LNLGIS experiment MIP/IS experiment	1° × 1°, monthly	Byrne et al. (2023); Baker et al. (2022)
SIF	GOME-2 Daily_Averaged_SIF	40 km × 40 km/80 km	Joiner et al. (2023)
FLUXCOM	FLUXCOMv1 NEE, RS_V006	0.08° × 0.08°, 8 d	Tramontana et al. (2016); Jung et al. (2020)
GFED	GFED v4.1s	0.25° × 0.25°, monthly	van der Werf et al. (2017, 2015)
$TRENDY_{selection}$	ORCHIDEE S3 ORCHIDEEv3 S3 CABLE-POP S3	0.5° × 0.5°* 2° × 2°* 1° × 1°*	Krinner et al. (2005) Vuichard et al. (2019) Haverd et al. (2018)
$TRENDY_{others}$	YIBs S3 OCN S3 ORCHIDEE-CNP S3 JSBACH S3 CLASSIC S3 LPJ S3 CLM5.0 S3 DLEM S3 IBIS S3 ISAM S3 ISBA-CTRIP S3 JULES-ES-1.0 S3 LPX-Bern S3 SDGVM S3 VISIT S3	1° × 1°* 1° × 1°* 2° × 2°* 1.86° × 1.88°* 2.80° × 2.81°* 0.5° × 0.5°* 0.94° × 1.25°* 0.5° × 0.5°* 1° × 1°* 0.5° × 0.5°* 1° × 1°* 1.25° × 1.88°* 0.5° × 0.5°* 1° × 1°* 0.5° × 0.5°*	Yue and Unger (2015) Zaehle et al. (2010) Goll et al. (2018) Reick et al. (2021) Melton et al. (2020) Poulter et al. (2011) Lawrence et al. (2019) Tian et al. (2015) Yuan et al. (2014) Meiyappan et al. (2015) Delire et al. (2020) Sellar et al. (2019) Lienert and Joos (2018) Walker et al. (2017) Kato et al. (2013)
ERA5 meteorological data	ERA5-Land data total precipitation, upper-layer soil moisture, temperature	1° × 1°, monthly	Muñoz Sabater (2019)
MODIS	MODIS (MCD12C1) data	0.05° × 0.05°, 2015	Friedl and Sulla-Menashe (2022)

* All TRENDY model data are provided at a monthly temporal resolution.

Table A2. Monthly fluxes of TM5-4DVar/GOSAT + IS in southern Africa. The monthly fluxes of TM5-4DVar/RemoTeC + IS ("RT + IS"), TM5-4DVar/ACOS + IS (ACOS + IS), and the mean of both are given in teragrams of carbon per month for the whole study region.

Year	Month	RT + IS	ACOS + IS	Mean	Year	Month	RT + IS	ACOS + IS	Mean
2009	4	−157.56	−195.50	−176.53	2014	3	−218.74	−194.84	−206.79
2009	5	−83.13	−102.61	−92.87	2014	4	−160.54	−153.89	−157.21
2009	6	6.71	6.29	6.50	2014	5	−84.72	−81.25	−82.99
2009	7	93.92	109.99	101.96	2014	6	30.42	42.46	36.44
2009	8	163.05	163.17	163.11	2014	7	82.04	99.66	90.85
2009	9	219.63	198.25	208.94	2014	8	95.93	122.13	109.03
2009	10	232.99	144.91	188.95	2014	9	215.17	154.74	184.96
2009	11	140.76	88.81	114.79	2014	10	229.27	176.57	202.92
2009	12	−32.79	−44.05	−38.42	2014	11	199.23	168.02	183.62
2010	1	−144.40	−113.34	−128.87	2014	12	36.93	−35.25	0.84
2010	2	−153.14	−157.85	−155.50	2015	1	−73.64	−86.37	−80.01
2010	3	−144.99	−172.86	−158.93	2015	2	−139.19	−135.31	−137.25
2010	4	−74.81	−121.29	−98.05	2015	3	−153.79	−149.43	−151.61
2010	5	−57.83	−84.45	−71.14	2015	4	−144.28	−131.81	−138.04
2010	6	24.59	16.57	20.58	2015	5	−62.78	−63.61	−63.19
2010	7	69.44	86.01	77.73	2015	6	2.16	22.31	12.24
2010	8	129.28	152.92	141.10	2015	7	49.88	85.39	67.64
2010	9	208.69	202.44	205.57	2015	8	117.11	107.91	112.51
2010	10	239.32	194.63	216.98	2015	9	189.95	139.90	164.93
2010	11	262.58	166.15	214.37	2015	10	225.03	150.79	187.91
2010	12	57.84	−24.29	16.78	2015	11	259.19	212.22	235.70
2011	1	−189.14	−146.26	−167.70	2015	12	112.16	78.85	95.50
2011	2	−229.46	−193.03	−211.24	2016	1	−72.92	−69.47	−71.20
2011	3	−156.96	−183.26	−170.11	2016	2	−148.67	−155.69	−152.18
2011	4	−111.27	−115.31	−113.29	2016	3	−176.60	−134.03	−155.32
2011	5	−70.44	−72.17	−71.31	2016	4	−159.32	−128.91	−144.11
2011	6	22.49	39.77	31.13	2016	5	−77.83	−56.86	−67.35
2011	7	88.88	101.56	95.22	2016	6	28.77	72.38	50.58
2011	8	170.18	183.09	176.63	2016	7	61.68	117.42	89.55
2011	9	214.57	202.08	208.32	2016	8	111.76	166.74	139.25
2011	10	215.25	137.67	176.46	2016	9	178.65	176.21	177.43
2011	11	108.61	83.75	96.18	2016	10	278.49	178.25	228.37
2011	12	−69.23	−42.93	−56.08	2016	11	344.93	213.55	279.24
2012	1	−198.76	−174.22	−186.49	2016	12	126.39	48.90	87.64
2012	2	−204.51	−185.68	−195.09	2017	1	−141.60	−144.98	−143.29
2012	3	−201.66	−209.21	−205.43	2017	2	−218.16	−157.23	−187.70
2012	4	−157.34	−149.79	−153.56	2017	3	−266.37	−195.15	−230.76
2012	5	−85.64	−61.66	−73.65	2017	4	−171.98	−145.48	−158.73
2012	6	26.99	55.95	41.47	2017	5	−87.55	−94.62	−91.09
2012	7	81.80	111.87	96.84	2017	6	−4.45	17.30	6.43
2012	8	105.47	131.05	118.26	2017	7	36.00	108.33	72.17
2012	9	182.86	156.69	169.77	2017	8	125.62	175.62	150.62
2012	10	216.78	172.23	194.51	2017	9	191.89	212.30	202.10
2012	11	130.49	155.95	143.22	2017	10	285.32	197.40	241.36
2012	12	−29.84	−24.57	−27.20	2017	11	233.14	175.95	204.54
2013	1	−195.13	−142.42	−168.78	2017	12	3.21	3.05	3.13
2013	2	−181.41	−141.65	−161.53	2018	1	−131.45	−111.65	−121.55
2013	3	−150.87	−134.34	−142.60	2018	2	−119.89	−127.09	−123.49
2013	4	−133.19	−113.00	−123.10	2018	3	−167.60	−135.00	−151.30
2013	5	−72.44	−40.57	−56.51	2018	4	−208.14	−153.04	−180.59
2013	6	34.37	52.38	43.38	2018	5	−137.36	−102.90	−120.13
2013	7	64.78	85.80	75.29	2018	6	−21.20	23.47	1.14
2013	8	96.91	130.53	113.72	2018	7	29.86	98.30	64.08
2013	9	176.64	185.33	180.99	2018	8	110.99	163.25	137.12
2013	10	219.32	178.29	198.80	2018	9	202.02	201.28	201.65
2013	11	249.06	191.11	220.08	2018	10	182.51	179.17	180.84
2013	12	202.08	64.14	133.11	2018	11	223.74	184.91	204.33
2014	1	−79.09	−119.87	−99.48	2018	12	226.30	148.33	187.31
2014	2	−187.16	−169.20	−178.18					

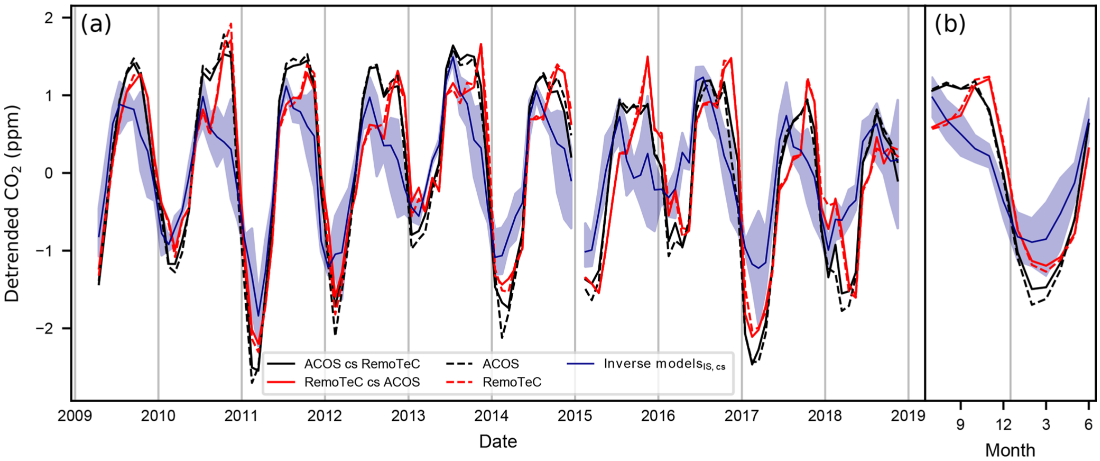

Figure A1. Monthly southern African detrended CO_2 concentrations measured by GOSAT. GOSAT/ACOS is given in black, while GOSAT/RemoTeC is given in red. Dashed lines show the mean CO_2 concentrations over the whole dataset. The mean CO_2 concentrations of the soundings included in both datasets, ACOS and RemoTeC, are given as solid lines. "cs" stands for co-sampled and indicates that only soundings also included in the other dataset are considered. The deviations due to different sampling are on a sub-part-per-million scale and do not explain the differences between ACOS and RemoTeC. Modeled posterior CO_2 concentrations of the in-situ-only inversions are co-sampled (cs) on GOSAT and depicted as the mean (in blue) for comparison. The shading indicates the range among the individual in-situ-only inversions. Panel **(b)** shows the mean seasonal cycle for 2009–2018, with the standard deviation over the years given as shading.

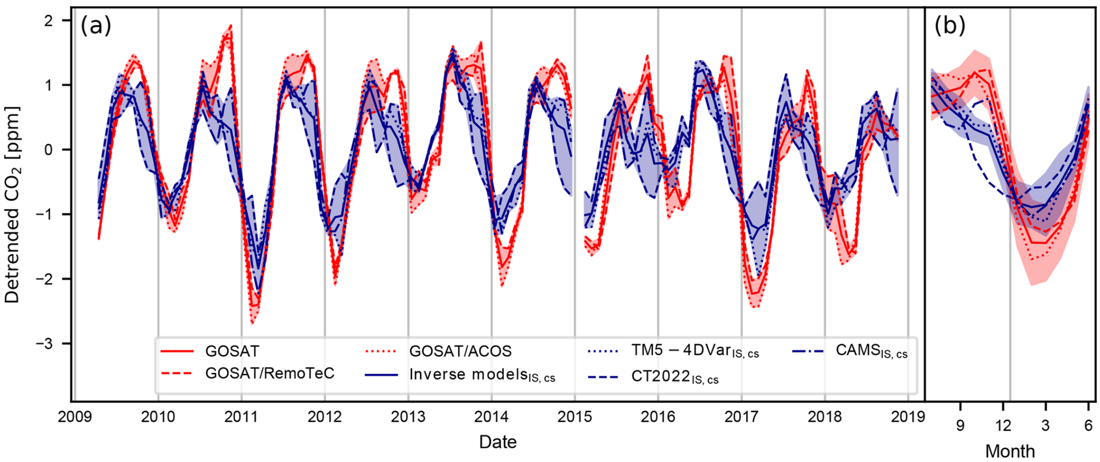

Figure A2. Monthly southern African detrended CO_2 concentrations given by inversions and satellites. Like Fig. 1 but with detrended XCO_2 of individual in-situ-only inversions co-sampled (cs) on the GOSAT measurements in dark blue (CT2022 – dashed; CAMS – dot-dash; and TM5-4DVar/IS – dotted). Panel **(a)** gives the monthly mean CO_2 concentrations, whereas panel **(b)** shows the mean seasonal cycle for 2009–2018. The shading indicates the range among GOSAT/ACOS and GOSAT/RemoTeC and the range among the three in-situ-only inversions in panel **(a)**. In panel **(b)**, the shading indicates the standard deviation over the year.

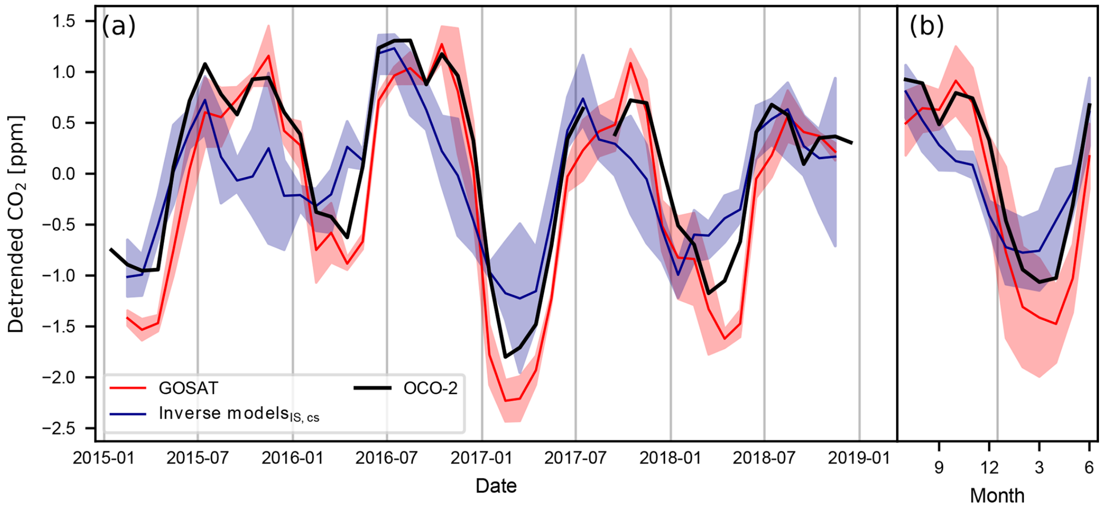

Figure A3. Monthly southern African detrended CO_2 concentrations given by inversions and satellites. Like Fig. 1 but with detrended XCO_2 measurements of OCO-2 (in black) for the time period from 2015 to 2018. Panel **(a)** gives the monthly mean CO_2 concentrations, whereas panel **(b)** shows the mean seasonal cycle for 2015–2018. The shading indicates the range among GOSAT/ACOS and GOSAT/RemoTeC and the range among the three in-situ-only inversions in panel **(a)**. In panel **(b)**, the shading indicates the standard deviation over the years.

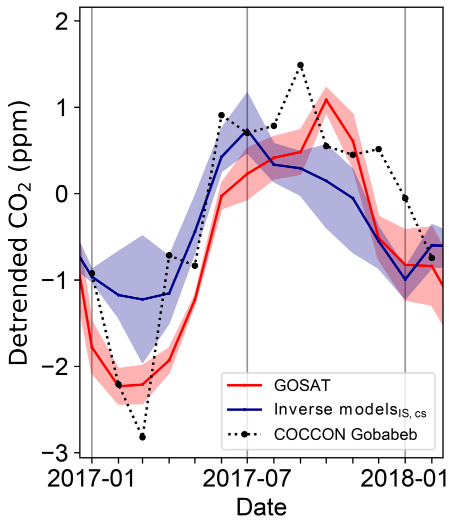

Figure A4. Monthly southern African detrended CO_2 concentrations given by inversions, satellites, and COCCON measurements. Like Fig. 1 but only for January 2017–February 2018 and with detrended XCO_2 measurements from the Gobabeb COCCON station (in black). The full dataset of COCCON measurements is used, without performing a co-sampling on GOSAT measurements or further filtering.

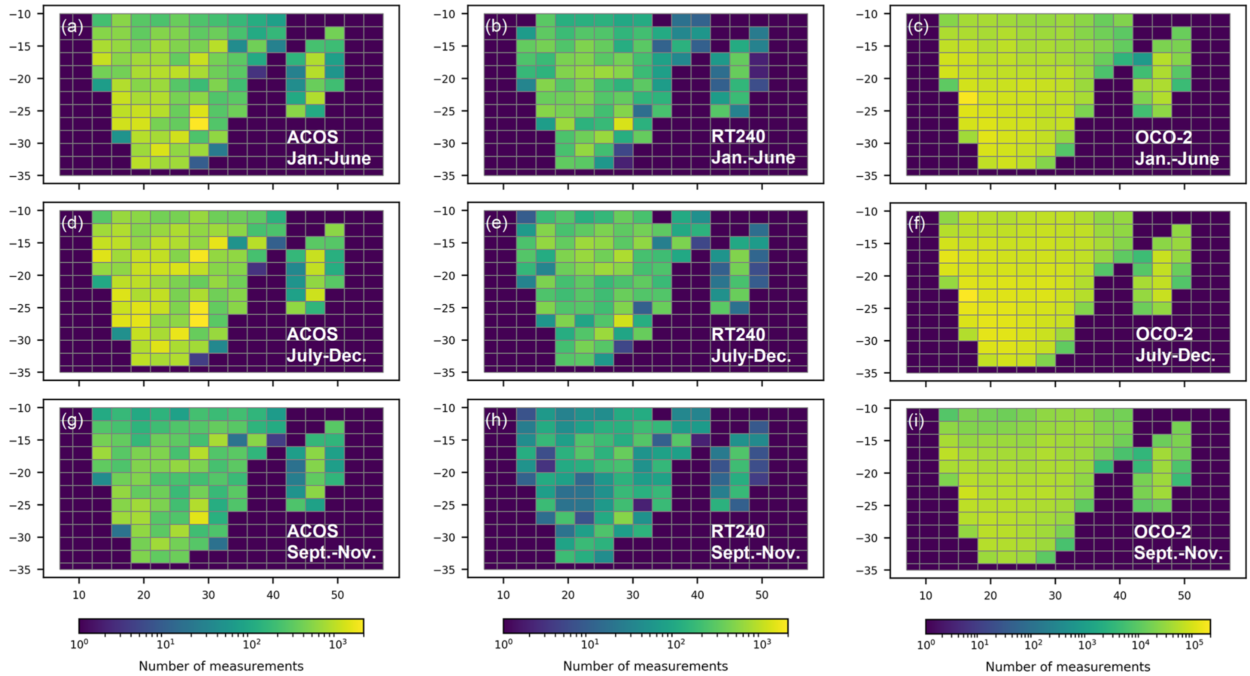

Figure A5. Number and distribution of satellite CO_2 concentration measurements above southern Africa. **(a, d, g)** Total number of GOSAT/ACOS, **(b, e, h)** GOSAT/RemoTeC, and **(c, f, i)** OCO-2 data per 3° × 2° grid cell for **(a–c)** the months of carbon uptake (January–June), **(d–f)** the emission season (July–December), and **(g–i)** the month with the strongest emissions. GOSAT/ACOS and GOSAT/RemoTeC measurements from 2009 to 2018 and OCO-2 measurements from September 2014 to 2018 are included. The maximum of the color scale is the same for all time periods but different for OCO-2 compared with GOSAT/ACOS and GOSAT/RemoTeC. Compared with GOSAT/ACOS, GOSAT/RemoTeC has a reduced number of measurements, as the RemoTeC algorithm applies stricter filtering of the GOSAT soundings.

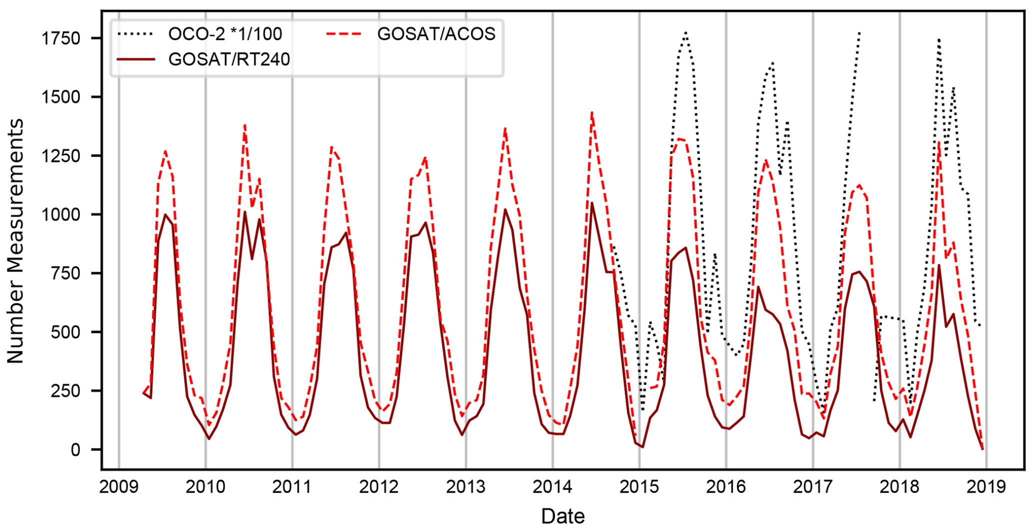

Figure A6. Number of satellite measurements per month. The numbers of satellite measurements in the GOSAT/ACOS (dashed red line), GOSAT/RemoTeC (solid dark-red line), and OCO-2 (dotted gray line) datasets are given. Note that the number of OCO-2 measurements is shown divided by 100 to enable a comparison to the much less abundant GOSAT measurements.

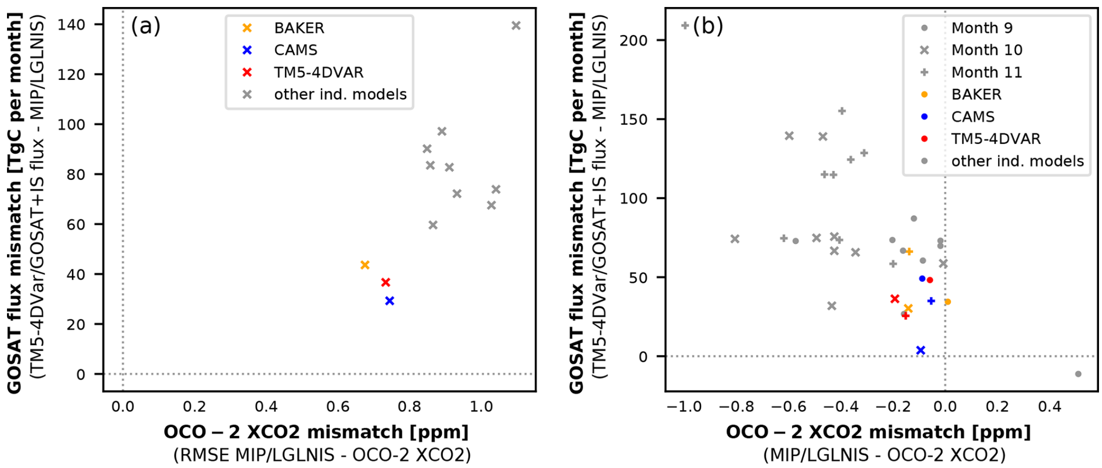

Figure A7. Mismatch between GOSAT-informed and OCO-2-informed fluxes versus the mismatch between OCO-2-informed simulated XCO_2 and OCO-2-measured XCO_2. For the MIP/OCO-2 + IS inversions, 5 % of the OCO-2 measurements are withheld for validation purposes and modeled XCO_2 values co-sampled on the measurements are provided for each model except CSU. Panel **(a)** gives the RMSE of the OCO-2 measurements and the modeled co-sampled XCO_2 from September to November for each model. In panel **(b)**, the mean differences in the OCO-2 measurements and modeled co-samples for each month and model are given. In both panels, the OCO-2 XCO_2 mismatch is plotted against the difference in the monthly TM5-4DVar/GOSAT + IS and individual MIP/OCO-2 + IS CO_2 fluxes for the strongest emission period from September to November. The MIP models Baker, CAMS, and TM5-4DVar are highlighted in yellow, blue, and red, respectively. The other individual MIP models are given in gray. The three highlighted models show the smallest OCO-2 XCO_2 mismatch and the smallest difference from the monthly fluxes of TM5-4DVar/GOSAT + IS (with the exception of Baker in September; **b**).

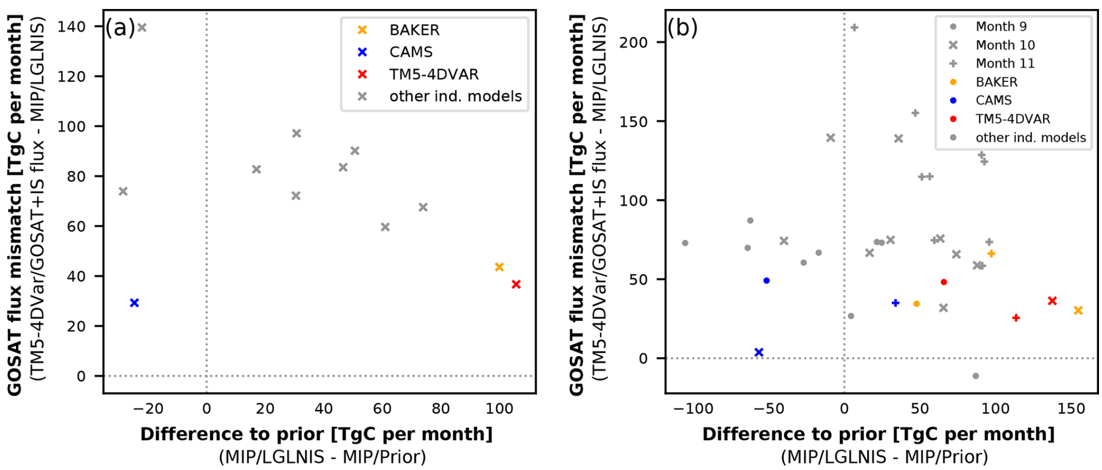

Figure A8. Mismatch between GOSAT-informed and OCO-2-informed fluxes versus the difference between OCO-2-informed fluxes and model prior fluxes. The individual MIP models differ with respect to their assumed prior fluxes. In this figure, the differences in the monthly posterior to the prior fluxes (x axis) and to the GOSAT-based fluxes (TM5-4DVar/GOSAT + IS, y axis) are compared. Differences are calculated using the monthly flux over the whole study region and the time period from 2015 to 2018. Panel **(a)** shows the mean over September to November, the time of the strongest CO_2 emissions. In panel **(b)**, the differences are given for each of the three individual months. The MIP models Baker, CAMS, and TM5-4DVar are highlighted in yellow, blue, and red, respectively. The other individual MIP models are given in gray. For most of the models, the assimilation of OCO-2 measurements increases the mean monthly fluxes from September to November (difference from prior larger than zero). Only for CAMS, UT, and some models in September are the mean posterior fluxes smaller than the prior fluxes.

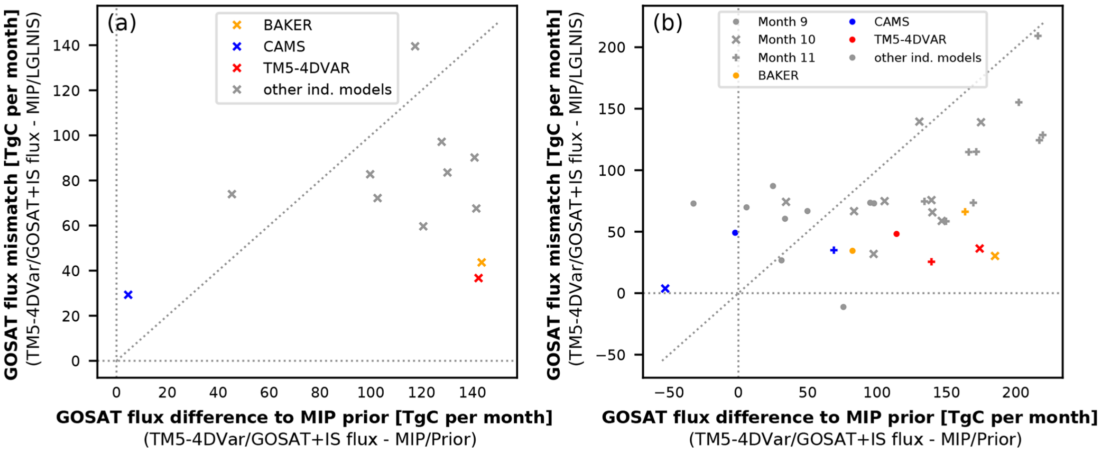

Figure A9. Mismatch between GOSAT-informed and OCO-2-informed fluxes versus the difference between GOSAT-informed fluxes and OCO-2 MIP prior fluxes. The differences in the monthly GOSAT inversion fluxes (TM5-4DVar/GOSAT + IS) compared with the MIP posterior (y axis) and MIP prior fluxes (x axis) for the individual MIP models are given. Panel **(a)** gives the mean differences for the months from September to November. Panel **(b)** shows the differences for the individual months. The MIP models Baker, CAMS, and TM5-4DVar are highlighted in yellow, blue, and red, respectively. The other individual MIP models are given in gray. The 1 : 1 line is given as a dotted gray line. For most of the MIP models, assimilating OCO-2 reduces the flux difference to the GOSAT-based fluxes (i.e., markers are below the 1 : 1 line).

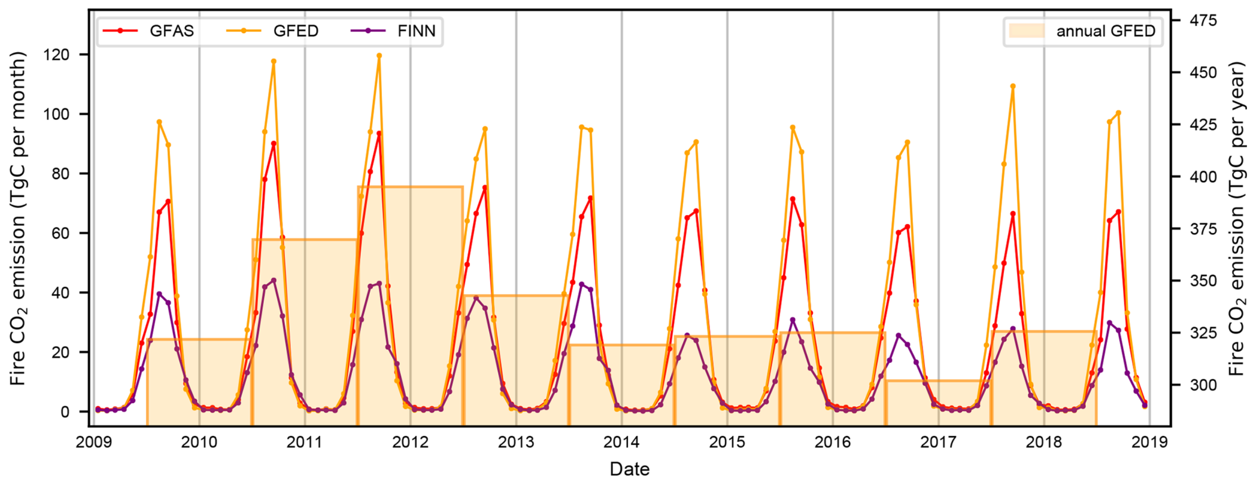

Figure A10. The CO_2 fire emissions in southern Africa. The monthly CO_2 fire emissions collected by three fire emission databases: GFED (in orange), the Global Fire Assimilation System (GFAS; Kaiser et al., 2012; Copernicus Atmosphere Monitoring Service, 2022; in red), and the Fire INventory from NCAR (FINN; Wiedinmyer et al., 2011, 2021; in purple). Furthermore, the annual (July–June) GFED fire emissions are shown on the right-hand y axis. Please note that the right-hand y axis starts at $280\,\mathrm{TgC\,yr^{-1}}$ for better visualization of the fire emissions.

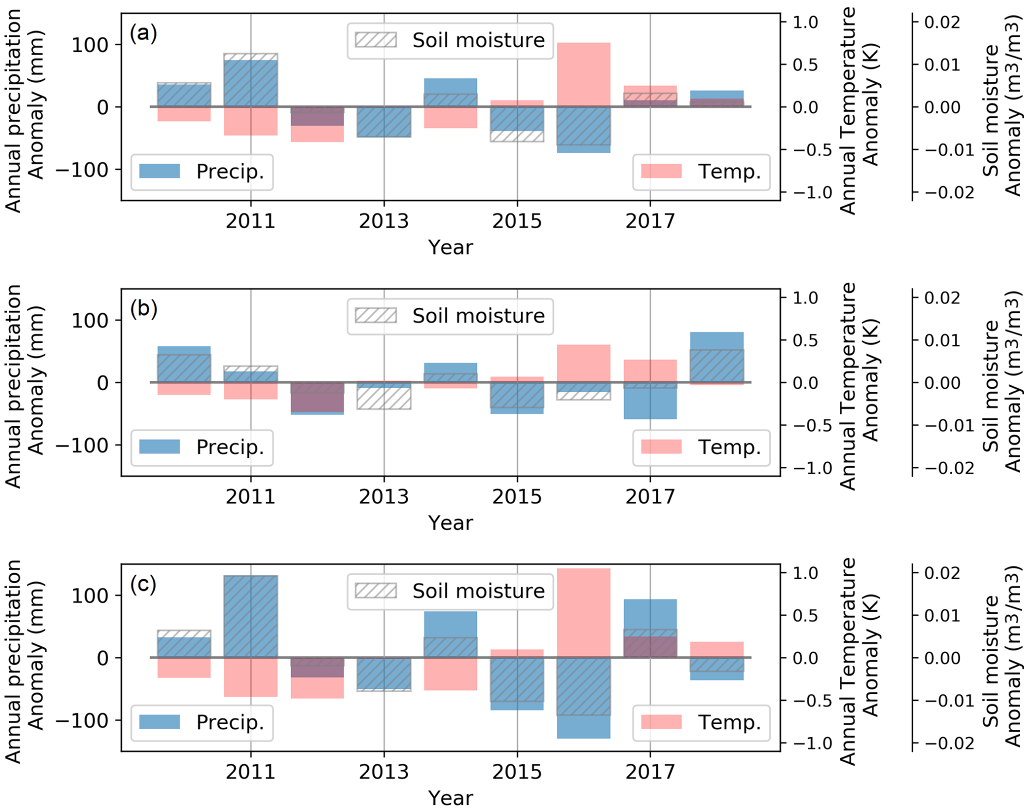

Figure A11. Climate anomalies. The annual anomalies of ERA5 precipitation, temperature, and upper-layer soil moisture are displayed using solid blue, solid red, and gray hatching, respectively. The annual anomalies are calculated by subtracting the individual long-term mean of the annual values and are given for the whole study region in panel **(a)**, for the northern subregion in panel **(b)**, and for the southern subregion in panel **(c)**.

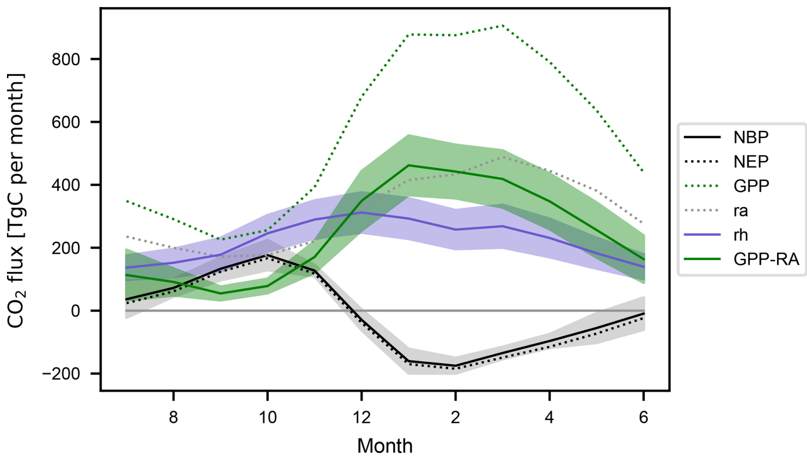

Figure A12. Mean monthly CO_2 net and gross fluxes. Like Fig. 8a but also including the GPP and RA of the TRENDY selection.

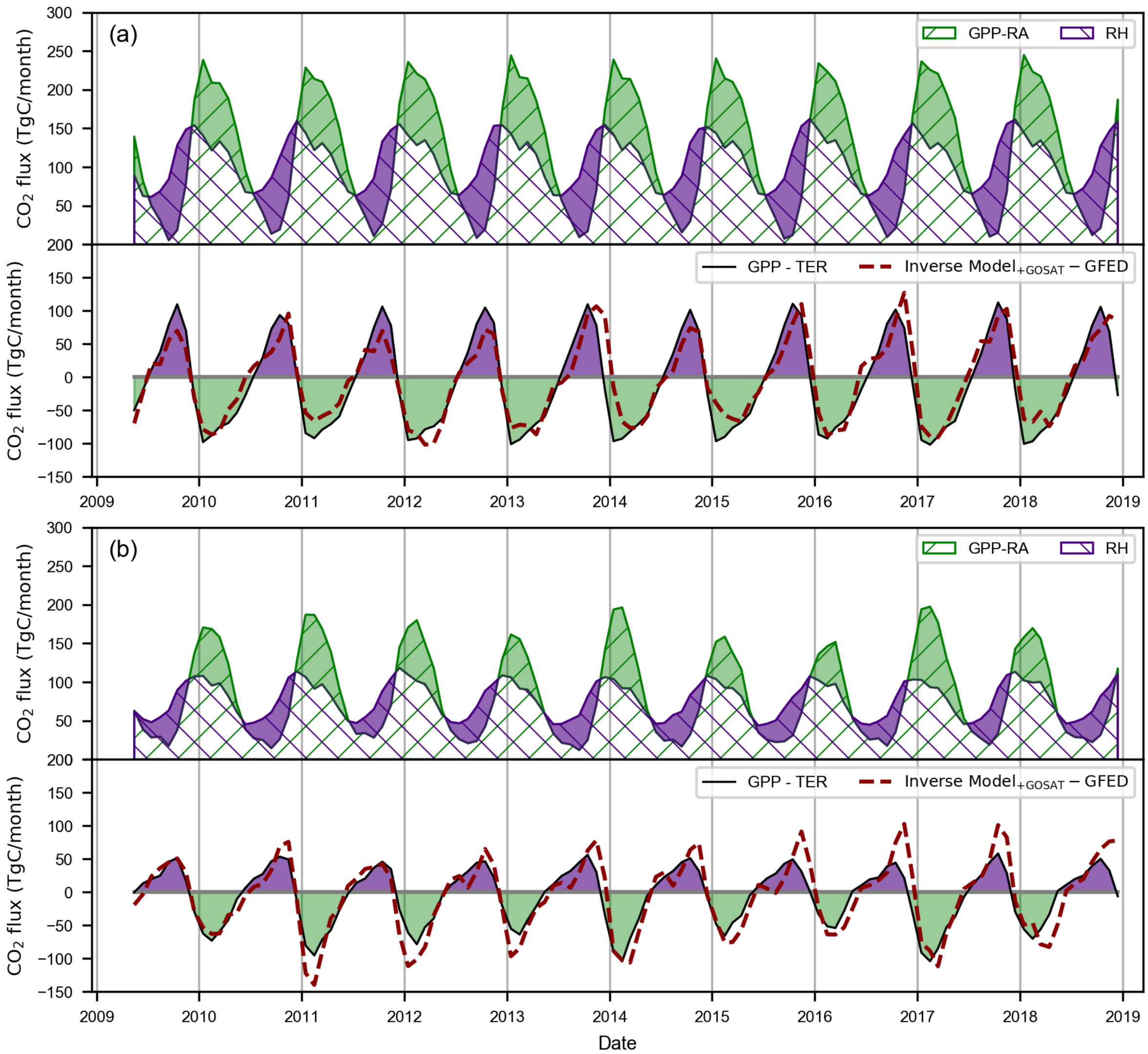

Figure A13. Monthly CO_2 fluxes in the northern **(a)** and southern **(b)** subregions. The monthly NEE, NPP (GPP − RA), and RH fluxes from the selected TRENDY models are given in black, green, and violet, respectively, for the northern southern African region in panel **(a)**. The TM5-4DVar/GOSAT + IS–GFED NEE fluxes are additionally shown as a dotted red line. The same is given in panel **(b)** for the southern subregion.

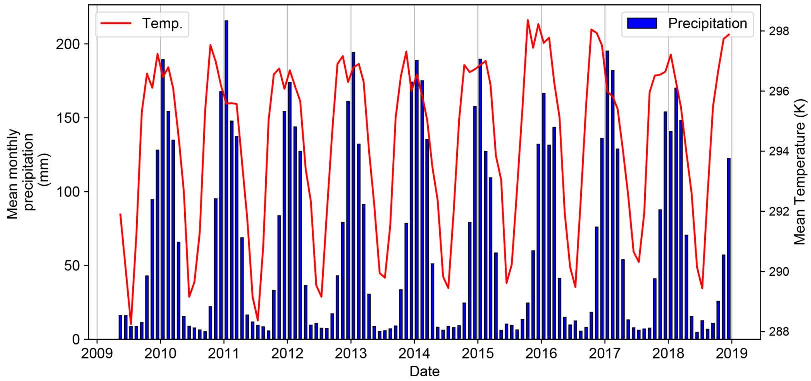

Figure A14. Mean monthly precipitation and mean temperature over southern Africa. The mean monthly precipitation is given as blue bars, whereas the mean temperature is shown using a solid red line.

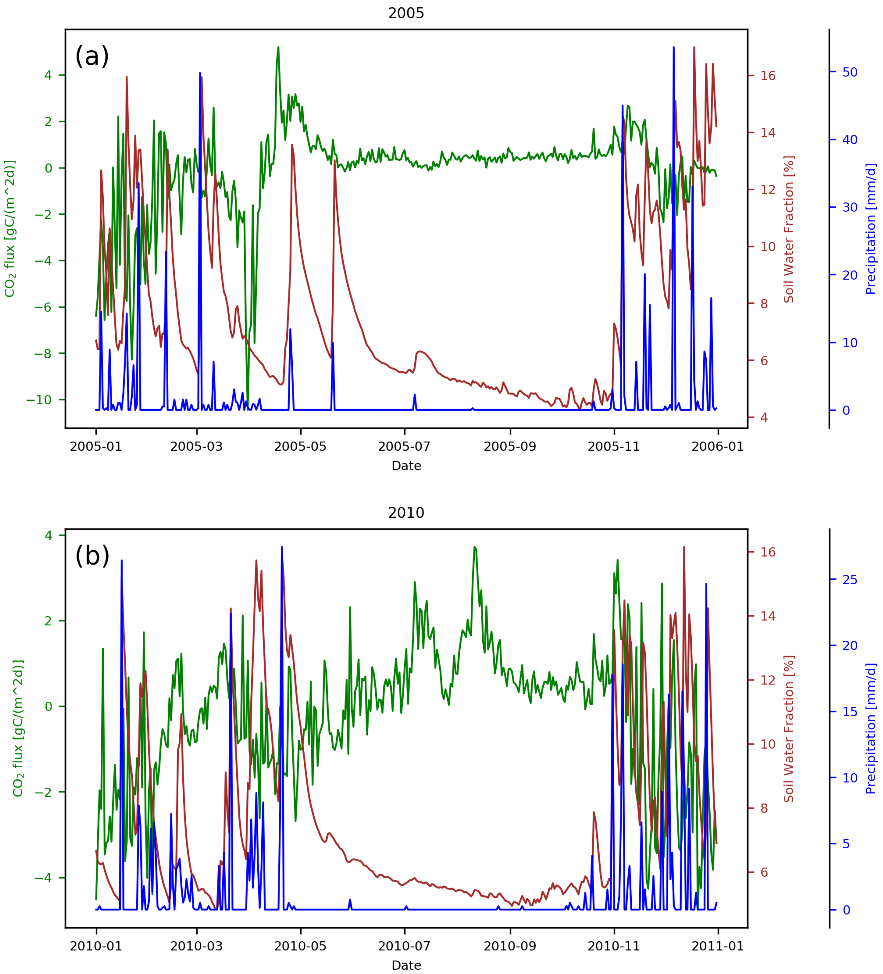

Figure A15. Local data from the FLUXNET eddy-covariance flux tower in Kruger National Park. Daily mean net carbon fluxes (green), precipitation (blue), and soil moisture (red) measured by the ZA-Kru FLUXNET station (Archibald et al., 2009; Scholes, 2013). Panel **(a)** shows the year 2005, whereas panel **(b)** shows 2010.

Code availability. The code used in this study is available from https://doi.org/10.5281/zenodo.12528504 (Metz, 2024) or GitHub (https://github.com/ATMO-IUP-UHEI/MetzEtAl2024, last access: 25 June 2024).

Data availability. GOSAT/RemoTeC2.4.0 XCO_2 data can be obtained from Zenodo: https://doi.org/10.5281/zenodo.5886662 (Butz, 2022). GOSAT/ACOS data are available from https://oco2.gesdisc.eosdis.nasa.gov/data/GOSAT_TANSO_Level2/ACOS_L2_Lite_FP.9r/ (OCO-2 Science Team, 2019, https://doi.org/10.5067/VWSABTO7ZII4). OCO-2 data are available from https://doi.org/10.5067/8E4VLCK16O6Q (OCO-2/OCO-3 Science Team et al., 2022). CarbonTracker CT2022 CO_2 fluxes and concentrations can be downloaded from https://gml.noaa.gov/aftp/products/carbontracker/co2/CT2022/fluxes/monthly/ and https://gml.noaa.gov/aftp/products/carbontracker/co2/CT2022/molefractions/co2_total_monthly/ (Jacobson et al., 2023, https://doi.org/10.25925/z1gj-3254), respectively. CAMS concentrations and fluxes can be found at https://ads.atmosphere.copernicus.eu/cdsapp#!/dataset/cams-global-greenhouse-gas-inversion (Copernicus Atmosphere Monitoring Service, 2020). GFAS emission records are available from https://ads.atmosphere.copernicus.eu/datasets/cams-global-fire-emissions-gfas (Copernicus Atmosphere Monitoring Service, 2022). CAMS and GFAS data were generated using Copernicus Atmosphere Monitoring Service information 2021; neither the European Commission nor the European Centre for Medium-Range Weather Forecasts (ECMWF) is responsible for any use that may be made of the information they contain. The MIP data can be downloaded from https://gml.noaa.gov/ccgg/OCO2_v10mip/ (Baker et al., 2022). GFED fire emissions are available from https://www.geo.vu.nl/~gwerf/GFED/GFED4/ (van der Werf et al., 2015). FINN data were retrieved from the American National Center for Atmospheric Research: https://www.acom.ucar.edu/Data/fire/ (Wiedinmyer et al., 2021). ERA5-Land data records contain modified Copernicus Atmosphere Monitoring Service information 2021 available from the Climate Data Store https://cds.climate.copernicus.eu/cdsapp#!/dataset/reanalysis-era5-land-monthly-means (Muñoz Sabater, 2019, https://doi.org/10.24381/cds.68d2bb30). TRENDYv9 model output is available upon request from https://mdosullivan.github.io/GCB/ (Sitch et al., 2020). FLUXCOM products are available from http://fluxcom.org/CF-Download/ (Jung et al., 2020, https://doi.org/10.5194/bg-17-1343-2020; Tramontana et al., 2016, https://doi.org/10.5194/bg-13-4291-2016). Data from the ZA-Kru FLUXNET station can be downloaded from FLUXNET: https://fluxnet.org/data/fluxnet2015-dataset/ (Scholes, 2013, https://doi.org/10.18140/FLX/1440188). The Gobabeb COCCON station data are available from https://secondary-data-archive.nilu.no/evdc/ftir/coccon/gobabeb/version2/ (Dubravica et al., 2021, https://doi.org/10.48477/coccon.pf10.gobabeb.R02). MODIS MCD12C1 data are available from https://search.earthdata.nasa.gov/search with the following DOI: https://doi.org/10.5067/MODIS/MCD12C1.061 (Friedl and Sulla-Menashe, 2022). "L2 Daily Solar-Induced Fluorescence (SIF) from MetOp-A GOME-2" V2 data are available from https://search.earthdata.nasa.gov/ (Joiner et al., 2023, https://doi.org/10.3334/ORNLDAAC/2292). Monthly TM5-4DVar data are given in Table A2.

Author contributions. SNV, AB, and EMM were involved in the conceptualization process and the development of the methodology. SB performed the dedicated TM5-4DVar runs. EMM conducted the formal analysis and created the figures, under the supervision of AB and SNV. EMM wrote the original draft. All authors contributed to the interpretation of the results and the editing and review of the manuscript.

Competing interests. The contact author has declared that none of the authors has any competing interests.

Disclaimer. Publisher's note: Copernicus Publications remains neutral with regard to jurisdictional claims made in the text, published maps, institutional affiliations, or any other geographical representation in this paper. While Copernicus Publications makes every effort to include appropriate place names, the final responsibility lies with the authors.

Acknowledgements. The authors gratefully acknowledge the SDS@hd data storage service, supported by the Ministry of Science, Research and the Arts Baden-Württemberg (MWK), and the computing resources provided by the Deutsche Klimarechenzentrum (DKRZ; project no. bb1170). Eva-Marie Metz acknowledges a doctoral scholarship from the German Academic Scholarship Foundation. The authors also wish to thank the Japanese Aerospace Exploration Agency, the National Institute for Environmental Studies, and the Ministry of Environment for the GOSAT data and their continuous support as part of a joint research agreement. Moreover, we thank the OCO-2 science team for producing the GOSAT/ACOS L2 XCO_2 data. OCO-2 data were produced by the OCO-2 project at the Jet Propulsion Laboratory, California Institute of Technology, and obtained from the OCO-2 data archive maintained at the NASA Goddard Earth Science Data and Information Services Center. CarbonTracker CT2022 results were provided by NOAA ESRL, Boulder, Colorado, USA: http://carbontracker.noaa.gov (last access: 17 September 2024). Finally, we thank Stephen Sitch, Pierre Friedlingstein, and all modelers of the "Trends and drivers of the regional scale terrestrial sources and sinks of carbon dioxide" (TRENDY) project. The long-term operation of the Gobabeb COCCON site in Namibia is supported by ESA via the COCCON-PROCEEDS series of projects (contract no. 4000121212) and COCCON-OPERA (contract no. 4000140431/23/I-DT-Ir).

Financial support. Funding for the development of RemoTeC was provided by the German Research Foundation (DFG; grant BU2599/1-1); operations and data storage were also supported by the DFG (grant no. INST 35/1503-1 FUGG). Sourish Basu was supported by NASA (grant no. 80NSSC20K0818).

Review statement. This paper was edited by Kerneels Jaars and reviewed by Thomas E. Taylor and one anonymous referee.

References

Ahlström, A., Raupach, M. R., Schurgers, G., Smith, B., Arneth, A., Jung, M., Reichstein, M., Canadell, J. G., Friedlingstein, P., Jain, A. K., Kato, E., Poulter, B., Sitch, S., Stocker, B. D., Viovy, N., Wang, Y. P., Wiltshire, A., Zaehle, S., and Zeng, N.: The dominant role of semi-arid ecosystems in the trend and variability of the land CO_2 sink, Science, 348, 895–899, https://doi.org/10.1126/science.aaa1668, 2015.

Archibald, S. A., Kirton, A., van der Merwe, M. R., Scholes, R. J., Williams, C. A., and Hanan, N.: Drivers of inter-annual variability in Net Ecosystem Exchange in a semi-arid savanna ecosystem, South Africa, Biogeosciences, 6, 251–266, https://doi.org/10.5194/bg-6-251-2009, 2009.

Baker, D. F., Basu, S., Bertolacci, M., Chevallier, F., Cressie, N., Crowell, S., Deng, F., He, W., Jacobson, A. R., Janardanan, R., Jiang, F., Johnson, M. S., Jones, D. B. A., Liu, J., Liu, Z., Maksyutov, S., Miller, S. M., Philip, S., Schuh, A., Weir, B., Zammit-Mangion, A., and Zeng, N.: v10 Orbiting Carbon Observatory-2 model intercomparison project, NOAA Global Monitoring Laboratory [data set], https://gml.noaa.gov/ccgg/OCO2_v10mip/ (last access: 6 May 2022), 2022.

Bastos, A., O'Sullivan, M., Ciais, P., Makowski, D., Sitch, S., Friedlingstein, P., Chevallier, F., Rödenbeck, C., Pongratz, J., Luijkx, I. T., Patra, P. K., Peylin, P., Canadell, J. G., Lauerwald, R., Li, W., Smith, N. E., Peters, W., Goll, D. S., Jain, A. K., Kato, E., Lienert, S., Lombardozzi, D. L., Haverd, V., Nabel, J. E. M. S., Poulter, B., Tian, H., Walker, A. P., and Zaehle, S.: Sources of Uncertainty in Regional and Global Terrestrial CO_2 Exchange Estimates, Global Biogeochem. Cy., 34, e2019GB006393, https://doi.org/10.1029/2019GB006393, 2020.

Basu, S., Guerlet, S., Butz, A., Houweling, S., Hasekamp, O., Aben, I., Krummel, P., Steele, P., Langenfelds, R., Torn, M., Biraud, S., Stephens, B., Andrews, A., and Worthy, D.: Global CO2 fluxes estimated from GOSAT retrievals of total column CO2, Atmos. Chem. Phys., 13, 8695–8717, https://doi.org/10.5194/acp-13-8695-2013, 2013.

Birch, H. F.: Mineralisation of plant nitrogen following alternate wet and dry conditions, Plant Soil, 20, 43–49, https://doi.org/10.1007/bf01378096, 1964.

Buchwitz, M., Reuter, M., Schneising, O., Hewson, W., Detmers, R. G., Boesch, H., Hasekamp, O. P., Aben, I., Bovensmann, H., Burrows, J. P., Butz, A., Chevallier, F., Dils, B., Frankenberg, C., Heymann, J., Lichtenberg, G., Mazière, M. de, Notholt, J., Parker, R., Warneke, T., Zehner, C., Griffith, D., Deutscher, N. M., Kuze, A., Suto, H., and Wunch, D.: Global satellite observations of column-averaged carbon dioxide and methane: The GHG-CCI XCO_2 and XCH4 CRDP3 data set, Remote Sens. Environ., 203, 276–295, https://doi.org/10.1016/j.rse.2016.12.027, 2017.

Butz, A.: RemoTeC full-physics retrieval GOSAT/TANSO-FTS Level 2 bias-corrected XCO_2 version 2.4.0 operated at Heidelberg University, Zenodo [data set], https://doi.org/10.5281/zenodo.5886662, 2022.

Butz, A., Guerlet, S., Hasekamp, O., Schepers, D., Galli, A., Aben, I., Frankenberg, C., Hartmann, J.-M., Tran, H., Kuze, A., Keppel-Aleks, G., Toon, G., Wunch, D., Wennberg, P., Deutscher, N., Griffith, D., Macatangay, R., Messerschmidt, J., Notholt, J., and Warneke, T.: Toward accurate CO_2 and CH_4 observations from GOSAT, Geophys. Res. Lett., 38, L14812, https://doi.org/10.1029/2011GL047888, 2011.

Byrne, B., Baker, D. F., Basu, S., Bertolacci, M., Bowman, K. W., Carroll, D., Chatterjee, A., Chevallier, F., Ciais, P., Cressie, N., Crisp, D., Crowell, S., Deng, F., Deng, Z., Deutscher, N. M., Dubey, M. K., Feng, S., García, O. E., Griffith, D. W. T., Herkommer, B., Hu, L., Jacobson, A. R., Janardanan, R., Jeong, S., Johnson, M. S., Jones, D. B. A., Kivi, R., Liu, J., Liu, Z., Maksyutov, S., Miller, J. B., Miller, S. M., Morino, I., Notholt, J., Oda, T., O'Dell, C. W., Oh, Y.-S., Ohyama, H., Patra, P. K., Peiro, H., Petri, C., Philip, S., Pollard, D. F., Poulter, B., Remaud, M., Schuh, A., Sha, M. K., Shiomi, K., Strong, K., Sweeney, C., Té, Y., Tian, H., Velazco, V. A., Vrekoussis, M., Warneke, T., Worden, J. R., Wunch, D., Yao, Y., Yun, J., Zammit-Mangion, A., and Zeng, N.: National CO_2 budgets (2015–2020) inferred from atmospheric CO_2 observations in support of the global stocktake, Earth Syst. Sci. Data, 15, 963–1004, https://doi.org/10.5194/essd-15-963-2023, 2023.

Chevallier, F., Engelen, R. J., and Peylin, P.: The contribution of AIRS data to the estimation of CO_2 sources and sinks, Geophys. Res. Lett., 32, L23801, https://doi.org/10.1029/2005GL024229, 2005.

Chevallier, F., Ciais, P., Conway, T. J., Aalto, T., Anderson, B. E., Bousquet, P., Brunke, E. G., Ciattaglia, L., Esaki, Y., and Fröhlich, M.: CO_2 surface fluxes at grid point scale estimated from a global 21 year reanalysis of atmospheric measurements, J. Geophys. Res.-Atmos., 115, D21307, https://doi.org/10.1029/2010JD013887, 2010.

Chevallier, F., Remaud, M., O'Dell, C. W., Baker, D., Peylin, P., and Cozic, A.: Objective evaluation of surface- and satellite-driven carbon dioxide atmospheric inversions, Atmos. Chem. Phys., 19, 14233–14251, https://doi.org/10.5194/acp-19-14233-2019, 2019.

Ciais, P., Piao, S.-L., Cadule, P., Friedlingstein, P., and Chédin, A.: Variability and recent trends in the African terrestrial carbon balance, Biogeosciences, 6, 1935–1948, https://doi.org/10.5194/bg-6-1935-2009, 2009.

Copernicus Atmosphere Monitoring Service: CAMS global inversion-optimised greenhouse gas fluxes and concentrations, Copernicus Atmosphere Monitoring Service (CAMS) Atmosphere Data Store [data set], https://ads.atmosphere.copernicus.eu/cdsapp#!/dataset/cams-global-greenhouse-gas-inversion (last access: 7 October 2021), 2020.

Copernicus Atmosphere Monitoring Service: CAMS global biomass burning emissions based on fire radiative power (GFAS), Copernicus Atmosphere Monitoring Service (CAMS) Atmosphere Data Store [data set], https://ads.atmosphere.copernicus.eu/datasets/cams-global-fire-emissions-gfas (last access: 2 February 2024), 2022.

Delire, C., Séférian, R., Decharme, B., Alkama, R., Calvet, J.-C., Carrer, D., Gibelin, A.-L., Joetzjer, E., Morel, X., Rocher, M., and Tzanos, D.: The Global Land Carbon Cycle Simulated With ISBA-CTRIP: Improvements Over the

Last Decade, J. Adv. Model. Earth Sy., 12, e2019MS001886, https://doi.org/10.1029/2019MS001886, 2020.

Detmers, R. G., Hasekamp, O., Aben, I., Houweling, S., Leeuwen, T. T., Butz, A., Landgraf, J., Köhler, P., Guanter, L., and Poulter, B.: Anomalous carbon uptake in Australia as seen by GOSAT, Geophys. Res. Lett., 42, 8177–8184, https://doi.org/10.1002/2015GL065161, 2015.

Dubravica, D., Hase, F., Alberti, C., Frey, M., and Marais, E.: COCCON Version 2 dataset from atmospheric observatory of Gobabeb (Namibia) available at the EVDC Data Handling Facilities covering start date Jan 9th 2017 to end date Nov 27th 2020, COCCON – Central Facility/EVDC – ESA Atmospheric Validation Data Centre [data set], https://doi.org/10.48477/coccon.pf10.gobabeb.R02, 2021 (data available at: https://secondary-data-archive.nilu.no/evdc/ftir/coccon/gobabeb/version2/, last access: 27 March 2023).

Edwards, D. P., Emmons, L. K., Gille, J. C., Chu, A., Attié, J.-L., Giglio, L., Wood, S. W., Haywood, J., Deeter, M. N., Massie, S. T., Ziskin, D. C., and Drummond, J. R.: Satellite-observed pollution from Southern Hemisphere biomass burning, J. Geophys. Res., 111, D14312, https://doi.org/10.1029/2005JD006655, 2006.

Ernst, Y., Archibald, S., Balzter, H., Chevallier, F., Ciais, P., Fischer, C. G., Gaubert, B., Higginbottom, T., Higgins, S., Lawal, S., Lacroix, F., Lauerwald, R., Lourenco, M., Martens, C., Mengistu, A. G., Merbold, L., Mitchard, E., Moyo, M., Nguyen, H., O'sullivan, M., Rodríguez-Veiga, P., Rosan, T., Rosentreter, J., Ryan, C., Scheiter, S., Sitch, S., Stevens, N., Tagesson, T., Tian, H., Wang, M., Woon, J. S., Zheng, B., Zhou, Y., and Scholes, R. J.: The African Regional Greenhouse Gases Budget (2010–2019), Global Biogeochem. Cy., 38, e2023GB008016, https://doi.org/10.1029/2023GB008016, 2024.

Fan, Z., Neff, J. C., and Hanan, N. P.: Modeling pulsed soil respiration in an African savanna ecosystem, Agr. Forest Meteorol., 200, 282–292, https://doi.org/10.1016/j.agrformet.2014.10.009, 2015.

Foster, K. T., Sun, W., Shiga, Y. P., Mao, J., and Michalak, A. M.: Multiscale assessment of North American terrestrial carbon balance, Biogeosciences, 21, 869–891, https://doi.org/10.5194/bg-21-869-2024, 2024.

Frey, M., Sha, M. K., Hase, F., Kiel, M., Blumenstock, T., Harig, R., Surawicz, G., Deutscher, N. M., Shiomi, K., Franklin, J. E., Bösch, H., Chen, J., Grutter, M., Ohyama, H., Sun, Y., Butz, A., Mengistu Tsidu, G., Ene, D., Wunch, D., Cao, Z., Garcia, O., Ramonet, M., Vogel, F., and Orphal, J.: Building the COllaborative Carbon Column Observing Network (COCCON): long-term stability and ensemble performance of the EM27/SUN Fourier transform spectrometer, Atmos. Meas. Tech., 12, 1513–1530, https://doi.org/10.5194/amt-12-1513-2019, 2019.

Frey, M. M., Hase, F., Blumenstock, T., Dubravica, D., Groß, J., Göttsche, F., Handjaba, M., Amadhila, P., Mushi, R., Morino, I., Shiomi, K., Sha, M. K., de Mazière, M., and Pollard, D. F.: Long-term column-averaged greenhouse gas observations using a COCCON spectrometer at the high-surface-albedo site in Gobabeb, Namibia, Atmos. Meas. Tech., 14, 5887–5911, https://doi.org/10.5194/amt-14-5887-2021, 2021.

Friedl, M. and Sulla-Menashe, D.: MODIS/Terra+Aqua Land Cover Type Yearly L3 Global 0.05Deg CMG V061, NASA EOSDIS Land Processes Distributed Active Archive Center [data set], https://doi.org/10.5067/MODIS/MCD12C1.061, 2022 (data available at: https://search.earthdata.nasa.gov/search, last access: 24 March 2024).

Friedlingstein, P., O'Sullivan, M., Jones, M. W., Andrew, R. M., Hauck, J., Olsen, A., Peters, G. P., Peters, W., Pongratz, J., Sitch, S., Le Quéré, C., Canadell, J. G., Ciais, P., Jackson, R. B., Alin, S., Aragão, L. E. O. C., Arneth, A., Arora, V., Bates, N. R., Becker, M., Benoit-Cattin, A., Bittig, H. C., Bopp, L., Bultan, S., Chandra, N., Chevallier, F., Chini, L. P., Evans, W., Florentie, L., Forster, P. M., Gasser, T., Gehlen, M., Gilfillan, D., Gkritzalis, T., Gregor, L., Gruber, N., Harris, I., Hartung, K., Haverd, V., Houghton, R. A., Ilyina, T., Jain, A. K., Joetzjer, E., Kadono, K., Kato, E., Kitidis, V., Korsbakken, J. I., Landschützer, P., Lefèvre, N., Lenton, A., Lienert, S., Liu, Z., Lombardozzi, D., Marland, G., Metzl, N., Munro, D. R., Nabel, J. E. M. S., Nakaoka, S.-I., Niwa, Y., O'Brien, K., Ono, T., Palmer, P. I., Pierrot, D., Poulter, B., Resplandy, L., Robertson, E., Rödenbeck, C., Schwinger, J., Séférian, R., Skjelvan, I., Smith, A. J. P., Sutton, A. J., Tanhua, T., Tans, P. P., Tian, H., Tilbrook, B., van der Werf, G., Vuichard, N., Walker, A. P., Wanninkhof, R., Watson, A. J., Willis, D., Wiltshire, A. J., Yuan, W., Yue, X., and Zaehle, S.: Global Carbon Budget 2020, Earth Syst. Sci. Data, 12, 3269–3340, https://doi.org/10.5194/essd-12-3269-2020, 2020.

Friedlingstein, P., O'Sullivan, M., Jones, M. W., Andrew, R. M., Bakker, D. C. E., Hauck, J., Landschützer, P., Le Quéré, C., Luijkx, I. T., Peters, G. P., Peters, W., Pongratz, J., Schwingshackl, C., Sitch, S., Canadell, J. G., Ciais, P., Jackson, R. B., Alin, S. R., Anthoni, P., Barbero, L., Bates, N. R., Becker, M., Bellouin, N., Decharme, B., Bopp, L., Brasika, I. B. M., Cadule, P., Chamberlain, M. A., Chandra, N., Chau, T.-T.-T., Chevallier, F., Chini, L. P., Cronin, M., Dou, X., Enyo, K., Evans, W., Falk, S., Feely, R. A., Feng, L., Ford, D. J., Gasser, T., Ghattas, J., Gkritzalis, T., Grassi, G., Gregor, L., Gruber, N., Gürses, Ö., Harris, I., Hefner, M., Heinke, J., Houghton, R. A., Hurtt, G. C., Iida, Y., Ilyina, T., Jacobson, A. R., Jain, A., Jarníková, T., Jersild, A., Jiang, F., Jin, Z., Joos, F., Kato, E., Keeling, R. F., Kennedy, D., Klein Goldewijk, K., Knauer, J., Korsbakken, J. I., Körtzinger, A., Lan, X., Lefèvre, N., Li, H., Liu, J., Liu, Z., Ma, L., Marland, G., Mayot, N., McGuire, P. C., McKinley, G. A., Meyer, G., Morgan, E. J., Munro, D. R., Nakaoka, S.-I., Niwa, Y., O'Brien, K. M., Olsen, A., Omar, A. M., Ono, T., Paulsen, M., Pierrot, D., Pocock, K., Poulter, B., Powis, C. M., Rehder, G., Resplandy, L., Robertson, E., Rödenbeck, C., Rosan, T. M., Schwinger, J., Séférian, R., Smallman, T. L., Smith, S. M., Sospedra-Alfonso, R., Sun, Q., Sutton, A. J., Sweeney, C., Takao, S., Tans, P. P., Tian, H., Tilbrook, B., Tsujino, H., Tubiello, F., van der Werf, G. R., van Ooijen, E., Wanninkhof, R., Watanabe, M., Wimart-Rousseau, C., Yang, D., Yang, X., Yuan, W., Yue, X., Zaehle, S., Zeng, J., and Zheng, B.: Global Carbon Budget 2023, Earth Syst. Sci. Data, 15, 5301–5369, https://doi.org/10.5194/essd-15-5301-2023, 2023.

Goll, D. S., Joetzjer, E., Huang, M., and Ciais, P.: Low Phosphorus Availability Decreases Susceptibility of Tropical Primary Productivity to Droughts, Geophys. Res. Lett., 45, 8231–8240, https://doi.org/10.1029/2018GL077736, 2018.

Haverd, V., Smith, B., Nieradzik, L., Briggs, P. R., Woodgate, W., Trudinger, C. M., Canadell, J. G., and Cuntz, M.: A new version of the CABLE land surface model (Subversion revision r4601) incorporating land use and land cover change, woody vegetation demography, and a novel optimisation-based approach to plant coordination of photosynthesis, Geosci. Model Dev., 11, 2995–3026, https://doi.org/10.5194/gmd-11-2995-2018, 2018.

He, W., Jiang, F., Ju, W., Byrne, B., Xiao, J., Nguyen, N. T., Wu, M., Wang, S., Wang, J., Rödenbeck, C., Li, X., Scholze, M., Monteil, G., Wang, H., Zhou, Y., He, Q., and Chen, J. M.: Do State-Of-The-Art Atmospheric CO_2 Inverse Models Capture Drought Impacts on the European Land Carbon Uptake?, J. Adv. Model. Earth Sy., 15, e2022MS003150, https://doi.org/10.1029/2022MS003150, 2023.

Jacobson, A. R., Schuldt, K. N., Tans, P., Arlyn Andrews, Miller, J. B., Oda, T., Mund, J., Weir, B., Ott, L., Aalto, T., Abshire, J. B., Aikin, K., Aoki, S., Apadula, F., Arnold, S., Baier, B., Bartyzel, J., Beyersdorf, A., Biermann, T., Biraud, S. C., Boenisch, H., Brailsford, G., Brand, W. A., Chen, G., Huilin Chen, Lukasz Chmura, Clark, S., Colomb, A., Commane, R., Conil, S., Couret, C., Cox, A., Cristofanelli, P., Cuevas, E., Curcoll, R., Daube, B., Davis, K. J., Wekker, S. de, Della Coletta, J., Delmotte, M., DiGangi, E., DiGangi, J. P., Di Sarra, A. G., Dlugokencky, E., Elkins, J. W., Emmenegger, L., Shuangxi Fang, Fischer, M. L., Forster, G., Frumau, A., Galkowski, M., Gatti, L. V., Gehrlein, T., Gerbig, C., Francois Gheusi, Gloor, E., Gomez-Trueba, V., Goto, D., Griffis, T., Hammer, S., Hanson, C., Haszpra, L., Hatakka, J., Heimann, M., Heliasz, M., Hensen, A., Hermansen, O., Hintsa, E., Holst, J., Ivakhov, V., Jaffe, D. A., Jordan, A., Joubert, W., Karion, A., Kawa, S. R., Kazan, V., Keeling, R. F., Keronen, P., Kneuer, T., Kolari, P., Kateřina Komínková, Kort, E., Kozlova, E., Krummel, P., Kubistin, D., Labuschagne, C., Lam, D. H., Lan, X., Langenfelds, R. L., Laurent, O., Laurila, T., Lauvaux, T., Lavric, J., Law, B. E., Lee, J., Lee, O. S., Lehner, I., Lehtinen, K., Leppert, R., Leskinen, A., Leuenberger, M., Levin, I., Levula, J., Lin, J., Lindauer, M., Loh, Z., Lopez, M., Luijkx, I. T., Lunder, C. R., Machida, T., Mammarella, I., Manca, G., Manning, A., Manning, A., Marek, M. V., Martin, M. Y., Matsueda, H., McKain, K., Meijer, H., Meinhardt, F., Merchant, L., N. Mihalopoulos, Miles, N. L., Miller, C. E., Mitchell, L., Mölder, M., Montzka, S., Moore, F., Moossen, H., Morgan, E., Josep-Anton Morgui, Morimoto, S., Müller-Williams, J., J. William Munger, Munro, D., Myhre, C. L., Shin-Ichiro Nakaoka, Jaroslaw Necki, Newman, S., Nichol, S., Niwa, Y., Obersteiner, F., O'Doherty, S., Paplawsky, B., Peischl, J., Peltola, O., Piacentino, S., Jean-Marc Pichon, Pickers, P., Piper, S., Pitt, J., Plass-Dülmer, C., Platt, S. M., Prinzivalli, S., Ramonet, M., Ramos, R., Reyes-Sanchez, E., Richardson, S. J., Riris, H., Rivas, P. P., Ryerson, T., Saito, K., Sargent, M., Sasakawa, M., Scheeren, B., Schuck, T., Schumacher, M., Seifert, T., Sha, M. K., Shepson, P., Shook, M., Sloop, C. D., Smith, P., Stanley, K., Steinbacher, M., Stephens, B., Sweeney, C., Thoning, K., Timas, H., Torn, M., Tørseth, K., Trisolino, P., Turnbull, J., van den Bulk, P., van Dinther, D., Vermeulen, A., Viner, B., Vitkova, G., Walker, S., Watson, A., Wofsy, S. C., Worsey, J., Worthy, D., Dickon Young, Zaehle, S., Zahn, A., and Zimnoch, M.: CarbonTracker CT2022, Global Monitoring Laboratory [data set], https://doi.org/10.25925/z1gj-3254, 2023 (data available at: https://gml.noaa.gov/aftp/products/carbontracker/co2/CT2022/fluxes/monthly/, last access: 17 April 2023 and https://gml.noaa.gov/aftp/products/carbontracker/co2/CT2022/molefractions/co2_total_monthly/, last access: 17 September 2024).

Jacobs, N., O'Dell, C. W., Taylor, T. E., Logan, T. L., Byrne, B., Kiel, M., Kivi, R., Heikkinen, P., Merrelli, A., Payne, V. H., and Chatterjee, A.: The importance of digital elevation model accuracy in X_{CO_2} retrievals: improving the Orbiting Carbon Observatory 2 Atmospheric Carbon Observations from Space version 11 retrieval product, Atmos. Meas. Tech., 17, 1375–1401, https://doi.org/10.5194/amt-17-1375-2024, 2024.

Jarvis, P., Rey, A., Petsikos, C., Wingate, L., Rayment, M., Pereira, J., Banza, J., David, J., Miglietta, F., Borghetti, M., Manca, G., and Valentini, R.: Drying and wetting of Mediterranean soils stimulates decomposition and carbon dioxide emission: the "Birch effect", Tree Physiol., 27, 929–940, https://doi.org/10.1093/treephys/27.7.929, 2007.

Joiner, J., Yoshida, Y., Zhang, Y., Duveiller, G., Jung, M., Lyapustin, A., Wang, Y., and Tucker, C. J.: Estimation of Terrestrial Global Gross Primary Production (GPP) with Satellite Data-Driven Models and Eddy Covariance Flux Data, Remote Sens., 10, 1346, https://doi.org/10.3390/rs10091346, 2018.

Joiner, J., Yoshida, Y., Koehler, P., Frankenberg, C., and Parazoo, N. C.: L2 Daily Solar-Induced Fluorescence (SIF) from MetOp-A GOME-2, 2007–2018, V2, ORNL DAAC, Oak Ridge, Tennessee, USA [data set], https://doi.org/10.3334/ORNLDAAC/2292, 2023 (data available at: https://search.earthdata.nasa.gov/, last access: 29 May 2024).

Jung, M., Schwalm, C., Migliavacca, M., Walther, S., Camps-Valls, G., Koirala, S., Anthoni, P., Besnard, S., Bodesheim, P., Carvalhais, N., Chevallier, F., Gans, F., Goll, D. S., Haverd, V., Köhler, P., Ichii, K., Jain, A. K., Liu, J., Lombardozzi, D., Nabel, J. E. M. S., Nelson, J. A., O'Sullivan, M., Pallandt, M., Papale, D., Peters, W., Pongratz, J., Rödenbeck, C., Sitch, S., Tramontana, G., Walker, A., Weber, U., and Reichstein, M.: Scaling carbon fluxes from eddy covariance sites to globe: synthesis and evaluation of the FLUXCOM approach, Biogeosciences, 17, 1343–1365, https://doi.org/10.5194/bg-17-1343-2020, 2020 (data available at: http://fluxcom.org/CF-Download/, last access: 21 January 2025).

Kaiser, J. W., Heil, A., Andreae, M. O., Benedetti, A., Chubarova, N., Jones, L., Morcrette, J.-J., Razinger, M., Schultz, M. G., Suttie, M., and van der Werf, G. R.: Biomass burning emissions estimated with a global fire assimilation system based on observed fire radiative power, Biogeosciences, 9, 527–554, https://doi.org/10.5194/bg-9-527-2012, 2012.

Kato, E., Kinoshita, T., Ito, A., Kawamiya, M., and Yamagata, Y.: Evaluation of spatially explicit emission scenario of land-use change and biomass burning using a process-based biogeochemical model, J. Land Use Sci., 8, 104–122, https://doi.org/10.1080/1747423X.2011.628705, 2013.

Krinner, G., Viovy, N., Noblet-Ducoudré, N. de, Ogée, J., Polcher, J., Friedlingstein, P., Ciais, P., Sitch, S., and Prentice, I. C.: A dynamic global vegetation model for studies of the coupled atmosphere-biosphere system, Global Biogeochem. Cy., 19, GB1015, https://doi.org/10.1029/2003GB002199, 2005.

Lasslop, G., Hantson, S., Harrison, S. P., Bachelet, D., Burton, C., Forkel, M., Forrest, M., Li, F., Melton, J. R., Yue, C., Archibald, S., Scheiter, S., Arneth, A., Hickler, T., and Sitch, S.: Global ecosystems and fire: Multi-model assessment of fire-induced tree-cover and carbon storage reduction, Glob. Change Biol., 26, 5027–5041, https://doi.org/10.1111/gcb.15160, 2020.

Lawrence, D. M., Fisher, R. A., Koven, C. D., Oleson, K. W., Swenson, S. C., Bonan, G., Collier, N., Ghimire, B., Kampenhout, L., Kennedy, D., Kluzek, E., Lawrence, P. J., Li, F., Li, H., Lombardozzi, D., Riley, W. J., Sacks, W. J., Shi, M., Vertenstein, M., Wieder, W. R., Xu, C., Ali, A. A., Badger, A. M., Bisht, G., Broeke, M., Brunke, M. A., Burns, S. P., Buzan, J., Clark, M., Craig, A., Dahlin, K., Drewniak, B., Fisher, J. B., Flanner, M., Fox, A. M., Gentine, P., Hoffman, F., Keppel-Aleks, G., Knox, R., Kumar, S., Lenaerts, J., Leung, L. R., Lipscomb, W. H., Lu, Y., Pandey, A., Pelletier, J. D., Perket, J., Randerson, J. T., Ricciuto, D. M., Sanderson, B. M., Slater, A., Subin, Z. M., Tang, J., Thomas, R. Q., Val Martin, M., and Zeng, X.: The Community Land Model Version 5: Description of New Features, Benchmarking, and Impact of Forcing Uncertainty, J. Adv. Model. Earth Sy., 11, 4245–4287, https://doi.org/10.1029/2018MS001583, 2019.

Le Quéré, C., Andres, R. J., Boden, T., Conway, T., Houghton, R. A., House, J. I., Marland, G., Peters, G. P., van der Werf, G. R., Ahlström, A., Andrew, R. M., Bopp, L., Canadell, J. G., Ciais, P., Doney, S. C., Enright, C., Friedlingstein, P., Huntingford, C., Jain, A. K., Jourdain, C., Kato, E., Keeling, R. F., Klein Goldewijk, K., Levis, S., Levy, P., Lomas, M., Poulter, B., Raupach, M. R., Schwinger, J., Sitch, S., Stocker, B. D., Viovy, N., Zaehle, S., and Zeng, N.: The global carbon budget 1959–2011, Earth Syst. Sci. Data, 5, 165–185, https://doi.org/10.5194/essd-5-165-2013, 2013.

Li, X., Xiao, J., He, B., Altaf Arain, M., Beringer, J., Desai, A. R., Emmel, C., Hollinger, D. Y., Krasnova, A., Mammarella, I., Noe, S. M., Ortiz, P. S., Rey-Sanchez, A. C., Rocha, A. V., and Varlagin, A.: Solar-induced chlorophyll fluorescence is strongly correlated with terrestrial photosynthesis for a wide variety of biomes: First global analysis based on OCO-2 and flux tower observations, Glob. Change Biol., 24, 3990–4008, https://doi.org/10.1111/gcb.14297, 2018.

Lienert, S. and Joos, F.: A Bayesian ensemble data assimilation to constrain model parameters and land-use carbon emissions, Biogeosciences, 15, 2909–2930, https://doi.org/10.5194/bg-15-2909-2018, 2018.

MacBean, N., Scott, R. L., Biederman, J. A., Peylin, P., Kolb, T., Litvak, M. E., Krishnan, P., Meyers, T. P., Arora, V. K., Bastrikov, V., Goll, D., Lombardozzi, D. L., Nabel, Julia E. M. S., Pongratz, J., Sitch, S., Walker, A. P., Zaehle, S., and Moore, D. J. P.: Dynamic global vegetation models underestimate net CO_2 flux mean and inter-annual variability in dryland ecosystems, Environ. Res. Lett., 16, 94023, https://doi.org/10.1088/1748-9326/ac1a38, 2021.

Masarie, K. A., Peters, W., Jacobson, A. R., and Tans, P. P.: ObsPack: a framework for the preparation, delivery, and attribution of atmospheric greenhouse gas measurements, Earth Syst. Sci. Data, 6, 375–384, https://doi.org/10.5194/essd-6-375-2014, 2014.

Meiyappan, P., Jain, A. K., and House, J. I.: Increased influence of nitrogen limitation on CO_2 emissions from future land use and land use change, Global Biogeochem. Cy., 29, 1524–1548, https://doi.org/10.1002/2015GB005086, 2015.

Melton, J. R., Arora, V. K., Wisernig-Cojoc, E., Seiler, C., Fortier, M., Chan, E., and Teckentrup, L.: CLASSIC v1.0: the open-source community successor to the Canadian Land Surface Scheme (CLASS) and the Canadian Terrestrial Ecosystem Model (CTEM) – Part 1: Model framework and site-level performance, Geosci. Model Dev., 13, 2825–2850, https://doi.org/10.5194/gmd-13-2825-2020, 2020.

Mengistu, A. G. and Mengistu Tsidu, G.: On the performance of satellite-based observations of XCO_2 in capturing the NOAA Carbon Tracker model and ground-based flask observations over Africa's land mass, Atmos. Meas. Tech., 13, 4009–4033, https://doi.org/10.5194/amt-13-4009-2020, 2020.

Metz, E.-M.: ATMO-IUP-UHEI/MetzEtAl2024: v1.0.0, Zenodo [code], https://doi.org/10.5281/zenodo.12528504, 2024.

Metz, E.-M., Vardag, S. N., Basu, S., Jung, M., Ahrens, B., El-Madany, T., Sitch, S., Arora, V. K., Briggs, P. R., Friedlingstein, P., Goll, D. S., Jain, A. K., Kato, E., Lombardozzi, D., Nabel, Julia E. M. S., Poulter, B., Séférian, R., Tian, H., Wiltshire, A., Yuan, W., Yue, X., Zaehle, S., Deutscher, N. M., Griffith, D. W. T., and Butz, A.: Soil respiration-driven CO_2 pulses dominate Australia's flux variability, Science, 379, 1332–1335, https://doi.org/10.1126/science.add7833, 2023.

Muñoz Sabater, J.: ERA5-Land monthly averaged data from 1950 to present, Copernicus Climate Change Service (C3S) Climate Data Store (CDS) [data set], https://doi.org/10.24381/cds.68d2bb30, 2019 (data available at: https://cds.climate.copernicus.eu/cdsapp#!/dataset/reanalysis-era5-land-monthly-means, last access: 13 October 2023).

NOAA: Global Monitoring Laboratory: Trends in Atmospheric Carbon Dioxide, https://www.esrl.noaa.gov/gmd/ccgg/trends/gl_gr.html, last access: 8 January 2024.

OCO-2/OCO-3 Science Team, Payne, V., and Chatterjee, A.: OCO-2 Level 2 bias-corrected XCO_2 and other select fields from the full-physics retrieval aggregated as daily files, Retrospective processing V11.1r, last access: 28 July 2020, Greenbelt, MD, USA, Goddard Earth Sciences Data and Information Services Center (GES DISC) [data set], https://doi.org/10.5067/8E4VLCK16O6Q, 2022.

OCO-2 Science Team, Gunson, M., and Eldering, A.: ACOS GOSAT/TANSO-FTS Level 2 bias-corrected XCO_2 and other select fields from the full-physics retrieval aggregated as daily files V9r, Greenbelt, MD, USA, Goddard Earth Sciences Data and Information Services Center (GES DISC) [data set], https://doi.org/10.5067/VWSABTO7ZII4, 2019 (data available at: https://oco2.gesdisc.eosdis.nasa.gov/data/GOSAT_TANSO_Level2/ACOS_L2_Lite_FP.9r/, last access: 28 July 2020).

Pandey, S., Miller, J. B., Basu, S., Liu, J., Weir, B., Byrne, B., Chevallier, F., Bowman, K. W., Liu, Z., Deng, F., O'Dell, C. W., and Chatterjee, A.: Toward low-latency estimation of atmospheric CO_2 growth rates using satellite observations: Evaluating sampling errors of satellite and in situ observing approaches, AGU Adv., 5, e2023AV001145, https://doi.org/10.1029/2023AV001145, 2024.

Pan, S., Yang, J., Tian, H., Shi, H., Chang, J., Ciais, P., Francois, L., Frieler, K., Fu, B., Hickler, T., Ito, A., Nishina, K., Ostberg, S., Reyer, C. P., Schaphoff, S., Steinkamp, J., and Zhao, F.: Climate Extreme Versus Carbon Extreme: Responses of Terrestrial Carbon Fluxes to Temperature and Precipitation, J. Geophys. Res.-Biogeo., 125, e2019JG005252, https://doi.org/10.1029/2019JG005252, 2020.

Peters, W., Jacobson, A. R., Sweeney, C., Andrews, A. E., Conway, T. J., Masarie, K., Miller, J. B., Bruhwiler, L. M. P., Pétron, G., Hirsch, A. I., Worthy, D. E. J., van der Werf, G. R., Randerson, J. T., Wennberg, P. O., Krol, M. C., and Tans, P. P.: An atmospheric perspective on North American carbon dioxide exchange: CarbonTracker, P. Natl. Acad. Sci. USA, 104, 18925–18930, https://doi.org/10.1073/pnas.0708986104, 2007.

Piao, S., Wang, X., Wang, K., Li, X., Bastos, A., Canadell, J. G., Ciais, P., Friedlingstein, P., and Sitch, S.: Interannual variation of terrestrial carbon cycle: Issues and perspectives, Glob. Change Biol., 26, 300–318, https://doi.org/10.1111/gcb.14884, 2020.

Pierrat, Z., Magney, T., Parazoo, N. C., Grossmann, K., Bowling, D. R., Seibt, U., Johnson, B., Helgason, W., Barr, A., Bortnik, J., Norton, A., Maguire, A., Frankenberg, C., and Stutz, J.: Diurnal and Seasonal Dynamics of Solar-Induced Chlorophyll Fluorescence, Vegetation Indices, and Gross Primary Productivity in the Boreal Forest, J. Geophys. Res.-Biogeo., 127, e2021JG006588, https://doi.org/10.1029/2021JG006588, 2022.

Poulter, B., Ciais, P., Hodson, E., Lischke, H., Maignan, F., Plummer, S., and Zimmermann, N. E.: Plant functional type mapping for earth system models, Geosci. Model Dev., 4, 993–1010, https://doi.org/10.5194/gmd-4-993-2011, 2011.

Poulter, B., Frank, D., Ciais, P., Myneni, R. B., Andela, N., Bi, J., Broquet, G., Canadell, J. G., Chevallier, F., Liu, Y. Y., Running, S. W., Sitch, S., and van der Werf, G. R.: Contribution of semi-arid ecosystems to interannual variability of the global carbon cycle, Nature, 509, 600–603, https://doi.org/10.1038/nature13376, 2014.

Ramo, R., Roteta, E., Bistinas, I., van Wees, D., Bastarrika, A., Chuvieco, E., and van der Werf, G. R.: African burned area and fire carbon emissions are strongly impacted by small fires undetected by coarse resolution satellite data, P. Natl. Acad. Sci. USA, 118, e2011160118, https://doi.org/10.1073/pnas.2011160118, 2021.

Randerson, J. T., Thompson, M. V., Malmstrom, C. M., Field, C. B., and Fung, I. Y.: Substrate limitations for heterotrophs: Implications for models that estimate the seasonal cycle of atmospheric CO_2, Global Biogeochem. Cy., 10, 585–602, https://doi.org/10.1029/96GB01981, 1996.

Reick, C. H., Gayler, V., Goll, D., Hagemann, S., Heidkamp, M., Nabel, Julia E. M. S., Raddatz, T., Roeckner, E., Schnur, R., and Wilkenskjeld, S.: JSBACH 3 – The land component of the MPI Earth System Model: documentation of version 3.2, Reports on Earth System Science, 240, https://doi.org/10.17617/2.3279802, 2021.

Scholes, B.: FLUXNET2015 ZA-Kru Skukuza (2000–2013) [data set], last access: https://doi.org/10.18140/FLX/1440188, 2013 (data available at: https://fluxnet.org/data/fluxnet2015-dataset/, last access: 21 November 2023).

Sellar, A. A., Jones, C. G., Mulcahy, J. P., Tang, Y., Yool, A., Wiltshire, A., O'Connor, F. M., Stringer, M., Hill, R., Palmieri, J., Woodward, S., de Mora, L., Kuhlbrodt, T., Rumbold, S. T., Kelley, D. I., Ellis, R., Johnson, C. E., Walton, J., Abraham, N. L., Andrews, M. B., Andrews, T., Archibald, A. T., Berthou, S., Burke, E., Blockley, E., Carslaw, K., Dalvi, M., Edwards, J., Folberth, G. A., Gedney, N., Griffiths, P. T., Harper, A. B., Hendry, M. A., Hewitt, A. J., Johnson, B., Jones, A., Jones, C. D., Keeble, J., Liddicoat, S., Morgenstern, O., Parker, R. J., Predoi, V., Robertson, E., Siahaan, A., Smith, R. S., Swaminathan, R., Woodhouse, M. T., Zeng, G., and Zerroukat, M.: UKESM1: Description and evaluation of the UK Earth System Model, J. Adv. Model. Earth Sy., 11, 4513–4558, 2019.

Sellers, P. J., Schimel, D. S., Moore, B., Liu, J., and Eldering, A.: Observing carbon cycle–climate feedbacks from space, P. Natl. Acad. Sci. USA, 115, 7860–7868, https://doi.org/10.1073/pnas.1716613115, 2018.

Shi, Y., Matsunaga, T., Saito, M., Yamaguchi, Y., and Chen, X.: Comparison of global inventories of CO_2 emissions from biomass burning during 2002–2011 derived from multiple satellite products, Environ. Pollut., 206, 479–487, https://doi.org/10.1016/j.envpol.2015.08.009, 2015.

Sitch, S., Arora, V. K., Briggs, P., Friedlingstein, P., Goll, D. S., Jain, A. K., Kato, E., Krinner, G., Lienert, S., Lombardozzi, D., Nabel, J. E. M. S., Poulter, B., Séférian, R., Tian, H., Vuichard, N., Walker, A. P., Wiltshire, A., Yuan, W., Yue, X., and Zaehle, S.: TRENDY: Trends in the land carbon cycle, Trendy v9 [data set], available upon request at https://mdosullivan.github.io/GCB/ (last access: 24 January 2025), 2020.

Steiner, A. L.: Role of the Terrestrial Biosphere in Atmospheric Chemistry and Climate, Accounts Chem. Res., 53, 1260–1268, https://doi.org/10.1021/acs.accounts.0c00116, 2020.

Sun, Y., Frankenberg, C., Jung, M., Joiner, J., Guanter, L., Köhler, P., and Magney, T.: Overview of Solar-Induced chlorophyll Fluorescence (SIF) from the Orbiting Carbon Observatory-2: Retrieval, cross-mission comparison, and global monitoring for GPP, Remote Sens. Environ., 209, 808–823, https://doi.org/10.1016/j.rse.2018.02.016, 2018.

Taylor, T. E., O'Dell, C. W., Crisp, D., Kuze, A., Lindqvist, H., Wennberg, P. O., Chatterjee, A., Gunson, M., Eldering, A., Fisher, B., Kiel, M., Nelson, R. R., Merrelli, A., Osterman, G., Chevallier, F., Palmer, P. I., Feng, L., Deutscher, N. M., Dubey, M. K., Feist, D. G., García, O. E., Griffith, D. W. T., Hase, F., Iraci, L. T., Kivi, R., Liu, C., De Mazière, M., Morino, I., Notholt, J., Oh, Y.-S., Ohyama, H., Pollard, D. F., Rettinger, M., Schneider, M., Roehl, C. M., Sha, M. K., Shiomi, K., Strong, K., Sussmann, R., Té, Y., Velazco, V. A., Vrekoussis, M., Warneke, T., and Wunch, D.: An 11-year record of XCO_2 estimates derived from GOSAT measurements using the NASA ACOS version 9 retrieval algorithm, Earth Syst. Sci. Data, 14, 325–360, https://doi.org/10.5194/essd-14-325-2022, 2022.

Taylor, T. E., O'Dell, C. W., Baker, D., Bruegge, C., Chang, A., Chapsky, L., Chatterjee, A., Cheng, C., Chevallier, F., Crisp, D., Dang, L., Drouin, B., Eldering, A., Feng, L., Fisher, B., Fu, D., Gunson, M., Haemmerle, V., Keller, G. R., Kiel, M., Kuai, L., Kurosu, T., Lambert, A., Laughner, J., Lee, R., Liu, J., Mandrake, L., Marchetti, Y., McGarragh, G., Merrelli, A., Nelson, R. R., Osterman, G., Oyafuso, F., Palmer, P. I., Payne, V. H., Rosenberg, R., Somkuti, P., Spiers, G., To, C., Weir, B., Wennberg, P. O., Yu, S., and Zong, J.: Evaluating the consistency between OCO-2 and OCO-3 XCO_2 estimates derived from the NASA ACOS version 10 retrieval algorithm, Atmos. Meas. Tech., 16, 3173–3209, https://doi.org/10.5194/amt-16-3173-2023, 2023.

Tian, H., Chen, G., Lu, C., Xu, X., Hayes, D. J., Ren, W., Pan, S., Huntzinger, D. N., and Wofsy, S. C.: North American terrestrial CO_2 uptake largely offset by CH_4 and N_2O emissions: toward a full accounting of the greenhouse gas budget, Climatic Change, 129, 413–426, https://doi.org/10.1007/s10584-014-1072-9, 2015.

Tramontana, G., Jung, M., Schwalm, C. R., Ichii, K., Camps-Valls, G., Ráduly, B., Reichstein, M., Arain, M. A., Cescatti, A., Kiely, G., Merbold, L., Serrano-Ortiz, P., Sickert, S., Wolf, S., and Papale, D.: Predicting carbon dioxide and energy fluxes across global FLUXNET sites with regression algorithms, Biogeosciences, 13, 4291–4313, https://doi.org/10.5194/bg-13-4291-2016, 2016 (data available at: http://fluxcom.org/CF-Download/, last access: 21 January 2025).

Valentini, R., Arneth, A., Bombelli, A., Castaldi, S., Cazzolla Gatti, R., Chevallier, F., Ciais, P., Grieco, E., Hartmann, J., Henry, M., Houghton, R. A., Jung, M., Kutsch, W. L., Malhi, Y., Mayorga, E., Merbold, L., Murray-Tortarolo, G., Papale, D., Peylin, P., Poulter, B., Raymond, P. A., Santini, M., Sitch, S., Vaglio Laurin, G., van der Werf, G. R., Williams, C. A., and Scholes, R. J.: A full greenhouse gases budget of Africa: synthesis, uncertainties, and vulnerabilities, Biogeosciences, 11, 381–407, https://doi.org/10.5194/bg-11-381-2014, 2014.

van der Velde, I. R., van der Werf, G. R., van Wees, D., Schutgens, N. A. J., Vernooij, R., Houweling, S., Tonucci, E., Chuvieco, E., Randerson, J. T., Frey, M. M., Borsdorff, T., and Aben, I.: Small Fires, Big Impact: Evaluating Fire Emission Estimates in Southern Africa Using New Satellite Imagery of Burned Area and Carbon Monoxide, Geophys. Res. Lett., 51, e2023GL106122, https://doi.org/10.1029/2023GL106122, 2024.

van der Werf, G. R., Randerson, J. T., Giglio, L., van Leeuwen, T. T., Chen, Y., Rogers, B. M., Mu, M., van Marle, M. J. E., Morton, D. C., Collatz, G. J., Yokelson, R. J., and Kasibhatla, P. S.: Global Fire Emissions Database, Version 4.1 (GFED4s) [data set], https://www.geo.vu.nl/~gwerf/GFED/GFED4/ (last access: 10 July 2020), 2015.

van der Werf, G. R., Randerson, J. T., Giglio, L., van Leeuwen, T. T., Chen, Y., Rogers, B. M., Mu, M., van Marle, M. J. E., Morton, D. C., Collatz, G. J., Yokelson, R. J., and Kasibhatla, P. S.: Global fire emissions estimates during 1997–2016, Earth Syst. Sci. Data, 9, 697–720, https://doi.org/10.5194/essd-9-697-2017, 2017.

van Marle, M. J. E., Kloster, S., Magi, B. I., Marlon, J. R., Daniau, A.-L., Field, R. D., Arneth, A., Forrest, M., Hantson, S., Kehrwald, N. M., Knorr, W., Lasslop, G., Li, F., Mangeon, S., Yue, C., Kaiser, J. W., and van der Werf, G. R.: Historic global biomass burning emissions for CMIP6 (BB4CMIP) based on merging satellite observations with proxies and fire models (1750–2015), Geosci. Model Dev., 10, 3329–3357, https://doi.org/10.5194/gmd-10-3329-2017, 2017.

Vuichard, N., Messina, P., Luyssaert, S., Guenet, B., Zaehle, S., Ghattas, J., Bastrikov, V., and Peylin, P.: Accounting for carbon and nitrogen interactions in the global terrestrial ecosystem model ORCHIDEE (trunk version, rev 4999): multi-scale evaluation of gross primary production, Geosci. Model Dev., 12, 4751–4779, https://doi.org/10.5194/gmd-12-4751-2019, 2019.

Walker, A. P., Quaife, T., van Bodegom, P. M., Kauwe, M. G. de, Keenan, T. F., Joiner, J., Lomas, M. R., MacBean, N., Xu, C., Yang, X., and Woodward, F. I.: The impact of alternative trait-scaling hypotheses for the maximum photosynthetic carboxylation rate (Vcmax) on global gross primary production, New Phytol., 215, 1370–1386, https://doi.org/10.1111/nph.14623, 2017.

Weber, U., Jung, M., Reichstein, M., Beer, C., Braakhekke, M. C., Lehsten, V., Ghent, D., Kaduk, J., Viovy, N., Ciais, P., Gobron, N., and Rödenbeck, C.: The interannual variability of Africa's ecosystem productivity: a multi-model analysis, Biogeosciences, 6, 285–295, https://doi.org/10.5194/bg-6-285-2009, 2009.

Weir, B., Ott, L. E., Collatz, G. J., Kawa, S. R., Poulter, B., Chatterjee, A., Oda, T., and Pawson, S.: Bias-correcting carbon fluxes derived from land-surface satellite data for retrospective and near-real-time assimilation systems, Atmos. Chem. Phys., 21, 9609–9628, https://doi.org/10.5194/acp-21-9609-2021, 2021.

Wiedinmyer, C., Akagi, S. K., Yokelson, R. J., Emmons, L. K., Al-Saadi, J. A., Orlando, J. J., and Soja, A. J.: The Fire INventory from NCAR (FINN): a high resolution global model to estimate the emissions from open burning, Geosci. Model Dev., 4, 625–641, https://doi.org/10.5194/gmd-4-625-2011, 2011.

Wiedinmyer, C., Akagi, S. K., Yokelson, R. J., Emmons, L. K., Al-Saadi, J. A., Orlando, J. J., and Soja, A. J.: Fire INventory from NCAR (FINN), Version 1.5 [data set], https://www.acom.ucar.edu/Data/fire/ (last access: 18 November 2020), 2021.

Williams, C. A., Hanan, N. P., Neff, J. C., Scholes, R. J., Berry, J. A., Denning, A. S., and Baker, D. F.: Africa and the global carbon cycle, Carbon balance and management, 2, 3, https://doi.org/10.1186/1750-0680-2-3, 2007.

Williams, C. A., Hanan, N. P., Baker, I., COLLATZ, G. J., Berry, J., and Denning, A. S.: Interannual variability of photosynthesis across Africa and its attribution, J. Geophys. Res., 113, G04015, https://doi.org/10.1029/2008JG000718, 2008.

Wunch, D., Toon, G. C., Blavier, J.-F. L., Washenfelder, R. A., Notholt, J., Connor, B. J., Griffith, D. W. T., Sherlock, V., and Wennberg, P. O.: The Total Carbon Column Observing Network, Philos. T. Roy. Soc. A., 369, 2087–2112, https://doi.org/10.1098/rsta.2010.0240, 2011.

Yuan, W., Liu, D., Dong, W., Liu, S., Zhou, G., Yu, G., Zhao, T., Feng, J., Ma, Z., Chen, J., Chen, Y., Chen, S., Han, S., Huang, J., Li, L., Liu, H., Liu, S., Ma, M., Wang, Y., Xia, J., Xu, W., Zhang, Q., Zhao, X., and Zhao, L.: Multi-year precipitation reduction strongly decreases carbon uptake over northern China, J. Geophys. Res.-Biogeo., 119, 881–896, https://doi.org/10.1002/2014JG002608, 2014.

Yue, X. and Unger, N.: The Yale Interactive terrestrial Biosphere model version 1.0: description, evaluation and implementation into NASA GISS ModelE2, Geosci. Model Dev., 8, 2399–2417, https://doi.org/10.5194/gmd-8-2399-2015, 2015.

Zaehle, S., Friend, A. D., Friedlingstein, P., Dentener, F., Peylin, P., and Schulz, M.: Carbon and nitrogen cycle dynamics in the O-CN land surface model: 2. Role of the nitrogen cycle in the historical terrestrial carbon balance, Global Biogeochem. Cy., 24, GB1006, https://doi.org/10.1029/2009GB003522, 2010.

Zeng, N., Mariotti, A., and Wetzel, P.: Terrestrial mechanisms of interannual CO_2 variability, Global Biogeochem. Cy., 19, GB1016, https://doi.org/10.1029/2004gb002273, 2005.

Zhang, X., Wang, Y.-P., Peng, S., Rayner, P. J., Ciais, P., Silver, J. D., Piao, S., Zhu, Z., Lu, X., and Zheng, X.: Dominant regions and drivers of the variability of the global land carbon sink across timescales, Glob. Change Biol., 24, 3954–3968, https://doi.org/10.1111/gcb.14275, 2018.

Zhang, Y., Guanter, L., Berry, J. A., van der Tol, C., Yang, X., Tang, J., and Zhang, F.: Model-based analysis of the relationship between sun-induced chlorophyll fluorescence and gross primary production for remote sensing applications, Remote Sens. Environ., 187, 145–155, https://doi.org/10.1016/j.rse.2016.10.016, 2016a.

Zhang, Y., Xiao, X., Jin, C., Dong, J., Zhou, S., Wagle, P., Joiner, J., Guanter, L., Zhang, Y., Zhang, G., Qin, Y., Wang, J., and Moore, B.: Consistency between sun-induced chlorophyll fluorescence and gross primary production of vegetation in North America, Remote Sens. Environ., 183, 154–169, https://doi.org/10.1016/j.rse.2016.05.015, 2016b.

2.4. Publication 3: CO_2 Release During Soil Rewetting Shapes the Seasonal Carbon Dynamics in South American Temperate Region

Sanam N. Vardag, Eva-Marie Metz, Lukas Artelt, Sourish Basu, André Butz

From

Vardag, S. N., Metz, E.-M., Artelt, L., Basu, S., and Butz, A.: CO_2 Release During Soil Rewetting Shapes the Seasonal Carbon Dynamics in South American Temperate Region, Geophysical Research Letters, 52(8):e2024GL111725, https://doi.org/10.1029/2024GL111725, 2025.

ADVANCING EARTH AND SPACE SCIENCES

Geophysical Research Letters

RESEARCH LETTER
10.1029/2024GL111725

CO_2 Release During Soil Rewetting Shapes the Seasonal Carbon Dynamics in South American Temperate Region

Sanam N. Vardag[1,2], **Eva-Marie Metz**[1], **Lukas Artelt**[1], **Sourish Basu**[3,4], and **André Butz**[1,2,5]

[1]Institut für Umweltphysik, Heidelberg University, Heidelberg, Germany, [2]Heidelberg Center for the Environment, Heidelberg University, Heidelberg, Germany, [3]NASA Goddard Space Flight Center, Greenbelt, MD, USA, [4]Earth System Science Interdisciplinary Center, University of Maryland, College Park, MD, USA, [5]Interdisciplinary Center for Scientific Computing, Heidelberg University, Heidelberg, Germany

Key Points:

- Combining ecosystem models with satellite-based top-down fluxes enhances our understanding of carbon dynamics in remote regions
- In the South American Temperate (SAT) region, an early increase in heterotrophic respiration after the dry season leads to a net carbon release
- Soil rewetting processes dominate seasonal carbon flux variability in SAT region

Supporting Information:

Supporting Information may be found in the online version of this article.

Correspondence to:

S. N. Vardag,
sanam.vardag@uni-heidelberg.de

Citation:

Vardag, S. N., Metz, E.-M., Artelt, L., Basu, S., & Butz, A. (2025). CO_2 release during soil rewetting shapes the seasonal carbon dynamics in South American Temperate region. *Geophysical Research Letters*, *52*, e2024GL111725. https://doi.org/10.1029/2024GL111725

Received 1 AUG 2024
Accepted 26 FEB 2025

Author Contributions:

Conceptualization: Sanam N. Vardag, Eva-Marie Metz, André Butz
Formal analysis: Eva-Marie Metz, Lukas Artelt
Methodology: Sanam N. Vardag, Eva-Marie Metz, André Butz
Software: Sourish Basu
Supervision: Sanam N. Vardag, André Butz
Visualization: Eva-Marie Metz, Lukas Artelt
Writing – original draft: Sanam N. Vardag
Writing – review & editing: Sanam N. Vardag, Eva-Marie Metz, Lukas Artelt, Sourish Basu, André Butz

Abstract Processes driving the terrestrial carbon fluxes in the South American Temperate (SAT) region are not well understood due to limited availability of in situ and flux tower measurements. This study leverages atmospheric CO_2 measurements by the Greenhouse Gases Observing Satellite to additionally constrain net carbon fluxes in the SAT region. By identifying Dynamic Global Vegetation Models that closely align with observational data, we pinpoint the processes driving the seasonal land-atmosphere CO_2 exchange. We reveal that the onset of rainfall triggers an early increase in heterotrophic respiration while autotrophic respiration and gross primary production are delayed leading to an increase in net ecosystem exchange in September to October. Our findings suggest that soil rewetting processes in semi-arid areas dominate seasonal carbon dynamics and need to be accurately represented in global carbon cycle models to improve the global carbon budget.

Plain Language Summary Understanding the patterns of carbon dynamics in the South American Temperate region is challenging because there are not many ground-based measurements available. This study uses satellite data, along with computer models, to examine what influences the seasonal changes of carbon fluxes in this region from 2009 to 2018. Our study finds that the start of the rainy season causes a quick rise in carbon release from soil. However, the carbon uptake by plants happens later leading to an increase of CO_2 flux in the middle of the year. These results suggest that the rewetting of dry soils plays a major role in controlling carbon cycles in semi-arid areas. Therefore, it is important to include these processes accurately in global carbon cycle models to improve our understanding of the global carbon budget.

1. Introduction

Anthropogenic CO_2 emissions are released to the atmosphere and are increasing the global CO_2 concentration. On average, land and ocean sinks take up roughly half of the emitted CO_2 and therefore slow down the rise of atmospheric CO_2 (Friedlingstein et al., 2023). How much CO_2 is taken up by the land sink is driven by terrestrial processes and varies considerably from year to year due to the ecosystems' dependence on environmental and climatic conditions such as soil moisture and temperature (Piao et al., 2020; Wang et al., 2016). Understanding the terrestrial processes is a prerequisite of forecasting global biospheric uptake and release of CO_2 under climate change and changing environmental stressors (Steiner, 2020).

Semi-arid ecosystems contribute substantially to interannual variability of the global carbon cycle (Ahlström et al., 2015; Poulter et al., 2014). These regions can eventually become even more important, as in future, arid and semi-arid regions may spread due to climate change—especially in the Southern Hemisphere (Cherlet et al., 2018; Pokhrel et al., 2021). Gross CO_2 fluxes are controlled by hydrological and meteorological conditions (MacBean et al., 2021). Increased soil moisture can enhance carbon uptake by promoting gross primary production (GPP) and can affect microbial activity in the soil (Bond-Lamberty et al., 2024). Local studies showed that rain pulses in semi-arid ecosystems can suddenly activate soil microbes, which respire accumulated substrate leading to respiration pulses. This effect is referred to as Birch effect (Birch, 1964)and the magnitude depends strongly on the rain pulse intensity (Huxman et al., 2004; Silva et al., 2024). The regional scale net effect for semi-arid regions is still unknown as it depends on the timing and magnitude of the rain pulses, on the ecosystem type, on the available carbon stocks and on the prevailing prior environmental conditions such as drought (Silva et al., 2024). This makes it especially difficult to generalize patterns found in local eddy-covariance flux measurements to inform on the regional carbon budget, although these direct flux measurements provide the ground truth of local carbon dynamics.

In order to obtain an understanding of the terrestrial processes, Dynamic Global Vegetation Models (DGVMs) can be used as they represent the biogenic carbon cycle and its dynamics given environmental conditions such as temperature, precipitation and land-use types (Sitch et al., 2015). This approach enables deeper understanding of the causes influencing the carbon budget. However, model results for net CO_2 exchange vary considerably between different models as they include different processes, interactions and constants (Foster et al., 2024; Metz et al., 2023; Teckentrup et al., 2021). As photosynthetic and respiratory gross fluxes can be large, this adds additional complexity to the accurate determination of net fluxes. Therefore, it is important to determine which DGVM performs well for the area of interest. Atmospheric observations can be used to determine the net carbon fluxes (Foster et al., 2024). Eddy-covariance flux measurements provide local constraints but are typically not representative of larger regional scales. Ground-based in situ observations assimilated into inverse atmospheric transport models can inform on regional carbon dynamics from the top-down perspective (Chevallier et al., 2010; Gurney et al., 2008; Rödenbeck et al., 2003). However, in regions with sparse in situ observations, uncertainties in retrieved fluxes are large (J. S. Wang et al., 2018). In these regions, satellite observations can provide additional top-down constraints on CO_2 fluxes (Basu et al., 2013; He et al., 2022, 2023; Sellers et al., 2018). Recently, based on satellite measurements of XCO_2 (column-average dry-air mole fraction of CO_2), Metz et al. (2023) revealed a continental-scale CO_2 pulse after heavy rain events over the semi-arid regions of Australia and associated it with soil respiration after rainfall. Combining the complementary strengths of process-based ecosystem models with top-down approaches can enhance our understanding of both, the magnitude of the carbon fluxes on continental scale, but also the processes driving the carbon dynamics.

Here we focus on the South American Temperate (SAT) region as it has large dry areas and contributes considerably to uncertainties in the global carbon budget (Bastos et al., 2020). Therefore, the SAT region offers an opportunity to better understand the carbon dynamics in dry areas and reduce global carbon budget uncertainties. In this study, we use the combination of bottom-up and top-down approaches to analyze the drivers of the seasonal carbon dynamics in the SAT region. Understanding the drivers of the carbon cycle in this region will aid understanding the role of semi-arid regions for the global carbon budget.

2. Data and Methods

2.1. South American Temperate (SAT) Region

We use the SAT region definition from the TRANSCOM-3 experiment (colored in Figure S1 in Supporting Information S1). The region lies south and east of the Amazon rainforest and incorperates large drylands (Cherlet et al., 2018; Mitsugi, 2019). It exhibits a range of different landcovers with mainly barren or sparsely vegetated land in the west and grasslands and savannas in the east (see Figure S2 in Supporting Information S1). As a criterion to distinguish humid and arid regions, we use a mean monthly precipitation rate of 1 mm/day/grid cell for at least four consecutive months as threshold. Applying this threshold divides the SAT region into two approximately equally sized parts. As the arid region is divided by the humid region in the middle, we later further differentiate the arid region into east and west. More details on the region and threshold are given in Text S1 in Supporting Information S1.

2.2. DGVMs–TRENDYv9 Ensemble

To assess the underlying processes of the carbon cycle, we used the S3 in Supporting Information S1 simulations of the "Trends and drivers of the regional scale terrestrial sources and sinks of carbon dioxide" (TRENDY) 2023 ensemble version 9 consisting of process-based DGVMs that can simulate vegetation dynamics driven by meteorological input data (Friedlingstein et al., 2020; Sitch et al., 2015). In total, we use 18 DGVMs, namely CLASSIC, OCN, ISBA-CTRIP, ISAM, YIBs, ORCHIDEE, SDGVM, VISIT, LPX-Bern, CLM5.0, ORCHIDEEv3, ORCHIDEE-CNP, LPJ, JULES-ES-1p0, JSBACH, CABLE-POP, DLEM and IBIS, which are listed in Table S1 in Supporting Information S1. The models are run globally and provide outputs for net biome production (NBP), GPP and terrestrial ecosystem respiration (TER), as well as for heterotrophic respiration (Rh) and autotrophic respiration (Ra). Few models additionally give non-respiratory fluxes, such as fire and land use change fluxes, explicitly, while others do not account for fire and land use change fluxes. Net ecosystem exchange (NEE) is then given as:

$$\mathrm{NEE} = \mathrm{NBP} - \mathrm{non} - \mathrm{respiratory\ fluxes} = \mathrm{TER} - \mathrm{GPP} = \mathrm{Ra} + \mathrm{Rh} - \mathrm{GPP},$$

Note that with the above definition, net CO_2 release into the atmosphere has a positive sign, net CO_2 uptake from the atmosphere has a negative sign, and that individual gross fluxes are strictly positive by definition. Lateral fluxes such as riverine fluxes are neglected as DGVMs do not account for them and as they are small compared to the gross fluxes in the SAT region (Liu et al., 2024).

2.3. TM5-4DVAR–Top-Down CO_2 fluxes

In an inversion, CO_2 observations are assimilated to obtain CO_2 fluxes between the atmosphere and the biosphere and ocean. We use the Tracer Model-5 four-dimensional variational inversion system (TM5-4DVAR) for this purpose (Basu et al., 2013), which assimilates atmospheric CO_2 mole fractions and estimates CO_2 fluxes considering prior flux estimates and uncertainties in measurements and prior fluxes.

We use two different data sets as input for the inversion system:

1. In situ CO_2 data only: CO_2 GLOBALVIEWplus v5.0 ObsPack

This is a collection of worldwide in situ measurements of the atmospheric CO_2 mole fractions (Cooperative Global Atmospheric Data Integration Project, 2019). The global spatial coverage is inhomogeneous and the Southern Hemisphere is sparsely covered. Apart from monthly aircraft profiles over Amazonia, there are only three surface stations in the entire SAT region, one located in the Amazon forest, one in the east of Brazil and one in the south. We name the resulting fluxes TM5-4DVAR/IS.

2. In situ CO_2 data plus XCO_2 from the Greenhouse Gases Observing Satellite (GOSAT)

In addition to the in situ data set (i), we leverage GOSAT XCO_2 from 2009 to 2018. Due to its good coverage over the SAT region this adds novel and substantial information to the inversion. We use data obtained from the radiative transfer and retrieval algorithm RemoTeC v.2.4.0 (Butz, 2022; Butz et al., 2011), as well as the NASA Atmospheric CO_2 Observations from Space (ACOS) algorithm v.9 (Taylor et al., 2022). The XCO_2 records and individual CO_2 fluxes of both retrieval algorithms are shown in Figure S3 in Supporting Information S1 along with further information on data selection and sampling (Texts S2.1 and S2.2 in Supporting Information S1). In the following, we refer to the mean of atmospheric inversions assimilating the two retrieval products as TM5-4DVAR/IS+GOSAT, while the spread between the two inversions is a measure of uncertainty. Prior fluxes for the biosphere were taken from the Carnegie-Ames-Stanford-Approach (CASA) biogeochemical model (van der Werf et al., 2010). All prior fluxes are based on climatological averages and exhibit a yearly repetitive seasonal cycle without interannual variability (Metz et al., 2023).

In our setting, TM5-4DVAR is configured to estimate weekly biosphere and oceanic fluxes on a regular 3° (longitude) × 2° (latitude) global grid while fire and fossil emissions are imposed from the Quick Fire Emissions Data set and the Open-source Data Inventory for Anthropogenic CO2, respectively. To avoid large sampling effects on the coastline, all flux data sets are mapped on a 1° × 1° grid before applying the TRANSCOM region mask to aggregate over the entire region and 1 month.

2.4. ERA5-Data

To understand the relation between carbon fluxes and climatic conditions, we use temperature, upper layer soil moisture (0–7 cm depth), and precipitation data sets of the European Center for Medium Range Weather Forecasts ERA5-land reanalysis product (Muñoz Sabater, 2019). ERA5 data has a spatial resolution of 0.25° × 0.25° and provides monthly averages. ERA5 data sets are aggregated on a 1° × 1° grid before performing the region selection.

3. Results

3.1. Bottom-Up: DGVMs Show Inconsistent Carbon Dynamics

We analyze the NEE of 18 different TRENDY models from 2009 to 2018 and find substantial deviations from each other, both in magnitude and seasonal cycle (see gray lines in Figure 1). The models suggest fundamentally different carbon dynamics for the SAT region. They differ in the interannual variability, as well as in the seasonal cycle. While some models show an uptake in the austral summer months, others show an uptake in the winter months. Finally, also the magnitude of the monthly fluxes is different by up to an order of magnitude. The large

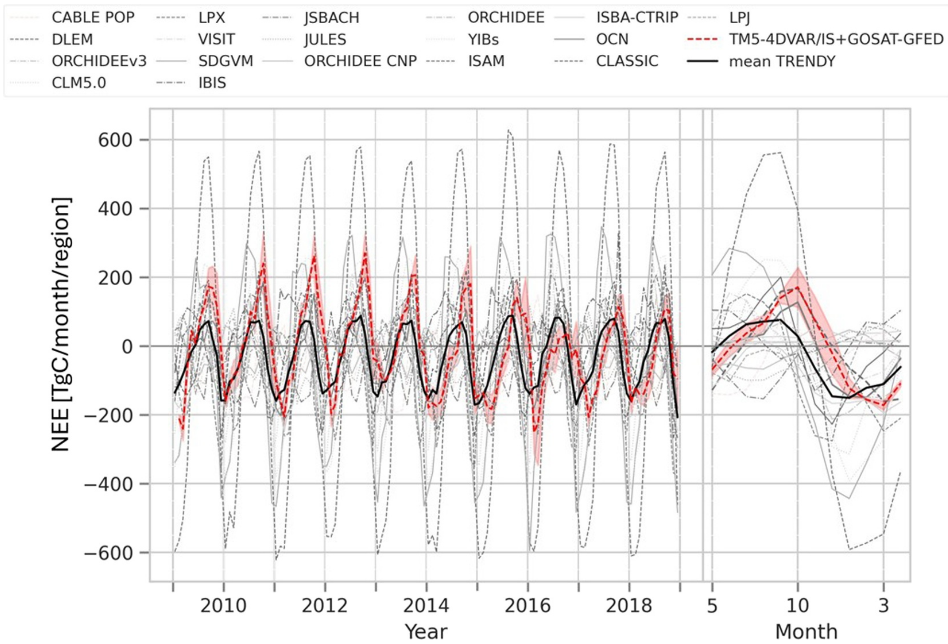

Figure 1. (a) Monthly Net ecosystem exchange (NEE) flux of the entire South American Temperate (SAT) region of the 18 TRENDY models (in gray) and of the TM5-4DVAR/IS+GOSAT minus GFED 4.1 fire fluxes (Randerson et al., 2018) (red). The shading indicates the spread between the two retrievals RemoTeC and Atmospheric CO2 Observations from Space (TM5-4DVAR/IS+RemoTeC and TM5-4DVAR/IS+ACOS). The mean of all TRENDY models is shown as black line. Panel (b) shows the mean seasonal cycle from 2009 to 2018 of the TM5-4DVAR/IS+GOSAT inversions-GFED 4.1 and of all TRENDY models and their mean. The shading indicates the standard deviation of the years.

differences suggest that the carbon balance of the SAT region is not well understood and cannot be constrained by multiple DGVMs alone.

One must be cautious when using the mean of these models, as it can be disproportionately influenced by those with large seasonal amplitudes, which may result in biased results for the model mean. This reinforces the recent findings by Foster et al. (2024) who analyzed the North American carbon budget and found that many DGVMs are not consistent amongst each other. This diagnosis requires independent measurement-based information on the actual net fluxes to identify the models representing the seasonal carbon dynamics in the SAT region well. Therefore, we use the satellite-based top-down CO_2 fluxes to analyze the carbon fluxes over the SAT region from 2009 to 2018.

3.2. Top-Down: TM5-4DVAR CO_2 fluxes Exhibit Discriminating Power

We analyze the top-down fluxes TM5-4DVAR/IS and TM5/4DVAR/IS+GOSAT to provide independent information on the net CO_2 fluxes over SAT region. While the timing of the seasonal cycle agrees well between the two inversion fluxes, the magnitude of the peaks and dips differ slightly (Figure S5 in Supporting Information S1). The differences are smaller than differences between the TRENDY models and are most likely due to sparseness of the in situ data offering limited information on SAT fluxes (see Text S2.3.2 in Supporting Information S1 for more details). To this end, in the following we use the TM5-4DVAR/IS+GOSAT fluxes to fully exploit all available measurements within the inversion. We find that every year the maxima of the TM5-4DVAR/IS+GOSAT fluxes occur in September or October while the minima occur between January and March (red line in Figure 1). While the timing of the seasonal cycle stays constant over the course of the years, the magnitude shows some inter-annual variations (Figure 1 and Figure S5 in Supporting Information S1). However, in this study, we focus further investigations on the mean seasonal cycle as it is consistent throughout the entire time periods.

10.1029/2024GL111725

While not the focus of this study, we additionally compare to the fluxes from the OCO-2 MIP ensemble (Byrne et al., 2023) for the available shorter period, 2015–2018, and find that the timing of the seasonal cycle agrees well with TM5-4DVAR/IS+GOSAT fluxes, but OCO-2 MIP shows a slightly smaller amplitude (Figure S6 and S7, Text S3 in Supporting Information S1). The difference in the magnitude of the flux maxima and minima between GOSAT and OCO-2 based fluxes are much smaller than the spread of the TRENDY model ensemble.

The consistent seasonal cycle of the top-down constraints on net CO_2 fluxes for the SAT region, creates a discriminating power for the TRENDY products. The net fluxes of TM5-4DVAR/IS+GOSAT provide the required novel and independent information to select those DGVMs, which are able to capture the seasonal cycle correctly.

3.3. Combining Bottom-Up and Top-Down to Gain Process Understanding

We identify the DGVMs whose NEE compares best to the TM5-4DVAR/IS+GOSAT net fluxes minus GFED fire emissions in the SAT region. Then, we examine the gross fluxes from these selected DGVMs to better understand the driving processes. Grouping the DGVMs, we find models with the same timing and magnitude as the TM5-4DVAR/IS+GOSAT estimate (selected strict models: CLASSIC and OCN). Some models show a similar timing and magnitude, but the match of the individual DGVMs is worse than those of the selected strict models (selected loose: ISBA-CTRIP, ISAM, YIBs and ORCHIDEE). Seven models show a clear time shift with respect to TM5-4DVAR/IS+GOSAT fluxes and a much higher amplitude (other high amplitude: VISIT, DLEM, CABLE-POP, LPX-Bern, ORCHIDEEv3, CLM5.0 and SDGVM). Finally, the five remaining models (other low amplitude) do not capture the top-down seasonal cycle at all. They generally have a smaller amplitude and further they show pronounced time shifts in their seasonal cycle compared to the top-down estimate (Figure S8 in Supporting Information S1). The selection of models does not change when using NBP (see Figure S9 in Supporting Information S1) rather than NEE (see Figure 1).

We focus on the DGVMs, which can represent the carbon dynamics of the SAT region in accordance with the TM5-4DVAR/IS+GOSAT inversions (selected strict models) to examine the processes underlying the net carbon dynamics. Note that the analysis of the selected loose models leads to the same findings as for the strict models despite a slightly worse agreement of the individual models to TM5-4DVAR/IS+GOSAT.

To get insights into the processes leading to the observed net fluxes, we partition the NEE into the gross fluxes GPP and TER, of which the latter consists of Ra and Rh for the selected strict models (see Figure 2). While the general shape of GPP and TER is similar with a minimum in July to September and a maximum in December to January, TER precedes the rise of GPP, leading to the net positive NEE flux with maximal emissions in September to October. The net negative NEE in the months December to March, however, is mainly due to a difference in the magnitude of both gross fluxes, while their timing is in phase. Differentiating TER further, one can see that the early rise of respiration is driven by Rh whereas Ra remains in phase with the GPP signal.

A similar pattern of a dephasing between Rh and GPP was found by Metz et al. (2023) over the semi-arid regions of Australia occurring shortly after rainfall events following dry periods. To study if the wetting of dry soils may also play a role in the SAT region, we further divide the area into humid and arid parts and conduct a sub-regional analysis of fluxes in conjunction with precipitation, temperature and soil moisture.

3.4. Sub-Regional Analysis: Arid Regions Influence Seasonal Cycle

We analyze the relation between environmental parameters and the observed ecosystem fluxes in the humid, arid east, and arid west regions of the SAT region as outlined in Sect. 2.1 and shown in Figure S1 in Supporting Information S1, as well as Figure 3. For all three regions, precipitation is higher between October and April than in the rest of the year. During this time, the arid regions receive a considerable amount of precipitation. The upper soil water content is mainly driven by precipitation and evaporation. In average, the arid regions have considerably lower soil water content than the humid regions. The arid east region exhibits a pronounced seasonal cycle of soil water content with low values from July to September ($<0.2\ m^3/m^3$). Details on precipitation, evaporation, soil moisture and temperature are given in Figures 3d–3f.

We analyze the DGVM fluxes and compare them to TM5-4DVAR/IS+GOSAT for the three subregions. Note that the percentage uncertainties of inversely derived CO_2 fluxes—such as those from TM5-4DVAR—increase as

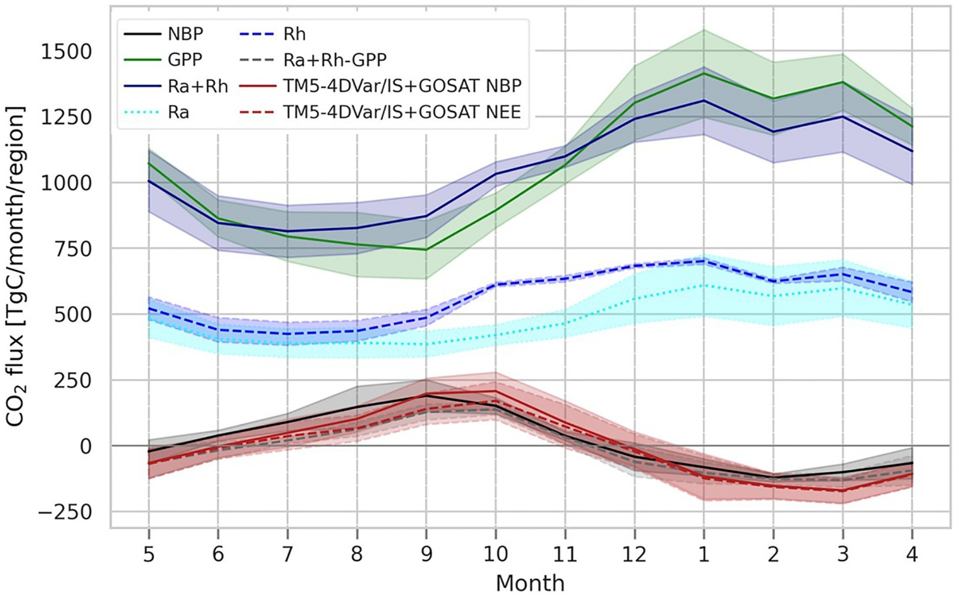

Figure 2. NEE from TRENDY (gray, selected strict) can be further partitioned into gross primary production (GPP) (green) and terrestrial ecosystem respiration (Ra+Rh, dark blue), with the latter being the sum of autotrophic (Ra, cyan dotted) and heterotrophic (Rh, blue dashed) respiration. The NEE (NBP-GFED) from TM5-4DVAR/IS+GOSAT is shown in red dashed. Net biome production for TRENDY (black) and TM5-4DVAR (red) are shown additionally, but fire emissions are small compared to the mean net fluxes. Note that respiration fluxes release CO_2 into the atmosphere and GPP takes up carbon from the atmosphere. However, both are illustrated as positive fluxes.

the subregion size decreases (Chevallier et al., 2010; Zhang et al., 2023). Studying net and gross CO_2 fluxes for these three identified regions (see Figures 3a–3c) along with the precipitation, we find that the humid area exhibits much larger gross fluxes of GPP and respiration compared to both arid regions. However, the net fluxes in the arid east region are slightly larger than the net flux in the humid region. The reason is that for the humid area (Figure 3b), GPP and Ra and Rh are in phase. However, for the arid east region (and to a lesser extent in the arid west region), we find an early increase of Rh with respect to GPP and Ra. The different land cover types in the arid east and arid west region (Figure S2 in Supporting Information S1) affect their sensitivity to climate (Poulter et al., 2011; Teckentrup et al., 2023) and therefore explain the slightly different behavior of both arid regions. The increase of Rh coincides with precipitation onset and soil rewetting after a dry period. The shift in the mean seasonal cycle of Rh with respect to GPP and Ra leads to a positive net flux of CO_2 into the atmosphere reaching a maximum amplitude in September and October and dominating the seasonal carbon dynamics of the entire SAT region. The sensitivity of Rh to soil rewetting after the dry season can also be seen over the course of the entire time series. The magnitude of the soil respiration correlates to the magnitude of precipitation in the rewetting month (Figure S10 in Supporting Information S1).

Flux tower measurements can provide the ground truth on local and short-term carbon dynamics and support findings from regional analyzes as conducted here, however they are rare in the semi-arid parts of the SAT region. There is only one FLUXNET station (BR-CST Caatinga Serra Talhada station (Antonino, 2022), Text S4 in Supporting Information S1) in the semi-arid parts of our study region. The measurements show an immediate response of respiration triggered by rain pulses after dry periods and preceding the uptake by GPP (see Figures S11 and S12 in Supporting Information S1). While these data are not representative of the entire SAT region, and only 1 year of measurements exists, this local flux behavior is consistent with the mechanism found on continental scale in this study. It demonstrates the existence of local rain induced short term respiration pulses at the beginning of the rainy season. The sum of local pulses may explain the large-scale signal seen in DGVMs and from the inversion.

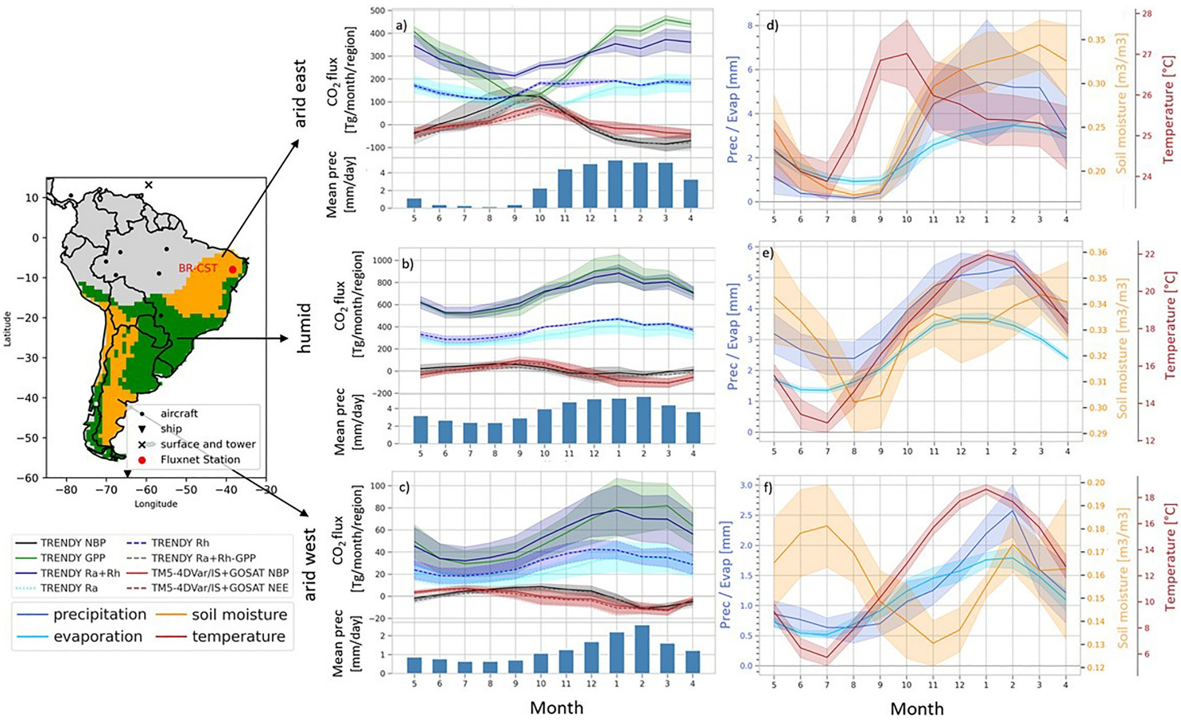

Figure 3. Left: Map of SAT region (colored) with separation between arid (yellow) and humid (green) areas. For more detail see Figure S1 in Supporting Information S1. Left column: Mean seasonal cycle of TRENDY fluxes (NBP, GPP, Ra+Rh, Rh, Ra and NEE) in the arid east (a), humid (b) and arid west (c) of the SAT region. As a reference, also the TM5-4DVAR/IS+GOSAT NEE and NBP for the respective subregion is shown although uncertainties of the inversion increase with smaller areas. The colored area around each line indicates the standard deviation from the mean of the models. In the lower part of each panel, the ERA5 precipitation is shown as bar plot. Right column: Mean seasonal cycles of monthly precipitation per day, temperature, upper layer soil water content and evaporation, all taken from ERA5, for the arid east region (d), humid region (e) and arid west region (f). The colored areas around each line represent the standard deviation from the year-to-year variability. Note that the y-scale differs for each region.

4. Conclusions

The SAT region is poorly constrained in terms of carbon fluxes. This follows from a low density of in situ CO_2 and flux tower measurements in this region. Therefore, large uncertainties in carbon flux estimates exist, hampering an understanding of relevant carbon exchange processes. We analyzed the seasonal cycle of the land-atmosphere carbon fluxes in the SAT region from 2009 to 2018. The missing process understanding of terrestrial gross fluxes manifests itself in the large disagreement between different DGVMs and calls for considering additional independent information to quantify the carbon dynamics. We used GOSAT XCO_2 measurements along with in situ CO_2 measurements in a TM5-4DVAR atmospheric inversion to obtain net carbon fluxes in the SAT region and to identify the TRENDY models that are most consistent with TM5-4DVAR CO_2 fluxes. While the top-down approach only provided the net CO_2 flux, it enabled the selection of the consistent process-based models to analyze the gross fluxes and drivers.

The CLASSIC and OCN models matched the TM5-4DVAR/IS+GOSAT fluxes best. A mean of the fluxes of these two models (selected strict TRENDY models) was calculated. Within the selected strict TRENDY models, we further differentiated into the gross biospheric fluxes GPP, heterotrophic and autotrophic respiration. We found that an early increase in heterotrophic respiration compared to the rise in GPP and autotrophic respiration leads to a maximum release in NBP in September to October. The early increase of heterotrophic respiration coincided with the start of precipitation and soil rewetting after the dry season. While none of the models account for soil microbial activity explicitly, a quick reaction of Rh to precipitation seems to be a necessary, but not sufficient prerequisite for models to accurately capture the CO_2 flux dynamics in semi-arid SAT region (Text S5 in Supporting Information S1).

We next analyzed what region drives the seasonal cycle in the SAT subcontinent. We found that the humid regions exhibit the largest gross fluxes. However, nevertheless the arid east region dominates the net flux of the SAT region due to a distinct early rise of heterotrophic respiration triggered by precipitation after long periods of drought. In the humid region, GPP, heterotrophic and autotrophic respiration are large, but in phase such that the gross fluxes mostly compensate each other and do not contribute as much to the net flux seasonal cycle as the arid east region. While the dominant role of the arid regions for the seasonal carbon cycle may be unexpected as gross fluxes are considerably smaller than in the humid area, the importance of other semi-arid regions has been reported elsewhere (Ahlström et al., 2015; Poulter et al., 2014). Our findings strengthen the importance of semi-arid regions for the SAT region.

In particular, the fast increase of NEE after rainfall was also observed in other semi-arid regions (Jarvis et al., 2007; Metz et al., 2023). Metz et al. (2023) found a CO_2 pulse at the end of the dry season in Australia, which they linked to soil microbes that were dormant during the dry period and were activated when the soil was re-wetted. Our results suggest that soil rewetting processes in semi-arid areas play an important role in the SAT region, as well. Therefore, soil rewetting must be represented in vegetation and climate models accurately to constrain the regional carbon dynamics and finally reduce uncertainties of the global carbon budget.

Data Availability Statement

GOSAT/RemoTeC2.4.0 XCO_2 data can be obtained from https://doi.org/10.5281/zenodo.5886662 (Butz, 2022) (last access: 2024-05-15). GOSAT/ACOS data are available at https://oco2.gesdisc.eosdis.nasa.gov/data/GOSAT_TANSO_Level2/ACOS_L2_Lite_FP.9r/ (OCO-2 Science Team et al., 2019, https://doi.org/10.5067/VWSABTO7ZII4). OCO-2 data are available at https://disc.gsfc.nasa.gov/datasets/OCO2_L2_Lite_FP_10r/summary (OCO-2/OCO-3 Science Team et al., 2022). The monthly CO_2 net biome productivity data for SAT region using TM5-4DVAR can be obtained from Artelt et al. (2024). The processing code can be obtained from Artelt and Metz (2024). The MIP data can be downloaded from https://www.gml.noaa.gov/ccgg/OCO2_v10mip/ (Baker et al., 2022) (last access: 2022-11-06). ERA5-land data records contain modified Copernicus Atmosphere Service Information [2021] available at the Climate Data Store https://cds.climate.copernicus.eu/datasets/reanalysis-era5-land-monthly-means (Muñoz Sabater, 2019, last access: 2021-12-20). Eddy covariance data was collected by the FLUXNET community and is part of the AmeriFlux network available under the AmeriFluxCC-BY-4.0License at https://ameriflux.lbl.gov/login/?redirect_to=/data/download-data/. TRENDYv9 model output is available upon request from https://mdosullivan.github.io/GCB/ (Sitch et al., 2020). GFED fire emissions are available from https://www.geo.vu.nl/~gwerf/GFED/GFED4/ (Randerson et al., 2018). MODIS MCD12C1 data are available from https://search.earthdata.nasa.gov/search with the following DOI: https://doi.org/10.5067/MODIS/MCD12C1.061 (Friedl and Sulla-Menashe, 2022).

Acknowledgments

S.N.V., A.B. and E.-M.M. were involved in conceptualization and methodology. S.B. performed the dedicated TM5-4DVAR runs. E.-M.M. and L.A. conducted the formal analysis and the visualization under the supervision of A.B. and S.N.V. S.N.V. wrote the original draft. All authors contributed to the editing and review of the manuscript. We acknowledge the computing resources provided by the DKRZ under project bb1170 as well as the data storage service SDS@hd and the bwHPC computing resources supported by the state of Baden-Württemberg (Ministry of Science, Research and the Arts) and the German Research Foundation (DFG) through grants INST 35/1503-1 FUGG and INST 35/1597-1 FUGG. E.-M.M. acknowledges a doctoral scholarship from the German National Academic Foundation. We thank Stephen Sitch, Pierre Friedlingstein, and all modelers of the Trends in Net Land-Atmosphere Exchange project (TRENDY; https://blogs.exeter.ac.uk/trendy/). We thank the Japanese Aerospace Exploration Agency, the National Institute for Environmental Studies, and the Ministry of Environment for the GOSAT data and their continuous support as part of the Joint Research Agreement. We thank the OCO-2 science team for producing the GOSAT/ACOS L2 XCO_2 data. OCO-2 data were produced by the OCO-2 project at the Jet Propulsion Laboratory, California Institute of Technology, and obtained from the OCO-2 data archive maintained at the NASA Goddard Earth Science Data and Information Services Center. The eddy covariance data shared by the FLUXNET community is part of the AmeriFlux network. Funding for the AmeriFlux data portal was provided by the U.S. Department of Energy Office of Science. Open Access funding enabled and organized by Projekt DEAL.

References

Ahlström, A., Raupach, M. R., Schurgers, G., Smith, B., Arneth, A., Jung, M., et al. (2015). The dominant role of semi-arid ecosystems in the trend and variability of the land CO2 sink. *Science*, *348*(6237), 895–899. https://doi.org/10.1126/science.aaa1668

Antonino, A. (2022). AmeriFlux FLUXNET-1F BR-CST Caatinga Serra Talhada (version 3-5) [Dataset]. *AmeriFlux*. https://doi.org/10.17190/AMF/1902820

Artelt, L., & Metz, E.-M. (2024). *lartelt/VardagEtAl2024: Code for VardagEtAl 2024 (V1.0)*. Zenodo. https://doi.org/10.5281/zenodo.13225469

Artelt, L., Metz, E.-M., & Vardag, S. (2024). Monthly TM5-4DVar CO_2 fluxes based on GOSAT and in situ measurements for the South American Temperate region from 2009 to 2018 (v1.0) [Dataset]. *Zenodo*. https://doi.org/10.5281/zenodo.13143297

Baker, D. F., Basu, S., Bertolacci, M., Chevallier, F., Cressie, N., Crowell, S., et al. (2022). v10 Orbiting Carbon Observatory-2 model intercomparison project, NOAA Global Monitoring Laboratory [Dataset]. Retrieved from https://gml.noaa.gov/ccgg/OCO2_v10mip/

Bastos, A., O'Sullivan, M., Ciais, P., Makowski, D., Sitch, S., Friedlingstein, P., et al. (2020). Sources of uncertainty in regional and global terrestrial CO2 exchange estimates. *Global Biogeochemical Cycles*, *34*(2), e2019GB006393. https://doi.org/10.1029/2019GB006393

Basu, S., Guerlet, S., Butz, A., Houweling, S., Hasekamp, O., Aben, I., et al. (2013). Global CO2 fluxes estimated from GOSAT retrievals of total column CO2. *Atmospheric Chemistry and Physics*, *13*(17), 8695–8717. https://doi.org/10.5194/acp-13-8695-2013

Birch, H. F. (1964). Mineralisation of plant nitrogen following alternate wet and dry conditions. *Plant and Soil*, *20*(1), 43–49. https://doi.org/10.1007/BF01378096

Bond-Lamberty, B., Ballantyne, A., Berryman, E., Fluet-Chouinard, E., Jian, J., Morris, K. A., et al. (2024). Twenty years of progress, challenges, and opportunities in measuring and understanding soil respiration. *Journal of Geophysical Research: Biogeosciences*, *129*(2), e2023JG007637. https://doi.org/10.1029/2023JG007637

Butz, A. (2022). RemoTeC full-physics retrieval GOSAT/TANSO-FTSLevel 2 bias-corrected XCO2 version 2.4.0 operated at Heidelberg University (RemoTeCv2.4.0) [Dataset]. *Zenodo*. https://doi.org/10.5281/zenodo.5886662

Butz, A., Guerlet, S., Hasekamp, O., Schepers, D., Galli, A., Aben, I., et al. (2011). Toward accurate CO_2 and CH_4 observations from GOSAT. *Geophysical Research Letters*, *38*(14), L14812. https://doi.org/10.1029/2011GL047888

Byrne, B., Baker, D. F., Basu, S., Bertolacci, M., Bowman, K. W., Carroll, D., et al. (2023). National CO_2 budgets (2015–2020) inferred from atmospheric CO_2 observations in support of the global stocktake. *Earth System Science Data*, *15*, 963–1004. https://doi.org/10.5194/essd-15-963-2023

Cherlet, M., Hutchinson, C., Reynolds, J., Hill, J., Sommer, S., & von Maltitz, G. (2018). *World Atlas of Desertification*. Publications Office of the European Union.

Chevallier, F., Ciais, P., Conway, T. J., Aalto, T., Anderson, B. E., Bousquet, P., et al. (2010). CO_2 surface fluxes at grid point scale estimated from a global 21-year reanalysis of atmospheric measurements. *Journal of Geophysical Research*, *115*(D21), D21307. https://doi.org/10.1029/2010JD013887

Cooperative Global Atmospheric Data Integration Project. (2019). Multi-laboratory compilation of atmospheric carbon dioxide data for the period 1957-2018 (obspack_co2_1_GLOBALVIEWplus_v5.0_2019_08_12) [Dataset]. *NOAA Earth System Research Laboratory, Global Monitoring Division*. https://doi.org/10.25925/20190812

Foster, K. T., Sun, W., Shiga, Y. P., Mao, J., & Michalak, A. M. (2024). Multiscale assessment of North American terrestrial carbon balance. *Biogeosciences*, *21*(3), 869–891. https://doi.org/10.5194/bg-21-869-2024

Friedl, M., & Sulla-Menashe, D. (2022). MODIS/Terra+Aqua land cover type yearly L3 global 0.05Deg CMG V061 NASA EOSDIS land processes distributed active archive center [Dataset]. https://doi.org/10.5067/MODIS/MCD12C1.061

Friedlingstein, P., O'Sullivan, M., Jones, M. W., Andrew, R. M., Bakker, D. C. E., Hauck, J., et al. (2023). Global carbon budget 2023. *Earth System Science Data*, *15*(12), 5301–5369. https://doi.org/10.5194/essd-15-5301-2023

Friedlingstein, P., O'Sullivan, M., Jones, M. W., Andrew, R. M., Hauck, J., Olsen, A., et al. (2020). Global carbon budget 2020. *Earth System Science Data*, *12*(4), 3269–3340. https://doi.org/10.5194/essd-12-3269-2020

Gurney, K. R., Baker, D., Rayner, P., & Denning, S. (2008). Interannual variations in continental-scale net carbon exchange and sensitivity to observing networks estimated from atmospheric CO_2 inversions for the period 1980 to 2005. *Global Biogeochemical Cycles*, *22*(3), GB3025. https://doi.org/10.1029/2007GB003082

He, W., Jiang, F., Ju, W., Byrne, B., Xiao, J., Nguyen, N. T., et al. (2023). Do state-of-the-art atmospheric CO_2 inverse models capture drought impacts on the European land carbon uptake? *Journal of Advances in Modeling Earth Systems*, *15*(6), e2022MS003150. https://doi.org/10.1029/2022MS003150

He, W., Jiang, F., Wu, M., Ju, W., Scholze, M., Chen, J. M., et al. (2022). China's terrestrial carbon sink over 2010–2015 constrained by satellite observations of atmospheric CO_2 and land surface variables. *Journal of Geophysical Research: Biogeosciences*, *127*(2), e2021JG006644. https://doi.org/10.1029/2021JG006644

Huxman, T. E., Cable, J. M., Ignace, D. D., Eilts, J. A., English, N. B., Weltzin, J., & Williams, D. G. (2004). Response of net ecosystem gas exchange to a simulated precipitation pulse in a semi-arid grassland: The role of native versus non-native grasses and soil texture. *Oecologia*, *141*(2), 295–305. https://doi.org/10.1007/s00442-003-1389-y

Jarvis, P., Rey, A., Petsikos, C., Wingate, L., Rayment, M., Pereira, J., et al. (2007). Drying and wetting of Mediterranean soils stimulates decomposition and carbon dioxide emission: The "Birch effect". *Tree Physiology*, *27*, 929–940. https://doi.org/10.1093/treephys/27.7.929

Liu, M., Raymond, P. A., Lauerwald, R., Zhang, Q., Trapp-Müller, G., Davis, K. L., et al. (2024). Global riverine land-to-ocean carbon export constrained by observations and multi-model assessment. *Nature Geoscience*, *17*(9), 896–904. https://doi.org/10.1038/s41561-024-01524-z

MacBean, N., Scott, R. L., Biedermann, J. A., Peylin, P., Kolb, T., Litvak, M. E., et al. (2021). Dynamic global vegetation models underestimate net CO_2 flux mean and inter-annual variability in dryland ecosystem. *Environmental Research Letters*, *16*(9), 094023. https://doi.org/10.1088/1748-9326/ac1a38

Metz, E.-M., Vardag, S. N., Basu, S., Jung, M., Ahrens, B., El-Madany, T., et al. (2023). Soil respiration–driven CO_2 pulses dominate Australia's flux variability. *Science*, *379*(6639), 1332–1335. https://doi.org/10.1126/science.add7833

Mitsugi, H. (2019). *Trees, forests and land use in drylands: The first global assessment: Full report* (Vol. 184). FAO Forestry Paper.

Muñoz Sabater, J. (2019). ERA5-Land monthly averaged data from 1981 to present [Dataset]. *Copernicus Climate Change Service (C3S) Climate Data Store (CDS)*. https://doi.org/10.24381/cds.68d2bb3

OCO-2 Science Team, Gunson, M., & Eldering, A. (2019). ACOS GOSAT/TANSO-FTS Level 2 bias-corrected XCO2 and other select fields from the full-physics retrieval aggregated as daily files V9r, Greenbelt, MD, USA, Goddard Earth Sciences Data and Information Services Center (GES DISC) [Dataset]. https://doi.org/10.5067/VWSABTO7ZII4

OCO-2/OCO-3 Science Team, Payne, V., & Chatterjee, A. (2022). OCO-2 Level 2 bias-corrected XCO2 and other select fields from the full-physics retrieval aggregated as daily files, Retrospective processing V11.1r, Goddard Earth Sciences Data and Information Services Center (GES DISC) [Dataset]. https://doi.org/10.5067/8E4VLCK16O6Q

Piao, S., Wang, X., Wang, K., Li, X., Bastos, A., Canadell, J. G., et al. (2020). Interannual variation of terrestrial carbon cycle: Issues and perspectives. *Global Change Biology*, *26*(1), 300–318. https://doi.org/10.1111/gcb.14884

Pokhrel, Y., Felfelani, F., Satoh, Y., Boulange, J., Burek, P., Gädeke, A., et al. (2021). Global terrestrial water storage and drought severity under climate change. *Nature Climate Change*, *11*(3), 226–233. https://doi.org/10.1038/s41558-020-00972-w

Poulter, B., Ciais, P., Hodson, E., Lischke, H., Maignan, F., Plummer, S., & Zimmermann, N. E. (2011). Plant functional type mapping for earth system models. *Geoscientific Model Development*, *4*, 993–1010. https://doi.org/10.5194/gmd-4-993-2011

Poulter, B., Frank, D., Ciais, P., Myneni, R. B., Andela, N., Bi, J., et al. (2014). Contribution of semi-arid ecosystems to interannual variability of the global carbon cycle. *Nature*, *509*(7502), 600–603. https://doi.org/10.1038/nature13376

Randerson, J. T., van der Werf, G. R., Giglio, L., Collatz, G. J., & Kasibhatla, P. S. (2018). Global Fire Emissions Database, Version 4.1 (GFEDv4) [Dataset]. *ORNL DAAC*. https://doi.org/10.3334/ORNLDAAC/1293

Rödenbeck, C., Houweling, S., Gloor, M., & Heimann, M. (2003). CO_2 flux history 1982–2001 inferred from atmospheric data using a global inversion of atmospheric transport. *Atmospheric Chemistry and Physics*, *3*, 1919–1964. https://doi.org/10.5194/acp-3-1919-2003

Sellers, P. J., Schimel, D. S., Moore, B., Liu, J., & Eldering, A. (2018). Observing carbon cycle–climate feedbacks from space. *Proceedings of the National Academy of Sciences of the United States of America*, *115*(31), 7860–7868. https://doi.org/10.1073/pnas.1716613115

Silva, C. M. S. e., Bezerra, B. G., Mendes, K. R., Mutti, P. R., Rodrigues, D. T., Costa, G. B., et al. (2024). Rainfall and rain pulse role on energy, water vapor and CO_2 exchanges in a tropical semiarid environment. *Agricultural and Forest Meteorology*, *345*, 109829. https://doi.org/10.1016/j.agrformet.2023.109829

Sitch, S., Arora, V. K., Briggs, P., Friedlingstein, P., Goll, D. S., Jain, A. K., et al. (2020). TRENDY: Trends in the land carbon cycle, Trendy v9 [Dataset]. Retrieved from https://mdosullivan.github.io/GCB/

Sitch, S., Friedlingstein, P., Gruber, N., Jones, S. D., Murray-Tortarolo, G., Ahlström, A., et al. (2015). Recent trends and drivers of regional sources and sinks of carbon dioxide. *Biogeosciences*, *12*(3), 653–679. https://doi.org/10.5194/bg-12-653-2015

Steiner, A. L. (2020). Role of the terrestrial biosphere in atmospheric chemistry and climate. *Accounts of Chemical Research*, *53*(7), 1260–1268. https://doi.org/10.1021/acs.accounts.0c00116

Taylor, T. E., O'Dell, C. W., Crisp, D., Kuze, A., Lindqvist, H., Wennberg, P. O., et al. (2022). An 11-year record of XCO2 estimates derived from GOSAT measurements using the NASA ACOS version 9 retrieval algorithm. *Earth System Science Data*, *14*(1), 325–360. https://doi.org/10.5194/essd-14-325-2022

Teckentrup, L., De Kauwe, M. G., Pitman, A. J., Goll, D. S., Haverd, V., Jain, A. K., et al. (2021). Assessing the representation of the Australian carbon cycle in global vegetation models. *Biogeosciences*, *18*(20), 5639–5668. https://doi.org/10.5194/bg-18-5639-2021

Teckentrup, L., De Kauwe, M. G., Abramowitz, G., Pitman, A. J., Ukkola, A. M., Hobeichi, S., et al. (2023). Opening Pandora's box: Reducing global circulation model uncertainty in Australian simulations of the carbon cycle. *Earth System Dynamics*, *14*, 549–576. https://doi.org/10.5194/esd-14-549-2023

van der Werf, G. R., Randerson, J. T., Giglio, L., Collatz, G. J., Mu, M., Kasibhatla, P. S., et al. (2010). Global fire emissions and the contribution of deforestation, savanna, forest, agricultural, and peat fires (1997-2009). *Atmospheric Chemistry and Physics*, *10*(23), 11707–11735. https://doi.org/10.5194/acp-10-11707-2010

Wang, J., Zeng, N., & Wang, M. (2016). Interannual variability of the atmospheric CO_2 growth rate: Roles of precipitation and temperature. *Biogeosciences*, *13*(8), 2339–2352. https://doi.org/10.5194/bg-13-2339-2016

Wang, J. S., Kawa, S. R., Collatz, G. J., Sasakawa, M., Gatti, L. V., Machida, T., et al. (2018). A global synthesis inversion analysis of recent variability in CO_2 fluxes using GOSAT and in situ observations. *Atmospheric Chemistry and Physics*, *18*(15), 11097–11124. https://doi.org/10.5194/acp-18-11097-2018

Zhang, L., Jiang, F., He, W., Wu, M., Wang, J., Ju, W., et al. (2023). A robust estimate of continental-scale terrestrial carbon sinks using GOSAT XCO2 retrievals. *Geophysical Research Letters*, *50*(6), e2023GL102815. https://doi.org/10.1029/2023GL102815

References From the Supporting Information

Delire, C., Séférian, R., Decharme, B., Alkama, R., Calvet, J.-C., Carrer, D., et al. (2020). The global land carbon cycle simulated with ISBA-CTRIP: Improvements over the last decade. *Journal of Advances in Modeling Earth Systems*, *12*(9), e2019MS001886. https://doi.org/10.1029/2019MS001886

Goll, D. S., Joetzjer, E., Huang, M., & Ciais, P. (2018). Low phosphorus availability decreases susceptibility of tropical primary productivity to droughts. *Geophysical Research Letters*, *45*(16), 8231–8240. https://doi.org/10.1029/2018GL077736

Haverd, V., Smith, B., Nieradzik, L., Briggs, P. R., Woodgate, W., Trudinger, C. M., et al. (2018). A new version of the CABLE land surface model (Subversion revision r4601) incorporating land use and land cover change, woody vegetation demography, and a novel optimisation-based approach to plant coordination of photosynthesis. *Geoscientific Model Development*, *11*(7), 2995–3026. https://doi.org/10.5194/gmd-11-2995-2018

Kato, E., Kinoshita, T., Ito, A., Kawamiya, M., & Yamagata, Y. (2013). Evaluation of spatially explicit emission scenario of land-use change and biomass burning using a process-based biogeochemical model. *Journal of Land Use Science*, *8*(1), 104–122. https://doi.org/10.1080/1747423X.2011.628705

Krinner, G., Viovy, N., de Noblet-Ducoudré, N., Ogée, J., Polcher, J., Friedlingstein, P., et al. (2005). A dynamic global vegetation model for studies of the coupled atmosphere-biosphere system. *Global Biogeochemical Cycles*, *19*(1), GB1015. https://doi.org/10.1029/2003GB002199

Lawrence, D. M., Fisher, R. A., Koven, C. D., Oleson, K. W., Swenson, S. C., Bonan, G., et al. (2019). The Community Land Model Version 5: Description of new features, benchmarking, and impact of forcing uncertainty. *Journal of Advances in Modeling Earth Systems*, *11*(12), 4245–4287. https://doi.org/10.1029/2018MS001583

Lienert, S., & Joos, F. (2018). A Bayesian ensemble data assimilation to constrain model parameters and land-use carbon emissions. *Biogeosciences*, *15*(9), 2909–2930. https://doi.org/10.5194/bg-15-2909-2018

Meiyappan, P., Jain, A. K., & House, J. I. (2015). Increased influence of nitrogen limitation on CO2 emissions from future land use and land use change. *Global Biogeochemical Cycles*, *29*(9), 1524–1548. https://doi.org/10.1002/2015GB005086

Melton, J. R., Arora, V. K., Wisernig-Cojoc, E., Seiler, C., Fortier, M., Chan, E., & Teckentrup, L. (2020). CLASSIC v1.0: The open-source community successor to the Canadian Land Surface Scheme (CLASS) and the Canadian Terrestrial Ecosystem Model (CTEM) – Part 1: Model framework and site-level performance. *Geoscientific Model Development*, *13*(6), 2825–2850. https://doi.org/10.5194/gmd-13-2825-2020

Reick, C. H., Gayler, V., Goll, D., Hagemann, S., Heidkamp, M., Nabel, J. E. M. S., et al. (2021). JSBACH 3—The land component of the MPI earth system model: Documentation of version 3.2. *MPI für Meteorologie*. https://doi.org/10.17617/2.3279802

Sellar, A. A., Jones, C. G., Mulcahy, J. P., Tang, Y., Yool, A., Wiltshire, A., et al. (2019). UKESM1: Description and evaluation of the UK earth system model. *Journal of Advances in Modeling Earth Systems*, *11*(12), 4513–4558. https://doi.org/10.1029/2019MS001739

Tian, H., Chen, G., Lu, C., Xu, X., Hayes, D. J., Ren, W., et al. (2015). North American terrestrial CO2 uptake largely offset by CH4 and N2O emissions: Toward a full accounting of the greenhouse gas budget. *Climatic Change*, *129*(3–4), 413–426. https://doi.org/10.1007/s10584-014-1072-9

Vuichard, N., Messina, P., Luyssaert, S., Guenet, B., Zaehle, S., Ghattas, J., et al. (2019). Accounting for carbon and nitrogen interactions in the global terrestrial ecosystem model ORCHIDEE (trunk version, rev 4999): Multi-scale evaluation of gross primary production. *Geoscientific Model Development*, *12*(11), 4751–4779. https://doi.org/10.5194/gmd-12-4751-2019

Walker, A. P., Quaife, T., van Bodegom, P. M., De Kauwe, M. G., Keenan, T. F., Joiner, J., et al. (2017). The impact of alternative trait-scaling hypotheses for the maximum photosynthetic carboxylation rate (Vcmax) on global gross primary production. *New Phytologist*, *215*(4), 1370–1386. https://doi.org/10.1111/nph.14623

Yuan, W., Liu, D., Dong, W., Liu, S., Zhou, G., Yu, G., et al. (2014). Multiyear precipitation reduction strongly decreases carbon uptake over northern China. *Journal of Geophysical Research: Biogeosciences*, *119*(5), 881–896. https://doi.org/10.1002/2014JG002608

Yue, X., & Unger, N. (2015). The Yale Interactive terrestrial Biosphere model version 1.0: Description, evaluation, and implementation into NASA.

Zaehle, S., Friend, A. D., Friedlingstein, P., Dentener, F., Peylin, P., & Schulz, M. (2010). Carbon and nitrogen cycle dynamics in the O-CN land surface model: 2. Role of the nitrogen cycle in the historical terrestrial carbon balance. *Global Biogeochemical Cycles*, *24*(1), GB1006. https://doi.org/10.1029/2009gb003522

AGU PUBLICATIONS

Geophysical Research Letter

Supporting Information for

CO_2 Release during Soil Rewetting Shapes the Seasonal Carbon Dynamics in South American Temperate Region

Sanam Noreen Vardag[1,2], Eva-Marie Metz[1], Lukas Artelt[1], Sourish Basu[3,4], André Butz[1,2,5]

[1] Institut für Umweltphysik, Heidelberg University, Heidelberg, Germany
[2] Heidelberg Center for the Environment, Heidelberg University, Heidelberg, Germany
[3] NASA Goddard Space Flight Center, Greenbelt, Maryland, USA
[4] Earth System Science Interdisciplinary Center, University of Maryland, College Park, USA
[5]Interdisciplinary Center for Scientific Computing, Heidelberg University, Heidelberg Germany

Contents of this file

Introduction

To provide the interested reader with background information, we have included supporting information on how we define and substructure the South American Temperate region (Figure S1), what landcover types cover the SAT region (Figure S2), the GOSAT XCO_2 data (Figure S3 and S4), the GOSAT based fluxes (Figure S5), OCO-2 XCO_2 data (Figure S6) and the OCO-2 MIP fluxes (Figure S7), the grouping of TRENDY models (Figure S8), the NBP of the TM5/4DVAR/IS+GOSAT flux compared to the NBP of the TRENDY models (Figure S9), the interannual variation of soil respiration response to precipitation (Figure S10) as well as the flux tower data from the site BR-CST (Figure S11 and S12). We provide some background on the TRENDYv9 models and their references in Table S1. We have included supporting information on how we define and substructure the South American Temperate region (Text S1), the GOSAT XCO_2 data (Text S2), the GOSAT based fluxes (Text S2), OCO-2 XCO_2 data (Text S3) and the OCO-2 MIP fluxes (Text S3), the flux tower data from the site BR-CST (Text S4) as well as additional information about the selected Trendy models (Text S5).

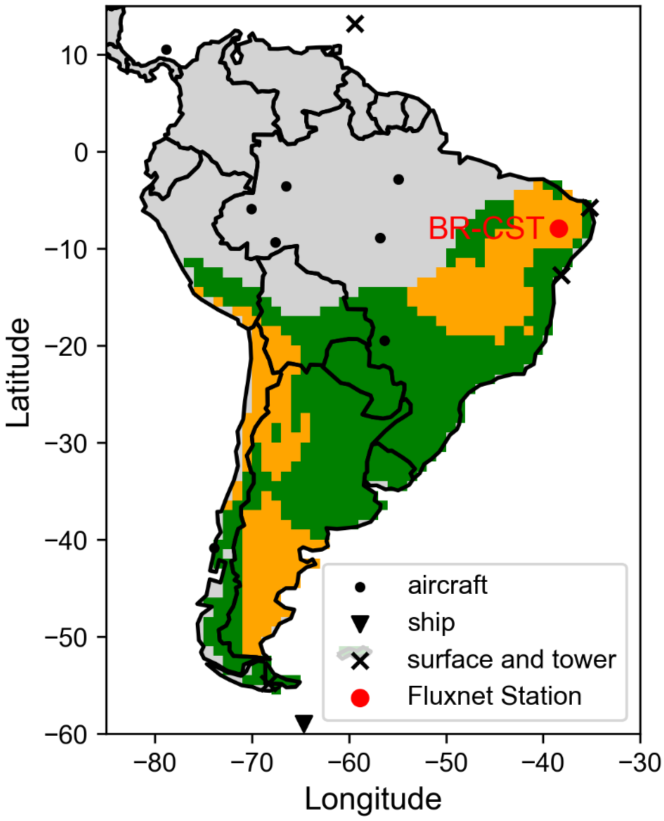

Figure S1. South American Temperate (SAT) region is shown colored. The yellow color denotes arid areas (value of <1 mm/day/grid cell mean monthly precipitation for at least four months) and green shows the humid part of the SAT region. Positions of aircraft profiling locations, shipboard sampling locations, in situ surface and tower CO_2 measurement and the FLUXNET station are marked as well.

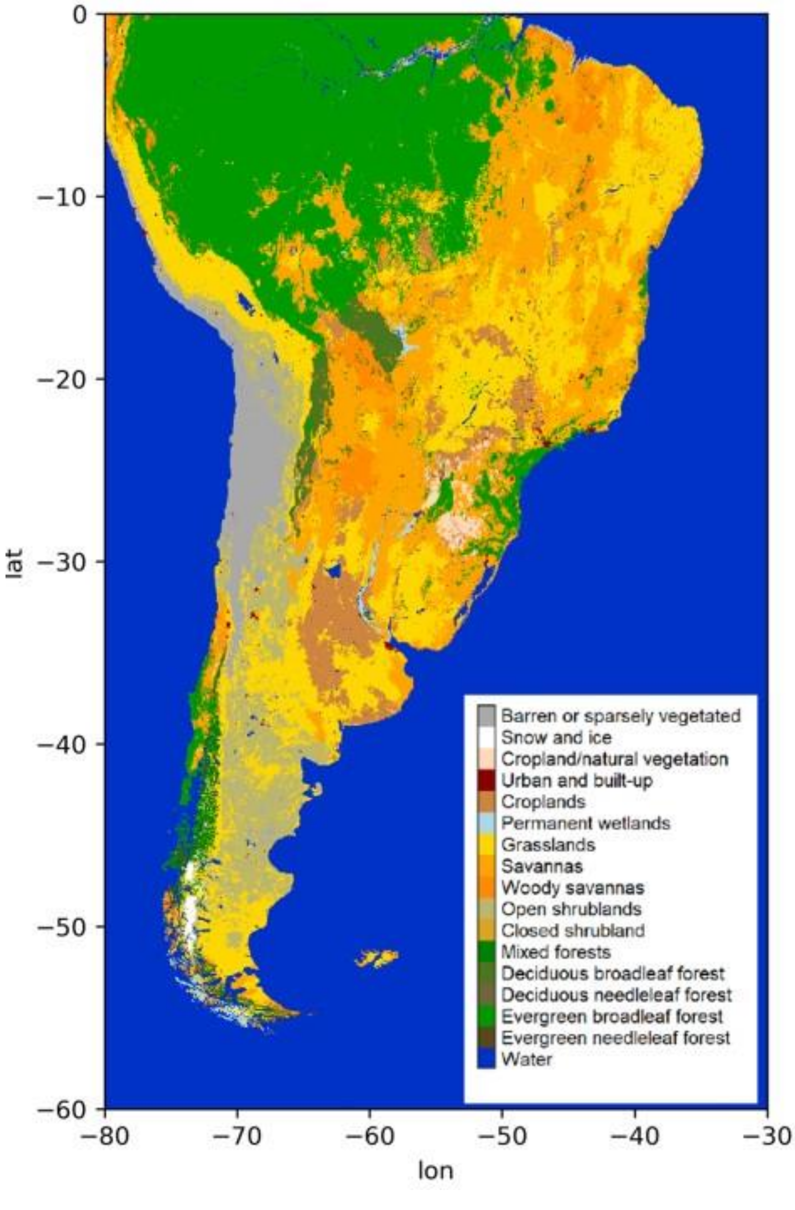

Fig. S2: Land cover map of South America based on based on MODIS (MCD12C1) data (Friedl and Sulla-Menashe, 2022).

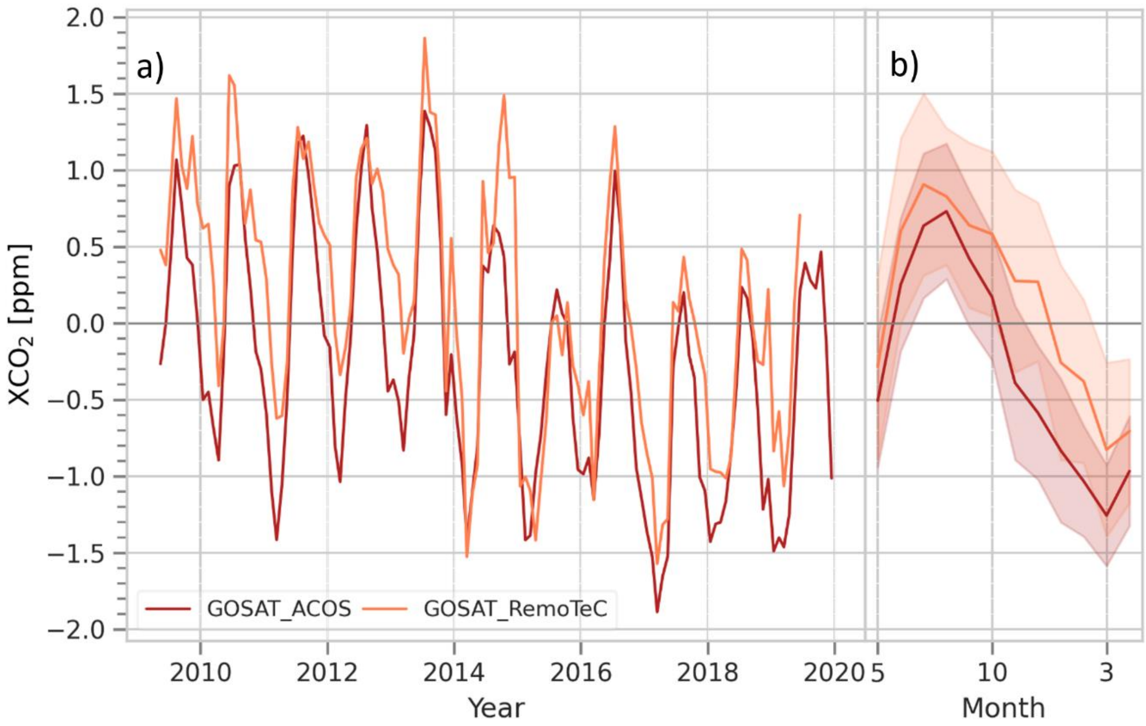

Figure S3: XCO_2 measurements by the satellite GOSAT (red: retrieved by ACOS, orange: retrieved by RemoTeC) for the SAT region. Panel (a) shows the total time series of monthly mean XCO_2 values 2009-2019. Panel (b) shows the mean seasonal cycle for the same time period. The shading in the right panel indicates the standard deviation from the mean flux value of each month.

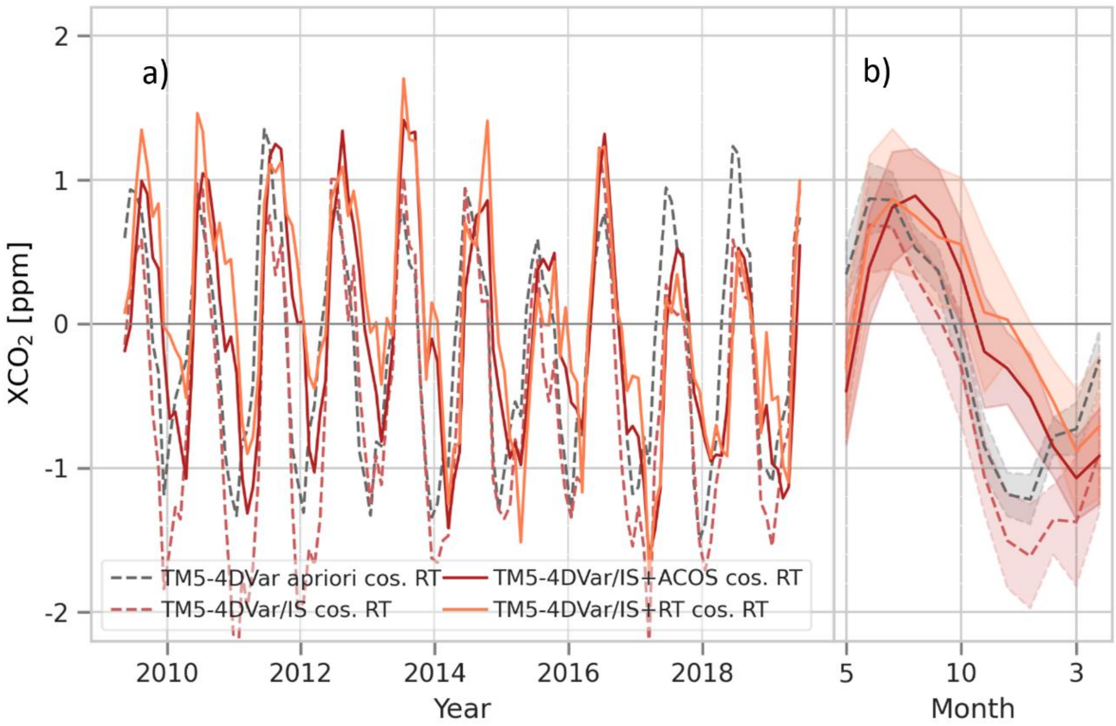

Figure S4: Seasonal cycle of XCO_2 in the SAT region calculated by TM5-4DVar from the optimized carbon flux when assimilating different data sets and co-sampling the XCO2 data on GOSAT-RemoTeC.

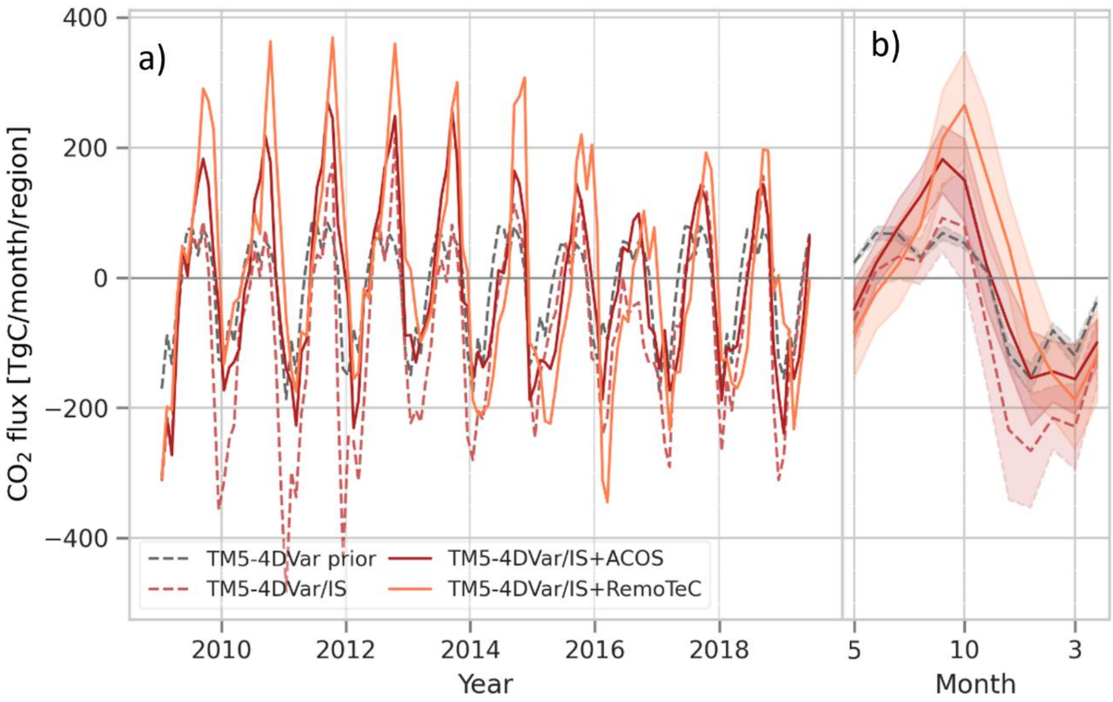

Figure S5: TM5-4DVar CO_2 fluxes in the SAT region assimilating different data sets for its optimization. Positive values represent carbon emissions, negative values a carbon uptake. The left panel of the figure shows the time series of monthly mean carbon flux values from 2009 to 2019. The right panel shows the MSC for the same time period. The shading in the right panel indicates the standard deviation from the mean flux value of each month.

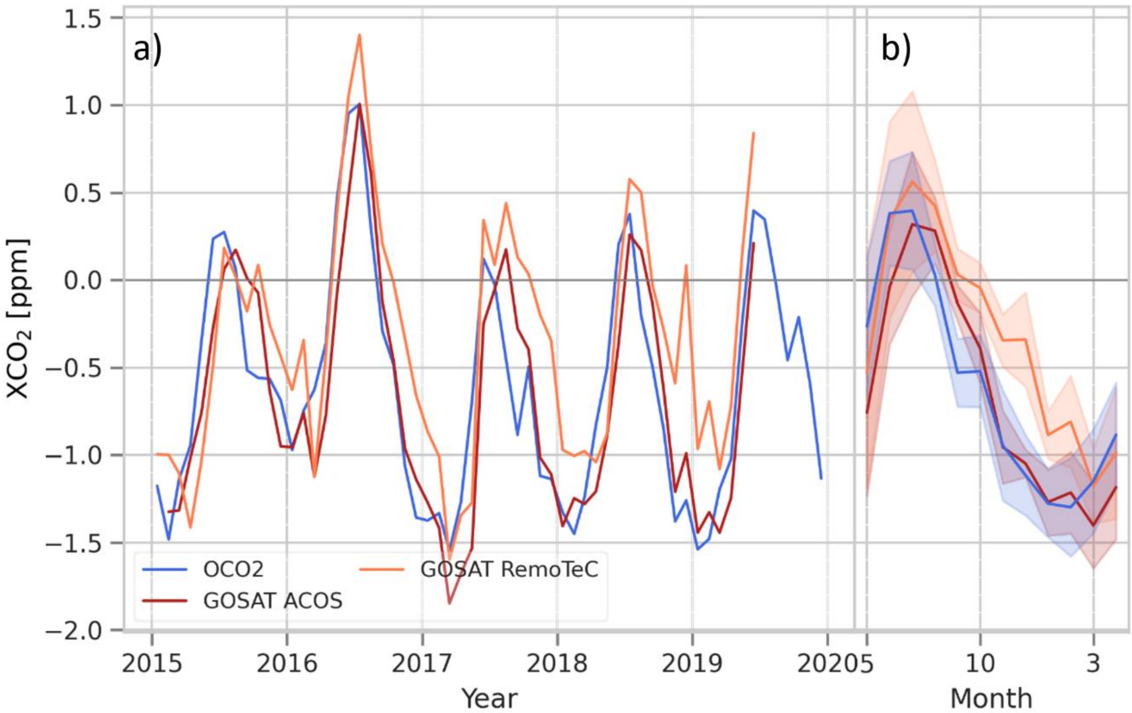

Figure S6: Measured OCO-2 XCO_2 values in SAT region from 2015-2020. Left: Whole time series of monthly mean XCO_2, right: Mean seasonal cycle over 2015-2020.

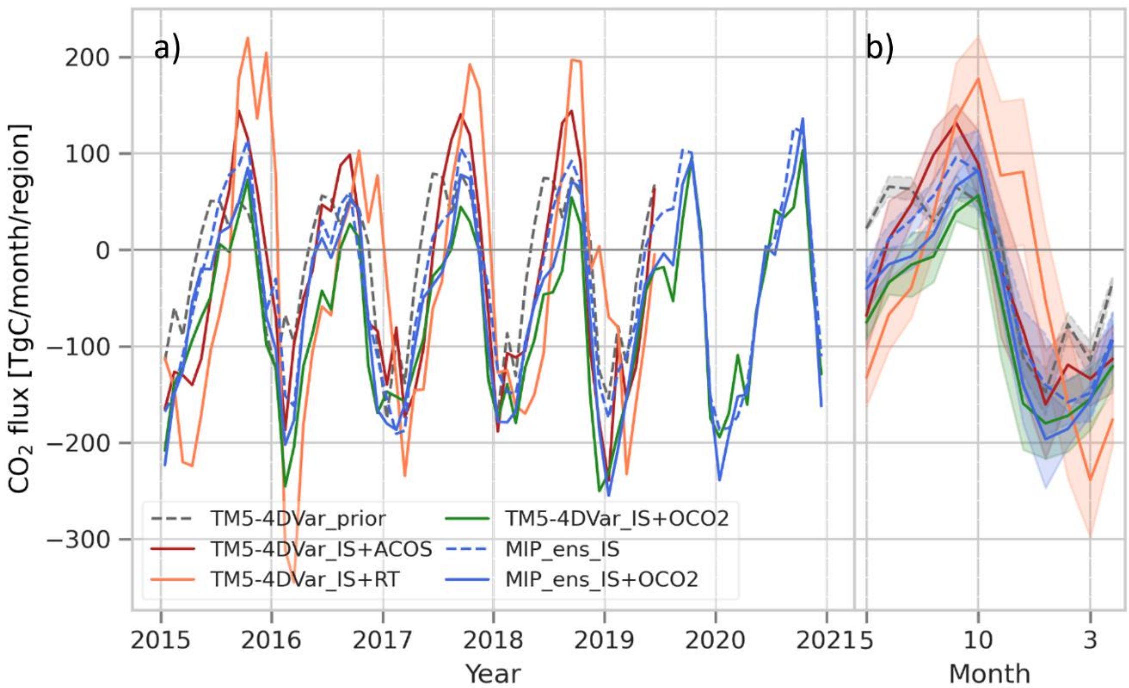

Figure S7: CO_2 fluxes in SAT region using different data sets for assimilation. Left: Time series. Right: Mean seasonal cycle (mean from 2015 to 2020).

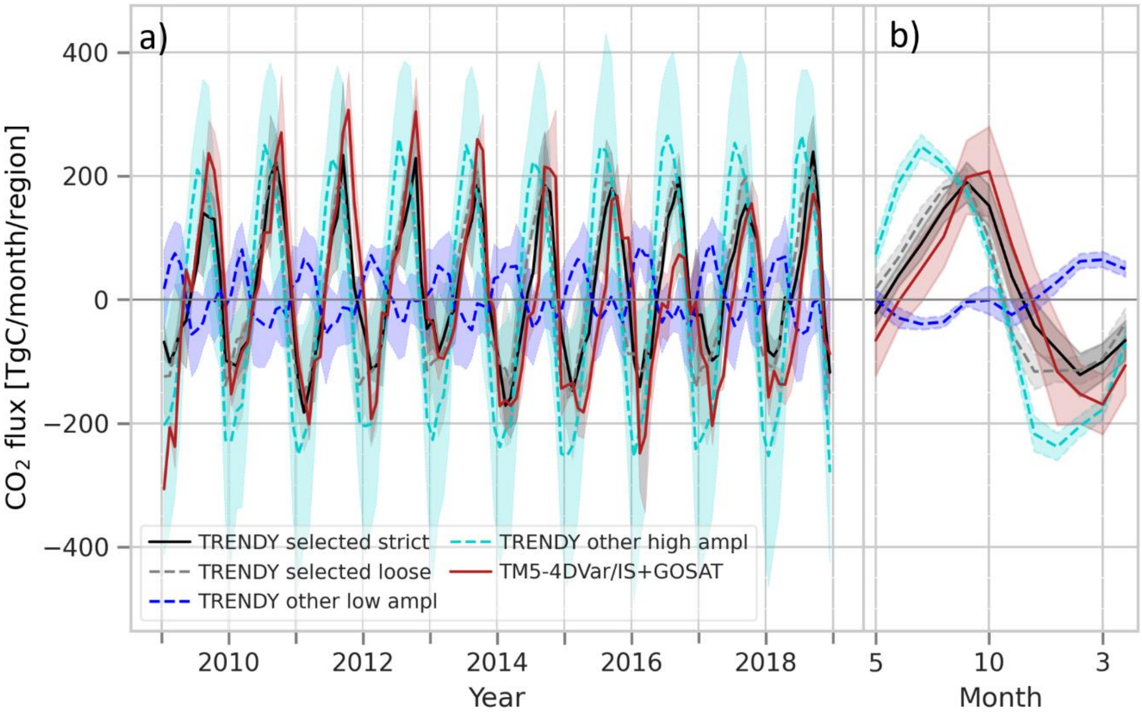

Figure S8: NBP in the SAT region as seen by the four TRENDY model groups compared to the TM5-4DVAR/IS+GOSAT flux. Panel (a) shows the entire time period. The shading of the TRENDY groups illustrates the standard deviation between the models of a group. The shading of TMs-4DVAR/IS+GOSAT shows the spread of TM5-4DVAR/IS+ACOS and TM5-4DVAR/IS+RT. Panel (b) shows the mean seasonal cycle. Here, the shading indicates the standard deviation over the years.

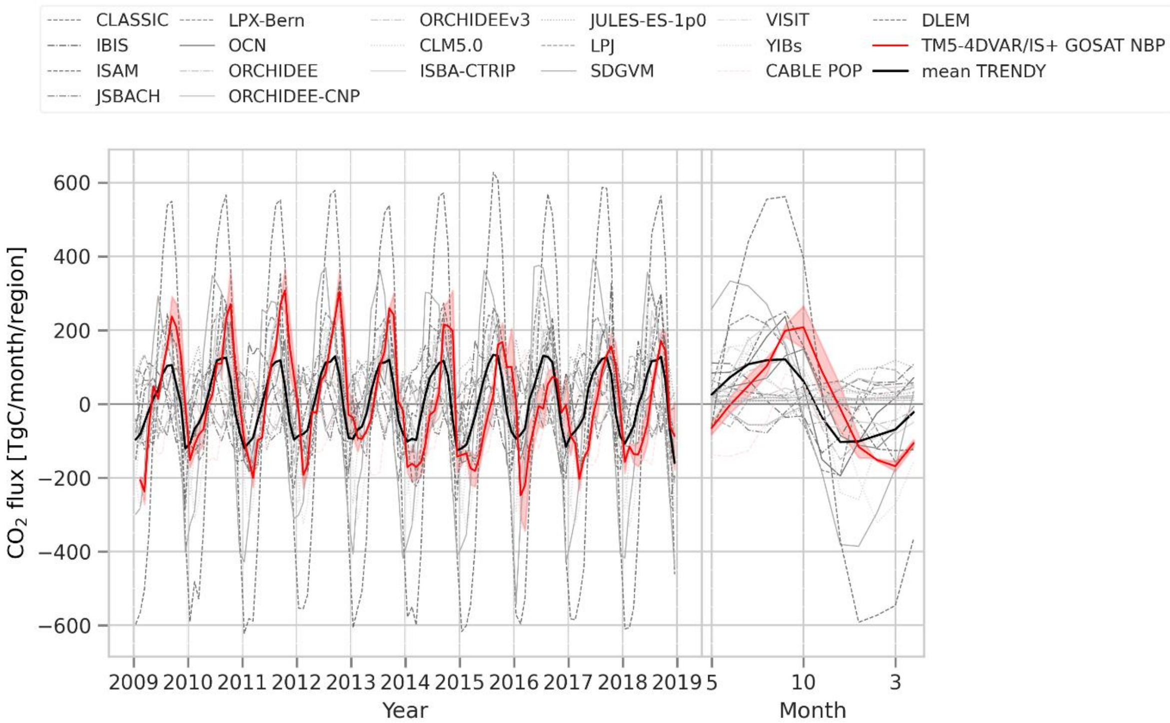

Figure S9: Total TM5/4DVAR/IS+GOSAT NBP flux (red) compared to the NBP of the TRENDY models (gray). Note that some of the TRENDY models account for fire fluxes, while others do not (see Table S1).

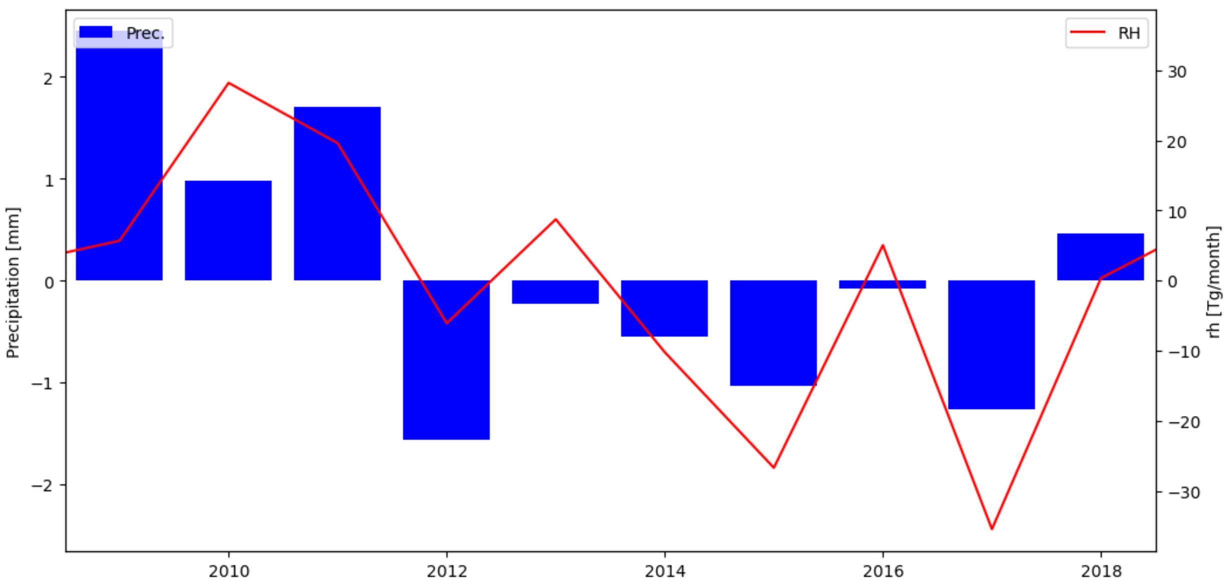

Figure S10: For the month of October (which is the onset month of precipitation after the dry season), we plot the precipitation and soil respiration anomalies, so the difference to the long-term (2009-2018) October mean in the arid east region.

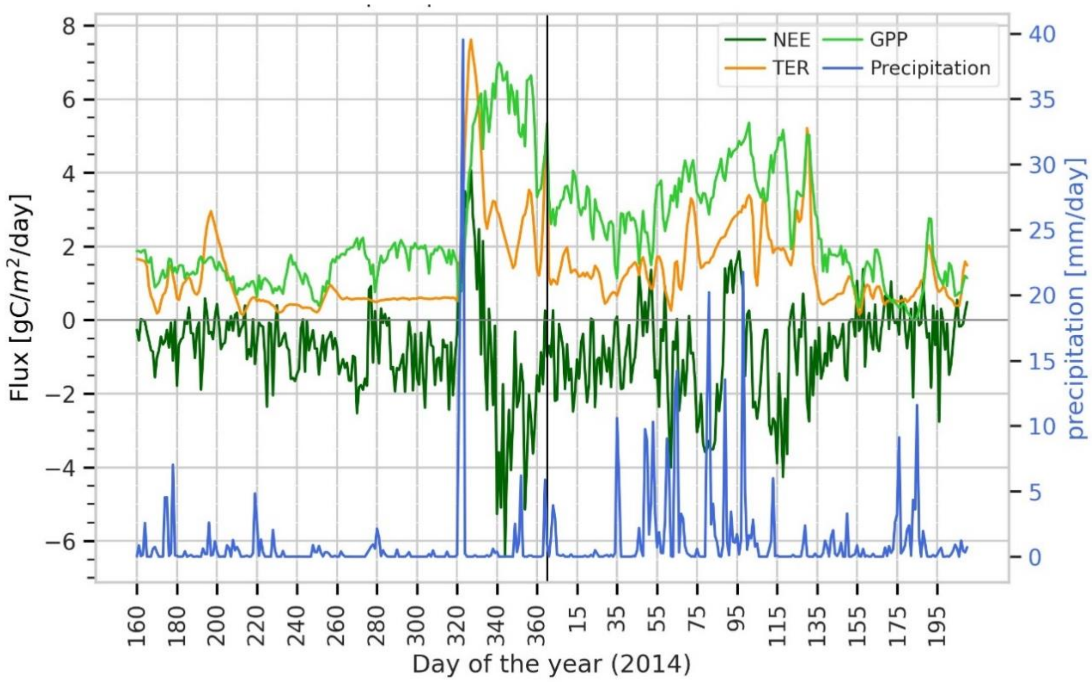

Figure S11: NEE (dark green) measured from 2014 to 2015 of the FLUXNET BR-CST station and precipitation (blue). TER (nighttime NEE) and GPP as provided in the FLUXNET data set are given in orange and light green, respectively. The time series starts on the 160th day of the year 2014 (9th of June) and ends on day 210 in year 2015 (29th of July). The black vertical line indicates the start of 2015.

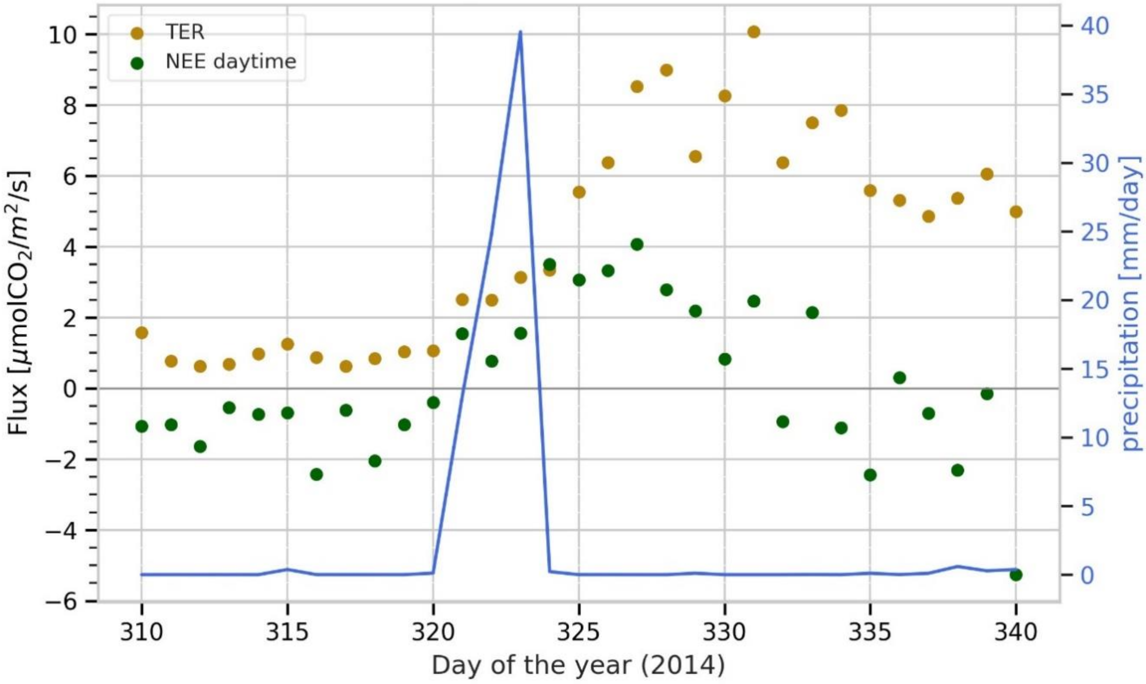

Figure S12: Mean of half-hourly nighttime NEE (= TER) (yellow) and daytime NEE (green) and the daily precipitation from the BR-CST AmeriFlux station of days 310 to 340 in 2014.

Table S1. TRENDYv9 DGVMs and their references and characteristics. S3 model runs were used for all models.

Model and reference number	Cable-pop [1]	Classic [2]	CLM5 [3]	DLME [4]	IBIS [5]	ISAM [6]	ISBA [7]	JSBACH [8]	JULES.ES.10 [9]	LPX.Bern [10]	LPJ [11]	OCN [12]	ORCHIDEE [13]	ORCHIDEE.CNP [14]	ORCHIDEEv3 [15]	SDGVM [16]	VISIT [17]	YIBs [18]
Selected	No	Yes	No	No	No	No	No	No	No	No	No	Yes	No	No	No	No	No	No
Original Resolution	1x1	2.185x2.185	1.25x0.9375	0.5x0.5	1x1	0.5x0.5	1x1	1.875x1.875	1.875x1.25	0.5x0.5	0.5x0.5	1x1	0.5x0.5	2x2	0.5x0.5	1x1	0.5x0.5	1x1
Fire	No	Yes	Yes	No	No	No	Yes	Yes	No	Yes	Yes	No	No	No	No	Yes	Yes	No
Harvest (wood + crops)	No	No	Yes	No	No	No	Yes	Yes	Yes	No	No	No	Yes:	Yes	No	No	No	No
Grazing	No	No	No	No	No	No	No	Yes	No	No	No	No	No	No	No	No	No	No
FLUC	No	Yes	Yes	No	No	Yes	Yes	Yes	Yes	No	No	Yes	Yes	Yes	Yes	Yes	Yes	Yes

[1]. V. Haverd, B. Smith, L. Nieradzik, P. R. Briggs, W. Woodgate, C. M. Trudinger, J. G. Canadell, M. Cuntz, A new version of the CABLE land surface model (Subversion revision r4601) incorporating land use and land cover change, woody vegetation demography, and a novel optimisation-based approach to plant coordination of photosynthesis. Geosci. Model Dev. 11, 2995–3026 (2018). doi:10.5194/gmd-11-2995-2018

[2] J. R. Melton, V. K. Arora, E. Wisernig-Cojoc, C. Seiler, M. Fortier, E. Chan, L. Teckentrup, CLASSIC v1.0: the open-source community successor to the Canadian Land Surface Scheme (CLASS) and the Canadian Terrestrial Ecosystem Model (CTEM) – Part 1: Model framework and site-level performance. Geosci. Model Dev.13, 2825–2850 (2020).

[3] D. M. Lawrence, R. A. Fisher, C. D. Koven, K. W. Oleson, S. C. Swenson, G. Bonan, N. Collier, B. Ghimire, L. van Kampenhout, D. Kennedy, E. Kluzek, P. J. Lawrence, F. Li, H. Li, D. Lombardozzi, W. J. Riley, W. J. Sacks, M. Shi, M. Vertenstein, W. R. Wieder, C. Xu, A. A. Ali, A. M. Badger, G. Bisht, M. van den Broeke, M. A. Brunke, S. P. Burns, J. Buzan, M. Clark, A. Craig, K. Dahlin, B. Drewniak, J. B. Fisher, M. Flanner, A. M. Fox, P. Gentine, F. Hoffman, G. Keppel-Aleks, R. Knox, S. Kumar, J. Lenaerts, L. R. Leung, W. H. Lipscomb, Y. Lu, A. Pandey, J. D. Pelletier, J. Perket, J. T. Randerson, D. M. Ricciuto, B. M. Sanderson, A. Slater, Z. M. Subin, J. Tang, R. Q. Thomas, M. Val Martin, X. Zeng, The Community Land Model Version 5: Description of new features, benchmarking, and impact of forcing uncertainty. J. Adv. Model. Earth Syst. 11, 4245–4287 (2019). doi:10.1029/2018MS001583

[4] H. Tian, G. Chen, C. Lu, X. Xu, D. J. Hayes, W. Ren, S. Pan, D. N. Huntzinger, S. C. Wofsy, North American terrestrial CO2 uptake largely offset by CH4 and N2O emissions: Toward a full accounting of the greenhouse gas budget. Clim. Change 129, 413–426 (2015). doi:10.1007/s10584-014-1072-9 Medline

[5] W. Yuan, D. Liu, W. Dong, S. Liu, G. Zhou, G. Yu, T. Zhao, J. Feng, Z. Ma, J. Chen, Y. Chen, S. Chen, S. Han, J. Huang, L. Li, H. Liu, S. Liu, M. Ma, Y. Wang, J. Xia, W. Xu, Q. Zhang, X. Zhao, L. Zhao, Multiyear precipitation reduction strongly decreases carbon uptake over northern China. J. Geophys. Res. Biogeosci. 119, 881–896 (2014). doi:10.1002/2014JG002608

[6] P. Meiyappan, A. K. Jain, J. I. House, Increased influence of nitrogen limitation on CO2 emissions from future land use and land use change. Global Biogeochem. Cycles 29, 1524–1548 (2015). doi:10.1002/2015GB005086

[7] C. Delire, R. Séférian, B. Decharme, R. Alkama, J.-C. Calvet, D. Carrer, A.-L. Gibelin, E. Joetzjer, X. Morel, M. Rocher, D. Tzanos, The global land carbon cycle simulated with ISBA-CTRIP: Improvements over the last decade. J. Adv. Model. Earth Syst. 12, e2019MS001886 (2020). doi:10.1029/2019MS001886

[8] C. H. Reick, V. Gayler, D. Goll, S. Hagemann, M. Heidkamp, J. E. M. S. Nabel, T. Raddatz, E. Roeckner, R. Schnur, S. Wilkenskjeld, "JSBACH 3 - The land component of the MPI Earth System Model: documentation of version 3.2" (MPI für Meteorologie, 2021); https://doi.org/10.17617/2.3279802.

[9] A. A. Sellar, C. G. Jones, J. P. Mulcahy, Y. Tang, A. Yool, A. Wiltshire, F. M. O'connor, M. Stringer, R. Hill, J. Palmieri, S. Woodward, L. Mora, T. Kuhlbrodt, S. T. Rumbold, D. I. Kelley, R. Ellis, C. E. Johnson, J. Walton, N. L. Abraham, M. B. Andrews, T. Andrews, A. T. Archibald, S. Berthou, E. Burke, E. Blockley, K. Carslaw, M. Dalvi, J. Edwards, G. A. Folberth, N. Gedney, P. T. Griffiths, A. B. Harper, M. A. Hendry, A. J. Hewitt, B. Johnson, A. Jones, C. D. Jones, J. Keeble, S. Liddicoat, O. Morgenstern, R. J. Parker, V. Predoi, E. Robertson, A. Siahaan, R. S. Smith, R. Swaminathan, M. T. Woodhouse, G. Zeng, M. Zerroukat, UKESM1: Description and evaluation of the UK Earth System Model. J. Adv. Model. Earth Syst. 11, 4513–4558 (2019). doi:10.1029/2019MS001739

[10] S. Lienert, F. Joos, A Bayesian ensemble data assimilation to constrain model parameters and land-use carbon emissions. Biogeosciences 15, 2909–2930 (2018). doi:10.5194/bg-15-2909-2018

[11] B. Poulter, P. Ciais, E. Hodson, H. Lischke, F. Maignan, S. Plummer, N. E. Zimmermann, Plant functional type mapping for earth system models. Geosci. Model Dev. 4, 993–1010 (2011). doi:10.5194/gmd-4-993-2011

[12] S. Zaehle, A. D. Friend, P. Friedlingstein, F. Dentener, P. Peylin, M. Schulz, Carbon and nitrogen cycle dynamics in the O-CN land surface model: 2. Role of the nitrogen cycle in the historical terrestrial carbon balance. Global Biogeochem. Cycles24, GB1006 (2010).

[13] G. Krinner, N. Viovy, N. de Noblet-Ducoudré, J. Ogée, J. Polcher, P. Friedlingstein, P. Ciais, S. Sitch, I. C. Prentice, A dynamic global vegetation model for studies of the coupled atmosphere-biosphere system. Global Biogeochem. Cycles 19, GB1015 (2005). doi:10.1029/2003GB002199

[14] D. S. Goll, E. Joetzjer, M. Huang, P. Ciais, Low Phosphorus Availability Decreases Susceptibility of Tropical Primary Productivity to Droughts. Geophys. Res. Lett. 45, 8231–8240 (2018). doi:10.1029/2018GL077736

[15] N. Vuichard, P. Messina, S. Luyssaert, B. Guenet, S. Zaehle, J. Ghattas, V. Bastrikov, P. Peylin, Accounting for carbon and nitrogen interactions in the global terrestrial ecosystem model ORCHIDEE (trunk version, rev 4999): Multi-scale evaluation of gross primary production. Geosci. Model Dev. 12, 4751–4779 (2019). doi:10.5194/gmd-12-4751-2019

[16]. A. P. Walker, T. Quaife, P. M. van Bodegom, M. G. De Kauwe, T. F. Keenan, J. Joiner, M. R. Lomas, N. MacBean, C. Xu, X. Yang, F. I. Woodward, The impact of alternative trait-scaling hypotheses for the maximum photosynthetic carboxylation rate (Vcmax) on global gross primary production. New Phytol. 215, 1370–1386 (2017). doi:10.1111/nph.14623 Medline

[17] E. Kato, T. Kinoshita, A. Ito, M. Kawamiya, Y. Yamagata, Evaluation of spatially explicit emission scenario of land-use change and biomass burning using a process-based biogeochemical model. J. Land Use Sci. 8, 104–122 (2013). doi:10.1080/1747423X.2011.628705

[18] X. Yue, N. Unger, The Yale Interactive terrestrial Biosphere model version 1.0: Description, evaluation and implementation into NASA GISS ModelE2. Geosci. Model Dev.8, 2399–2417 (2015).

Text S1. South American Temperate region

South America has large dry areas (i.e. hyper-arid, arid, semi-arid and dry sub-humid regions as defined by the United Nations Environment Programme World Conservation Monitoring Centre (UNEP-WCMC)) representing about 30% of the continent's total area and 9% of the global drylands (Mitsugi, 2019) – most of which are located in the SAT region. The SAT region as defined by the TRANSCOM-3 experiment (colored in Fig. S1) spans from south of the Amazon rainforest in the northern part down to Patagonia, encompassing a diverse array of climatic zones (Cherlet et al., 2018). The region consists of arid/semi-arid areas in the north-east and in the mountainous west and humid areas in the center (see Fig. S1). As a threshold for arid regions, we use a mean monthly precipitation rate of 1 mm/day/grid cell for at least four consecutive months. We choose this threshold such that we assure dry soils for several months in the arid regions. These drought conditions are required to observe effects such as the Birch effect (Metz et al., 2023). Applying this threshold divides the SAT region into two approximately equally sized parts. As the arid region is divided by the humid region in the middle, we further differentiate the arid region into east and west. While the east arid region is dominated by savannas and croplands, the western region is mostly covered by shrublands and bare soil due to high altitudes (see Fig. S2). Gross fluxes from the SAT area are aggregated on a 1°x1° grid before applying the TRANSCOM region mask. As the land-ocean masks among the TRENDY models differ, the mean flux is in units $\mu gCO2m^{-2}s^{-1}$, then multiplied by the SAT region area to obtain total fluxes and converted to TgC/month/region. Region refers to entire SAT region, humid, arid, arid east or arid west region.

Text S2. GOSAT

S.2.1. GOSAT XCO_2

Column-average dry-air mole fractions of CO_2 (XCO_2) are retrieved from GOSAT measurements from 2009 to 2018 using two different retrieval algorithms: RemoTeC radiative transfer and retrieval algorithm v.2.4.0 (Butz et al., 2011; Butz et al., 2022) as well as the NASA Atmospheric CO_2 Observations from Space (ACOS) algorithm v.9 (Taylor et al., 2022). Only measurements of good quality flag were used (e.g. xco2_quality_flag = 0 for ACOS). The provided data is already bias-corrected by comparing it to the Total Carbon Column Observing Network (TCCON) and deriving global correction factors. The ACOS retrieval keeps considerably more measurements than RemoTeC (roughly factor 2), especially over the Tropics and along the Andes mountains. This is due to stricter filter criteria applied by the RemoTeC algorithm. Concentrations are averaged and aggregated over a month over the whole region.

To analyze the regional XCO_2 enhancements, we remove the general increase of CO_2 concentrations in the atmosphere by detrending the concentration data with the annual mean CO_2 growth rates reported by the National Oceanic and Atmospheric Administration (NOAA) based on globally averaged marine surface data as described in Metz et al. (2023). The detrended XCO_2 measurements (Fig. S3) from RemoTeC show a clear decrease in 2014, but the amplitude remains approximately constant at 1.7 ppm. The ACOS retrieval shows a similar behavior and shift, but the amplitude reduces after the shift in 2014 from 2.2 ppm to 1.7 ppm. The origin of the shift is unclear due to lack of available reference data during this time period. It therefore remains an open question whether the shift is due to technical changes made during this period or if it has a biophysical origin.
XCO_2 measurements by GOSAT show a clear mean seasonal cycle reaching the highest XCO_2 values in July to August and lowest XCO_2 values in February to March (see Fig. S3). Both retrieval algorithms see the same seasonal pattern, but ACOS retrieves slightly lower XCO_2 enhancements compared to RemoTeC from September to February.

S.2.2 Sampling effect

Differences in the XCO_2 values between data products partly stem from the differences in the spatial coverage of the data over the SAT region. These differences are mainly caused by differences in filter criteria applied when using the two different algorithms ACOS and RemoTeC. To analyze the effect of sampling, we co-sample the forward transported fluxes to RemoTeC soundings (Fig. S4). One can see that TM5-4DVAR/IS+ACOS and TM5-4DVAR/IS+RemoTeC closely follow each other and show the same seasonal cycle. Therefore, differences in XCO_2 (Fig. S3) are mainly due to sampling effects. Both co-sampled satellite retrievals deviate substantially from the prior and the in situ based TM5-4DVAR XCO_2 concentration showing the added value of the satellite measurements for optimizing the CO_2

fluxes. These differences are expected as the coverage of in situ data is poor in the SAT region. This also leads to TM5-4DVAR/IS closely following the prior.

S.2.3. GOSAT fluxes

S.2.3.1 Comparison of CO_2 fluxes between ACOS and RemoTeC

To obtain fluxes, we assimilate observation data using TM5-4DVAR following Sect. 2.3. For both retrievals, individual fluxes over the SAT region are obtained. While we use the mean in the main manuscript, we here also discuss differences between fluxes from both retrieval algorithms. The flux maxima between the two retrievals (TM5-4DVAR/IS+RT and TM5-4DVAR/IS+ACOS) are slightly shifted by one month and the magnitude of fluxes differs by about 60 TgC/month/region (Fig. S5). Both retrievals have a similar shape and show larger maxima than the prior and the TM5-4DVAR/IS. For the minimum fluxes, the two TM5-4DVar/GOSAT setups agree better in magnitude, also better than the agreement to the TM5-4DVAR/IS setup but show slight differences in their shape. TM5-4DVAR/IS+RT fluxes exhibit a more distinct minimum than TM5-4DVAR/IS+ACOS. The general shape of both products is similar and deviates from TM5-4DVAR/IS in terms of amplitude.

S.2.3.2 Comparison between TM5-4DVAR CO_2 fluxes and prior

Consistently among TM5-4DVAR/IS and TM5-4DVAR/IS+GOSAT, the maxima of the estimated fluxes occur in September or October while the minima occur between January and March (Fig. S5). While the timing of the seasonal cycle coincides between the two inversions, there exist differences in the magnitude of the peaks (carbon release) and dips (carbon uptake) although differences are not as large as for the TRENDY models.

When assimilating the in situ data only (TM5-4DVAR/IS) the inversion estimates larger dips at the end of each year compared to the dips in the prior fluxes. When additionally assimilating GOSAT data, these dips become much less pronounced, but at the same time the peaks increase relative to TM5-4DVAR/IS and the prior. The large impact the additional assimilation of GOSAT XCO_2 has on the flux estimates suggests that, due to their sparseness, the in situ data alone have limited information about SAT fluxes.

The flux magnitude shows different interannual variations (Fig. S5). In particular, the TM5-4DVAR/IS+GOSAT inversion shows a shift in the year 2014. This shift is also present in the observed XCO_2 values over the SAT region, which are significantly lower after 2015 than before (see Fig. S3 und S4). While mean annual TM5-4DVAR/IS+GOSAT fluxes are positive from 2010 to 2013, they become negative thereafter suggesting a shift from a carbon source to a carbon sink. This behavior is not captured by TM5-4DVAR/IS fluxes (see Fig. S5). Due to lack of additional data constraints, the reason for this shift remains unclear. In this study, we focus our investigation on the mean seasonal cycle rather than on the interannual variability.

Text S3. OCO-2

S3.1. OCO-2 XCO_2

The Orbiting Carbon Observatory-2 (OCO-2) satellite is in orbit since 2014 and provides XCO_2 data with high resolution (<3km^2). OCO-2 measures in the NADIR and GLINT viewing geometries. The ACOS retrieval (v10) is used to retrieve XCO_2 data from measured spectra.
When comparing XCO_2 measurements from GOSAT and OCO-2 for the years 2015-2018, one finds a generally good agreement between both satellites – especially with respect to the shape of the XCO_2 enhancements and the timing of the peaks (see Fig. S6). The timing of the maximum and minimum XCO_2 coincides. OCO-2 has a slightly faster decrease in the CO_2 concentration after reaching its maximum, especially compared to GOSAT-RemoTeC. However, differences between GOSAT-RemoTeC and GOSAT-ACOS, which were shown to mainly originate from sampling errors, exceed differences between both satellites using the same ACOS retrieval.

S3.2 OCO-2 CO_2 fluxes

Within the Model Intercomparison Project (MIP) global OCO-2 measurements were assimilated for 14 different global flux inversion models (Byrne et al., 2023) and an ensemble mean was computed. Comparing the CO_2 fluxes from OCO-2 and GOSAT for the years 2015-2018 it becomes apparent that maximum and minimum in CO_2 fluxes align well (Fig. S7). The principal shape of the seasonal cycle is the same reinforcing the net seasonal cycle of the SAT region with maxima in August to October and minima from January to March. However, the MIP ensemble using OCO-2 and in situ measurements retrieves fluxes with a slightly smaller amplitude than the GOSAT-retrieved fluxes in close agreement to the MIP ensemble using in situ data only.

Text S.4. Local flux tower measurements

While the TM5-4DVAR CO_2 fluxes provide a regional estimate of the carbon dynamics in the SAT region, flux towers can provide an understanding of the local gross fluxes leading to the net effect and can help localize and understand the origin of the net flux. For now, only one flux tower station is available for a short time period (2014-2015) in the semi-arid region of the SAT region. The station is BR-CST Caatinga Serra Talhada station (Antonino, 2022). It is part of the FLUXNET towers within the AmeriFlux network. The station is located at 7.968 °E, 38.384 °S at an altitude of 468m above sea level in a seasonal tropical dry forest (Caatinga) in the semi-arid region of Brazil. The measured net flux can be further portioned into GPP and TER assuming that nighttime respiration can be interpolated into the day under consideration of temperature changes. The whole time series of net carbon fluxes is shown in Fig. S11. We find one heavy rain event following a period of low precipitation. This event was in November 2014 (Day 321-323), on which precipitation reached 40 mm/day.

Fig. S12 shows the precipitation event on days 321-323, which was followed by a direct response of increasing NEE as soon as the first precipitation occurs. As there is no photosynthesis occurring at night, NEE at night corresponds to a pure respiration signal and can be interpolated to the entire day. Daytime NEE gives the net ecosystem exchange balancing photosynthesis and respiration. One can see that the precipitation event triggers an immediate increase in respiration (NEE nighttime) leading to a positive NEE (daytime). While respiration remains high in the consecutive days, the NEE (daytime) decreases and reaches its original value about a week after the rainfall event. A further partitioning between autotrophic and heterotrophic respiration is not possible and would require additional soil chamber measurements.

While the station is not representative of the entire arid SAT region, the local observations strengthen the assertion that the regional scale net flux could indeed be attributed to local responses of respiration to rain pulses after dry periods as suggested by the DGVMs. This might indeed explain the large CO_2 peaks in September retrieved in flux inversions over the SAT region.

Text S5. Selected DGVMs: CLASSIC and OCN

In the CLASSIC model, both respiration and GPP are influenced by soil moisture. Soil respiration is categorized into two components: litter respiration, which is driven by moisture near the soil surface, and soil carbon respiration, which is driven by moisture deeper in the soil. GPP is regulated by soil moisture within the rooting zone. Consequently, litter respiration is immediately activated following precipitation events, whereas GPP increases delayed as the precipitation percolates into the deeper soil layers.

In the OCN model, GPP for grasses and rain-green plant functional types is contingent on surpassing a critical soil moisture threshold. For GPP to significantly increase, a sufficiently high leaf area index (LAI) must develop, which is driven by the available daily carbon. Both the requirement for soil moisture to accumulate after the onset of the rainy season and the allocation of carbon from below ground result in a delayed GPP increase. Concurrently, as GPP begins to rise, plant respiration is activated. Soil respiration is influenced by soil moisture throughout the entire soil profile, especially in the upper layers. Because of its sensitivity to moisture in the upper soil layers, soil respiration can increase rapidly following precipitation events.

2.5. Publication 4: Responses of Terrestrial Ecosystem Respiration to Soil Moisture Across Australia's Aridity Regimes

Eva-Marie Metz, Sanam N. Vardag, Andrew F. Feldman, Benjamin Poulter, Thomas Colligan, Brenden J. Fischer-Femal, André Butz

Submitted to *Environmental Research Letters*

Responses of Terrestrial Ecosystem Respiration to Soil Moisture Across Australia's Aridity Regimes

Eva-Marie Metz[1], Sanam N. Vardag[1,2], Andrew F. Feldman[3,4], Benjamin Poulter[3], Thomas Colligan[3,4], Brenden J. Fischer-Femal[3], André Butz[1,2,5]

[1]Institute of Environmental Physics, Heidelberg University, Heidelberg, Germany
[2]Heidelberg Center for the Environment (HCE), Heidelberg University, Heidelberg, Germany
[3]Biospheric Sciences Laboratory, NASA Goddard Space Flight Center, Greenbelt, Maryland, USA
[4]Earth System Science Interdisciplinary Center, University of Maryland, College Park, Maryland, USA
[5]Interdisciplinary Center for Scientific Computing, Heidelberg University, Heidelberg, Germany

Abstract

The terrestrial biosphere is the largest net sink of global CO_2, but its sink capacity varies considerably from year to year depending on environmental conditions. Recent work has highlighted the importance of semi-arid ecosystems in interannually varying global concentrations of atmospheric CO_2. We therefore need to better understand the dynamics and drivers of the CO_2 fluxes and their modelling along semi-arid to humid gradients. Respiration is an even more uncertain flux compared to photosynthetic fluxes and its spatially variability is not well understood. Here we focus on terrestrial ecosystem respiration (TER) in Australia, and, specifically, on disentangling the impacts of temperature and soil water on TER.

We use nighttime net ecosystem exchange (NEE) data as a viable proxy for daily TER collected by 40 flux tower stations within the OzFlux network over the last 20 years in Australia. These stations cover a broad range of climatic conditions enabling us to analyze the dependence of TER on soil moisture under varying aridity and temperature conditions. We find that the sensitivity of TER to soil moisture is the strongest in semi-arid regions. In these dry locations, the TER sensitivity to soil moisture increases strongly with temperature. Soil respiration fluxes at humid stations are large but exhibit low sensitivity to high soil moisture levels indicating that TER at humid stations is not water-limited. Using the dynamic global vegetation model LPJ, we show that common model approaches assuming increasing TER with increasing soil moisture for all soil moisture levels perform poorly in reproducing the observed TER patterns in Australia due to interactions with carbon availability and representation of soil hydrology. Hence a more sophisticated description of

the dependence of TER on soil moisture is necessary to capture TER dynamics under different climatic conditions accurately.

1. Introduction

Terrestrial ecosystems partly mitigate climate change by taking up around one third of anthropogenic CO_2 emissions (Friedlingstein *et al* 2025). The net uptake of CO_2 into the ecosystems is a balance of two gross CO_2 fluxes: The uptake of CO_2 by gross primary production (GPP) through photosynthesis and the release of carbon by terrestrial ecosystem respiration (TER) and fluxes due to disturbances like wildfires (Keenan and Williams, 2018). TER partly offsets GPP leading to a net uptake of CO_2 into the ecosystems. However, since TER and GPP fluxes are similar in magnitude, the net uptake is only a few percent of the TER fluxes (Friedlingstein *et al* 2025). Hence, even small changes in GPP or TER can have a major impact on the net terrestrial carbon sink. It is therefore crucial to understand the dynamics and drivers of these gross fluxes as well as their sensitivity to environmental parameters to be able to accurately predict the net CO_2 exchange between biosphere and atmosphere under a changing climate. While there exist vegetation proxies for GPP, such as solar-induced fluorescence (Frankenberg *et al* 2011), the normalized difference vegetation index (e.g., Zhou *et al* 2001) and the enhanced vegetation index (e.g., Shi *et al* 2017), there is no such proxy for TER. This hampers the analysis of TER on global and regional scale and calls for bottom-up TER simulations. Accurate TER simulations of present and future conditions require a good understanding and an adequate implementation of the sensitivity of TER to environmental conditions.

Temperature has a direct effect on TER by the kinetics of microbially linked enzymatic reactions being temperature dependent (Davidson *et al* 2006, Bond-Lamberty *et al* 2024). This temperature dependence is often referred to as intrinsic temperature sensitivity and described by the Q_{10} law and the Arrhenius formula (Davidson and Janssens, 2006, Tjoelker *et al* 2001). However, ecosystem respiration is not only driven by temperature but is also largely impacted by other changing environmental conditions, such as vegetation growth, the amount of root and microbial biomass, substrate supply, and desiccation stress (Davidson *et al* 2006, Unger *et al* 2012, Moyano *et al* 2013). These additional environmental impacts cause the apparent temperature sensitivity to differ from the intrinsic temperature sensitivity and lead to TER dynamics which cannot be explained by temperature variability alone. Precipitation and soil moisture thus have a major impact on TER, especially in dry environments (Moyano *et al* 2013). Reduced soil water can impose desiccation stress on microbe communities. Furthermore, variability in soil water also impacts supply and transport of substrate and oxygen conditions in the soil. Therefore, soil water can heavily reduce the rate of respiration compared to what would be theoretically possible given the ambient temperatures (Davidson *et al* 2006, Lellei-Kovacs *et al* 2011, Moyano *et al* 2013).

The parametrizations of TER dependence on soil water vary considerably among carbon cycle and vegetation models (Sierra *et al* 2015, Tucker and Reed, 2016). Current vegetation models can either output TER as the sum of heterotrophic and autotrophic respiration (Rh and Ra, respectively) or as the individual components. For Rh, for example, models agree on a reduction of respiration at low soil moisture levels, but they have parameterizations with considerably different functional dependencies (Sierra *et al* 2015). Furthermore, the models differ significantly in how Rh varies with high soil moisture. While some models assume a linear relationship for all soil moisture levels (Sierra *et al* 2015), others assume saturation (Sierra *et al* 2015, Sitch *et al* 2015) or declining sensitivities for high soil moistures (Sierra *et al* 2015, e.g., Melton *et al* 2015, Trudinger *et al* 2016, Haverd *et al* 2018). This leads to large uncertainties in TER carbon flux estimates.

Dryland regions cover about 40% of the global land surface (Wang *et al* 2022). It is known that semi-arid ecosystems have a substantial impact on the global terrestrial carbon sink (Poulter *et al* 2014, Ahlström *et al* 2015). As drought conditions can limit soil respiration, soil moisture dynamics can be a major source of TER variability in semi-arid or arid environments (MacBean *et al* 2021, Metz *et al* 2023). The importance of semi-arid regions for the global scale carbon cycle and the enhanced impact of soil water on TER under dry conditions emphasizes the need for an improved understanding of the TER – soil moisture relationship in these environments.

Here, we ask: How does the TER sensitivity to soil moisture vary across a range of aridity conditions and temperatures in Australia? To this end, we use eddy covariance data provided by the OzFlux network (Beringer *et al* 2022). We use daily-averaged nighttime net ecosystem exchange (NEE), temperature and soil moisture measurements of 40 flux towers collected over the past 20 years. The OzFlux stations are located in diverse regions of Australia to enable addressing our question (Beringer *et al* 2022). The dataset enables us to analyze the dependence of TER on soil moisture under varying aridity conditions and temperatures. In a second step we apply the analysis to modelled TER data using the Lund-Potsdam-Jena Earth Observation SIMulator (LPJ-EOSIM) vegetation model (Sitch *et al* 2003, Poulter *et al* 2011, Fischer-Femal *et al* 2025) to identify existing limitations in TER models and to point out possible improvements for the modelling of TER with respect to its soil moisture dependence under semi-arid conditions.

2. Data and Methods

2.1. The OzFlux network

The OzFlux network (https://www.ozflux.org.au/, Beringer *et al* 2022), established in 2001, comprises over 50 flux tower stations in Australia and New Zealand with 29 stations currently active. In our study we limit the stations used to those located in Australia (figure 1). In total, we use data from 36 stations with four stations reporting two datasets as flux towers are installed at different locations at the same site. A list of stations and their characteristics are given in table A1. In total, the used data sums up to 324 measurement years. The stations cover a broad range of biomes, soil types and climate conditions (Beringer *et al* 2022, OzFlux 2024). The mean annual precipitation amount varies from below 300 mm per year to up to 5700 mm and the recorded temperature ranges (-10°C up to 46°C) are large (OzFlux 2024). This leads to large differences in the mean soil moisture in the upper soil for the different stations as shown in figure 1 and figure A1.

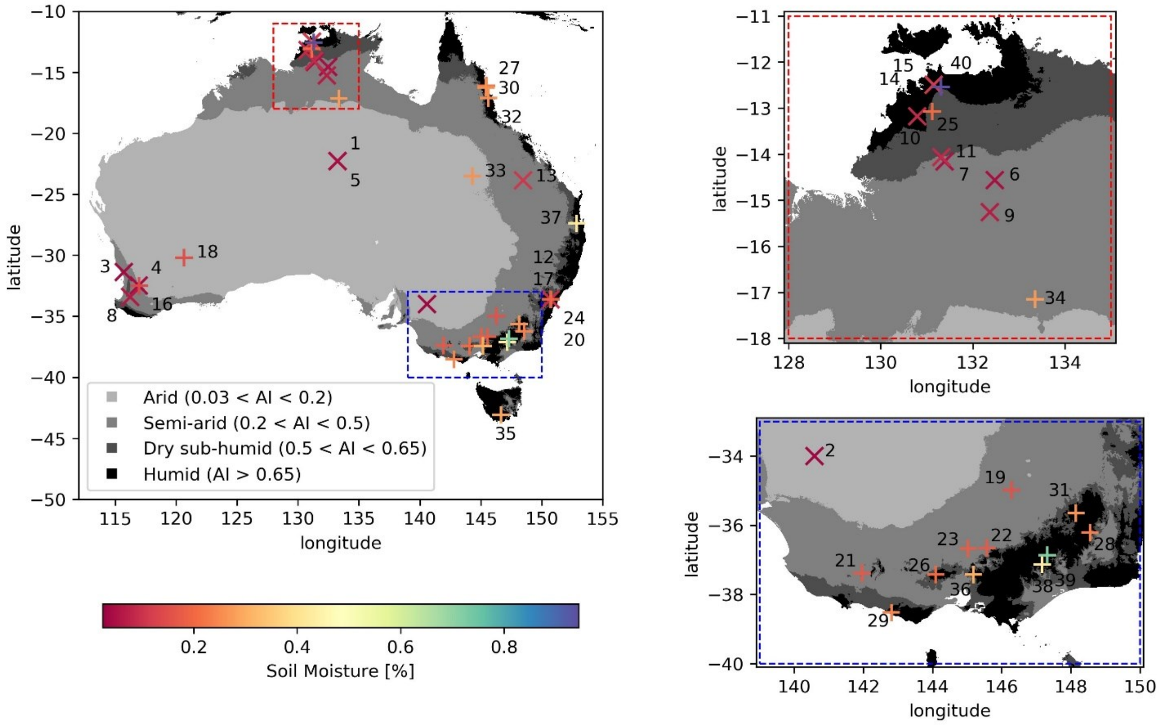

Figure 1: The OzFlux flux towers in Australia cover a broad range of soil moisture conditions. The locations of the used OzFlux stations are shown along with the mean measured soil moisture over the measurement period for the individual stations (color coding). Furthermore, the arid, semi-arid, dry sub-humid and humid regions in Australia based on the Global Aridity Index (AI) and Potential Evapotranspiration (ET0) Climate Database v3 (Zomer and Trabucco 2019, Zomer et al 2022) are given (gray tones). The stations are numbered according to increasing mean soil moisture. Stations classified as dry are displayed with 'x' markers, wet stations are given with upright crosses. The corresponding station names and more information about the OzFlux stations including the individual data reference can be found in table A1.

2.2. Night-time NEE as proxy for TER

We use the half-hourly non-gapfilled, quality filtered L3 data as provided by the OzFlux Data Center (https://data.ozflux.org.au/portal/). Only stations with at least one year of measurements are considered. We make use of the NEE, soil moisture, and soil temperature (Ts) data: we use the surface upward mole flux of carbon dioxide ('Fc' or 'Fco2'), the soil water content in the upper soil layer (depth varies between stations from 5 cm to 10 cm depth) given as volume fraction of condensed water in soil ('Sws'), and the soil temperature ('Ts'), respectively. We only use data which passes the quality filtering (QC = 0) and exclude 1.5 years of unreasonable soil water content data (constant zero values) for the Tri Tree East station. Only half-hourly data points with all three variables (NEE, Sws, and Ts) having valid measurements are kept. Data points with at least one of the three variables missing are discarded. Following other studies (e.g., Mahecha *et al* 2010, Barba *et al* 2018, Pastorello *et al* 2020, and Meng *et al* 2024), we use the nighttime NEE data as estimate for TER, assuming photosynthesis and therefore GPP only taking place under sufficient sunlight. As not all stations provide photosynthetically active or shortwave radiation, we define the nighttime as time with a sun elevation angle (get_altitude function of the python package pysolar.solar) below zero. Doing so, our nighttime definition is more conservative than other studies which use a threshold of 20 W/m² of photosynthetically active radiation (Barba *et al* 2018, Meng *et al* 2024). We calculate daily nighttime NEE averages for all days with at least five nighttime measurements.

2.3. Sensitivity Analyses

We use a linear regression between daily mean values of TER and Sws to determine the sensitivity of TER to soil moisture. We take the calculated slope as a measure for the sensitivity of TER to soil moisture and the coefficient of determination (R^2) as a measure of how much TER is driven by soil moisture alone. To account for the temperature effect on TER, we bin the data in 5°C temperature bins and perform the linear regression on the individual temperature bins. Only temperature bins with at least 100 daily data points are used in the analyses. Figure A2 shows the daily data of the Alice Springs station and the fitted slopes for the different temperature intervals as a typical example for stations with low soil moisture.

2.4. TER and Rh implementation in LPJ

We use the LPJ-EOSIM (hereafter LPJ) dynamic global vegetation model (DGVM) to perform the same sensitivity analyses as for the Ozflux measurements. LPJ is part of the "trends and drivers of the regional-scale sources and sinks of carbon dioxide" (TRENDY, Le Quéré *et al* 2013) intercomparison project. It was found to perform well for monthly carbon fluxes in Australia (Metz *et al* 2023). In Metz *et al* (2023), LPJ was one of the 5 out of 18 TRENDY models which was found to capture main features of the seasonal dynamics in Australia. We run LPJ with the same configuration as in the S3 simulations of TRENDY (Sitch *et al* 2024). We use the same forcing for the increase in CO_2 concentrations, and time-varying land-use change. Instead of the monthly CRU climate dataset as in TRENDY, we take daily MERRA-2 data (Poulter *et al* 2011, Gelaro *et al*

2017) available at 0.5 degree resolution. We use the LPJ simulations of the single gridcells closest to the locations of the OzFlux stations from 1900 to 2023, thereby only selecting the days in which we have quality-filtered data of the corresponding OzFlux station.

LPJ modeled TER is separated into Rh and Ra. Heterotrophic respiration Rh is simulated to be limited by temperature and soil moisture. As described in Sitch *et al* (2003), Rh is driven by decomposition of the soil carbon pools through first order kinetics:

$$Rh = \frac{dC}{dt} = -kC \tag{1}$$

where C is the carbon pool size [gC/m²], dC is the respiration as the amount of carbon emitted by the carbon pool in the chosen time (t) interval (dt) with the decomposition rate k [1/year]. The decomposition rate depends on the turnover times of the carbon pool t_{turn} [years], a functional response $g(T)$ to soil temperature T ([K]), and a functional response $f(swc)$ to soil water content changes (swc):

$$k = t_{turn} * g(T) * f(swc). \tag{2}$$

The response functions are implemented as follows:

$$g(T) = \exp[308.56K * (\frac{1}{56.02K} - \frac{1}{T+227.13K})], \tag{3}$$

which is a modified Arrhenius equation (Lloyd and Taylor 1994) and

$$f(swc) = \left(\frac{1-\exp(-swc)}{1-\exp(-1)}\right). \tag{4}$$

The functional response of Rh in dependence on *swc* is illustrated in figure A3.

Autotrophic respiration Ra is calculated for the individual plant components leaf, sapwood, and roots. For sapwood and roots, Ra is separated into maintenance and growth respiration. Maintenance respiration *Rm* depends on temperature (T_{air} for sapwood, T_{soil} for roots) as given in equation (3), and the carbon C and carbon nitrogen ratios *cn* in living biomass, which is built up by photosynthesis:

$$Rm_x = r * \frac{C_x}{cn_x} ph * g(T). \tag{5}$$

Thereby, x stands for sapwood or roots, r is a reference respiration rate at 10°C, and ph is the phenology status (ph=1 for sapwood). Growth respiration Rg is calculated as a fraction (25%) of modelled GPP minus maintenance respiration:

$$Rg_{roots+sapwood} = 0.25 * \left(GPP - Rm_{roots} - Rm_{sapwood}\right) \tag{6}$$

For leafs, Ra is calculated as fraction b of maximum rate of photosynthesis (A_{max}) following Haxeltine and Prentice (1996):

$$Ra_{leaf} = b * A_{max}$$

Low soil moisture indirectly limits Ra by reducing GPP and by triggering leaf senescence when dropping below a dynamic threshold. More details about photosynthesis and respiration are given in Sitch *et al* (2003) and Haxeltine and Prentice (1996).

The soil water content is implemented as a saturation fraction relative to the soil water holding capacity and wilting point. For posterior sensitivity studies, we converted LPJ's soil water content to volume fraction of condensed water in soil (Sws) as reported by the OzFlux stations.

3. Results and Discussion

3.1. Semi-arid stations show the largest sensitivity of TER to soil moisture

The sensitivity of our estimated TER to soil moisture varies substantially for the individual OzFlux stations and temperature intervals. Figure 2 shows the sensitivities for each station and 5°C interval. We find different response regimes. Stations with a mean soil moisture content of less than 12%, further called ‘dry stations’ show a distinct sensitivity of TER to soil moisture. Most dry stations (12 out of 15) are in arid or semi-arid areas in Australia (see figure 1). We find the highest sensitivities for semi-arid stations. The sensitivities significantly decline with increasing mean soil moisture. For more humid stations (mean soil moisture more than 12%, further called ‘wet stations’), we find low sensitivities of less than 18.9 $\frac{\mu mol}{m^2 s} / \frac{m^3}{m^3}$ (95% interval).

An analysis of variance (ANOVA) test (python scipy.stats.f_oneway) confirms that the sensitivities in the two regimes (dry stations and wet stations) differ significantly ($p < 0.001$). The dry regime is characterized by low soil moisture conditions. The soil moisture at the individual dry stations mainly (75% of the measurements) ranges between 0% and 16% (see figure A1). Such low soil moisture conditions have been found to limit microbial activity by causing osmotic stress and limited substrate diffusion (see text A1) and the direct dependency of TER on soil moisture is visible in the measurements (see figure A5). Therefore, we conclude that the high sensitivity of dry stations originates from the suboptimal soil moisture levels, and thus respiration is water-limited. In contrast, the more humid conditions at wet stations (soil moisture mainly above 10%, see figure A1) seem to be within an optimal soil moisture range, so that there is no water limitation for TER at these sites. Only two wet stations have higher sensitivities around 20°C, comparable with the sensitivities found for the dry stations. These sensitivities can be explained by the soil moisture at the stations being exceptionally low only for temperatures around 20°C (see text A1).

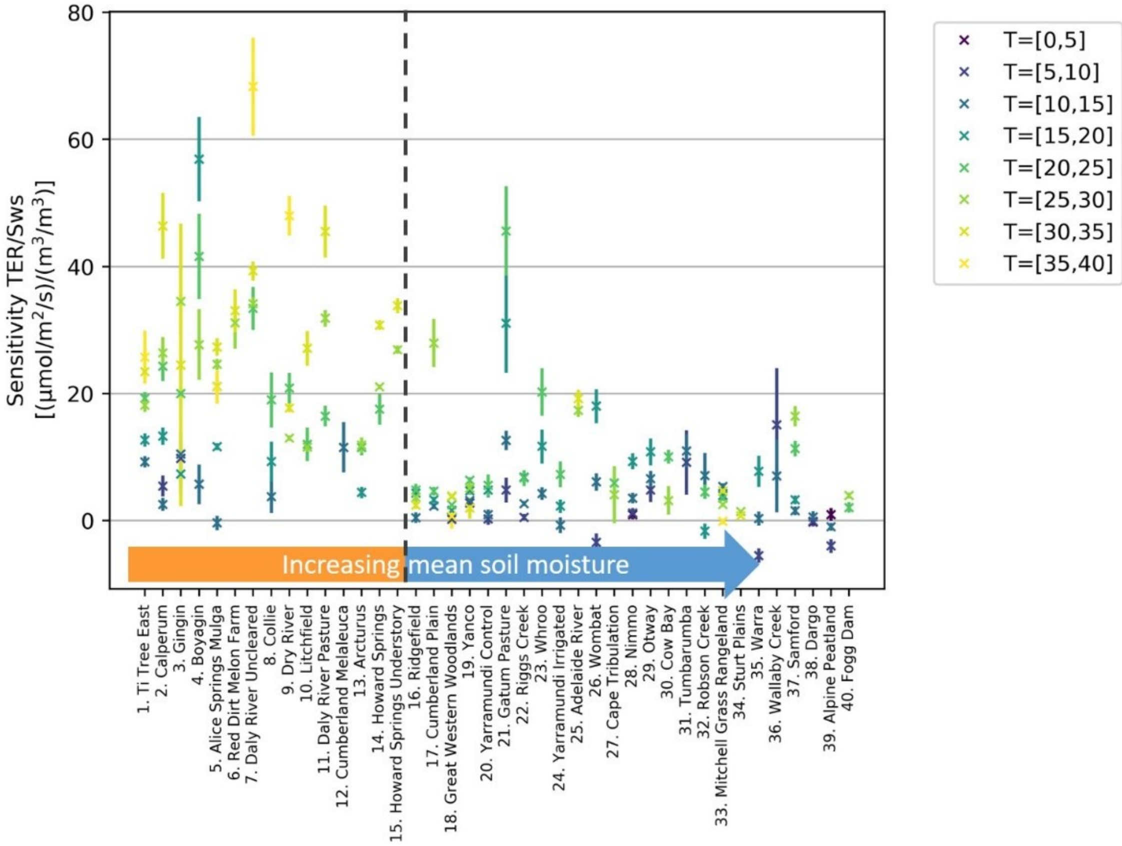

Figure 2: TER sensitivities to soil moisture for the OzFlux stations. The slopes of the individual linear regressions of TER [mu mol/m²/s] versus Sws [m³/m³] are used as a measure for the sensitivity of TER to soil moisture. They are given for each station and 5°C temperature intervals as colored markers. The OzFlux stations are ordered by the mean soil moisture measured at the individual station and numbered in agreement with the overview map in figure 1. The arrow at the bottom and the vertical dashed line indicate the grouping into dry (orange) and wet (blue) stations. The error bars show the standard error of the estimated slopes. The same figure, but with the mean soil moisture on the x-axis is given in figure A4.

Figure 2 also bins the station data into different temperature regimes. It is apparent that there exists a clear temperature dependence of the sensitivities. Especially when looking at the dry stations, the sensitivity increases with increasing temperatures. This effect is expected as it reflects the intrinsic temperature sensitivities of TER (Davidson and Janssens, 2006, see figure A3). Importantly, it appears that the temperature dependence alone does not drive the different dry and wet response regimes in figure 2, given that differences in sensitivities for low and high temperatures are observed across the dry and wet regimes. Soil moisture and temperature are likely co-variates, and the station characteristics span a wide range of combinations of temperature and soil moisture enabling an analysis of the soil moisture sensitivities for each temperature bin (figure 3).

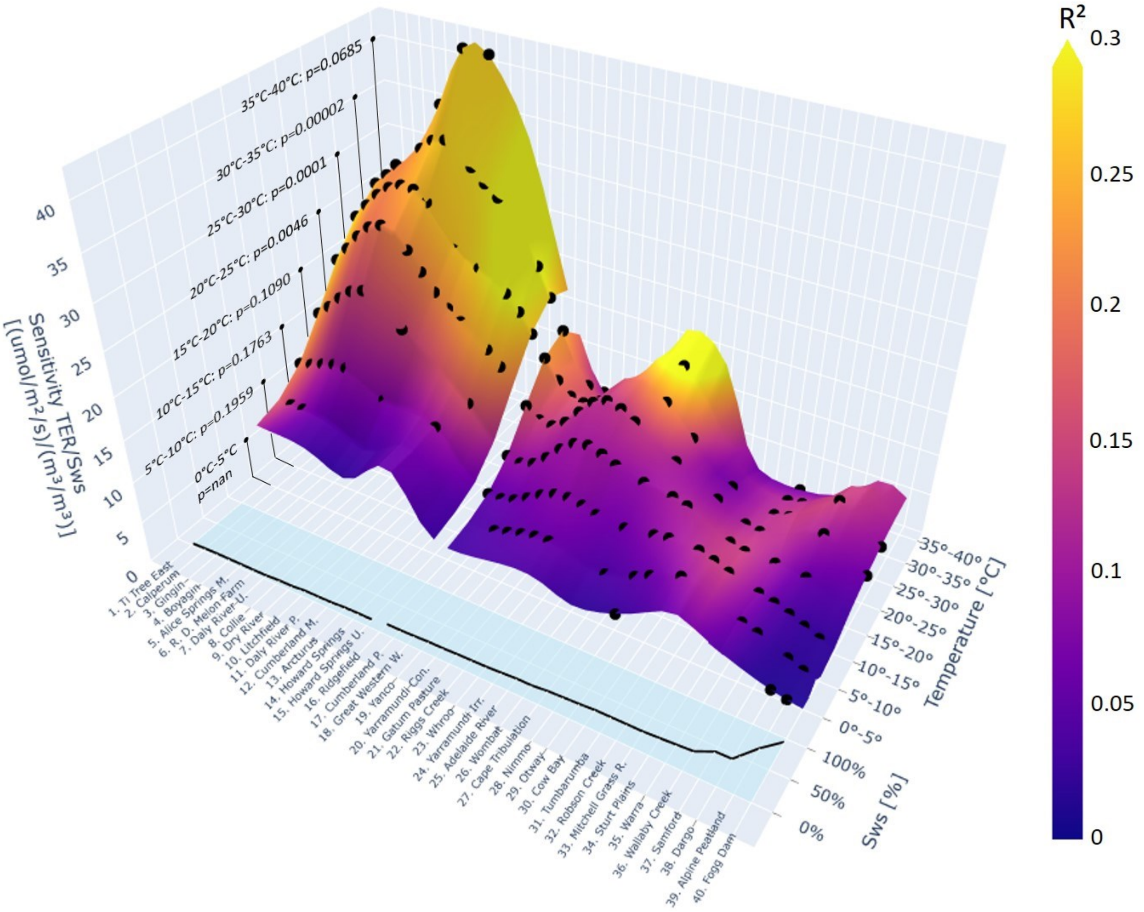

Figure 3: TER sensitivities to soil moisture for OzFlux stations grouped by temperature bins. The individual TER sensitivities for each station and temperature bin are smoothed with a Gaussian filter (standard deviation of 1 (stations) and 2 (temperatures)). Black dots indicate the temperature bins at each stations with sufficient measurements to calculate a sensitivity. The OzFlux stations are ordered by the mean soil moisture measured at the station, which is given as black graph above the station names. The stations are numbered in agreement with the overview map in figure 1. The gap in the surface and soil moisture graph indicates the grouping into dry (left) and wet (right) stations. The coefficient of determination for the individual TER-to-Sws fits is indicated by the color of the surface. The p-value of the Anova test comparing the mean sensitivities for the dry against the wet group for each temperature bin are given on the left side

of the figure. The original and unsmoothed sensitivities are given for each individual temperature bin in figure A6.

We find that the significant positive respiration response at the dry stations to soil moisture appears for temperature regimes above 20°C. For the temperature bins above 20°C, the sensitivity of the dry stations is significantly larger than for the wet stations (p=0.0046, p=0.0001, and p=0.00002 in the ANOVA test for the intervals 20°C – 25°C, 25°C – 30°C, 30°C – 35°C, respectively). Especially for the temperature intervals 20°C – 25°C and 25°C – 30°C, TER in the different humidity regimes reacts differently to soil moisture (see figure 3, and figure A6e and A6f). For even higher temperatures, the number of measurements is too low to obtain reliable results, especially for the wet stations.

To determine how much TER is controlled by soil moisture, we calculate R^2 of the linear regression for TER and soil moisture at each individual site (see surface color in figure 3). While it is not expected that TER is driven by soil moisture alone, we find that R^2 is higher for the dry stations than for the wet stations. Moreover, the R^2 increases with temperature. The findings can be condensed by using the dry/wet grouping of the stations and conducting a statistical analysis on the R^2 values for each temperature bin and each group (figure 4).

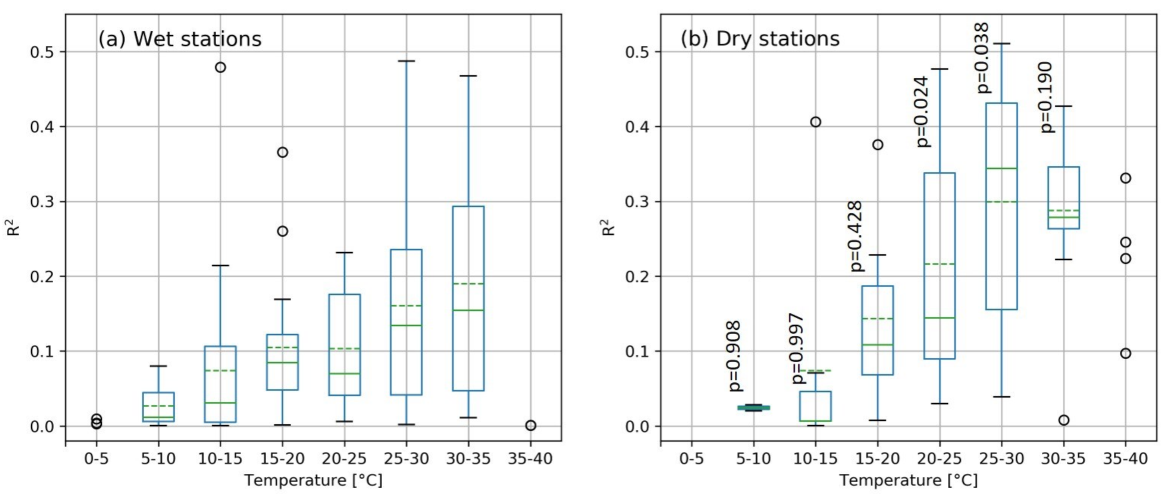

Figure 4. Coefficient of determination (R^2) for wet (panel a) and dry stations (panel b) grouped by

temperature. The R^2 values in each bin are given as boxplots, with the median and mean value given as green solid and dashed lines, respectively. An ANOVA test was performed comparing the R^2 values of the wet stations against those of the dry stations for each temperature bin. The p-values of the ANOVA test are given next to the corresponding temperatures boxplots in panel (b) for temperature bins with enough R^2 values.

Up to 15 °C, R^2 values are low (mean and median < 0.15) for dry and wet conditions, implying that soil moisture has no or an only minor effect on TER. For the temperatures above 20°C, R^2 increases for the dry stations up to 0.35 (median) and 0.50 (max), while staying low for the wet stations. The highest R^2 is reached for the temperature interval 25°C-30°C. Indeed, the ANOVA test confirms that there is a significant difference for the R^2 values between wet and dry stations for the temperature intervals 20°C – 25°C and 25°C – 30°C ($p < 0.05$, figure 4).

These findings underline the importance of soil moisture as driver of TER under dry conditions and high temperatures and, conversely, the small impact of soil moisture on TER in humid environments and under low temperatures. Our findings point towards different response mechanisms of TER to soil moisture in different soil moisture regimes. When modelling carbon fluxes in regions with large aridity ranges, accurately capturing the different response regimes is, therefore, crucial. Next, we explore the TER fluxes of the vegetation model LPJ to analyze whether the model can represent the response regimes found in the OzFlux data.

3.2. TER response to soil moisture in LPJ

To analyze the performance of the vegetation model LPJ, we calculate the sensitivities of TER to soil moisture using LPJ daily data. The sensitivities of TER (calculated as sum of Ra and Rh) to soil moisture are given in figure 5. They are nearly twice as high as found with the OzFlux measurements. As for the OzFlux analysis, the highest sensitivities occur at semi-arid stations. However, it is clearly visible that, contrary to our findings using the OzFlux measurements, the wet stations in LPJ show higher sensitivities of TER to soil moisture. The observed moisture gradient does not appear in the model: The sensitivities at the wet stations are comparable to those of the dry stations and there is no decline in sensitivities with increasing mean soil moisture per station. This is confirmed by an ANOVA test indicating that there is no significant difference between the mean sensitivities at the dry and wet stations ($p > 0.11$ for the various temperature bins). The different behavior of TER at high soil moisture levels for LPJ compared to OzFlux measurements is also clearly visible when looking at the measured and modeled TER and soil moisture values for wet stations (see figure A7 and figure A8). While TER in LPJ increases with increasing soil moisture, the OzFlux measurements do not show such a dependency. For the dynamics among the dry stations, sensitivities tend to decrease for the driest stations. This is also visible for the OzFlux measurements in figure 2. However, in both cases the low number of arid stations prohibits a statistical assessment.

These results show that the vegetation model is not capable of reproducing the different observed TER responses in the dry and wet regimes. As TER is modelled as the sum of Ra and Rh, in the following we explore their individual behavior to analyze the origin of the non-vanishing TER-to-soil moistures sensitivities for wet stations.

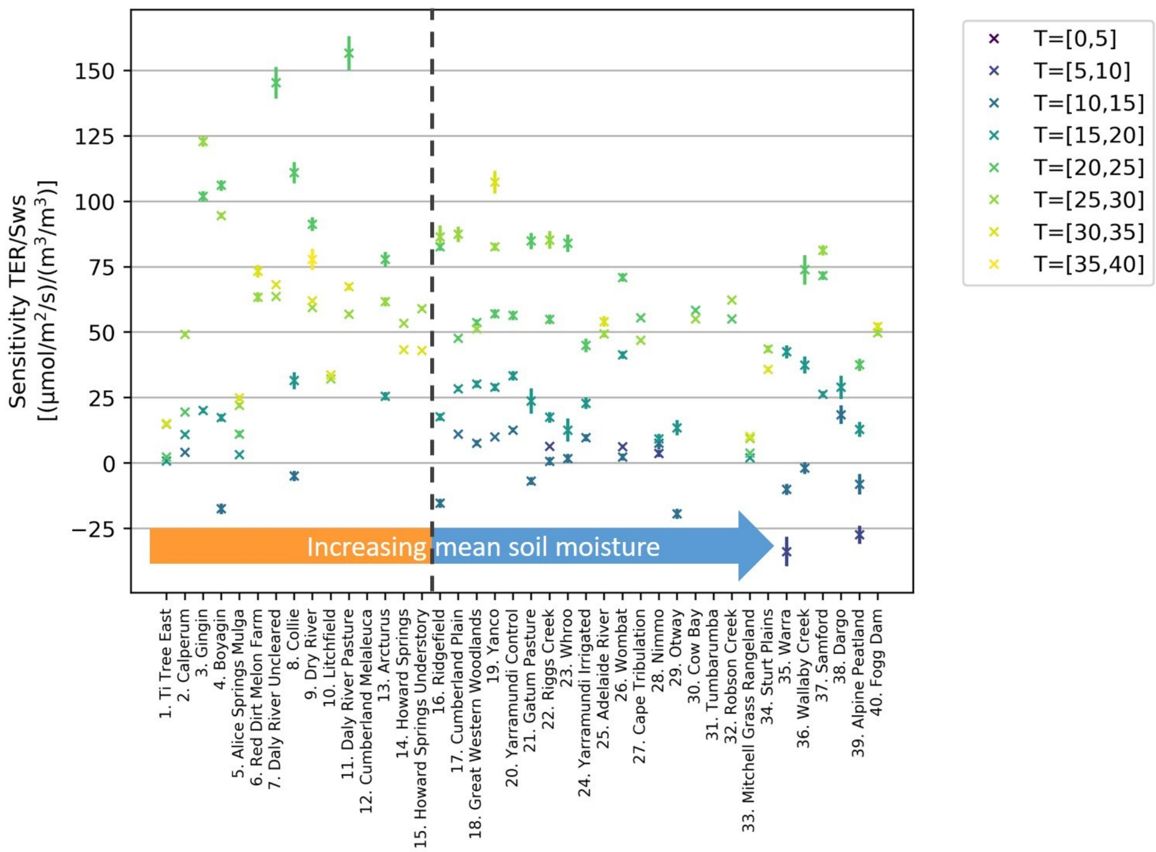

Figure 5: TER sensitivities given by the vegetation model LPJ. Like figure 2, but with LPJ data. Sensitivities are calculated for 5°C bins of the modelled soil temperature, as soil temperature is mainly used to drive Ra and Rh in LPJ (see Section 2.4). The LPJ sensitivities with air temperature binning are given in figure A9.

The modeled sensitivities of Rh and Ra to soil moisture are given in figure A10. They show similar dynamics of the sensitivities as for TER. In particular, both, Ra and Rh, show significant sensitivities to soil moisture for the wet stations. Thus, both respiratory fluxes do not match the findings of small sensitivities for wet stations based on the OzFlux measurements.

Looking at the implementation in LPJ, Ra and Rh are both dependent on soil moisture. Ra depends indirectly and non-linearly on soil moisture as photosynthesis and leaf carbon are reduced when soil moisture levels drop below a (dynamic) water stress threshold (Sitch *et al* 2003). Hence, Ra is only impacted by soil moisture if soil moisture drops below the water stress threshold. The considerable Ra sensitivities in LPJ, therefore, could indicate that water stress occurs for all wet stations contrasting OzFlux-based findings. A comprehensive evaluation of the soil moisture and the water stress threshold dynamics, among other tests, could help to improve the response of Ra to soil moisture in humid regions.

Rh is directly driven by soil moisture. As given in equations (2) and (4), and in figure A3, LPJ assumes steadily increasing Rh with increasing soil water content. Even though the slope of the *Rh(swc)* function (equation (4)) decreases with increasing soil water content, there is no saturation or negative sensitivity as found in the OzFlux measurements. This could cause LPJ to have considerable TER sensitivities to soil moisture for wet stations in contrast to the OzFlux sensitivities. Improving the functional response of *Rh(swc)* by using unimodal or saturating functions as also suggested by Moyano *et al* (2013) could improve the performance of LPJ in comparison to OzFlux. While such an implementation is beyond the scope of this study, our findings quantify the dependencies of TER on soil moisture and temperature and can be used as a basis to improve TER in dynamic global vegetation models.

4. Summary

We use daily nighttime NEE data as proxy for TER measured over the last 20 years by 40 flux towers of the OzFlux network in Australia. We calculate TER sensitivities to soil moisture by performing a linear regression for 5°C temperature bins for each measurement site. We find that the TER sensitivities to soil moisture are significantly higher at dry stations, than at wet sites. We explain the two different response regimes with the soil moisture distribution at the individual sites. Low soil moisture conditions are expected to cause osmotic stress or limited substrate transport which reduce TER. We find the highest sensitivities at semi-arid stations. At the wet stations, we find smaller limitation of TER to soil water availability and sensitivities are therefore close to zero for high soil moisture. Our findings demonstrate that under dry conditions soil moisture can be an important driver of TER while this is not the case for wet conditions. Furthermore, there is an additional temperature dependence where TER sensitivities to soil moisture at drier sites greatly increase above temperatures of 20°C. This underlines the importance of accurately implementing the TER sensitivity to soil moisture in vegetation models, especially in regions with large aridity gradients such as Australia.

We show that the vegetation model LPJ is unable to reproduce the two different response regimes of TER to soil moisture for the dry stations and wet stations. The model shows significant sensitivities in Ra and Rh to soil moisture for wet stations, contradicting our findings from the OzFlux measurements. Modelled Ra seems to react too strongly to soil moisture changes under humid conditions. This could point towards LPJ assuming water stress conditions for wet stations, which is in contrast to the small sensitivities found in the OzFlux results. For Rh, the larger sensitivities could be caused by the parameterization of Rh, steadily increasing with increasing soil water content. Our OzFlux results indicate that a more complex functional response of *Rh(swc)* with constant or declining Rh for high soil moistures would be needed to capture the Rh dynamics at Australian flux tower stations correctly.

Data Availability:

OzFlux L3 data can be downloaded from https://data.ozflux.org.au/portal/. Data of the Global Aridity Index (AI) and Potential Evapotranspiration (ET0) Climate Database can be downloaded from https://doi.org/10.6084/m9.figshare.7504448.v6. The code to run LPJ is available on GitHub (https://github.com/LPJ-EOSIM/LPJ-wsl_v2.0). The LPJ data used in the analysis can be downloaded from https://doi.org/10.5281/zenodo.15173378. The code used for the analyses is available on zenodo (https://doi.org/10.5281/zenodo.15173353).

Acknowledgements

E.-M.M., A.B., S.N.V., A.F.F. and B.P. were involved in conceptualization and methodology. E.-M.M. conducted the analysis and the visualization under the supervision of A.B., S.N.V.. E.-M.M. performed the LPJ runs with the help of T.C. and B.J.F.-F.. E.-M.M. wrote the original draft. All authors contributed to the editing and review of the manuscript.

The authors gratefully acknowledge the data storage service SDS@hd supported by the Ministry of Science, Research and the Arts Baden-Württemberg (MWK) and the German Research Foundation (DFG) through grant INST 35/1503-1 FUGG and the computing resources provided by the DKRZ under project bb1170. E.-M.M. acknowledges a doctoral scholarship from the German Academic Scholarship Foundation. B.P., A.F.F., T.C. and B.J.F.-F. acknowledge funding from NASA's Terrestrial Ecology Program. For the publication fee we acknowledge financial support by Heidelberg University. This work used eddy covariance data collected by the TERN-OzFlux facility. OzFlux would like to acknowledge the financial support of the Australian Federal Government via the National Collaborative Research Infrastructure Strategy and the Education Investment Fund.

Text A1: The driver of TER sensitivity to soil moisture

In section 3.1 we find two main regimes of TER sensitivity to soil moisture. While, for the dry stations, soil moisture has a significant impact on TER, TER at wet stations shows little sensitivity to soil moisture. Figure A1 shows the distribution of the measured soil moisture at the individual sites in the same site order as in figure 2.

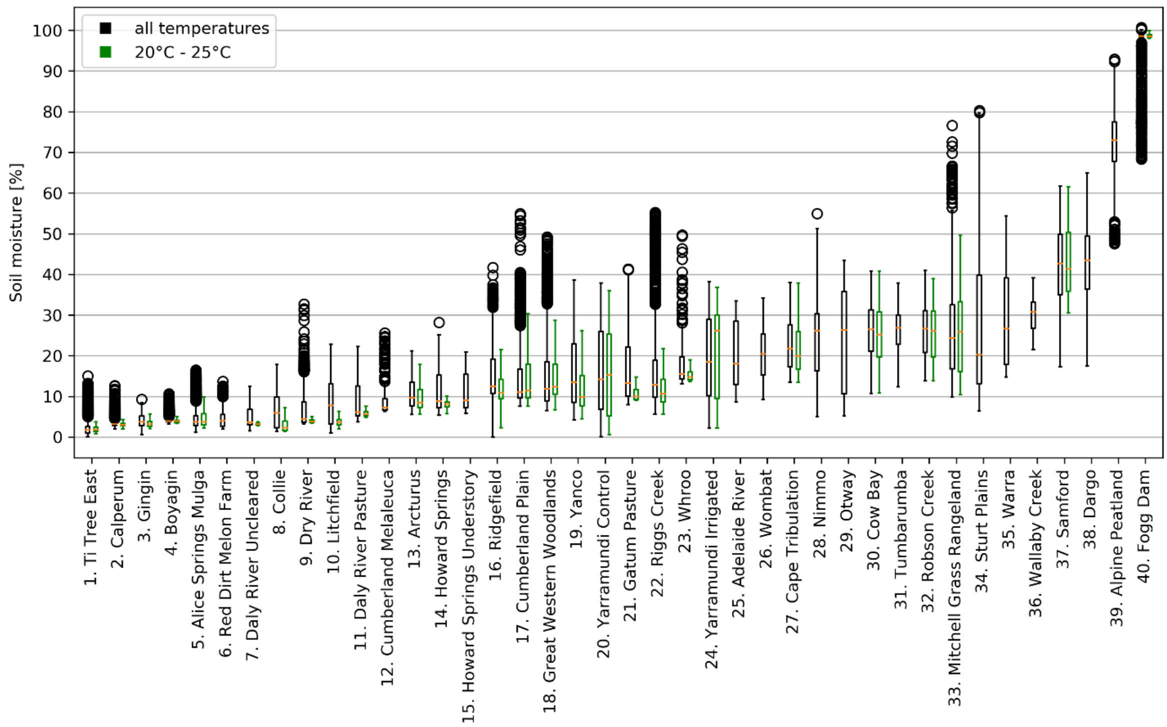

Figure A1: Soil moisture measurements at the individual OzFlux stations. The daily nightime soil moisture values of each station are given as boxplots. All moisture measurements are given in black; the green boxplots show the soil moistures for soil temperatures between 20°C and 25°C. Only boxplots with at least 100 soil moisture measurements are displayed. The stations are ordered according to their mean soil moisture measured.

For all dry stations the median of soil moisture is smaller than 10% and soil moisture mainly ranges between 0% and 16% (75% interval) and only some outliers at the Dry River station reach more than 30% soil moisture. For most wet stations, the soil moisture is mainly (75%) above 10% and mainly (75%) stays below 50%. The Alpine Peatland and Fogg Dam stations form exceptions with soil moistures values up to 100%. Both stations are exposed to extreme conditions limiting the measurement capabilities of the stations. While the Fogg Dam station is seasonally flooded, the Alpine Peatland station has around 3 months of snow cover on average (OzFlux 2024). When looking only at the soil moisture distribution at soil temperatures between 20°C to 25°C, the wet stations Gatum Pasture and to a lesser extent also Whroo have low soil moistures around 10% and 15%, respectively, which is at the lower end of their soil moisture range for all temperatures.

Taking into account our findings from Section 3.1 and the soil moisture distribution in Figure A1 suggests that the soil moisture at the wet stations is large enough for TER not being limited by water availability anymore. The dry stations, however, are (temporally) exposed to severe drought conditions leading to a drying out of the upper soil layer.

Laboratory and field experiments evaluating soil moisture sensitivity of TER under different aridity conditions found different soil moisture regimes with varying TER responses (e.g., Xu *et al* 2004, Lellei-Kovács *et al* 2011, Vicca *et al* 2014). Soil respiration is assumed to be the largest component of TER and exhibit similar temporal patterns (Law *et al* 2002, Barba *et al* 2018, Bond-Lamberty *et al* 2024). Lellei-Kovács *et al* (2011) and Vicca *et al* (2014) define soil moisture regimes with optimal, suboptimal and supra-optimal soil moisture conditions leading to varying soil respiration rates. In the latter two regimes, soil respiration is limited by soil moisture: While at suboptimal soil moisture conditions, microbial activity is reduced due to osmotic stress and limited substrate diffusion (Schimel *et al* 2007, Moyano *et al* 2013), supra-optimal high soil moisture conditions lead to low oxygen conditions limiting respiration (Davidson and Janssens, 2006). Investigating sandy soils, Lellei-Kovács *et al* (2011) found a threshold for optimal soil moisture of 7% above which soil respiration is not limited by soil water availability. This threshold is expected to be slightly higher in soils with high clay and silt content, due to the enhanced water holding capacity of the soils. All dry stations have median soil moisture below 10% and therefore fall in the range of suboptimal soil moisture conditions as found by Lellei-Kovács *et al* (2011). Hence, it is to be expected that reduced microbial activity and substrate diffusion limits soil respiration at the dry stations and that changes in soil moisture directly translate in changes in soil respiration and therefore TER. This explains the presence of high sensitivities for the dry stations. Also, for the two wet stations Gatum Pasture and Whroo, which show high sensitivities at around 20°C temperature, low soil moisture conditions are present in this temperature range even though they have in general a higher mean soil moisture. This water limitation explains their high sensitivities while being grouped in the wet stations.

For the wet stations the majority of soil moisture measurements (75%) have higher values than 10%. Our findings of no or low sensitivities to soil moisture at these stations therefore go along with the finding of a water-unlimited respiration regime by Lellei-Kovács *et al* (2011). Other studies found even negative TER sensitivity on soil moisture for supra-optimal soil moisture conditions (Sierra *et al* 2015). We mostly find no sensitivity of TER on soil moisture at the humid stations as for example shown in figure A7 but can identify single stations with negative sensitivities which could hint at a limitation of TER by limited oxygen transport (Yarramundi Control, figure A5).

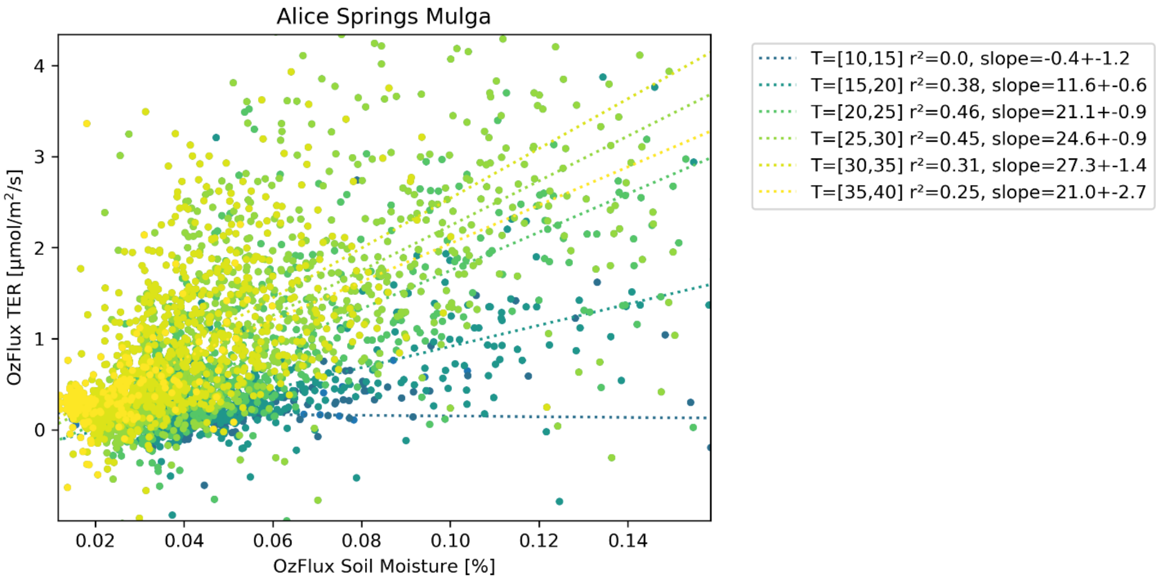

Figure A2: TER and soil moisture measured by the OzFlux station Alice Springs Mulga. Daily values are given colored according to the measured soil temperature. For each 5°C bin the linear regression fit is shown as colored dashed line. The calculated slope and R^2 values are given in the legend with the respective temperature.

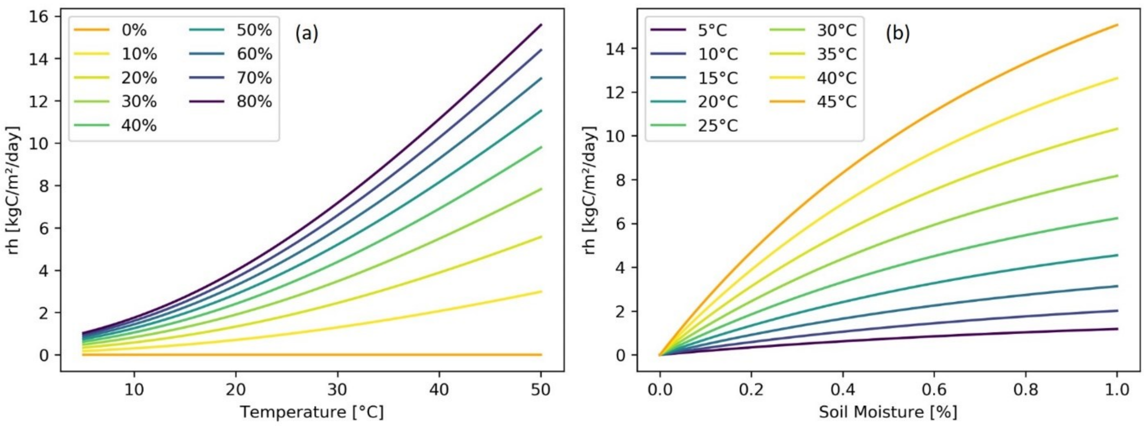

Figure A3: Response of heterotrophic respiration on soil water content changes and temperature. The heterotrophic respiration using the implementation of Rh in LPJ is given dependent on temperature and soil water content (swc) as saturation fraction. Panel a) shows the functional response of Rh to temperature for different swc and panel b) gives the response of Rh to swc for different temperatures. The corresponding functions are given in the main text (equations (3) and (4)).

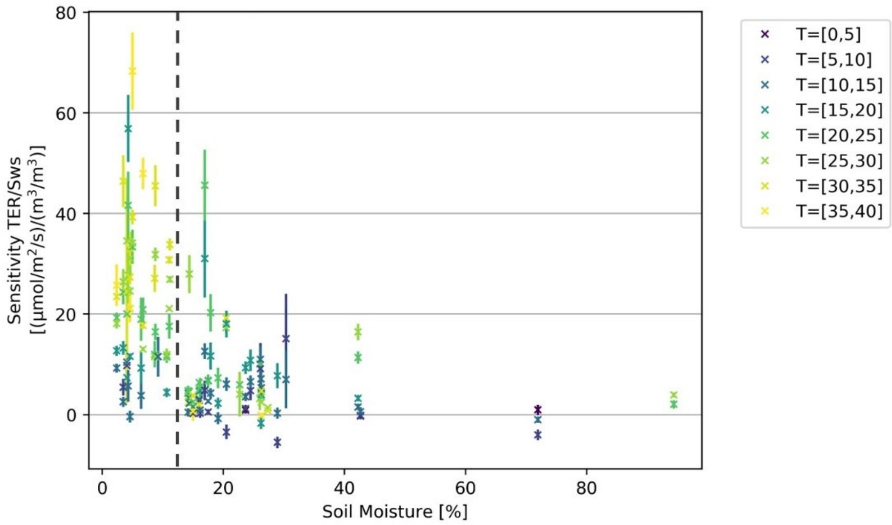

Figure A4: TER sensitivities to soil moisture for the OzFlux stations. The slopes of the individual linear regressions of TER [mu mol/m²/s] versus Sws [m³/m³] are used as a measure for the sensitivity of TER to soil moisture. They are given for each station and 5°C temperature intervals as colored markers. Like figure 2, but with mean measured soil moisture of the individual stations on the x axis instead of the station names. The vertical dashed line indicate the grouping into dry (left) and wet (right) stations. The error bars show the standard error of the estimated slopes.

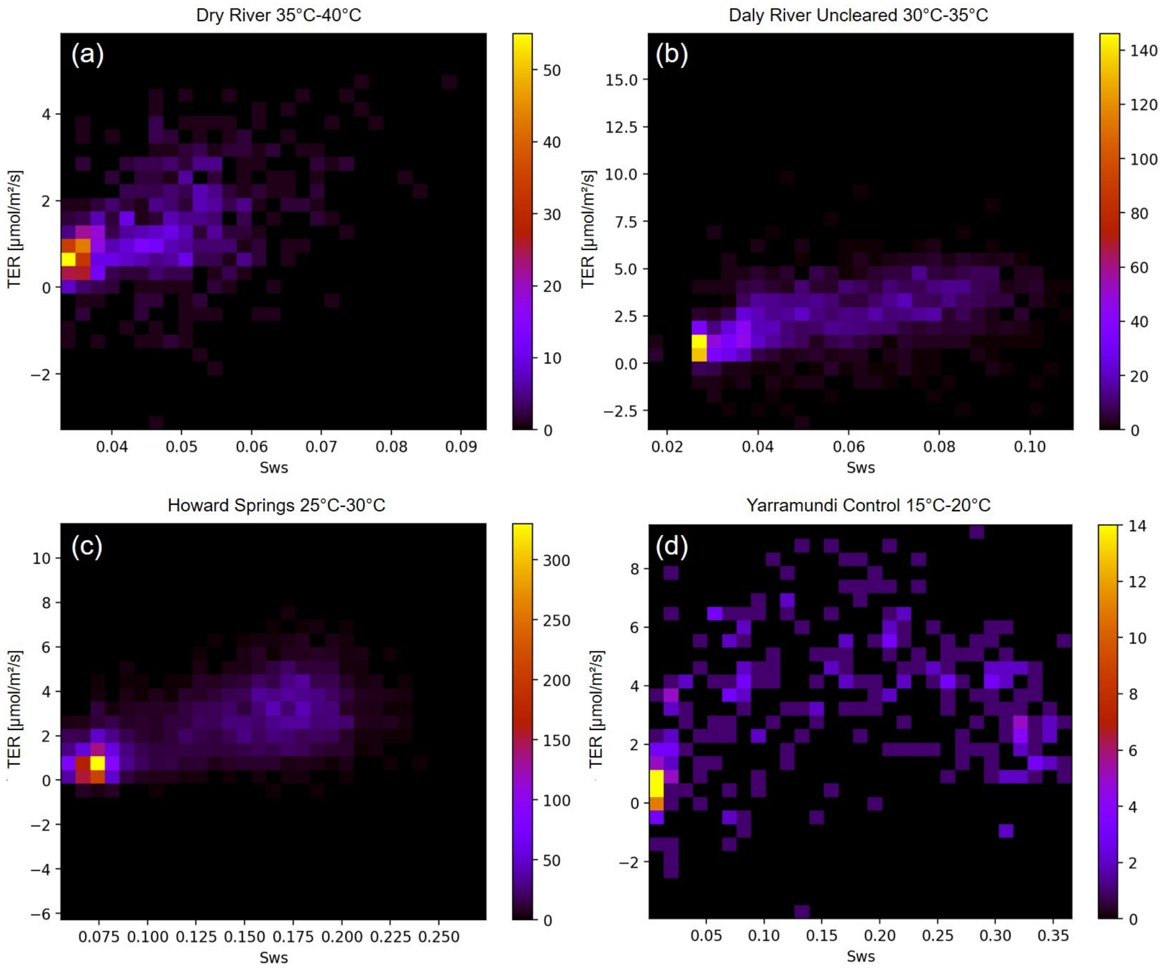

Figure A5: TER and soil moistures measured at individual OzFlux stations and temperature intervals. 2D histograms for the stations Dry River, Daly River Uncleared, Howard Springs, and Yarramundi Control are shown for the temperature ranges 35°C-40°C, 30°C-35°C, 25°C-30°C, and 15°C-20°C, respectively. The number of measurements in the individual TER and soil moisture bins is given with individual color bars.

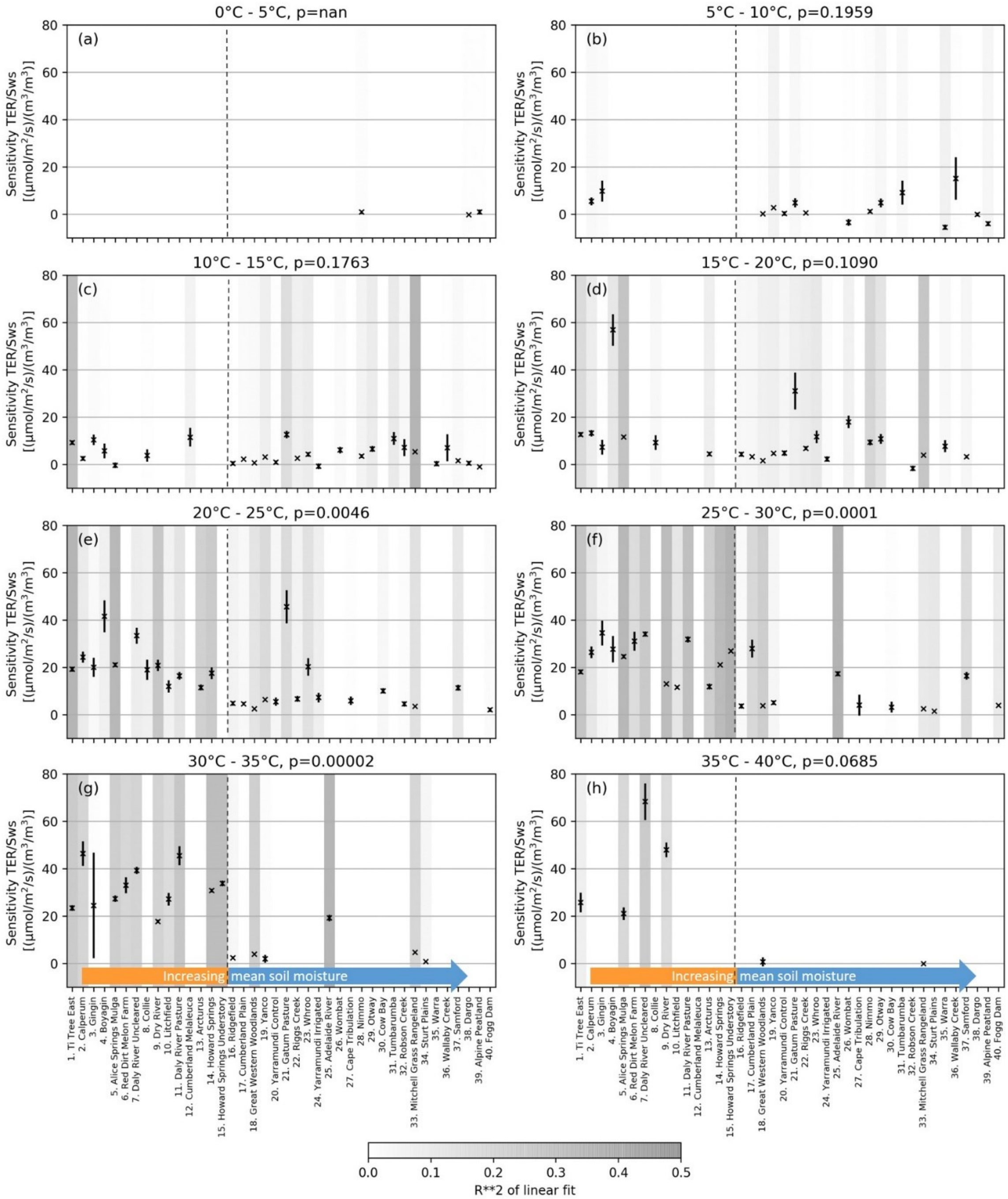

Figure A6: TER sensitivities to soil moisture for OzFlux stations grouped by temperature bins (panels a to h). The OzFlux stations are ordered by the mean soil moisture measured at the station and numbered in agreement with the overview map in figure 1. The arrow at the bottom and the vertical dashed line indicate the grouping into dry (orange) and wet (blue) stations. The error bars show the standard error of the estimated slopes. The coefficient of determination for the individual TER-to-Sws fits is given as grey background shading. The p-value of the Anova test comparing the mean sensitivities for the dry against the wet group are given in the panel titles.

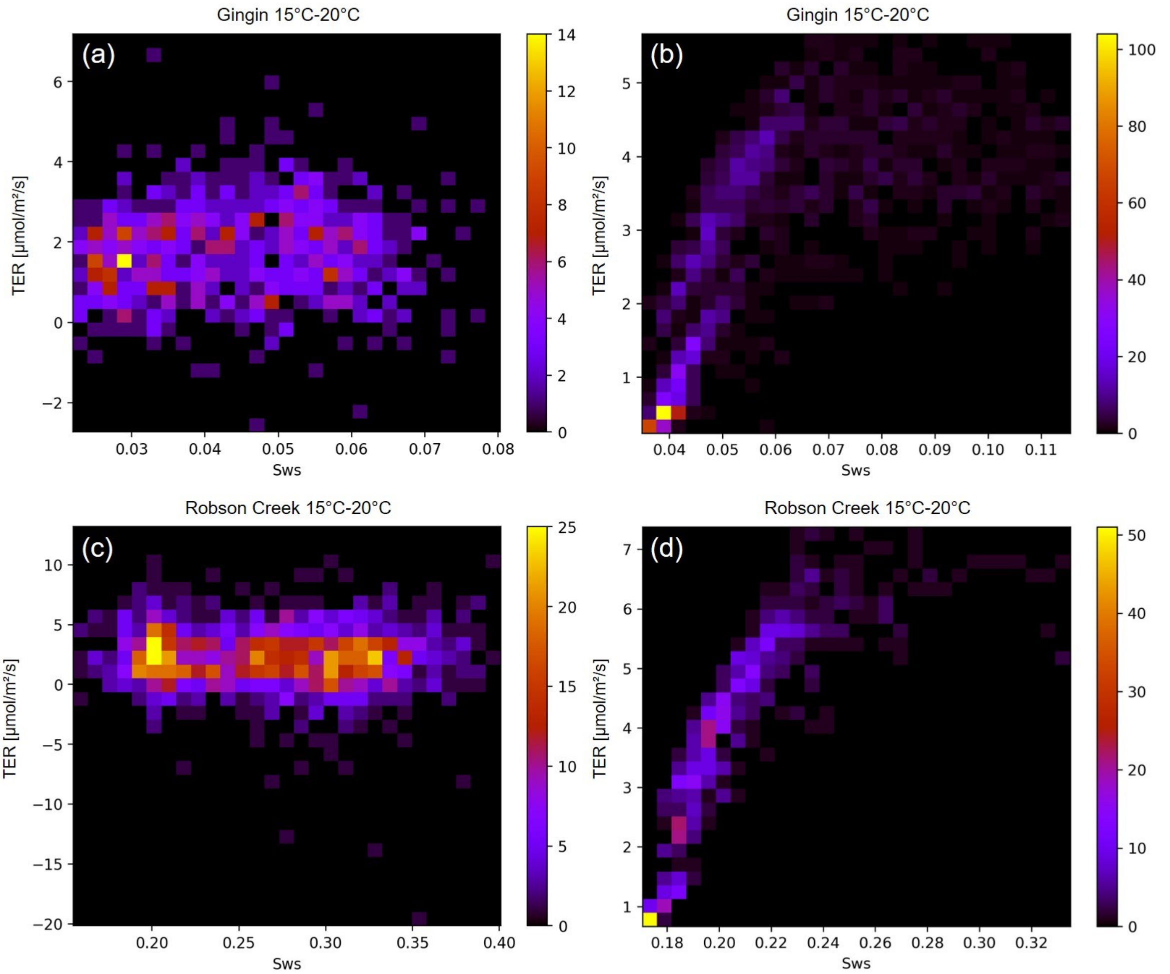

Figure A7: TER and soil moistures measured and modelled at Robson Creek and Gingin OzFlux stations. 2D histograms for the stations Robson Creek and Gingin are shown for the temperature range 15°C-20°C. The number of measurements in the individual TER and soil moisture bins is given with individual color bars. Panel a and c show the measured OzFlux values, Panel b and d show the modelled values with LPJ.

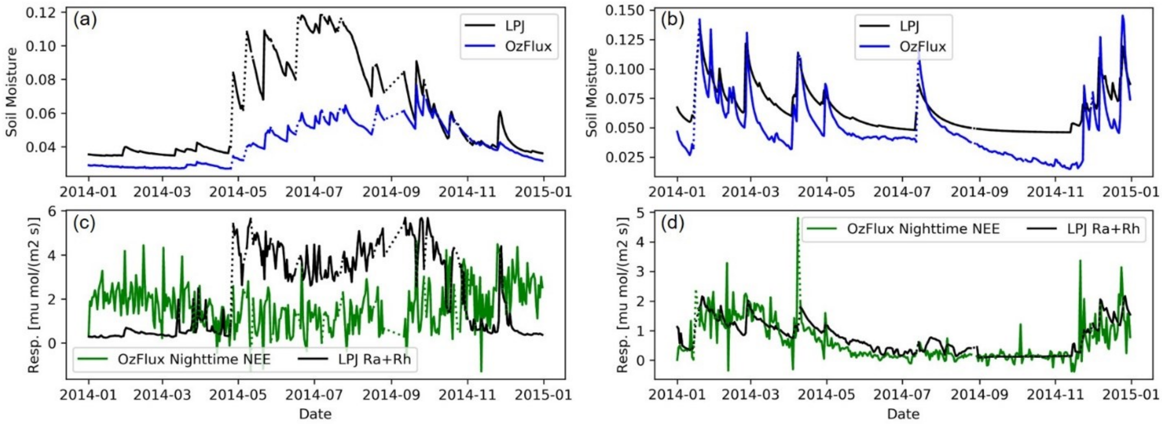

Figure A8: TER and soil moistures measured and modelled at Gingin and Alice Springs OzFlux stations for the year 2014. Panel a and b give the daily soil moistures as volume fractions measured by OzFlux (blue) and modeled by LPJ (black). Panel c and d show the nighttime NEE measured by OzFlux (green) and the Ra+Rh modeled by LPJ (black). The left panels (a and c) are for Gingin and the right panels for Alice Springs Mulga (panel b and d). The dotted lines indicate days without valid measurements. The respiratory fluxes for Alice Springs Mulga clearly show the same variability as the soil moisture for the OzFlux measurements as well for LPJ. For Gingin, however, only LPJ shows similar dynamics for Ra+Rh and the soil moisture. The measured TER at Gingin clearly does not follow the soil moisture dynamics.

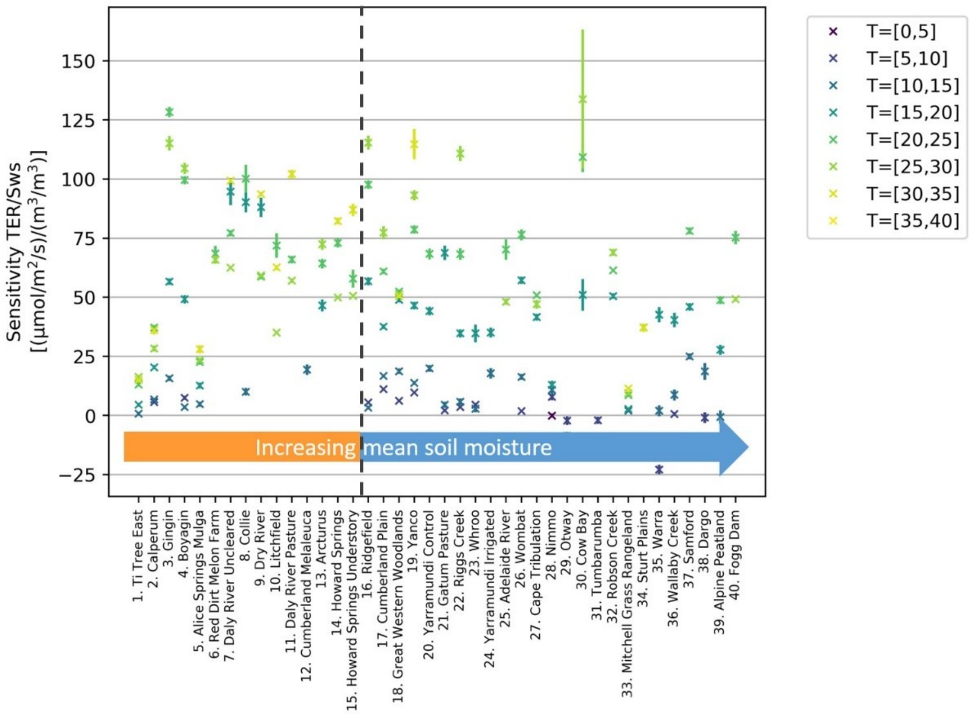

Figure A9: TER sensitivities to soil moisture given by the vegetation model LPJ. As LPJ mainly drives the TER components with the soil temperature, we use the soil temperature of LPJ for the 5°C-binning in figure 5 in the main text. In this figure, sensitivities are calculated for 5°C bins of the modelled air temperature. The sensitivities using air temperature binning result in the same findings as shown in figure 5 and described in the main text. Please note, that the soil and air temperatures of LPJ are in general lower than measured soil temperatures.

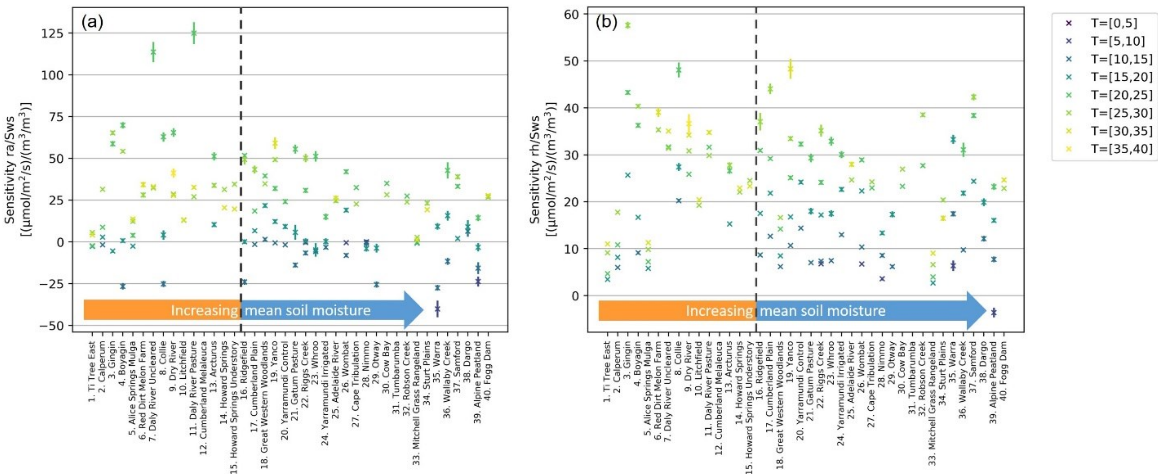

Figure A10: TER sensitivities to soil moisture given by the vegetation model LPJ. Like figure 2, but with LPJ data for Ra in Panel a and Rh in Panel b. Sensitivities are calculated for 5°C bins of the modelled soil temperature, as soil temperature is used to drive Rh and most of Ra in LPJ. Based on Rh(swc) in equation (2) and (4), we would expect slightly lower sensitivities for the wet stations than for the dry stations as the slope of Rh(swc) decreases with increasing soil water content. This is, however, not the case for the sensitivities given in panel (b). When taking a look at the litter modeled by LPJ (see figure A11); we see that most wet stations have higher amounts of litter than the dry stations. As Rh depends linearly on the litter content in equation (4), most likely the enhanced litter compensates for the decline in sensitivities expected by Rh(swc).

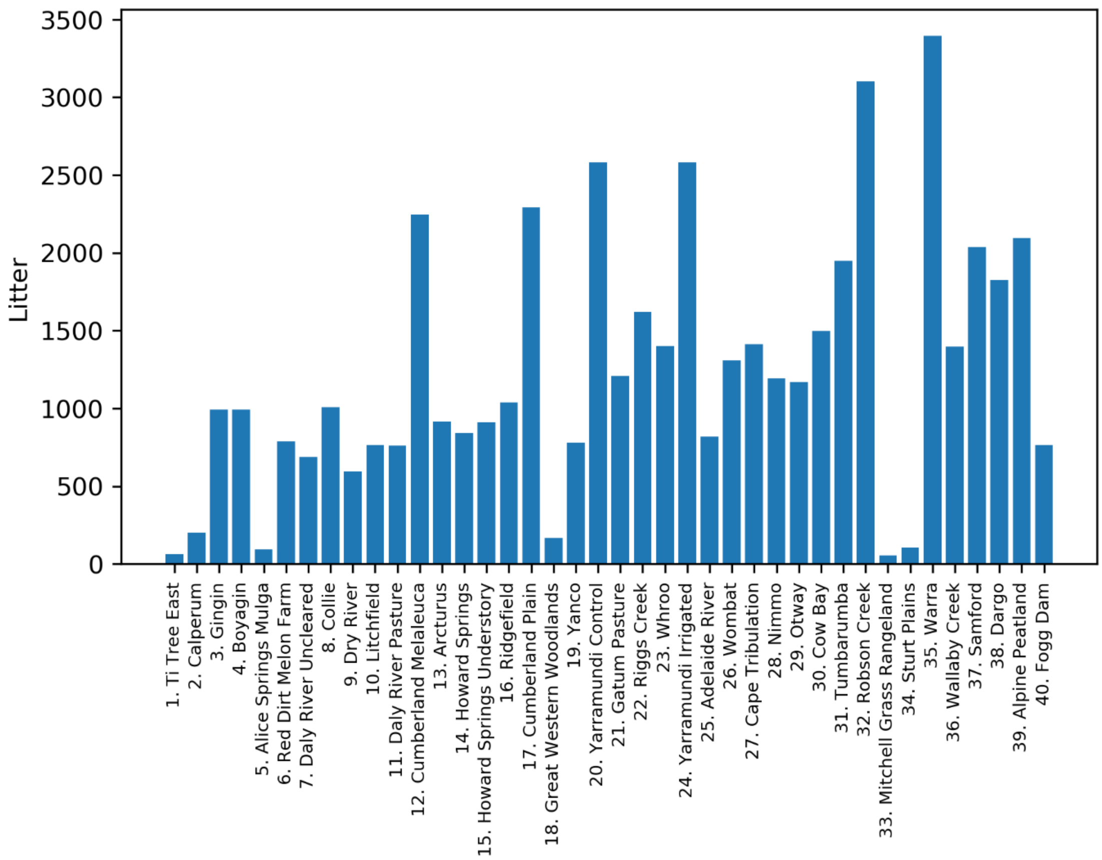

Figure A11: Organic carbon in litter modelled by LPJ at the OzFlux sites. The litter organic carbon [gC/m²] modelled by LPJ for each of the OzFlux stations is shown. Like in figure 2, the stations are ordered according to their mean soil moisture.

Table A1: OzFlux Station Characteristics

#	Station	Mean Precip. [mm] (1)	Sws (2)	Ecosystem (3)	Soil texture (clay/silt/sand) [%] (4)	Meas. height [m] (1)	Citation (1)
1	Ti Tree East	305	0.024	Desert & Shrub	18/6/77	10	Cleverly 2013
2	Calperum	240	0.035	Mediterranean forest and woodlands	16/8/76	20	Tech 2013
3	Gingin	641	0.041	Mediterranean forest and woodlands	10/8/82	15	Silberstein 2015
4	Boyagin	445	0.043	Mediterranean forest and woodlands	11/9/80	4	Beringer 2017
5	Alice Springs Mulga	306	0.046	Desert & Shrub	18/6/77	12	Cleverly 2011
6	Red Dirt Melon Farm		0.046	Trop. Grass, Savanna & Shrub	9/2/88	21	Beringer 2014a
7	Daly River Uncleared	1170	0.050	Trop. Grass, Savanna & Shrub	8/4/88	23	Beringer 2013a
8	Collie	933	0.064	Mediterranean forest and woodlands	9/7/85	35	Beringer 2018
9	Dry River	895	0.067	Trop. Grass, Savanna & Shrub	27/10/64	15	Beringer 2013b
10	Litchfield		0.088	Trop. Grass, Savanna & Shrub	16/14/70	31	Beringer 2015
11	Daly River Pasture	1250	0.088	Trop. Grass, Savanna & Shrub	13/4/83	15	Beringer 2013c
12	Cumberland Melaleuca	800	0.092	Temp. Broadleaf Forest	15/15/70	15	Griebel 2019

13	Arcturus	572	0.107	Trop. Grass, Savanna & Shrub	41/16/43	7	Schroder 2014
14	Howard Springs	1700	0.111	Trop. Grass, Savanna & Shrub	20/19/61	23	Beringer 2013d
15	Howard Springs Understory	1700	0.111	Trop. Grass, Savanna & Shrub	20/19/61	23	Beringer 2013e
16	Ridgefield	446	0.142	Mediterranean forest and woodlands	8/9/82	3	Beringer 2016
17	Cumberland Plain	800	0.144	Temp. Broadleaf Forest	14/14/72	29	Pendall 2015
18	Great Western Woodlands	240	0.150	Mediterranean forest and woodlands	17/11/72	35	Macfarlane 2013
19	Yanco	465	0.160	Temp. Grass, Savanna & Shrub	37/12/50	8	Beringer 2013f
20	Yarramundi Control	728	0.162	Temp. Broadleaf Forest	15/28/58	2	Ewenz 2022a
21	Gatum Pasture	736	0.170	Temp. Broadleaf Forest	13/18/68	3	Silva 2022
22	Riggs Creek	650	0.175	Temp. Grass, Savanna & Shrub	15/22/63	3	Beringer 2014b
23	Whroo	558	0.179	Temp. Broadleaf Forest	16/24/60	36	Beringer 2013g
24	Yarramundi Irrigated	728	0.191	Temp. Broadleaf Forest	15/28/58	2	Ewenz 2022b
25	Adelaide River	1730	0.205	Trop. Grass, Savanna & Shrub	14/14/72	15	Beringer 2013h
26	Wombat	650	0.205	Temp. Broadleaf Forest	22/21/57	30	Arndt 2013
27	Cape Tribulation	5700	0.227	Trop. Moist Broadleaf Forest	39/27/34	45	Liddell 2013a
28	Nimmo	1700	0.237	Mont. Grass & Shrub	20/25/55	2	Simpson 2012a

29	Otway	800	0.245	Temp. Broadleaf Forest	14/14/72	5	Van Gorsel 2012
30	Cow Bay	4000	0.260	Trop. Moist Broadleaf Forest	33/29/38	35	Liddell 2013c
31	Tumbarumba	1000	0.261	Mont. Grass & Shrub	20/25/55	70	Woodgate 2013
32	Robson Creek	2236	0.262	Trop. Moist Broadleaf Forest	42/24/35	40	Liddell 2013b
33	Mitchell Grass Rangeland		0.263	Trop. Grass, Savanna & Shrub	44/13/42	4	Grace 2019
34	Sturt Plains	640	0.274	Trop. Grass, Savanna & Shrub	30/15/55	5	Beringer 2013i
35	Warra	1700	0.289	Temp. Broadleaf Forest	30/22/48	81	Phillips 2015
36	Wallaby Creek	1700	0.304	Temp. Broadleaf Forest	24/24/52	5	Beringer 2013j
37	Samford	1102	0.423	Temp. Broadleaf Forest	29/24/47	2	Rowlings 2011
38	Dargo	1900	0.427	Mont. Grass & Shrub	20/25/55	2	Simpson 2012b
39	Alpine Peatland	1274	0.720	Mont. Grass & Shrub	19/25/57	2	Gunawardha 2022
40	Fogg Dam	1411	0.944	Trop. Grass, Savanna & Shrub	46/32/23	15	Beringer 2013k

(1) https://www.ozflux.org.au/monitoringsites/index.html

(2) Mean over OzFlux measurements

(3) Beringer *et al* 2022

(4) https://soilgrids.org/

References

Ahlström A *et al* 2015 The dominant role of semi-arid ecosystems in the trend and variability of the land CO_2 sink Science 348 895–9

Arndt S 2013, Wombat State Forest OzFlux-tower site OzFlux, Australian and New Zealand Flux Research and Monitoring [dataset]; http://hdl.handle.net/102.100.100/14237.

Barba J *et al* 2018 Comparing ecosystem and soil respiration: Review and key challenges of tower-based and soil measurements Agricultural and Forest Meteorology 249 434–43

Beringer J 2013a Daly Uncleared OzFlux tower site OzFlux, Australian and New Zealand Flux Research and Monitoring [dataset]; http://hdl.handle.net/102.100.100/14239.

Beringer J 2013b Dry River OzFlux tower site OzFlux, Australian and New Zealand Flux Research and Monitoring [dataset]; http://hdl.handle.net/102.100.100/14229.

Beringer J 2013c Daly Pasture OzFlux tower site OzFlux, Australian and New Zealand Flux Research and Monitoring [dataset]; http://hdl.handle.net/102.100.100/14238.

Beringer J 2013d Howard Springs OzFlux tower site OzFlux, Australian and New Zealand Flux Research and Monitoring [dataset]; http://hdl.handle.net/102.100.100/14234.

Beringer J 2013e Howard Springs Understory OzFlux tower site OzFlux, Australian and New Zealand Flux Research and Monitoring [dataset]; http://hdl.handle.net/102.100.100/14240.

Beringer J 2013f Yanco JAXA OzFlux tower site OzFlux, Australian and New Zealand Flux Research and Monitoring [dataset]; http://hdl.handle.net/102.100.100/14235.

Beringer J 2013g Whroo OzFlux tower site OzFlux, Australian and New Zealand Flux Research and Monitoring [dataset]; http://hdl.handle.net/102.100.100/14232.

Beringer J 2013h Adelaide River OzFlux tower site OzFlux, Australian and New Zealand Flux Research and Monitoring [dataset]; http://hdl.handle.net/102.100.100/14228.

Beringer J 2013i Sturt Plains OzFlux tower site OzFlux, Australian and New Zealand Flux Research and Monitoring [dataset]; http://hdl.handle.net/102.100.100/14230.

Beringer J 2013j Wallaby Creek OzFlux tower site OzFlux, Australian and New Zealand Flux Research and Monitoring [dataset]; http://hdl.handle.net/102.100.100/14231.

Beringer J 2013k Fogg Dam OzFlux tower site OzFlux: Australian and New Zealand Flux Resarch and Monitoring [dataset]; http://hdl.handle.net/102.100.100/14233.

Beringer J 2014a Red Dirt Melon Farm OzFlux tower site OzFlux, Australian and New Zealand Flux Research and Monitoring [dataset]; http://hdl.handle.net/102.100.100/14245.

Beringer J 2014b Riggs Creek OzFlux tower site OzFlux, Australian and New Zealand Flux Research and Monitoring [dataset]; http://hdl.handle.net/102.100.100/14246.

Beringer J 2015 Litchfield OzFlux tower site OzFlux, Australian and New Zealand Flux Research and Monitoring [dataset]; http://hdl.handle.net/102.100.100/25690.

Beringer J 2016 Ridgefield OzFlux tower site OzFlux, Australian and New Zealand Flux Research and Monitoring [dataset]; http://hdl.handle.net/102.100.100/33951.

Beringer J 2017 Boyagin OzFlux tower site OzFlux, Australian and New Zealand Flux Research and Monitoring [dataset]; http://hdl.handle.net/102.100.100/61760.

Beringer J 2018 Collie OzFlux, Australian and New Zealand Flux Research and Monitoring [dataset]; http://hdl.handle.net/102.100.100/70007.

Beringer J *et al* 2022 Bridge to the future: Important lessons from 20 years of ecosystem observations made by the OzFlux network Global Change Biology 28 3489–514

Bond-Lamberty B, Ballantyne A, Berryman E, Fluet-Chouinard E, Jian J, Morris K A, Rey A and Vargas R 2024 Twenty Years of Progress, Challenges, and Opportunities in Measuring and Understanding Soil Respiration J. Geophys. Res. Biogeosci. 129

Cleverly J 2011 Alice Springs Mulga OzFlux site OzFlux, Australian and New Zealand Flux Research and Monitoring [dataset]; http://hdl.handle.net/102.100.100/14217.

Cleverly J 2013 Ti Tree East OzFlux Site OzFlux, Australian and New Zealand Flux Research and Monitoring [dataset]; http://hdl.handle.net/102.100.100/14225.

Davidson E A and Janssens I A 2006 Temperature sensitivity of soil carbon decomposition and feedbacks to climate change Nature 440 165–73

Davidson E A, Janssens I A and Luo Y 2006 On the variability of respiration in terrestrial ecosystems: moving beyond Q10 Glob Change Biol 12 154–64

Ewenz C 2022a Yarramundi Control Paddock OzFlux: Australian and New Zealand Flux Research and Monitoring local [dataset]: MONc20ea067-9418-48ee-93d4-acab854dc664

Ewenz C 2022b Yarramundi Irrigated Paddock OzFlux: Australian and New Zealand Flux Research and Monitoring local [dataset]: MON1ee45abb-ed2f-4f11-bbd0-054f5fff3889

Fischer-Femal B J, Poulter B, Basu S, Miller J B, Lehman S J, Kaushik A, Colligan T and Michel S E 2025 Global Terrestrial C, 13C, and 14C Budgets from LPJ-iso, a New Isotope-Enabled Dynamic Global Vegetation Model

Frankenberg C *et al* 2011 New global observations of the terrestrial carbon cycle from GOSAT: Patterns of plant fluorescence with gross primary productivity Geophys. Res. Lett. 38 n/a-n/a

Friedlingstein P et al 2025 Global Carbon Budget 2024 Earth Syst. Sci. Data 17 965–1039

Gelaro R et al 2017 The Modern-Era Retrospective Analysis for Research and Applications, Version 2 (MERRA-2) Journal of Climate Volume 30 5419–54

Grace P 2019 Longreach Mitchell Grass Rangelands OzFlux tower site OzFlux, Australian and New Zealand Flux Research and Monitoring [dataset]; http://hdl.handle.net/102.100.100/100147.

Griebel A 2019 CumberlandPlain Melaleuca OzFlux, Australian and New Zealand Flux Research and Monitoring [dataset]; http://hdl.handle.net/102.100.100/77413.

Gunawardha D 2022 Alpine Peatland OzFlux: Australian and New Zealand Flux Research and Monitoring local [dataset]: MON7af69cc1-457b-48dd-8b78-54a6ea9bfdad

Haverd V, Smith B, Nieradzik L, Briggs P R, Woodgate W, Trudinger C M, Canadell J G and Cuntz M 2018 A new version of the CABLE land surface model (Subversion revision r4601) incorporating land use and land cover change, woody vegetation demography, and a novel optimisation-based approach to plant coordination of photosynthesis Geosci. Model Dev. 11 2995–3026

Haxeltine A and Prentice I C 1996 BIOME3: An equilibrium terrestrial biosphere model based on ecophysiological constraints, resource availability, and competition among plant functional types Global Biogeochem. Cycles 10 693–709

Keenan T F and Williams C A 2018 The Terrestrial Carbon Sink Annu. Rev. Environ. Resour. 43 219–43

Law B et al 2002 Environmental controls over carbon dioxide and water vapor exchange of terrestrial vegetation Agricultural and Forest Meteorology 113 97–120

Le Quéré C *et al* 2013 The global carbon budget 1959–2011 Earth Syst. Sci. Data 5 165–85

Lellei-Kovács E, Kovács-Láng E, Botta-Dukát Z, Kalapos T, Emmett B and Beier C 2011 Thresholds and interactive effects of soil moisture on the temperature response of soil respiration European Journal of Soil Biology 47 247–55

Liddell M 2013a Cape Tribulation OzFlux tower site OzFlux, Australian and New Zealand Flux Research and Monitoring [dataset]; http://hdl.handle.net/102.100.100/14242.

Liddell M 2013b Robson Creek OzFlux tower site OzFlux, Australian and New Zealand Flux Research and Monitoring [dataset]; http://hdl.handle.net/102.100.100/14243.

Liddell M 2013c Cow Bay OzFlux tower site OzFlux, Australian and New Zealand Flux Research and Monitoring [dataset]; http://hdl.handle.net/102.100.100/14244.

Lloyd J and Taylor J A 1994 On the Temperature Dependence of Soil Respiration Functional Ecology 8 315

MacBean N *et al* 2021 Dynamic global vegetation models underestimate net CO_2 flux mean and inter-annual variability in dryland ecosystems Environ. Res. Lett. 16 94023

Macfarlane C 2013 Great Western Woodlands OzFlux, Australian and New Zealand Flux Research and Monitoring [dataset]; http://hdl.handle.net/102.100.100/14226.

Mahecha M D *et al* 2010 Global convergence in the temperature sensitivity of respiration at ecosystem level Science 329 838–40

Melton J R, Shrestha R K and Arora V K 2015 The influence of soils on heterotrophic respiration exerts a strong control on net ecosystem productivity in seasonally dry Amazonian forests Biogeosciences 12 1151–68

Meng C, Xiao X, Wagle P, Zhang C, Pan L, Pan B, Qin Y and Newman G S 2024 Exponential or Unimodal Relationships Between Nighttime Ecosystem Respiration and Temperature at the Eddy Covariance Flux Tower Sites Ecology Letters 27 e14532

Metz E-M *et al* 2023 Soil respiration-driven CO_2 pulses dominate Australia's flux variability Science 379 1332–5

Moyano F E, Manzoni S and Chenu C 2013 Responses of soil heterotrophic respiration to moisture availability: An exploration of processes and models Soil Biology and Biochemistry 59 72–85

OzFlux 2025 OzFlux: Australian and New Zealand Flux Research and Monitoring https://www.ozflux.org.au/ (accessed 14 Feb 2025)

Pastorello G *et al* 2020 The FLUXNET2015 dataset and the ONEFlux processing pipeline for eddy covariance data Scientific Data 7 225

Pendall E 2015 Cumberland Plain OzFlux Tower Site OzFlux, Australian and New Zealand Flux Research and Monitoring [dataset]; http://hdl.handle.net/102.100.100/25164.

Phillips A 2015 Warra OzFlux tower site OzFlux, Australian and New Zealand Flux Research and Monitoring [dataset]; http://hdl.handle.net/102.100.100/22566.

Poulter B, Ciais P, Hodson E, Lischke H, Maignan F, Plummer S and Zimmermann N E 2011 Plant functional type mapping for earth system models Geosci. Model Dev. 4 993–1010

Poulter B *et al* 2014 Contribution of semi-arid ecosystems to interannual variability of the global carbon cycle Nature 509 600–3

Rowlings D 2011 Samford Ecological Research Facility OzFlux tower site OzFlux, Australian and New Zealand Flux Research and Monitoring [dataset]; http://hdl.handle.net/102.100.100/14219.

Schimel J, Balser T C and Wallenstein M 2007 Microbial stress-response physiology and its implications for ecosystem function Ecology 88 1386–94

Schroder I 2014 Arcturus Emerald OzFlux tower site OzFlux, Australian and New Zealand Flux Research and Monitoring [dataset]; http://hdl.handle.net/102.100.100/14249.

Shi H *et al* 2017 Assessing the ability of MODIS EVI to estimate terrestrial ecosystem gross primary production of multiple land cover types Ecological Indicators 72 153–64

Sierra C A, Trumbore S E, Davidson E A, Vicca S and Janssens I 2015 Sensitivity of decomposition rates of soil organic matter with respect to simultaneous changes in temperature and moisture J. Adv. Model. Earth Syst. 7 335–56

Silberstein R 2015, Gingin OzFlux, Australian and New Zealand Flux Research and Monitoring [dataset]; http://hdl.handle.net/102.100.100/22677.

Silva M 2022, Gatum Pasture OzFlux, Australian and New Zealand Flux Research and Monitoring; local [dataset]: MON34708884-3e7d-4c5a-ba8c-1597e1ff867d.

Simpson R 2012a Nimmo High Plains OzFlux Tower Site OzFlux, Australian and New Zealand Flux Research and Monitoring [dataset]; http://hdl.handle.net/102.100.100/14220.

Simpson R 2012b Dargo High Plains OzFlux Tower Site OzFlux, Australian and New Zealand Flux Research and Monitoring [dataset]; http://hdl.handle.net/102.100.100/14221.

Sitch S *et al* 2003 Evaluation of ecosystem dynamics, plant geography and terrestrial carbon cycling in the LPJ dynamic global vegetation model Glob Change Biol 9 161–85

Sitch S *et al* 2015 Recent trends and drivers of regional sources and sinks of carbon dioxide Biogeosciences 12 653–79

Sitch S *et al* 2024 Trends and Drivers of Terrestrial Sources and Sinks of Carbon Dioxide: An Overview of the TRENDY Project Global Biogeochem. Cycles 38

Tech C 2013 Calperum Chowilla OzFlux tower site OzFlux, Australian and New Zealand Flux Research and Monitoring [dataset]; http://hdl.handle.net/102.100.100/14236.

Tjoelker M G, Oleksyn J and Reich P B 2001 Modelling respiration of vegetation: evidence for a general temperature-dependent Q10 Glob Change Biol 7 223–30

Trudinger C M, Haverd V, Briggs P R and Canadell J G 2016 Interannual variability in Australia's terrestrial carbon cycle constrained by multiple observation types Biogeosciences 13 6363–83

Tucker C L and Reed S C 2016 Low soil moisture during hot periods drives apparent negative temperature sensitivity of soil respiration in a dryland ecosystem: a multi-model comparison Biogeochemistry 128 155–69

Unger S, Máguas C, Pereira J S, David T S and Werner C 2012 Interpreting post-drought rewetting effects on soil and ecosystem carbon dynamics in a Mediterranean oak savannah Agricultural and Forest Meteorology 154 9–18

Van Gorsel E 2012 Otway OzFlux tower site OzFlux, Australian and New Zealand Flux Research and Monitoring [dataset]; http://hdl.handle.net/102.100.100/14222.

Vicca S *et al* 2014 Can current moisture responses predict soil CO_2 efflux under altered precipitation regimes? A synthesis of manipulation experiments Biogeosciences 11 2991–3013

Wang L, Jiao W, MacBean N, Rulli M C, Manzoni S, Vico G and D'Odorico P 2022 Dryland productivity under a changing climate Nat. Clim. Chang. 12 981–94

Woodgate W 2013 Tumbarumba OzFlux tower site OzFlux, Australian and New Zealand Flux Research and Monitoring [dataset]; http://hdl.handle.net/102.100.100/14241.

Xu L, Baldocchi D D and Tang J 2004 How soil moisture, rain pulses, and growth alter the response of ecosystem respiration to temperature Global Biogeochem. Cycles 18

Zhou L, Tucker C J, Kaufmann R K, Slayback D, Shabanov N V and Myneni R B 2001 Variations in northern vegetation activity inferred from satellite data of vegetation index during 1981 to 1999 J. Geophys. Res. 106 20069–83

Zomer R and Trabucco A 2019 Global Aridity Index and Potential Evapotranspiration (ET0) Database: Version 3. figshare. Dataset. https://doi.org/10.6084/m9.figshare.7504448.v6

Zomer R J, Xu J and Trabucco A 2022 Version 3 of the Global Aridity Index and Potential Evapotranspiration Database Scientific Data 9 409

3. Discussion

In this thesis, three semiarid regions in the Southern Hemisphere are analyzed: Australia (Metz et al., 2023, 2025b), southern Africa (Metz et al., 2025a), and the South American Temperate region (Vardag et al., 2025). This chapter takes up the discussions included in the individual publications and provides a comprehensive analysis of shared findings among the studies. To this end, the first section, Section 3.1, addresses the opportunities given by the increasing amount of satellite CO_2 concentration measurements. The following Section 3.2 discusses the role of TER as a driver of CO_2 flux variability in semiarid environments. Section 3.3 compares and discusses the TRENDY model selections for the individual study regions and provides specific recommendations on how to improve the accuracy of the models. Finally, Section 3.4 follows up with a discussion of systematic errors in ensemble means.

3.1. The Potential of Satellite Measurements to Improve CO_2 Flux Estimates in Southern Hemispheric Regions

Metz et al. (2023), Metz et al. (2025a), and Vardag et al. (2025) investigate the information content that in situ and satellite CO_2 measurements can provide in atmospheric inversions estimating CO_2 fluxes in the Southern Hemisphere. The results show that in-situ-only inversions mostly stick close to the prior fluxes. This is a sign for a largely under-constrained inversion in which the measurements (in this case due to their sparseness) cannot add much information in the inversion. The posterior fluxes of the inversion therefore strongly rely on the assumed prior fluxes. This causes large uncertainties in the flux estimates which manifest in the large deviations among the three in-situ-only inversions CAMS, CarbonTracker, TM5-4DVar/IS (Metz et al., 2023, 2025a) and the in-situ-only inversions in the MIP/IS ensemble (Metz et al., 2025a). As the assumed prior fluxes of the models differ, their posterior estimates also differ substantially. Hence, when using in-situ-only inversions in regions with sparse in situ measurements one needs to keep in mind that their flux estimates contain only to a limited extent information about the state of the atmosphere and largely reflect the used prior information with the associated uncertainties. This is especially important because inversions normally do not provide the associated posterior uncertainty estimates, which could indicate the degree of uncertainty reduction reached by the assimilation of measurements. Therefore, a thorough analysis of the information content remains vital. Also FLUXCOM is affected by the general sparseness of measurements in semiarid regions. We find deviations of FLUXCOM from the other flux estimates (Metz et al., 2023, 2025a) indicating large uncertainties in the estimated fluxes. These uncertainties can be caused by a lack of training data in semiarid regions, as also pointed out by Jung et al. (2020). A newer version of FLUXCOM (FLUXCOM-X, Nelson et al., 2024) makes use of the growing measurement network capacities and, for example, includes more OzFlux flux towers in Australia to reduce uncertainty of estimates. Concluding, the sparse coverage of in situ measurements causes high uncertainties in CO_2 flux estimates of in situ measurement-based approaches in the study regions.

The satellites GOSAT and OCO-2 provide an extensive measurement coverage in the Southern Hemisphere. We find a good consistency of the satellite CO_2 products. In general, CO_2 concentrations and fluxes based on the two GOSAT datasets (ACOS and RemoTeC) agree well with each other and with those based on OCO-2. The small differences in the XCO_2 data from the two GOSAT retrievals can be partly explained by the different data sampling due to different filtering of the measurements, but are likely also caused by methodological differences in the retrievals (see Section 1.2.1, Figure A1 in Metz et al. (2025a), and Text S.2.2 in Vardag et al. (2025)). Furthermore, we find slightly smaller amplitudes in OCO-2-based CO_2 fluxes (MIP/OCO-2+IS) compared to GOSAT-based CO_2 fluxes in all three regions. This is likely caused by the slightly smaller seasonal amplitudes in OCO-2 XCO_2 in Australia and southern Africa compared to GOSAT XCO_2. Still, these differences are small and the seasonal timing of the OCO-2 and GOSAT CO_2 products agrees well. Hence, the satellites show a consistent picture of the land-atmosphere CO_2 exchange in southern hemispheric regions, which agrees well with (sparsely available) validation measurements of TCCON and COCCON.

Metz et al. (2023), Metz et al. (2025a), and Vardag et al. (2025) show that satellite data can fill the gaps of in situ measurements in the Southern Hemisphere. Assimilating GOSAT data in TM5-4DVar led to changes in the estimated posterior fluxes compared to TM5-4DVar/IS and prior fluxes. This proves that satellites provide additional information that is not contained in the prior fluxes or in situ measurements. In all three study regions, TM5-4DVar/GOSAT+IS shows larger fluxes than TM5-4DVar/IS. This results in seasonal amplitudes, which are larger by 38% for Australia, 67% for southern Africa and 6% for the South American Temperate region (see Table B.1). Furthermore, in Australia and less significantly in southern Africa, the TM5-4DVar/GOSAT+IS fluxes show a different seasonality than the fluxes of

TM5-4DVar/IS and the used prior. In the South American Temperate region, the seasonal timing of TM5-4DVar/GOSAT+IS and TM5-4DVar/IS agrees quite well, verifying that the prior fluxes already capture well the seasonal timing of the fluxes. Concluding, these findings underline the importance of taking into account satellite data, where in situ measurements do not provide sufficient information. Assimilating both together in an inversion enhances the accuracy of the estimated carbon fluxes by taking into account all available CO_2 measurement information.

In this thesis, we only use one atmospheric inversion, TM5-4DVar, to estimate CO_2 fluxes based on GOSAT measurements. To test the impact of the chosen atmospheric inversion model on flux estimates, we perform a detailed analysis of the different inversion models in the OCO-2 MIP ensembles (MIP/OCO-2+IS and MIP/IS) for southern Africa (Metz et al., 2025a). The models differ strongly in the estimated posterior fluxes even though they assimilate the same (in situ or OCO-2 satellite) measurements. The deviations among the posterior fluxes reduce when assimilating OCO-2 and in situ measurements together (MIP/OCO-2+IS) compared to MIP/IS and the prior fluxes. This confirms that the satellite provides additional information in the inversions as discussed above. However, also for MIP/OCO-2+IS the differences among the models remain substantial. We find that these deviations originate in different weights which the inversions put on the measurements, for example, by using different measurement uncertainties. We were able to show that the models putting the most weight on the OCO-2 data agreed the best with each other and with TM5-4DVar/GOSAT+IS fluxes. This confirms that satellite-based inversions show a consistent picture of CO_2 fluxes when weighting the satellite measurements sufficiently. Unfortunately, the inversions do not provide other evaluation metrics, for example, the covariance matrices used or other parameters like the averaging kernel or information content for the Bayesian inversions. Such metrics would enable a more profound analysis of how much the assumed measurement uncertainties drive the differences between the inversions compared to other parameters such as differences in the modeled atmospheric transport and inversion strategies. Concluding, the OCO-2 MIP analysis demonstrates that not only the used measurement data, but also the implementation of those heavily influence the flux estimates. Measurements must be sufficiently weighted to obtain a reliable flux estimate. If done so, the MIP/OCO-2+IS inversions agree well with the TM5-4DVar/GOSAT+IS inversions and confirm the findings described above.

In conclusion, Metz et al. (2023), Metz et al. (2025a), and Vardag et al. (2025) clearly show the high value of the long records of satellite XCO_2 measurements to improve regional scale CO_2 flux estimates, in the whole Southern Hemisphere. These results add to the growing number of studies that point out the advantages of satellites to complement in situ measurements in atmospheric inversions (e.g. Basu et al., 2013;

Detmers et al., 2015; Ma et al., 2016; Villalobos et al., 2020). GOSAT now provides 16 years of measurements and is still measuring. The dataset is and will continuously be complemented by OCO-2 and future CO_2 satellite missions with more extensive measurements. Already now the dataset covers three strong El Nino periods and one strong La Nina year. With more occurrences of such repeating climate patterns, more analyses of the climatic drivers of global carbon fluxes and the contributing regions will be possible. Furthermore, such a long-term dataset will enable multidecadal trend analyses of CO_2 concentrations and fluxes.

3.2. Vegetation Processes Driving the Carbon Cycle in Semiarid Regions

This thesis identifies dominant CO_2 exchange processes that drive the variability of CO_2 fluxes in semiarid regions. The publications included in this thesis jointly show that respiration, especially Rh emissions, plays an important role in the carbon flux dynamics in semiarid regions. Metz et al. (2023) shows that soil respiration causes large CO_2 emission pulses at the end of the dry season in semiarid areas, which drive the interannual and seasonal variability of CO_2 fluxes in Australia. Metz et al. (2025a) and Vardag et al. (2025) find that such respiration emissions in response to the start of the rainy season also occur in semiarid parts of southern Africa and the South American Temperate region. In these two regions, these emissions largely impact the seasonal variability of the continental-scale carbon fluxes. Thereby, the results are robust with respect to the exact definition of semiarid regions, as the respiration signal dominates the CO_2 flux variability in the whole study regions.

We identify soil moisture as a main driver of TER and Rh in our study regions. Metz et al. (2025b) shows that the sensitivity of TER to soil moisture across aridity gradients in Australia is the highest in semiarid regions. In humid parts of Australia, soil moisture has only a minor impact on TER. The respiration pulses in Metz et al. (2023), Metz et al. (2025a) and Vardag et al. (2025) are driven by increasing soil moisture at the beginning of the rainy season. They also only occur in the semiarid parts of the study regions and are not found in the humid areas. Soil moisture-driven respiration emissions are therefore found to be important and characteristic for the carbon cycle in semiarid regions.

Metz et al. (2023), Metz et al. (2025a) and Vardag et al. (2025) find that the continental-scale Rh emission pulses are not only driven by increasing soil moisture but are also conditional on rewetting of formerly dry soils. This finding is consistent with local observations of immediate and rapid increases in measured CO_2 emissions with precipitation events on a daily timescale (see Figure S11 in Metz et al. (2023),

Figure A15 in Metz et al. (2025a) and Figure S11 in Vardag et al. (2025)). Such rapid responses of microbial respiration to soil rewetting events are described in literature under the term "Birch effect" and have been shown to release more CO_2 than constantly moist soils (Birch, 1964; Jarvis et al., 2007; Casals et al., 2011; Singh et al., 2023, see also Section 1.1.4). Our studies now indicate that the Birch effect impacts the carbon flux dynamics in Australia, southern Africa and the South American Temperate region and mainly drives the observed early rapid increase in respiration at the beginning of the rainy season. With that, we suggest that this formerly only locally known effect is also relevant for the seasonality and interannual variability of carbon fluxes on continental scale.

Concluding, we find respiration dynamics driven by soil moisture and rewetting of soils to have a significant contribution to the CO_2 flux variability in all three semiarid study regions and thus throughout the Southern Hemisphere and potentially in other global semi-arid regions. Hence, respiration dynamics are a large contributor to the variability of the global carbon sink. In particular, we discover the important role of rewetting-driven respiration pulses and find different TER response regimes to soil moisture. With these findings, we are able to demonstrate that precipitation and soil moisture are important drivers of interannual and seasonal variability in the land CO_2 sink of semiarid regions. We further show that the impact of precipitation and soil moisture on the carbon exchange in semiarid regions also originates from their large impact on soil respiration and not only from their impact on GPP like found in Piao et al. (2020) and Haverd et al. (2017).

3.3. Process Implementations in the TRENDY Models

In all three study regions in the Southern Hemisphere, Australia (Metz et al., 2023), southern Africa (Metz et al., 2025a), and the South American Temperate region (Vardag et al., 2025), we are able to identify TRENDY models that agree well with the NBP and NEE estimates of the TM5-4DVar/GOSAT+IS inversion. We identify implemented processes they have in common and which can therefore be assumed to play a dominant role in the carbon cycle in the study regions. Based on our findings, we were able to derive suggestions on how to improve the TRENDY models in semiarid regions.

TRENDY model selections for the individual study regions

The following models were identified out of the 18 TRENDY models to perform best in the individual regions:

- Australia:
  LPJ, JSBACH, **YIBs**, **<u>OCN</u>**, and **CLASSIC**
- Southern Africa:
  CABLE-POP, **ORCHIDEE**, ORCHIDEEv3 (**<u>OCN</u>**)
- South American Temperate region:
  CLASSIC, **<u>OCN</u>** (**ORCHIDEE**, **YIBs**, ISAM, ISBA-CTRIP).

The models listed in two regions are given in **bold**, those listed in three regions are **<u>bold-underlined</u>**. The models in brackets do not belong to the final selection. In the South American Temperate region they have only been included in the loose selection, which fits slightly worse to TM5-4DVar/GOSAT+IS NBP (see Figure S8 in Vardag et al. (2025)). In southern Africa, the model in the bracket only passed the NEE and NBP comparison but failed in the SIF comparison. There is no model which belongs to the final strict selection in all three regions. OCN is in the final selection for Australia and the South American Temperate region but gets excluded in southern Africa as OCN GPP does not align well with GOME-2 SIF. It is important to note, that the SIF comparison was only performed in southern Africa and not in Australia and the South American Temperate region (see Section 1.5.3). The exclusion of OCN in southern Africa underlines the importance of not only constraining net fluxes but also gross fluxes. This is especially important when the gross fluxes vary, like in southern Africa. For Australia and the South American Temperate region, the gross fluxes of the selected TRENDY models are largely consistent.

Commonalities of the selected models

In all three publications, we identify a temporal dephasing between the increase of GPP and the increase of Rh ('GPP-Rh-dephasing') in semiarid areas at the beginning of the rainy season to be needed to accurately capture the NBP and NEE fluxes. All selected models have parameterizations so that Rh increases rapidly with the start of the rainy season, while GPP increases delayed or independently (see Section 1.4.1). In terms of vegetation processes, these parameterizations translate in soil microbes being located mainly close to the surface as for example shown by Taylor et al. (2002) and reacting to the increasing shallow soil moisture with the beginning of the rainy season. For GPP, the sensitivity to deep soil moisture refers to plant roots being located in deeper soils, which get rewetted delayed compared to shallow soils. The 'growing degree days'-implementation translates to plants sprouting and needing to develop a relevant leave area before the plant biomass can grow.

In southern Africa and the South American Temperate region also some other models, that do not belong to the selected models, show the GPP-Rh-dephasing.

Therefore, the dephasing seems to be a necessary but not sufficient prerequisite to model the carbon fluxes in the regions accurately. This is to be expected as the dephasing shapes the seasonal cycle of the carbon fluxes but is not the only process driving the net CO_2 exchange between land and atmosphere. Carbon fluxes at other times than the beginning of the rainy season, as well as the seasonal amplitude of the fluxes also need to be modeled accurately.

Why does the model selection differ between the study regions?

By being selected, the TRENDY models proof to be able to capture carbon flux dynamics in semiarid areas correctly. Still, the model selections differ between the study regions. Hence, a model which accurately captures the CO_2 fluxes in one semiarid region does not necessarily perform well in other semiarid regions. This raises the question, why the selected models do not perform well in all semiarid study regions?

Most of the selected models were found to also have a GPP-Rh-dephasing in the other study regions. However, these models are not included in the other selections because they perform worse with respect to other important characteristics of the seasonality of CO_2 fluxes. An example of such a model is JSBACH. JSBACH shows the GPP-Rh-dephasing not only in Australia (see Figure B.1), where it belongs to the model selection, but also in southern Africa (see Figure B.2). However, JSBACH fails to accurately model the seasonal timing of GPP, TER and NBP in southern Africa. The fluxes are typically delayed by two months compared with TM5-4DVar/GOSAT+IS and the selected TRENDY models. Therefore, JSBACH does not belong to the selected models in southern Africa. There are multiple potential reasons for JSBACH to perform well in Australia but not in southern Africa. As shown in Figure B.3, PFTs of JSBACH in Australia differ from those in southern Africa. For example, there are more raingreen shrubs in Australia than in southern Africa and, vice versa, there are more tropical trees in southern Africa than in Australia. Hence, while JSBACH performs well in the PFTs dominating Australia, it could perform worse for those in southern Africa. Furthermore, different climate conditions in the study regions can be another reason for the different performance of JSBACH. For example, the mean precipitation in southern Africa is higher than in Australia (see Figure 3c in Metz et al. (2023) and Figure A14 in Metz et al. (2025a)). This could lead to deviations, such as time delays, in the response of CO_2 fluxes to the different amounts of precipitation.

There are also some of the selected models which do not have a GPP-Rh-dephasing in the other study regions and, therefore, directly disqualify for the model selections there. YiBs is one of these models. It belongs to the selected models in Australia, but in southern Africa it does not show a significant dephasing and is therefore unable to accurately capture the NBP fluxes (see Figures B.4 and B.5). Here again, the differences in the assumed PFTs (see Figure B.6) and in the climate conditions in the two regions could be the reason for the different behavior of YIBs with respect to the dephasing between the two regions.

Concluding, different climate conditions or different PFT distributions might explain why the model selections do not agree in all three regions. This goes along with the current literature showing that the assumed PFTs in a region can vary significantly between TRENDY models (Teckentrup et al., 2021, for Australia) and that, especially in dry regions, the assumed land cover classification significantly influences the sensitivity of the carbon fluxes to climate (Poulter et al., 2011). TRENDY ensemble runs with a common set of PFTs in all models could provide further insights into the differences between the models and their performances.

Possible Improvements for the TRENDY models

The publications in this thesis point out uncertainties in the modeling of CO_2 fluxes in semiarid regions and call for an improvement of the TER parameterizations in state-of-the-art vegetation models. This thesis presents concrete suggestions on how to improve the parameterization in vegetation models for semiarid ecosystems.

At the maximum, five out of the 18 TRENDY models are selected in the individual study regions. Hence, at least two-thirds of the TRENDY ensemble fail in capturing the carbon fluxes in the semiarid regions accurately. This underlines the large uncertainties of the TRENDY ensemble in semiarid regions and calls for improving the implementation of soil-rewetting processes in the majority of models. Thereby, a first and important step would be the implementation of different response times of Rh and GPP to soil rewetting. In the discussion above and in Section 1.4.1, the different parameterizations to achieve such a behavior are discussed. Using soil moisture in shallow and deeper soil depths to drive Rh and GPP, respectively, is a commonly used way to create the necessary time-lag.

Moreover, we show that also the selected models can be improved. Metz et al. (2025b) shows that the well-performing model LPJ in Australia has difficulties modeling TER in the transition of dry to humid soil conditions. We show that a more sophisticated parameterization of TER in response to soil moisture is necessary for the model to perform correctly in arid as well as in humid regions. This includes a more complex dependence of Rh on soil moisture. Low or even negative sensitivities of Rh to high soil moisture levels are needed to reflect limited Rh under supra-optimal soil moisture conditions. Furthermore, a comprehensive evaluation of soil moisture dynamics and the water-stress threshold for Ra is needed to improve the performance of Ra in LPJ.

Finally, the selected TRENDY models do not explicitly capture the Birch effect which we observe in our study regions. The parameterizations causing the GPP-Rh-dephasing are based on empirical relationships and generalize and consolidate existing processes. For example, the response function of Rh to soil moisture is described by simple functional dependencies (see e.g., Equation 4 in Metz et al., 2025b) found in empirical studies. Microbial communities, their dynamics, and the impact of rewetting on substrate availability are not modeled in the TRENDY models. They are, therefore, not able to model the Birch effect explicitly. The resulting gross fluxes are correct in the study regions and study times because the used generalized description incorporates the enhanced release of CO_2 caused by the Birch effect. For example, assuming a stronger general sensitivity of Rh to soil moisture than given in reality can compensate for an enhanced release of CO_2 by the Birch effect. However, as soon as environmental conditions change, the missing explicit process implementation can lead to inaccuracies in the estimated fluxes. Modeling the dynamics of microbial communities and the effect of rewetting on substrate availability explicitly could therefore improve the reliability of the DGVMs for semiarid regions.

3.4. Systematic Errors in Model Ensembles

This dissertation analyzes and discusses the source of uncertainties in multiple model ensembles, which estimate global CO_2 fluxes. The two most important ensemble datasets are the TRENDY ensemble of DGVMs and the OCO-2 MIP ensemble of atmospheric inversions. TRENDY flux estimates are used in the Global Carbon Project reports and are compared to top-down fluxes of atmospheric inversions. Thereby, the mean of the individual ensembles is used as the best flux estimate and the standard deviation (TRENDY) and range (atmospheric inversions) are used as uncertainty measure (Friedlingstein et al., 2025) .

In contrast to that, the publications in this thesis show that the mean of the TRENDY model ensemble and for southern Africa the mean of the OCO-2 MIP ensemble (MIP/OCO-2+IS) do not provide the best flux estimates for the study regions. Instead of simply using the ensemble mean of TRENDY and MIP/OCO-2+IS, we perform an informed selection of the best performing models for each region. We demonstrate that by using atmospheric constraints (TM5-4DVar/GOSAT+IS fluxes and SIF measurements for TRENDY, and OCO-2 cosamples for MIP/OCO-2+IS) on the ensembles we succeed in selecting the best performing models. This significantly reduces the uncertainties of the ensemble estimates. For example, through the selection of the TRENDY models, the ensemble uncertainty (mean standard deviation among the models) is reduced by a factor of 1.8, 2.6, and 2.6 for Australia, southern Africa, and the South American Temperate region, respectively. While the reduction of the uncertainty is obvious when performing a sub-selection, the magnitude of the uncertainty reduction is impressive.

We analyze why some models perform worse than others. We find systematic errors in the remaining ensemble members that do not belong to the selected models. In case of TRENDY, we identify an implementation of a dephasing between GPP and Rh at the beginning of the rainy season as a prerequisite for vegetation models to correctly capture the carbon flux dynamics in semiarid regions. Models without this implementation fail in capturing the carbon flux dynamics, and therefore introduce a systematic error in the TRENDY mean. In case of the MIP/OCO-2+IS models in southern Africa, we find that those models that put a considerable weight on the satellite measurements in the inversion align best with our GOSAT-based flux estimate. OCO-2 MIP models that do not sufficiently weight the measurements show much larger deviations. Here again, not accounting enough for the assimilated measurements introduces a systematic error in the ensemble mean of MIP/OCO-2+IS. These systematic errors, in contrast to statistical errors (e.g., due to a parameter choice), do not cancel out when the mean of the whole ensemble is taken. This underlines the value of using atmospheric constraints to exclude models with systematic errors.

Finally, it is important to note that there is no common set of models which performs best for all world regions and could be used globally. The differences in the TRENDY model selections in the three study regions (see Section 3.3) already make that clear. In order to obtain an improved global estimate, it would rather need a reliable uncertainty assessment for each model and each world region so that an uncertainty-weighted average can be calculated. This reinforces the call for developing and reporting uncertainty measures for atmospheric inversions. Furthermore, it underlines the importance of regional validation studies of vegetation models. Such studies can improve our process understanding and can identify the parameter implementations causing the largest uncertainties in the flux estimates. The presented publications take an important step in this direction by pointing out uncertainties in the individual CO_2 flux estimates, identifying driving processes of CO_2 exchange, and discovering deficiencies in respiration parameterizations of vegetation models for the entire Southern Hemisphere.

4. Summary

This thesis provides CO_2 flux estimates from 2009 to 2018 based on satellite measurements for three largely semiarid regions in the Southern Hemisphere: Australia, southern Africa, and the South American Temperate Transcom region. Furthermore, it deciphers vegetation processes that drive the seasonal and interannual CO_2 exchange in the regions and identifies their climatic drivers.

The presented work demonstrates that satellite data can improve sub-continental scale carbon flux estimates. We first show that CO_2 flux estimates by in-situ-only inversions have large uncertainties as the sparse in situ measurements cannot provide sufficient information about the carbon dynamics in the study regions. Satellite data is found to provide additional information, complementing in situ measurements. We show that the CO_2 concentration and flux products of the GOSAT and OCO-2 satellites compare well. The satellite-based flux estimates have significantly lower uncertainties compared to in-situ-only inversions. With that, this work underlines the importance of taking into account satellite CO_2 measurements in CO_2 flux estimates in the Southern Hemisphere.

Also bottom-up DGVMs of the TRENDY ensemble are found to deviate strongly in the study regions. We use the top-down satellite-based CO_2 fluxes and SIF measurements as atmospheric constraints to evaluate the DGVMs. This combination of top-down and bottom-up approaches allows us to use the advantages of both datasets. We make use of the robust GOSAT-based CO_2 flux estimate to only select vegetation models that capture the same flux dynamics. We then use the gross fluxes of the selected TRENDY models and the knowledge about their implemented processes. This allows us to decipher vegetation processes that drive the net ecosystem exchange of CO_2. We identify a dephasing in the increase of Rh and GPP in semiarid parts of the study regions to drive the net CO_2 flux variability. Using precipitation data and daily flux tower measurements, we show that soil rewetting at the beginning of the rainy season drives the early increase in Rh. We find short-term CO_2 emissions by soil respiration pulses in semiarid areas which are caused by precipitation events. These short-term rewetting-driven respiration pulses are known on local scale under the term "Birch effect". The results in Metz et al. (2023) indicate that these local pulses accumulate over Australia and cause large CO_2 emissions that drive the seasonal and interannual variability of the continents' CO_2 fluxes. We find a dephasing of Rh and

GPP and the occurrence of such rewetting-driven respiration pulses also in southern Africa and the South American Temperate region. In these two study regions, they are shown to substantially impact the seasonality of net fluxes. With our results, we reveal the large-scale relevance of the previously only locally known effect of soil respiration pulses. The accumulated effect is shown to be large enough to cause CO_2 emissions which drive the variability in the regional ecosystem CO_2 exchange and to be detected from space by satellite.

We investigate the sensitivity of TER to soil moisture in more detail using measurements of 40 flux tower stations in Australia. We find different response regimes of TER to soil moisture. Soil moisture emerges to be a limiting factor for TER in arid and semiarid regions which is reflected in the large sensitivities of TER to soil moisture. In humid regions, however, soil moisture is found to have no impact on TER indicating that TER is not water-limited. The publications included in this thesis jointly show that soil moisture-driven respiration emissions are an important and characteristic driver of the carbon cycle in semiarid regions.

Based on the results of this thesis, specific recommendations on how to improve the CO_2 flux estimates from DGVMs in semiarid regions are derived. We show that TRENDY models need to better represent soil rewetting processes. The necessary dephasing of Rh and GPP could be achieved by implementing different response times of Rh and GPP to the increase of soil moisture at the beginning of the rainy season. Explicitly implementing microbial community dynamics could further enhance the robustness of the modeled respiration. Finally, we find that DGVMs struggle in capturing the response of respiration fluxes to soil moisture in the transition from dry to humid regimes. We emphasize that a more sophisticated parameterization of TER sensitivity to soil moisture is necessary in models to perform correctly in arid as well as humid regions. For example, we show that a declining or negative sensitivity to high soil moisture levels is needed in the implementation of Rh.

In conclusion, this thesis improves our estimates and understanding of the carbon cycle in the entire Southern Hemisphere. Using the growing number of satellite measurements, we are able to reduce the uncertainties of current state-of-the-art regional CO_2 flux estimates significantly. We succeed in deciphering processes driving the variability in CO_2 fluxes and thereby reveal the continental scale relevance of the so far only locally known effect of soil respiration pulses. This work calls for improving the representation of soil rewetting processes in semiarid regions in DGVMs and provides specific recommendations to do so. With the findings of this thesis, we enhance the process understanding of semiarid ecosystems, which improves our ability to model the global carbon cycle in response to changing climate conditions in the future.

Bibliography

Ahlström, A., Raupach, M. R., Schurgers, G., Smith, B., Arneth, A., Jung, M., Reichstein, M., Canadell, J. G., Friedlingstein, P., Jain, A. K., Kato, E., Poulter, B., Sitch, S., Stocker, B. D., Viovy, N., Wang, Y. P., Wiltshire, A., Zaehle, S., and Zeng, N. (2015). The dominant role of semi-arid ecosystems in the trend and variability of the land CO_2 sink. *Science*, 348(6237):895–899. `https://doi.org/10.1126/science.aaa1668`.

Aubinet, M., Vesala, T., and Papale, D. (2012). *Eddy Covariance: A practical guide to measurement and data analysis.* Springer atmospheric sciences. Springer, Dordrecht and Heidelberg. ISBN: 9789400723504.

Austin, A. T., Yahdjian, L., Stark, J. M., Belnap, J., Porporato, A., Norton, U., Ravetta, D. A., and Schaeffer, S. M. (2004). Water pulses and biogeochemical cycles in arid and semiarid ecosystems. *Oecologia*, 141(2):221–235. `https://doi.org/10.1007/s00442-004-1519-1`.

Baldocchi, D., Falge, E., Gu, L., Olson, R., Hollinger, D., Running, S., Anthoni, P., Bernhofer, C., Davis, K., Evans, R., Fuentes, J., Goldstein, A., Katul, G., Law, B., Lee, X., Malhi, Y., Meyers, T., Munger, W., Oechel, W., Paw, K. T., Pilegaard, K., Schmid, H. P., Valentini, R., Verma, S., Vesala, T., Wilson, K., and Wofsy, S. (2001). FLUXNET: A new tool to study the temporal and spatial variability of ecosystem–scale carbon dioxide, water vapor, and energy flux densities. *Bulletin of the American Meteorological Society*, 82(11):2415–2434. https://doi.org/10.1175/1520-0477(2001)082<2415:FANTTS>2.3.CO;2.

Baldocchi, D., Ryu, Y., and Keenan, T. (2016). Terrestrial carbon cycle variability. *F1000Research*, 5. `https://doi.org/10.12688/f1000research.8962.1`.

Ballantyne, A. P., Alden, C. B., Miller, J. B., Tans, P. P., and White, J. W. C. (2012). Increase in observed net carbon dioxide uptake by land and oceans during the past 50 years. *Nature*, 488(7409):70–72. `https://doi.org/10.1038/nature11299`.

Barba, J., Cueva, A., Bahn, M., Barron-Gafford, G. A., Bond-Lamberty, B., Hanson, P. J., Jaimes, A., Kulmala, L., Pumpanen, J., Scott, R. L., Wohlfahrt, G., and

Vargas, R. (2018). Comparing ecosystem and soil respiration: Review and key challenges of tower-based and soil measurements. *Agricultural and Forest Meteorology*, 249:434–443. https://doi.org/10.1016/j.agrformet.2017.10.028.

Bastos, A., Naipal, V., Ahlström, A., MacBean, N., Smith, W. K., and Poulter, B. (2022). Semiarid ecosystems. In *Balancing Greenhouse Gas Budgets*, pages 311–335. Elsevier. https://doi.org/10.1016/B978-0-12-814952-2.00012-5.

Bastos, A., O'Sullivan, M., Ciais, P., Makowski, D., Sitch, S., Friedlingstein, P., Chevallier, F., Rödenbeck, C., Pongratz, J., Luijkx, I. T., Patra, P. K., Peylin, P., Canadell, J. G., Lauerwald, R., Li, W., Smith, N. E., Peters, W., Goll, D. S., Jain, A. K., Kato, E., Lienert, S., Lombardozzi, D. L., Haverd, V., Nabel, J. E. M. S., Poulter, B., Tian, H., Walker, A. P., and Zaehle, S. (2020). Sources of uncertainty in regional and global terrestrial CO_2 exchange estimates. *Global Biogeochemical Cycles*, 34(2):e2019GB006393. https://doi.org/10.1029/2019GB006393.

Basu, S., Guerlet, S., Butz, A., Houweling, S., Hasekamp, O., Aben, I., Krummel, P., Steele, P., Langenfelds, R., Torn, M., Biraud, S., Stephens, B., Andrews, A., and Worthy, D. (2013). Global CO_2 fluxes estimated from GOSAT retrievals of total column CO_2. *Atmospheric chemistry and physics*, 13(17):8695–8717. https://doi.org/10.5194/acp-13-8695-2013.

Bennedsen, M., Hillebrand, E., and Koopman, S. J. (2019). Trend analysis of the airborne fraction and sink rate of anthropogenically released CO_2. *Biogeosciences*, 16(18):3651–3663. https://doi.org/10.5194/bg-16-3651-2019.

Beringer, J., Hutley, L. B., McHugh, I., Arndt, S. K., Campbell, D., Cleugh, H. A., Cleverly, J., Resco de Dios, V., Eamus, D., Evans, B., Ewenz, C., Grace, P., Griebel, A., Haverd, V., Hinko-Najera, N., Huete, A., Isaac, P., Kanniah, K., Leuning, R., Liddell, M. J., Macfarlane, C., Meyer, W., Moore, C., Pendall, E., Phillips, A., Phillips, R. L., Prober, S. M., Restrepo-Coupe, N., Rutledge, S., Schroder, I., Silberstein, R., Southall, P., Yee, M. S., Tapper, N. J., van Gorsel, E., Vote, C., Walker, J., and Wardlaw, T. (2016). An introduction to the Australian and New Zealand flux tower network – OzFlux. *Biogeosciences*, 13(21):5895–5916. https://doi.org/10.5194/bg-13-5895-2016.

Beringer, J., Moore, C. E., Cleverly, J., Campbell, D. I., Cleugh, H., de Kauwe, M. G., Kirschbaum, M. U. F., Griebel, A., Grover, S., Huete, A., Hutley, L. B., Laubach, J., van Niel, T., Arndt, S. K., Bennett, A. C., Cernusak, L. A., Eamus, D., Ewenz, C. M., Goodrich, J. P., Jiang, M., Hinko-Najera, N., Isaac, P., Hobeichi, S., Knauer, J., Koerber, G. R., Liddell, M., Ma, X., Macfarlane, C., McHugh, I. D., Medlyn, B. E., Meyer, W. S., Norton, A. J., Owens, J., Pitman, A., Pendall, E., Prober, S. M., Ray, R. L., Restrepo-Coupe, N., Rifai, S. W., Rowlings, D., Schipper, L., Silberstein, R. P., Teckentrup, L., Thompson, S. E., Ukkola, A. M., Wall, A., Wang, Y.-P., Wardlaw, T. J., and Woodgate, W. (2022). Bridge to the future: Important lessons from 20 years of ecosystem observations made by the OzFlux network. *Global Change Biology*, 28(11):3489–3514. `https://doi.org/10.1111/gcb.16141`.

Birch, H. F. (1964). Mineralisation of plant nitrogen following alternate wet and dry conditions. *Plant and Soil*, 20(1):43–49. `https://doi.org/10.1007/bf01378096`.

Bond-Lamberty, B., Bailey, V. L., Chen, M., Gough, C. M., and Vargas, R. (2018). Globally rising soil heterotrophic respiration over recent decades. *Nature*, 560(7716):80–83. `https://doi.org/10.1038/s41586-018-0358-x`.

Bond-Lamberty, B., Ballantyne, A., Berryman, E., Fluet-Chouinard, E., Jian, J., Morris, K. A., Rey, A., and Vargas, R. (2024). Twenty years of progress, challenges, and opportunities in measuring and understanding soil respiration. *Journal of Geophysical Research: Biogeosciences*, 129(2). `https://doi.org/10.1029/2023JG007637`.

Buchwitz, M., Reuter, M., Schneising, O., Hewson, W., Detmers, R. G., Boesch, H., Hasekamp, O. P., Aben, I., Bovensmann, H., Burrows, J. P., Butz, A., Chevallier, F., Dils, B., Frankenberg, C., Heymann, J., Lichtenberg, G., de Mazière, M., Notholt, J., Parker, R., Warneke, T., Zehner, C., Griffith, D., Deutscher, N. M., Kuze, A., Suto, H., and Wunch, D. (2017). Global satellite observations of column-averaged carbon dioxide and methane: The GHG-CCI XCO_2 and XCH4 CRDP3 data set. *Remote Sensing of Environment*, 203:276–295. `https://doi.org/10.1016/j.rse.2016.12.027`.

Butz, A. (2022). RemoTeC full-physics retrieval GOSAT/TANSO-FTS Level 2 bias-corrected XCO_2 version 2.4.0 operated at Heidelberg University. `https://doi.org/10.5281/zenodo.5886662`.

Butz, A., Guerlet, S., Hasekamp, O., Schepers, D., Galli, A., Aben, I., Frankenberg, C., Hartmann, J.-M., Tran, H., Kuze, A., Keppel-Aleks, G., Toon, G., Wunch, D., Wennberg, P., Deutscher, N., Griffith, D., Macatangay, R., Messerschmidt, J., Notholt, J., and Warneke, T. (2011). Toward accurate CO_2 and CH_4 observations from GOSAT. *Geophysical Research Letters*, 38(14). `https://doi.org/10.1029/2011GL047888`.

Byrne, B., Baker, D. F., Basu, S., Bertolacci, M., Bowman, K. W., Carroll, D., Chatterjee, A., Chevallier, F., Ciais, P., Cressie, N., Crisp, D., Crowell, S., Deng, F., Deng, Z., Deutscher, N. M., Dubey, M. K., Feng, S., García, O. E., Griffith, D. W. T., Herkommer, B., Hu, L., Jacobson, A. R., Janardanan, R., Jeong, S., Johnson, M. S., Jones, D. B. A., Kivi, R., Liu, J., Liu, Z., Maksyutov, S., Miller, J. B., Miller, S. M., Morino, I., Notholt, J., Oda, T., O'Dell, C. W., Oh, Y.-S., Ohyama, H., Patra, P. K., Peiro, H., Petri, C., Philip, S., Pollard, D. F., Poulter, B., Remaud, M., Schuh, A., Sha, M. K., Shiomi, K., Strong, K., Sweeney, C., Té, Y., Tian, H., Velazco, V. A., Vrekoussis, M., Warneke, T., Worden, J. R., Wunch, D., Yao, Y., Yun, J., Zammit-Mangion, A., and Zeng, N. (2023). National CO_2 budgets (2015–2020) inferred from atmospheric CO_2 observations in support of the global stocktake. *Earth System Science Data*, 15(2):963–1004. https://doi.org/10.5194/essd-15-963-2023.

Byrne, B., Liu, J., Lee, M., Baker, I., Bowman, K. W., Deutscher, N. M., Feist, D. G., Griffith, D. W. T., Iraci, L. T., Kiel, M., Kimball, J. S., Miller, C. E., Morino, I., Parazoo, N. C., Petri, C., Roehl, C. M., Sha, M. K., Strong, K., Velazco, V. A., Wennberg, P. O., and Wunch, D. (2020). Improved constraints on northern extratropical CO_2 fluxes obtained by combining surface–based and space–based atmospheric CO_2 measurements. *Journal of Geophysical Research: Atmospheres*, 125(15). https://doi.org/10.1029/2019JD032029.

Carbontracker Team (2019). Compilation of near real time atmospheric carbon dioxide data; obspack_co2_1_NRT_v5.0_2019-08-13. https://doi.org/10.25925/20190813.

Casals, P., Lopez-Sangil, L., Carrara, A., Gimeno, C., and Nogués, S. (2011). Autotrophic and heterotrophic contributions to short-term soil CO_2 efflux following simulated summer precipitation pulses in a Mediterranean dehesa. *Global Biogeochemical Cycles*, 25(3). https://doi.org/10.1029/2010GB003973.

Chandra, N., Patra, P. K., Niwa, Y., Ito, A., Iida, Y., Goto, D., Morimoto, S., Kondo, M., Takigawa, M., Hajima, T., and Watanabe, M. (2022). Estimated regional CO_2 flux and uncertainty based on an ensemble of atmospheric CO_2 inversions. *Atmospheric Chemistry and Physics*, 22(14):9215–9243. https://doi.org/10.5194/acp-22-9215-2022.

Chen, Z., Liu, J., Henze, D. K., Huntzinger, D. N., Wells, K. C., Sitch, S., Friedlingstein, P., Joetzjer, E., Bastrikov, V., Goll, D. S., Haverd, V., Jain, A. K., Kato, E., Lienert, S., Lombardozzi, D. L., McGuire, P. C., Melton, J. R., Nabel, Julia E. M. S., Poulter, B., Tian, H., Wiltshire, A. J., Zaehle, S., and Miller, S. M. (2021). Linking global terrestrial CO_2 fluxes and environmental drivers: inferences from the Orbiting Carbon Observatory 2 satellite and terrestrial biospheric models. *Atmospheric Chemistry and Physics*, 21(9):6663–6680. https://doi.org/10.5194/acp-21-6663-2021.

Chevallier, F., Ciais, P., Conway, T. J., Aalto, T., Anderson, B. E., Bousquet, P., Brunke, E. G., Ciattaglia, L., Esaki, Y., and Fröhlich, M. (2010). CO_2 surface fluxes at grid point scale estimated from a global 21 year reanalysis of atmospheric measurements. *Journal of Geophysical Research: Atmospheres*, 115(D21). https://doi.org/10.1029/2010JD013887.

Chevallier, F., Engelen, R. J., and Peylin, P. (2005). The contribution of AIRS data to the estimation of CO_2 sources and sinks. *Geophysical Research Letters*, 32(23). https://doi.org/10.1029/2005GL024229.

Chevallier, F., Remaud, M., O'Dell, C. W., Baker, D., Peylin, P., and Cozic, A. (2019). Objective evaluation of surface- and satellite-driven carbon dioxide atmospheric inversions. *Atmospheric Chemistry and Physics*, 19(22):14233–14251. https://doi.org/10.5194/acp-19-14233-2019.

Chevallier, F., Viovy, N., Reichstein, M., and Ciais, P. (2006). On the assignment of prior errors in Bayesian inversions of CO_2 surface fluxes. *Geophysical Research Letters*, 33(13). https://doi.org/10.1029/2006GL026496.

Cooperative Global Atmospheric Data Integration Project (2019). Multi-laboratory compilation of atmospheric carbon dioxide data for the period 1957-2018; obspack_co2_1_GLOBALVIEWplus_v5.0_2019_08_12. https://doi.org/10.25925/20190812.

Crisp, D. (2008). NASA Orbiting Carbon Observatory: measuring the column averaged carbon dioxide mole fraction from space. *Journal of Applied Remote Sensing*, 2(1):023508. https://doi.org/10.1117/1.2898457.

Crisp, D., Dolman, H., Tanhua, T., McKinley, G. A., Hauck, J., Bastos, A., Sitch, S., Eggleston, S., and Aich, V. (2022). How well do we understand the land–ocean–atmosphere carbon cycle? *Reviews of Geophysics*, 60(2). https://doi.org/10.1029/2021RG000736.

Darmenov, A. S. and Da Silva, A. M. (2015). The Quick Fire Emissions Dataset (QFED): Documentation of versions 2.1, 2.2 and 2.4, In: Technical report series on global modeling and data assimilation, Volume 38. 2015. http://gmao.gsfc.nasa.gov/pubs/docs/Darmenov796.pdf.

Davidson, E. A. and Janssens, I. A. (2006). Temperature sensitivity of soil carbon decomposition and feedbacks to climate change. *Nature*, 440(7081):165–173. https://doi.org/10.1038/nature04514.

Davidson, E. A., Janssens, I. A., and Luo, Y. (2006). On the variability of respiration in terrestrial ecosystems: moving beyond Q10. *Global Change Biology*, 12(2):154–164. `https://doi.org/10.1111/j.1365-2486.2005.01065.x`.

Delire, C., Séférian, R., Decharme, B., Alkama, R., Calvet, J.-C., Carrer, D., Gibelin, A.-L., Joetzjer, E., Morel, X., Rocher, M., and Tzanos, D. (2020). The global land carbon cycle simulated with ISBA–CTRIP: Improvements over the last decade. *Journal of Advances in Modeling Earth Systems*, 12(9). `https://doi.org/10.1029/2019MS001886`.

Detmers, R. G., Hasekamp, O., Aben, I., Houweling, S., Leeuwen, T. T., Butz, A., Landgraf, J., Köhler, P., Guanter, L., and Poulter, B. (2015). Anomalous carbon uptake in Australia as seen by GOSAT. *Geophysical Research Letters*, 42(19):8177–8184. `https://doi.org/10.1002/2015GL065161`.

Ernst, Y., Archibald, S., Balzter, H., Chevallier, F., Ciais, P., Fischer, C. G., Gaubert, B., Higginbottom, T., Higgins, S., Lawal, S., Lacroix, F., Lauerwald, R., Lourenco, M., Martens, C., Mengistu, A. G., Merbold, L., Mitchard, E., Moyo, M., Nguyen, H., O'sullivan, M., Rodríguez-Veiga, P., Rosan, T., Rosentreter, J., Ryan, C., Scheiter, S., Sitch, S., Stevens, N., Tagesson, T., Tian, H., Wang, M., Woon, J. S., Zheng, B., Zhou, Y., and Scholes, R. J. (2024). The african regional greenhouse gases budget (2010–2019). *Global Biogeochemical Cycles*, 38(4). `https://doi.org/10.1029/2023GB008016`.

Fan, Z., Neff, J. C., and Hanan, N. P. (2015). Modeling pulsed soil respiration in an African savanna ecosystem. *Agricultural and Forest Meteorology*, 200:282–292. `https://doi.org/10.1016/j.agrformet.2014.10.009`.

FAO (2019). *Trees, forests and land use in drylands: The first global assessment, full report*, volume 184 of *FAO forestry paper*. Food and Agriculture Organization of the United Nations, Rome. `https://www.fao.org/3/ca7148en/CA7148EN.pdf`.

Feldman, A. F., Konings, A. G., Gentine, P., Cattry, M., Wang, L., Smith, W. K., Biederman, J. A., Chatterjee, A., Joiner, J., and Poulter, B. (2024a). Large global-scale vegetation sensitivity to daily rainfall variability. *Nature*, 636(8042):380–384. `https://doi.org/10.1038/s41586-024-08232-z`.

Feldman, A. F., Reed, S., Amaral, C., Babst-Kostecka, A., Babst, F., Biederman, J., Devine, C., Fu, Z., Green, J. K., Guo, J., Hanan, N. P., Kokaly, R., Litvak, M., MacBean, N., Moore, D., Ojima, D., Poulter, B., Scott, R. L., Smith, W. K., Swap, R., Tucker, C. J., Wang, L., Watts, J., Wessels, K., Zhang, F., and Zhang, W. (2024b). Adaptation and response in drylands (ARID): Community insights for scoping a NASA terrestrial ecology field campaign in drylands. *Earth's Future*, 12(9). `https://doi.org/10.1029/2024EF004811`.

Feng, S. and Fu, Q. (2013). Expansion of global drylands under a warming climate. *Atmospheric Chemistry and Physics*, 13(19):10081–10094. `https://doi.org/10.5194/acp-13-10081-2013`.

Foster, K. T., Sun, W., Shiga, Y. P., Mao, J., and Michalak, A. M. (2024). Multiscale assessment of North American terrestrial carbon balance. *Biogeosciences*, 21(3):869–891. `https://doi.org/10.5194/bg-21-869-2024`.

Frankenberg, C., Fisher, J. B., Worden, J., Badgley, G., Saatchi, S. S., Lee, J.-E., Toon, G. C., Butz, A., Jung, M., Kuze, A., and Yokota, T. (2011). New global observations of the terrestrial carbon cycle from GOSAT: Patterns of plant fluorescence with gross primary productivity. *Geophysical Research Letters*, 38(17). `https://doi.org/10.1029/2011GL048738`.

Frater, H., Schwanke, K., and Podbregar, N. (2009). *Wetter, Klima, Klimawandel*. Springer Berlin Heidelberg, Berlin, Heidelberg. ISBN: 978-3-540-79291-8.

Frey, M., Sha, M. K., Hase, F., Kiel, M., Blumenstock, T., Harig, R., Surawicz, G., Deutscher, N. M., Shiomi, K., Franklin, J. E., Bösch, H., Chen, J., Grutter, M., Ohyama, H., Sun, Y., Butz, A., Mengistu Tsidu, G., Ene, D., Wunch, D., Cao, Z., Garcia, O., Ramonet, M., Vogel, F., and Orphal, J. (2019). Building the COllaborative Carbon Column Observing Network (COCCON): long-term stability and ensemble performance of the EM27/SUN Fourier transform spectrometer. *Atmospheric Measurement Techniques*, 12(3):1513–1530. `https://doi.org/10.5194/amt-12-1513-2019`.

Friedlingstein, P., O'Sullivan, M., Jones, M. W., Andrew, R. M., Hauck, J., Landschützer, P., Le Quéré, C., Li, H., Luijkx, I. T., Olsen, A., Peters, G. P., Peters, W., Pongratz, J., Schwingshackl, C., Sitch, S., Canadell, J. G., Ciais, P., Jackson, R. B., Alin, S. R., Arneth, A., Arora, V., Bates, N. R., Becker, M., Bellouin, N., Berghoff, C. F., Bittig, H. C., Bopp, L., Cadule, P., Campbell, K., Chamberlain, M. A., Chandra, N., Chevallier, F., Chini, L. P., Colligan, T., Decayeux, J., Djeutchouang, L. M., Dou, X., Duran Rojas, C., Enyo, K., Evans, W., Fay, A. R., Feely, R. A., Ford, D. J., Foster, A., Gasser, T., Gehlen, M., Gkritzalis, T., Grassi, G., Gregor, L., Gruber, N., Gürses, Ö., Harris, I., Hefner, M., Heinke, J., Hurtt, G. C., Iida, Y., Ilyina, T., Jacobson, A. R., Jain, A. K., Jarníková, T., Jersild, A., Jiang, F., Jin, Z., Kato, E., Keeling, R. F., Klein Goldewijk, K., Knauer, J., Korsbakken, J. I., Lan, X., Lauvset, S. K., Lefèvre, N., Liu, Z., Liu, J., Ma, L., Maksyutov, S., Marland, G., Mayot, N., McGuire, P. C., Metzl, N., Monacci, N. M., Morgan, E. J., Nakaoka, S.-I., Neill, C., Niwa, Y., Nützel, T., Olivier, L., Ono, T., Palmer, P. I., Pierrot, D., Qin, Z., Resplandy, L., Roobaert, A., Rosan, T. M., Rödenbeck, C., Schwinger, J., Smallman, T. L., Smith, S. M., Sospedra-Alfonso, R., Steinhoff, T., Sun, Q., Sutton, A. J., Séférian, R., Takao, S., Tatebe, H., Tian, H., Tilbrook, B., Torres, O., Tourigny, E., Tsujino, H., Tubiello, F., van der Werf, G., Wanninkhof, R., Wang, X., Yang, D., Yang, X., Yu, Z., Yuan, W., Yue, X., Zaehle, S., Zeng, N., and Zeng, J. (2025). Global carbon budget 2024. *Earth System Science Data*, 17(3):965–1039. https://doi.org/10.5194/essd-17-965-2025.

Friedlingstein, P., O'sullivan, M., Jones, M. W., Andrew, R. M., Hauck, J., Olsen, A., Peters, G. P., Peters, W., Pongratz, J., Sitch, S., Le Quéré, C., Canadell, J. G., Ciais, P., Jackson, R. B., Alin, S., Aragão, Luiz E. O. C., Arneth, A., Arora, V., Bates, N. R., Becker, M., Benoit-Cattin, A., Bittig, H. C., Bopp, L., Bultan, S., Chandra, N., Chevallier, F., Chini, L. P., Evans, W., Florentie, L., Forster, P. M., Gasser, T., Gehlen, M., Gilfillan, D., Gkritzalis, T., Gregor, L., Gruber, N., Harris, I., Hartung, K., Haverd, V., Houghton, R. A., Ilyina, T., Jain, A. K., Joetzjer, E., Kadono, K., Kato, E., Kitidis, V., Korsbakken, J. I., Landschützer, P., Lefèvre, N., Lenton, A., Lienert, S., Liu, Z., Lombardozzi, D., Marland, G., Metzl, N., Munro, D. R., Nabel, Julia E. M. S., Nakaoka, S.-I., Niwa, Y., O'Brien, K., Ono, T., Palmer, P. I., Pierrot, D., Poulter, B., Resplandy, L., Robertson, E., Rödenbeck, C., Schwinger, J., Séférian, R., Skjelvan, I., Smith, A. J. P., Sutton, A. J., Tanhua, T., Tans, P. P., Tian, H., Tilbrook, B., van der Werf, G., Vuichard, N., Walker, A. P., Wanninkhof, R., Watson, A. J., Willis, D., Wiltshire, A. J., Yuan, W., Yue, X., and Zaehle, S. (2020). Global carbon budget 2020. *Earth System Science Data*, 12(4):3269–3340. https://doi.org/10.5194/essd-12-3269-2020.

Giglio, L., Randerson, J. T., and van der Werf, G. R. (2013). Analysis of daily, monthly, and annual burned area using the fourth–generation global fire emissions database (GFED4). *Journal of Geophysical Research: Biogeosciences*, 118(1):317–328. https://doi.org/10.1002/jgrg.20042.

Global Carbon Project (2003). Science Framework and Implementation. Earth System Science Partnership (IGBP, IHDP, WCRP, DIVERSITAS) Report No. 1; Global Carbon Project Report No. 1, 69pp, Canberra. https://www.globalcarbonproject.org/science/index.htm.

Gruber, N., Bakker, D. C. E., DeVries, T., Gregor, L., Hauck, J., Landschützer, P., McKinley, G. A., and Müller, J. D. (2023). Trends and variability in the ocean carbon sink. *Nature Reviews Earth & Environment*, 4(2):119–134. https://doi.org/10.1038/s43017-022-00381-x.

Guerlet, S., Butz, A., Schepers, D., Basu, S., Hasekamp, O. P., Kuze, A., Yokota, T., Blavier, J.-F., Deutscher, N. M., Griffith, D. W. T., Hase, F., Kyro, E., Morino, I., Sherlock, V., Sussmann, R., Galli, A., and Aben, I. (2013). Impact of aerosol and thin cirrus on retrieving and validating XCO_2 from GOSAT shortwave infrared measurements. *Journal of Geophysical Research: Atmospheres*, 118(10):4887–4905. `https://doi.org/10.1002/jgrd.50332`.

Hall, B. D., Crotwell, A. M., Kitzis, D. R., Mefford, T., Miller, B. R., Schibig, M. F., and Tans, P. P. (2021). Revision of the World Meteorological Organization Global Atmosphere Watch (WMO/GAW) CO_2 calibration scale. *Atmospheric Measurement Techniques*, 14(4):3015–3032. `https://doi.org/10.5194/amt-14-3015-2021`.

Harmon, M. E., Bond-Lamberty, B., Tang, J., and Vargas, R. (2011). Heterotrophic respiration in disturbed forests: A review with examples from North America. *Journal of Geophysical Research: Atmospheres*, 116. `https://doi.org/10.1029/2010JG001495`.

Haverd, V., Ahlström, A., Smith, B., and Canadell, J. G. (2017). Carbon cycle responses of semi-arid ecosystems to positive asymmetry in rainfall. *Global Change Biology*, 23(2):793–800. `https://doi.org/10.1111/gcb.13412`.

Haverd, V., Raupach, M. R., Briggs, P. R., J. G. Canadell., Davis, S. J., Law, R. M., Meyer, C. P., Peters, G. P., Pickett-Heaps, C., and Sherman, B. (2013). The Australian terrestrial carbon budget. *Biogeosciences*, 10(2):851–869. `https://doi.org/10.5194/bg-10-851-2013`.

Haverd, V., Smith, B., Nieradzik, L., Briggs, P. R., Woodgate, W., Trudinger, C. M., Canadell, J. G., and Cuntz, M. (2018). A new version of the CABLE land surface model (Subversion revision r4601) incorporating land use and land cover change, woody vegetation demography, and a novel optimisation-based approach to plant coordination of photosynthesis. *Geoscientific Model Development*, 11(7):2995–3026. `https://doi.org/10.5194/gmd-11-2995-2018`.

Humphrey, V., Berg, A., Ciais, P., Gentine, P., Jung, M., Reichstein, M., Seneviratne, S. I., and Frankenberg, C. (2021). Soil moisture–atmosphere feedback dominates land carbon uptake variability. *Nature*, 592(7852):65–69. `https://doi.org/10.1038/s41586-021-03325-5`.

Huxman, T. E., Snyder, K. A., Tissue, D., Leffler, A. J., Ogle, K., Pockman, W. T., Sandquist, D. R., Potts, D. L., and Schwinning, S. (2004). Precipitation pulses and carbon fluxes in semiarid and arid ecosystems. *Oecologia*, 141(2):254–268. `https://doi.org/10.1007/s00442-004-1682-4`.

IPCC (2023). Sections. In: Climate Change 2023: Synthesis Report. Contribution of Working Groups I, II and III to the Sixth Assessment Report of the Intergovernmental Panel on Climate Change [Core Writing Team, H. Lee and J. Romero (eds.)]. IPCC, Geneva, Switzerland, pp. 35-115. 2023. https://doi.org/10.59327/IPCC/AR6-9789291691647.

Jacobs, N., O'Dell, C. W., Taylor, T. E., Logan, T. L., Byrne, B., Kiel, M., Kivi, R., Heikkinen, P., Merrelli, A., Payne, V. H., and Chatterjee, A. (2024). The importance of digital elevation model accuracy in XCO_2 retrievals: improving the Orbiting Carbon Observatory 2 Atmospheric Carbon Observations from Space version 11 retrieval product. *Atmospheric Measurement Techniques*, 17(5):1375–1401. https://doi.org/10.5194/amt-17-1375-2024.

Jacobson, A. R., Schuldt, K. N., Miller, J. B., Oda, T., Tans, P., Arlyn Andrews, Mund, J., Ott, L., Collatz, G. J., Aalto, T., Afshar, S., Aikin, K., Aoki, S., Apadula, F., Baier, B., Bergamaschi, P., Beyersdorf, A., Biraud, S. C., Bollenbacher, A., Bowling, D., Brailsford, G., Abshire, J. B., Chen, G., Huilin Chen, Lukasz Chmura, Sites Climadat, Colomb, A., Conil, S., Cox, A., Cristofanelli, P., Cuevas, E., Curcoll, R., Sloop, C. D., Davis, K., de Wekker, S., Delmotte, M., DiGangi, J. P., Dlugokencky, E., Ehleringer, J., Elkins, J. W., Emmenegger, L., Fischer, M. L., Forster, G., Frumau, A., Galkowski, M., Gatti, L. V., Gloor, E., Griffis, T., Hammer, S., Haszpra, L., Hatakka, J., Heliasz, M., Hensen, A., Hermanssen, O., Hintsa, E., Holst, J., Jaffe, D., Karion, A., Kawa, S. R., Keeling, R., Keronen, P., Kolari, P., Kominkova, K., Kort, E., Krummel, P., Kubistin, D., Labuschagne, C., Langenfelds, R., Laurent, O., Laurila, T., Lauvaux, T., Law, B., Lee, J., Lehner, I., Leuenberger, M., Levin, I., Levula, J., Lin, J., Lindauer, M., Loh, Z., Lopez, M., Luijkx, I. T., Myhre, C. L., Machida, T., Mammarella, I., Manca, G., Manning, A., Manning, A., Marek, M. V., Marklund, P., Martin, M. Y., Matsueda, H., McKain, K., Meijer, H., Meinhardt, F., Miles, N., Miller, C. E., Mölder, M., Montzka, S., Moore, F., Josep-Anton Morgui, Morimoto, S., Munger, B., Jaroslaw Necki, Newman, S., Nichol, S., Niwa, Y., O'Doherty, S., Mikaell Ottosson-Löfvenius, Paplawsky, B., Peischl, J., Peltola, O., Jean-Marc Pichon, Piper, S., Plass-Dölmer, C., Ramonet, M., Reyes-Sanchez, E., Richardson, S., Riris, H., Ryerson, T., Saito, K., Sargent, M., Sasakawa, M., Sawa, Y., Say, D., Scheeren, B., Schmidt, M., Schmidt, A., Schumacher, M., Shepson, P., Shook, M., Stanley, K., Steinbacher, M., Stephens, B., Sweeney, C., Thoning, K., Torn, M., Turnbull, J., Tørseth, K., den van Bulk, P., van Dinther, D., Vermeulen, A., Viner, B., Vitkova, G., Walker, S., Weyrauch, D., Wofsy, S., Worthy, D., Dickon Young, and Miroslaw Zimnoch (2023a). CarbonTracker documentation CT2022 release. https://gml.noaa.gov/ccgg/carbontracker/CT2022/documentation.php.

Jacobson, A. R., Schuldt, K. N., Tans, P., Arlyn Andrews, Miller, J. B., Oda, T., Mund, J., Weir, B., Ott, L., Aalto, T., 775 Abshire, J. B., Aikin, K., Aoki, S., Apadula, F., Arnold, S., Baier, B., Bartyzel, J., Beyersdorf, A., Biermann, T., Biraud, S. C., Boenisch, H., Brailsford, G., Brand, W. A., Chen, G., Huilin Chen, Lukasz Chmura, Clark, S., Colomb, A., Commane, R., Conil, S., Couret, C., Cox, A., Cristofanelli, P., Cuevas, E., Curcoll, R., Daube, B., Davis, K. J., Wekker, S. de, Della Coletta, J., Delmotte, M., DiGangi, E., DiGangi, J. P., Di Sarra, A. G., Dlugokencky, E., Elkins, J. W., Emmenegger, L., Shuangxi Fang, Fischer, M. L., Forster, G., Frumau, A., Galkowski, M., Gatti, L. V., Gehrlein, T., Gerbig, C., Francois Gheusi, Gloor, E., Gomez-Trueba, V., Goto, D., Griffis, T., Hammer, S., Hanson, C., Haszpra, L., Hatakka, J., Heimann, M., Heliasz, M., Hensen, A., Hermansen, O., Hintsa, E., Holst, J., Ivakhov, V., Jaffe, D. A., Jordan, A., Joubert, W., Karion, A., Kawa, S. R., Kazan, V., Keeling, R. F., Keronen, P., Kneuer, T., Kolari, P., Kateřina Komínková, Kort, E., Kozlova, E., Krummel, P., Kubistin, D., Labuschagne, C., Lam, D. H., Lan, X., Langenfelds, R. L., Laurent, O., Laurila, T., Lauvaux, T., Lavric, J., Law, B. E., Lee, J., Lee, O. S., Lehner, I., Lehtinen, K., Leppert, R., Leskinen, A., Leuenberger, M., Levin, I., Levula, J., Lin, J., Lindauer, M., Loh, Z., Lopez, M., Luijkx, I. T., Lunder, C. R., Machida, T., Mammarella, I., Manca, G., Manning, A., Manning, A., Marek, M. V., Martin, M. Y., Matsueda, H., McKain, K., Meijer, H., Meinhardt, F., Merchant, L., N. Mihalopoulos, Miles, N. L., Miller, C. E., Mitchell, L., Mölder, M., Montzka, S., Moore, F., Moossen, H., Morgan, E., Josep-Anton Morgui, Morimoto, S., Müller-Williams, J., J. William Munger, Munro, D., Myhre, C. L., Shin-Ichiro Nakaoka, Jaroslaw Necki, Newman, S., Nichol, S., Niwa, Y., Obersteiner, F., O'Doherty, S., Paplawsky, B., Peischl, J., Peltola, O., Piacentino, S., Jean-Marc Pichon, Pickers, P., Piper, S., Pitt, J., Plass-Dülmer, C., Platt, S. M., Prinzivalli, S., Ramonet, M., Ramos, R., Reyes-Sanchez, E., Richardson, S. J., Riris, H., Rivas, P. P., Ryerson, T., Saito, K., Sargent, M., Sasakawa, M., Scheeren, B., Schuck, T., Schumacher, M., Seifert, T., Sha, M. K., Shepson, P., Shook, M., Sloop, C. D., Smith, P., Stanley, K., Steinbacher, M., Stephens, B., Sweeney, C., Thoning, K., Timas, H., Torn, M., Tørseth, K., Trisolino, P., Turnbull, J., van den Bulk, P., van Dinther, D., Vermeulen, A., Viner, B., Vitkova, G., Walker, S., Watson, A., Wofsy, S. C., Worsey, J., Worthy, D., Dickon Young, Zaehle, S., Zahn, A., Zimnoch, M., Vermeulen, A., Viner, B., Vitkova, G., Walker, S., Watson, A., Wofsy, S. C., Worsey, J., Worthy, D., Dickon Young, Zaehle, S., Zahn, A., and Miroslaw Zimnoch (2023b). CarbonTracker CT2022. `https://doi.org/10.25925/z1gj-3254`.

Jarvis, P., Rey, A., Petsikos, C., Wingate, L., Rayment, M., Pereira, J., Banza, J., David, J., Miglietta, F., Borghetti, M., Manca, G., and Valentini, R. (2007). Drying and wetting of Mediterranean soils stimulates decomposition and carbon dioxide emission: the "Birch effect". *Tree Physiology*, 27(7):929–940. https://doi.org/10.1093/treephys/27.7.929.

Joiner, J., Yoshida, Y., Koehler, P., Frankenberg, C., and Parazoo, N. C. (2023). L2 daily Solar-Induced Fluorescence (SIF) from MetOp-A GOME-2, 2007-2018, V2. https://doi.org/10.3334/ORNLDAAC/2292.

Joiner, J., Yoshida, Y., Zhang, Y., Duveiller, G., Jung, M., Lyapustin, A., Wang, Y., and Tucker, C. J. (2018). Estimation of terrestrial global gross primary production (GPP) with satellite data-driven models and eddy covariance flux data. *Remote Sensing*, 10(9):1346. https://doi.org/10.3390/rs10091346.

Jung, M., Schwalm, C., Migliavacca, M., Walther, S., Camps-Valls, G., Koirala, S., Anthoni, P., Besnard, S., Bodesheim, P., Carvalhais, N., Chevallier, F., Gans, F., Goll, D. S., Haverd, V., Köhler, P., Ichii, K., Jain, A. K., Liu, J., Lombardozzi, D., Nabel, Julia E. M. S., Nelson, J. A., O'Sullivan, M., Pallandt, M., Papale, D., Peters, W., Pongratz, J., Rödenbeck, C., Sitch, S., Tramontana, G., Walker, A., Weber, U., and Reichstein, M. (2020). Scaling carbon fluxes from eddy covariance sites to globe: synthesis and evaluation of the FLUXCOM approach. *Biogeosciences*, 17(5):1343–1365. https://doi.org/10.5194/bg-17-1343-2020.

Justice, C., Townshend, J., Vermote, E., Masuoka, E., Wolfe, R., Saleous, N., Roy, D., and Morisette, J. (2002). An overview of MODIS Land data processing and product status. *Remote Sensing of Environment*, 83(1-2):3–15. https://doi.org/10.1016/S0034-4257(02)00084-6.

Keenan, T. F. and Williams, C. A. (2018). The terrestrial carbon sink. *Annual Review of Environment and Resources*, 43(1):219–243. https://doi.org/10.1146/annurev-environ-102017-030204.

Krinner, G., Viovy, N., de Noblet-Ducoudré, N., Ogée, J., Polcher, J., Friedlingstein, P., Ciais, P., Sitch, S., and Prentice, I. C. (2005). A dynamic global vegetation model for studies of the coupled atmosphere-biosphere system. *Global Biogeochemical Cycles*, 19(1). https://doi.org/10.1029/2003GB002199.

Law, B., Falge, E., Gu, L., Baldocchi, D., Bakwin, P., Berbigier, P., Davis, K., Dolman, A., Falk, M., Fuentes, J., Goldstein, A., Granier, A., Grelle, A., Hollinger, D., Janssens, I., Jarvis, P., Jensen, N., Katul, G., Mahli, Y., Matteucci, G., Meyers, T., Monson, R., Munger, W., Oechel, W., Olson, R., Pilegaard, K., Paw U, K., Thorgeirsson, H., Valentini, R., Verma, S., Vesala, T., Wilson, K., and Wofsy, S. (2002). Environmental controls over carbon dioxide and water vapor exchange of terrestrial vegetation. *Agricultural and Forest Meteorology*, 113(1-4):97–120. https://doi.org/10.1016/S0168-1923(02)00104-1.

Le Quéré, C., Andres, R. J., Boden, T., Conway, T., Houghton, R. A., House, J. I., Marland, G., Peters, G. P., van der Werf, G. R., Ahlström, A., Andrew, R. M., Bopp, L., Canadell, J. G., Ciais, P., Doney, S. C., Enright, C., Friedlingstein, P., Huntingford, C., Jain, A. K., Jourdain, C., Kato, E., Keeling, R. F., Klein Goldewijk, K., Levis, S., Levy, P., Lomas, M., Poulter, B., Raupach, M. R., Schwinger, J., Sitch, S., Stocker, B. D., Viovy, N., Zaehle, S., and Zeng, N. (2013). The global carbon budget 1959–2011. *Earth System Science Data*, 5(1):165–185. https://doi.org/10.5194/essd-5-165-2013.

Le Quéré, C., Andrew, R. M., Friedlingstein, P., Sitch, S., Hauck, J., Pongratz, J., Pickers, P. A., Korsbakken, J. I., Peters, G. P., Canadell, J. G., Arneth, A., Arora, V. K., Barbero, L., Bastos, A., Bopp, L., Chevallier, F., Chini, L. P., Ciais, P., Doney, S. C., Gkritzalis, T., Goll, D. S., Harris, I., Haverd, V., Hoffman, F. M., Hoppema, M., Houghton, R. A., Hurtt, G., Ilyina, T., Jain, A. K., Johannessen, T., Jones, C. D., Kato, E., Keeling, R. F., Goldewijk, K. K., Landschützer, P., Lefèvre, N., Lienert, S., Liu, Z., Lombardozzi, D., Metzl, N., Munro, D. R., Nabel, Julia E. M. S., Nakaoka, S.-I., Neill, C., Olsen, A., Ono, T., Patra, P., Peregon, A., Peters, W., Peylin, P., Pfeil, B., Pierrot, D., Poulter, B., Rehder, G., Resplandy, L., Robertson, E., Rocher, M., Rödenbeck, C., Schuster, U., Schwinger, J., Séférian, R., Skjelvan, I., Steinhoff, T., Sutton, A., Tans, P. P., Tian, H., Tilbrook, B., Tubiello, F. N., van der Laan-Luijkx, I. T., van der Werf, G. R., Viovy, N., Walker, A. P., Wiltshire, A. J., Wright, R., Zaehle, S., and Zheng, B. (2018). Global carbon budget 2018. *Earth System Science Data*, 10(4):2141–2194. https://doi.org/10.5194/essd-10-2141-2018.

Li, X., Xiao, J., He, B., Altaf Arain, M., Beringer, J., Desai, A. R., Emmel, C., Hollinger, D. Y., Krasnova, A., Mammarella, I., Noe, S. M., Ortiz, P. S., Rey-Sanchez, A. C., Rocha, A. V., and Varlagin, A. (2018). Solar-induced chlorophyll fluorescence is strongly correlated with terrestrial photosynthesis for a wide variety of biomes: First global analysis based on OCO-2 and flux tower observations. *Global Change Biology*, 24(9):3990–4008. https://doi.org/10.1111/gcb.14297.

Liu, J., Baker, D., Basu, S., Bowman, K., Byrne, B., Chevallier, F., He, W., Jiang, F., Johnson, M. S., Kubar, T. L., Li, X., Liu, Z., Miller, S. M., Philip, S., Xiao, J., Yun, J., and Zeng, N. (2024a). The reduced net carbon uptake over Northern Hemisphere land causes the close-to-normal CO_2 growth rate in 2021 La Niña. *Science Advances*, 10(23):eadl2201. https://doi.org/10.1126/sciadv.adl2201.

Liu, J., Bowman, K. W., Schimel, D. S., Parazoo, N. C., Jiang, Z., Lee, M., Bloom, A. A., Wunch, D., Frankenberg, C., Sun, Y., O'Dell, C. W., Gurney, K. R., Menemenlis, D., Gierach, M., Crisp, D., and Eldering, A. (2017). Contrasting carbon cycle responses of the tropical continents to the 2015-2016 El Niño. *Science*, 358(6360). `https://doi.org/10.1126/science.aam5690`.

Liu, M., Raymond, P. A., Lauerwald, R., Zhang, Q., Trapp-Müller, G., Davis, K. L., Moosdorf, N., Xiao, C., Middelburg, J. J., Bouwman, A. F., Beusen, A. H. W., Peng, C., Lacroix, F., Tian, H., Wang, J., Li, M., Zhu, Q., Cohen, S., van Hoek, W. J., Li, Y., Li, Y., Yao, Y., and Regnier, P. (2024b). Global riverine land-to-ocean carbon export constrained by observations and multi-model assessment. *Nature Geoscience*, 17(9):896–904. `https://doi.org/10.1038/s41561-024-01524-z`.

Ma, X., Huete, A., Cleverly, J., Eamus, D., Chevallier, F., Joiner, J., Poulter, B., Zhang, Y., Guanter, L., Meyer, W., Xie, Z., and Ponce-Campos, G. (2016). Drought rapidly diminishes the large net CO_2 uptake in 2011 over semi-arid Australia. *Scientific Reports*, 6(1):37747. `https://doi.org/10.1038/srep37747`.

MacBean, N., Scott, R. L., Biederman, J. A., Peylin, P., Kolb, T., Litvak, M. E., Krishnan, P., Meyers, T. P., Arora, V. K., Bastrikov, V., Goll, D., Lombardozzi, D. L., Nabel, Julia E. M. S., Pongratz, J., Sitch, S., Walker, A. P., Zaehle, S., and Moore, D. J. P. (2021). Dynamic global vegetation models underestimate net CO_2 flux mean and inter-annual variability in dryland ecosystems. *Environmental Research Letters*, 16(9):094023. `https://doi.org/10.1088/1748-9326/ac1a38`.

Mahecha, M. D., Reichstein, M., Carvalhais, N., Lasslop, G., Lange, H., Seneviratne, S. I., Vargas, R., Ammann, C., Arain, M. A., Cescatti, A., Janssens, I. A., Migliavacca, M., Montagnani, L., and Richardson, A. D. (2010). Global convergence in the temperature sensitivity of respiration at ecosystem level. *Science*, 329(5993):838–840. `https://doi.org/10.1126/science.1189587`.

Manzoni, S., Schaeffer, S. M., Katul, G., Porporato, A., and Schimel, J. P. (2014). A theoretical analysis of microbial eco-physiological and diffusion limitations to carbon cycling in drying soils. *Soil Biology and Biochemistry*, 73:69–83. `https://doi.org/10.1016/j.soilbio.2014.02.008`.

Masarie, K. A., Peters, W., Jacobson, A. R., and Tans, P. P. (2014). ObsPack: a framework for the preparation, delivery, and attribution of atmospheric greenhouse gas measurements. *Earth System Science Data*, 6(2):375–384. `https://doi.org/10.5194/essd-6-375-2014`.

Melton, J. R., Arora, V. K., Wisernig-Cojoc, E., Seiler, C., Fortier, M., Chan, E., and Teckentrup, L. (2020). CLASSIC v1.0: the open-source community successor to the Canadian Land Surface Scheme (CLASS) and the Canadian Terrestrial Ecosystem Model (CTEM) – Part 1: Model framework and site-level performance. *Geoscientific Model Development*, 13(6):2825–2850. https://doi.org/10.5194/gmd-13-2825-2020.

Meng, C., Xiao, X., Wagle, P., Zhang, C., Pan, L., Pan, B., Qin, Y., and Newman, G. S. (2024). Exponential or unimodal relationships between nighttime ecosystem respiration and temperature at the eddy covariance flux tower sites. *Ecology Letters*, 27(10):e14532. https://doi.org/10.1111/ele.14532.

Meroni, M., Rossini, M., Guanter, L., Alonso, L., Rascher, U., Colombo, R., and Moreno, J. (2009). Remote sensing of solar-induced chlorophyll fluorescence: Review of methods and applications. *Remote Sensing of Environment*, 113(10):2037–2051. https://doi.org/10.1016/j.rse.2009.05.003.

Metz, E.-M., Vardag, S. N., Basu, S., Jung, M., Ahrens, B., El-Madany, T., Sitch, S., Arora, V. K., Briggs, P. R., Friedlingstein, P., Goll, D. S., Jain, A. K., Kato, E., Lombardozzi, D., Nabel, Julia E. M. S., Poulter, B., Séférian, R., Tian, H., Wiltshire, A., Yuan, W., Yue, X., Zaehle, S., Deutscher, N. M., Griffith, D. W. T., and Butz, A. (2023). Soil respiration-driven CO_2 pulses dominate Australia's flux variability. *Science*, 379(6639):1332–1335. https://doi.org/10.1126/science.add7833.

Metz, E.-M., Vardag, S. N., Basu, S., Jung, M., and Butz, A. (2024). Reply on RC1 in seasonal and interannual variability in CO_2 fluxes in southern Africa seen by GOSAT. https://doi.org/10.5194/egusphere-2024-1955-AC1.

Metz, E.-M., Vardag, S. N., Basu, S., Jung, M., and Butz, A. (2025a). Seasonal and interannual variability in CO_2 fluxes in southern Africa seen by GOSAT. *Biogeosciences*, 22(2):555–584. https://doi.org/10.5194/bg-22-555-2025.

Metz, E.-M., Vardag, S. N., Feldman, A. F., Poulter, B., Colligan, T., Fischer-Femal, B. J., and Butz, A. (2025b). Responses of terrestrial ecosystem respiration to soil moisture across Australia's aridity regimes. *unpublished manuscript*.

Middleton, D. and Thomas, D. (1993). *World atlas of desertification*. Edward Arnold, London. ISBN: 0340555122.

Moyano, F. E., Manzoni, S., and Chenu, C. (2013). Responses of soil heterotrophic respiration to moisture availability: An exploration of processes and models. *Soil Biology and Biochemistry*, 59:72–85. https://linkinghub.elsevier.com/retrieve/pii/S0038071713000138.

Nelson, J. A., Walther, S., Gans, F., Kraft, B., Weber, U., Novick, K., Buchmann, N., Migliavacca, M., Wohlfahrt, G., Šigut, L., Ibrom, A., Papale, D., Göckede, M., Duveiller, G., Knohl, A., Hörtnagl, L., Scott, R. L., Dušek, J., Zhang, W., Hamdi, Z. M., Reichstein, M., Aranda-Barranco, S., Ardö, J., op de Beeck, M., Billesbach, D., Bowling, D., Bracho, R., Brümmer, C., Camps-Valls, G., Chen, S., Cleverly, J. R., Desai, A., Dong, G., El-Madany, T. S., Euskirchen, E. S., Feigenwinter, I., Galvagno, M., Gerosa, G. A., Gielen, B., Goded, I., Goslee, S., Gough, C. M., Heinesch, B., Ichii, K., Jackowicz-Korczynski, M. A., Klosterhalfen, A., Knox, S., Kobayashi, H., Kohonen, K.-M., Korkiakoski, M., Mammarella, I., Gharun, M., Marzuoli, R., Matamala, R., Metzger, S., Montagnani, L., Nicolini, G., O'Halloran, T., Ourcival, J.-M., Peichl, M., Pendall, E., Ruiz Reverter, B., Roland, M., Sabbatini, S., Sachs, T., Schmidt, M., Schwalm, C. R., Shekhar, A., Silberstein, R., Silveira, M. L., Spano, D., Tagesson, T., Tramontana, G., Trotta, C., Turco, F., Vesala, T., Vincke, C., Vitale, D., Vivoni, E. R., Wang, Y., Woodgate, W., Yepez, E. A., Zhang, J., Zona, D., and Jung, M. (2024). X-BASE: the first terrestrial carbon and water flux products from an extended data-driven scaling framework, FLUXCOM-X. *Biogeosciences*, 21(22):5079–5115. https://doi.org/10.5194/bg-21-5079-2024.

NOAA (2024). Trends in Atmospheric Carbon Dioxide. https://www.esrl.noaa.gov/gmd/ccgg/trends/gl_gr.html.

Novick, K. A., Biederman, J. A., Desai, A. R., Litvak, M. E., Moore, D., Scott, R. L., and Torn, M. S. (2018). The AmeriFlux network: A coalition of the willing. *Agricultural and Forest Meteorology*, 249:444–456. https://doi.org/10.1016/j.agrformet.2017.10.009.

OCO-2 Science Team, Michael Gunson, and Annmarie Eldering (2020). OCO-2 Level 2 bias-corrected XCO_2 and other select fields from the full-physics retrieval aggregated as daily files, Retrospective processing V10r,. *Greenbelt, MD, USA, Goddard Earth Sciences Data and Information Services Center (GES DISC)*. https://doi.org/10.5067/E4E140XDMPO2.

OCO-2/OCO-3 Science Team, Payne, V., and Chatterjee, A. (2022). OCO-2 Level 2 bias-corrected XCO_2 and other select fields from the full-physics retrieval aggregated as daily files, Retrospective processing V11.1r. *Greenbelt, MD, USA, Goddard Earth Sciences Data and Information Services Center (GES DISC) [data set]*. https://doi.org/10.5067/8E4VLCK16O6Q.

Oda, T. and Maksyutov, S. (2011). A very high-resolution (1 km×1 km) global fossil fuel CO_2 emission inventory derived using a point source database and satellite observations of nighttime lights. *Atmospheric Chemistry and Physics*, 11(2):543–556. https://doi.org/10.5194/acp-11-543-2011.

Oda, T., Maksyutov, S., and Andres, R. J. (2018). The Open-source Data Inventory for Anthropogenic Carbon dioxide (CO_2), version 2016 (ODIAC2016): A global, monthly fossil-fuel CO_2 gridded emission data product for tracer transport simulations and surface flux inversions. *Earth System Science Data*, 10(1):87–107. https://doi.org/10.5194/essd-10-87-2018.

Palmer, P. I., Feng, L., Baker, D., Chevallier, F., Bösch, H., and Somkuti, P. (2019). Net carbon emissions from African biosphere dominate pan-tropical atmospheric CO_2 signal. *Nature communications*, 10(1):1–9. https://doi.org/10.1038/s41467-019-11097-w.

Pan, G., Xu, Y., and Ma, J. (2021). The potential of CO_2 satellite monitoring for climate governance: A review. *Journal of environmental management*, 277:111423. https://doi.org/10.1016/j.jenvman.2020.111423.

Pan, S., Yang, J., Tian, H., Shi, H., Chang, J., Ciais, P., Francois, L., Frieler, K., Fu, B., Hickler, T., Ito, A., Nishina, K., Ostberg, S., Reyer, C. P., Schaphoff, S., Steinkamp, J., and Zhao, F. (2020). Climate extreme versus carbon extreme: Responses of terrestrial carbon fluxes to temperature and precipitation. *Journal of Geophysical Research: Biogeosciences*, 125(4). https://doi.org/10.1029/2019JG005252.

Pastorello, G., Trotta, C., Canfora, E., Chu, H., Christianson, D., Cheah, Y.-W., Poindexter, C., Chen, J., Elbashandy, A., Humphrey, M., Isaac, P., Polidori, D., Reichstein, M., Ribeca, A., van Ingen, C., Vuichard, N., Zhang, L., Amiro, B., Ammann, C., Arain, M. A., Ardö, J., Arkebauer, T., Arndt, S. K., Arriga, N., Aubinet, M., Aurela, M., Baldocchi, D., Barr, A., Beamesderfer, E., Marchesini, L. B., Bergeron, O., Beringer, J., Bernhofer, C., Berveiller, D., Billesbach, D., Black, T. A., Blanken, P. D., Bohrer, G., Boike, J., Bolstad, P. V., Bonal, D., Bonnefond, J.-M., Bowling, D. R., Bracho, R., Brodeur, J., Brümmer, C., Buchmann, N., Burban, B., Burns, S. P., Buysse, P., Cale, P., Cavagna, M., Cellier, P., Chen, S., Chini, I., Christensen, T. R., Cleverly, J., Collalti, A., Consalvo, C., Cook, B. D., Cook, D., Coursolle, C., Cremonese, E., Curtis, P. S., D'Andrea, E., Da Rocha, H., Dai, X., Davis, K. J., de Cinti, B., de Grandcourt, A., de Ligne, A., de Oliveira, R. C., Delpierre, N., Desai, A. R., Di Bella, C. M., Di Tommasi, P., Dolman, H., Domingo, F., Dong, G., Dore, S., Duce, P., Dufrêne, E., Dunn, A., Dušek, J., Eamus, D., Eichelmann, U., ElKhidir, H. A. M., Eugster, W., Ewenz, C. M., Ewers, B., Famulari, D., Fares, S., Feigenwinter, I., Feitz, A., Fensholt, R., Filippa, G., Fischer, M., Frank, J., Galvagno, M., Gharun, M., Gianelle, D., Gielen, B., Gioli, B., Gitelson, A., Goded, I., Goeckede, M., Goldstein, A. H., Gough, C. M., Goulden, M. L., Graf, A., Griebel, A., Gruening, C., Grünwald, T., Hammerle, A., Han, S., Han, X., Hansen, B. U., Hanson, C., Hatakka, J., He, Y., Hehn, M., Heinesch, B., Hinko-Najera, N., Hörtnagl, L., Hutley, L., Ibrom, A., Ikawa, H., Jackowicz-Korczynski, M., Janouš, D., Jans, W., Jassal, R., Jiang, S., Kato, T., Khomik, M., Klatt, J., Knohl, A., Knox, S., Kobayashi, H., Koerber, G., Kolle, O., Kosugi, Y., Kotani, A., Kowalski, A., Kruijt, B., Kurbatova, J., Kutsch, W. L., Kwon, H., Launiainen, S., Laurila, T., Law, B., Leuning, R., Li, Y., Liddell, M., Limousin, J.-M., Lion, M., Liska, A. J., Lohila, A., López-Ballesteros, A., López-Blanco, E., Loubet, B., Loustau, D., Lucas-Moffat, A., Lüers, J., Ma, S., Macfarlane, C., Magliulo, V., Maier, R., Mammarella, I., Manca, G., Marcolla, B., Margolis, H. A., Marras, S., Massman, W., Mastepanov, M., Matamala, R., Matthes, J. H., Mazzenga, F., McCaughey, H., McHugh, I., McMillan, A. M. S., Merbold, L., Meyer, W., Meyers, T., Miller, S. D., Minerbi, S., Moderow, U., Monson, R. K., Montagnani, L., Moore, C. E., Moors, E., Moreaux, V., Moureaux, C., Munger, J. W., Nakai, T., Neirynck, J., Nesic, Z., Nicolini, G., Noormets, A., Northwood, M., Nosetto, M., Nouvellon, Y., Novick, K., Oechel, W., Olesen, J. E., Ourcival, J.-M., Papuga, S. A., Parmentier, F.-J., Paul-Limoges, E., Pavelka, M., Peichl, M., Pendall, E., Phillips, R. P., Pilegaard, K., Pirk, N., Posse, G., Powell, T., Prasse, H., Prober, S. M., Rambal, S., Rannik, Ü., Raz-Yaseef, N., Rebmann, C., Reed, D., de Dios, V. R., Restrepo-Coupe, N., Reverter, B. R., Roland, M., Sabbatini, S., Sachs, T., Saleska, S. R., Sánchez-Cañete, E. P., Sanchez-Mejia, Z. M., Schmid, H. P., Schmidt, M., Schneider, K., Schrader, F., Schroder, I., Scott, R. L., Sedlák, P., Serrano-Ortíz, P., Shao, C., Shi, P., Shironya, I., Siebicke, L., Šigut, L., Silberstein, R., Sirca, C., Spano, D., Steinbrecher, R., Stevens, R. M., Sturtevant, C., Suyker, A., Tagesson, T., Takanashi, S., Tang, Y., Tapper, N., Thom, J., Tomassucci, M., Tuovinen, J.-P., Urbanski, S., Valentini, R., van der Molen, M., van Gorsel, E., van Huissteden, K., Varlagin, A., Verfaillie, J., Vesala, T., Vincke, C., Vitale, D., Vygodskaya, N., Walker, J. P., Walter-Shea, E., Wang, H., Weber, R., Westermann, S., Wille, C., Wofsy, S., Wohlfahrt, G., Wolf, S., Woodgate, W., Li, Y., Zampedri, R., Zhang, J., Zhou, G., Zona, D., Agarwal, D., Biraud, S., Torn, M., and Papale, D. (2020). The FLUXNET2015 dataset and the ONEFlux processing pipeline for eddy covariance data. *Scientific Data*, 7(1):225. `https://doi.org/10.1038/s41597-020-0534-3`.

Peiro, H., Crowell, S., Schuh, A., Baker, D. F., O'Dell, C., Jacobson, A. R., Chevallier, F., Liu, J., Eldering, A., Crisp, D., Deng, F., Weir, B., Basu, S., Johnson, M. S., Philip, S., and Baker, I. (2022). Four years of global carbon cycle observed from the

Orbiting Carbon Observatory 2 (OCO-2) version 9 and in situ data and comparison to OCO-2 version 7. *Atmospheric Chemistry and Physics*, 22(2):1097–1130. https://doi.org/10.5194/acp-22-1097-2022.

Peters, W., Jacobson, A. R., Sweeney, C., Andrews, A. E., Conway, T. J., Masarie, K., Miller, J. B., Bruhwiler, L. M. P., Pétron, G., Hirsch, A. I., Worthy, D. E. J., van der Werf, G. R., Randerson, J. T., Wennberg, P. O., Krol, M. C., and Tans, P. P. (2007). An atmospheric perspective on North American carbon dioxide exchange: CarbonTracker. *Proceedings of the National Academy of Sciences of the United States of America*, 104(48):18925–18930. https://doi.org/10.1073/pnas.0708986104.

Piao, S., Wang, X., Wang, K., Li, X., Bastos, A., Canadell, J. G., Ciais, P., Friedlingstein, P., and Sitch, S. (2020). Interannual variation of terrestrial carbon cycle: Issues and perspectives. *Global Change Biology*, 26(1):300–318. https://doi.org/10.1111/gcb.14884.

Pierrat, Z., Magney, T., Parazoo, N. C., Grossmann, K., Bowling, D. R., Seibt, U., Johnson, B., Helgason, W., Barr, A., Bortnik, J., Norton, A., Maguire, A., Frankenberg, C., and Stutz, J. (2022). Diurnal and seasonal dynamics of solar–induced chlorophyll fluorescence, vegetation indices, and gross primary productivity in the boreal forest. *Journal of Geophysical Research: Biogeosciences*, 127(2). https://doi.org/10.1029/2021JG006588.

Poulter, B., Ciais, P., Hodson, E., Lischke, H., Maignan, F., Plummer, S., and Zimmermann, N. E. (2011). Plant functional type mapping for earth system models. *Geoscientific Model Development*, 4(4):993–1010. https://doi.org/10.5194/gmd-4-993-2011.

Poulter, B., Frank, D., Ciais, P., Myneni, R. B., Andela, N., Bi, J., Broquet, G., Canadell, J. G., Chevallier, F., Liu, Y. Y., Running, S. W., Sitch, S., and van der Werf, G. R. (2014). Contribution of semi-arid ecosystems to interannual variability of the global carbon cycle. *Nature*, 509(7502):600–603. https://doi.org/10.1038/nature13376.

Raupach, M. R., Gloor, M., Sarmiento, J. L., Canadell, J. G., Frölicher, T. L., Gasser, T., Houghton, R. A., Le Quéré, C., and Trudinger, C. M. (2014). The declining uptake rate of atmospheric CO_2 by land and ocean sinks. *Biogeosciences*, 11(13):3453–3475. https://doi.org/10.5194/bg-11-3453-2014.

Rödenbeck, C., Houweling, S., Gloor, M., and Heimann, M. (2003). CO_2 flux history 1982–2001 inferred from atmospheric data using a global inversion of atmospheric transport. *Atmospheric Chemistry and Physics*, 3(6):1919–1964. https://doi.org/10.5194/acp-3-1919-2003.

Rodgers, C. D. (2000). *Inverse methods for atmospheric sounding: Theory and practice*, volume 2 of *Series on atmospheric oceanic and planetary physics*. World Scientific, Hackensack, NJ. ISBN: 981-02-2740-X.

Schimel, J., Balser, T. C., and Wallenstein, M. (2007). Microbial stress-response physiology and its implications for ecosystem function. *Ecology*, 88(6):1386–1394. https://doi.org/10.1890/06-0219.

Schulze, E.-D. (2006). Biological control of the terrestrial carbon sink. *Biogeosciences*, 3(2):147–166. https://doi.org/10.5194/bg-3-147-2006.

Seiler, C., Melton, J. R., Arora, V. K., Sitch, S., Friedlingstein, P., Anthoni, P., Goll, D., Jain, A. K., Joetzjer, E., Lienert, S., Lombardozzi, D., Luyssaert, S., Nabel, Julia E. M. S., Tian, H., Vuichard, N., Walker, A. P., Yuan, W., and Zaehle, S. (2022). Are terrestrial biosphere models fit for simulating the global land carbon sink? *Journal of Advances in Modeling Earth Systems*, 14(5). https://doi.org/10.1029/2021MS002946.

Sellers, P. J., Schimel, D. S., Moore, B., Liu, J., and Eldering, A. (2018). Observing carbon cycle–climate feedbacks from space. *Proceedings of the National Academy of Sciences of the United States of America*, 115(31):7860–7868. https://doi.org/10.1073/pnas.1716613115.

Singh, S., Mayes, M. A., Kivlin, S. N., and Jagadamma, S. (2023). How the Birch effect differs in mechanisms and magnitudes due to soil texture. *Soil Biology and Biochemistry*, 179:108973. https://doi.org/10.1016/j.soilbio.2023.108973.

Sun, Y., Frankenberg, C., Jung, M., Joiner, J., Guanter, L., Köhler, P., and Magney, T. (2018). Overview of Solar-Induced chlorophyll Fluorescence (SIF) from the Orbiting Carbon Observatory-2: Retrieval, cross-mission comparison, and global monitoring for GPP. *Remote Sensing of Environment*, 209:808–823. https://doi.org/10.1016/j.rse.2018.02.016.

Suto, H., Kataoka, F., Kikuchi, N., Knuteson, R. O., Butz, A., Haun, M., Buijs, H., Shiomi, K., Imai, H., and Kuze, A. (2021). Thermal and near-infrared sensor for carbon observation Fourier transform spectrometer-2 (TANSO-FTS-2) on the Greenhouse gases Observing SATellite-2 (GOSAT-2) during its first year in orbit. *Atmospheric Measurement Techniques*, 14(3):2013–2039. https://doi.org/10.5194/amt-14-2013-2021.

Taylor, J., Wilson, B., Mills, M., and Burns, R. (2002). Comparison of microbial numbers and enzymatic activities in surface soils and subsoils using various techniques. *Soil Biology and Biochemistry*, 34(3):387–401. https://doi.org/10.1016/s0038-0717(01)00199-7.

Taylor, T. E., O'Dell, C. W., Crisp, D., Kuze, A., Lindqvist, H., Wennberg, P. O., Chatterjee, A., Gunson, M., Eldering, A., Fisher, B., Kiel, M., Nelson, R. R., Merrelli, A., Osterman, G., Chevallier, F., Palmer, P. I., Feng, L., Deutscher, N. M., Dubey, M. K., Feist, D. G., García, O. E., Griffith, D. W. T., Hase, F., Iraci, L. T., Kivi, R., Liu, C., de Mazière, M., Morino, I., Notholt, J., Oh, Y.-S., Ohyama, H., Pollard, D. F., Rettinger, M., Schneider, M., Roehl, C. M., Sha, M. K., Shiomi, K., Strong, K., Sussmann, R., Té, Y., Velazco, V. A., Vrekoussis, M., Warneke, T., and Wunch, D. (2022). An 11-year record of XCO_2 estimates derived from GOSAT measurements using the NASA ACOS version 9 retrieval algorithm. *Earth System Science Data*, 14(1):325–360. https://doi.org/10.5194/essd-14-325-2022.

Teckentrup, L., de Kauwe, M. G., Pitman, A. J., Goll, D. S., Haverd, V., Jain, A. K., Joetzjer, E., Kato, E., Lienert, S., Lombardozzi, D., et al. (2021). Assessing the representation of the Australian carbon cycle in global vegetation models. *Biogeosciences*, 18(20):5639–5668. https://doi.org/10.5194/bg-18-5639-2021.

Tramontana, G., Jung, M., Schwalm, C. R., Ichii, K., Camps-Valls, G., Ráduly, B., Reichstein, M., Arain, M. A., Cescatti, A., Kiely, G., Merbold, L., Serrano-Ortiz, P., Sickert, S., Wolf, S., and Papale, D. (2016). Predicting carbon dioxide and energy fluxes across global FLUXNET sites with regression algorithms. *Biogeosciences*, 13(14):4291–4313. https://doi.org/10.5194/bg-13-4291-2016.

Unger, S., Máguas, C., Pereira, J. S., David, T. S., and Werner, C. (2012). Interpreting post-drought rewetting effects on soil and ecosystem carbon dynamics in a Mediterranean oak savannah. *Agricultural and Forest Meteorology*, 154:9–18. https://doi.org/10.1016/j.agrformet.2011.10.007.

van der Werf, G. R., Randerson, J. T., Giglio, L., van Leeuwen, T. T., Chen, Y., Rogers, B. M., Mu, M., van Marle, M. J. E., Morton, D. C., COLLATZ, G. J., Yokelson, R. J., and Kasibhatla, P. S. (2017). Global fire emissions estimates during 1997–2016. *Earth System Science Data*, 9(2):697–720. https://doi.org/10.5194/essd-9-697-2017.

Vardag, S. N., Metz, E.-M., Artelt, L., Basu, S., and Butz, A. (2025). CO_2 release during soil rewetting shapes the seasonal carbon dynamics in South American Temperate region. *Geophysical Research Letters*, 52(8):e2024GL111725. https://doi.org/10.1029/2024GL111725.

Villalobos, Y., Canadell, J. G., Keller, E. D., Briggs, P. R., Bukosa, B., Giltrap, D. L., Harman, I., Hilton, T. W., Kirschbaum, M. U. F., Lauerwald, R., Liang, L. L., Maavara, T., Mikaloff-Fletcher, S. E., Rayner, P. J., Resplandy, L., Rosentreter, J., Metz, E.-M., Serrano, O., and Smith, B. (2023). A comprehensive assessment of anthropogenic and natural sources and sinks of Australasia's carbon budget. *Global Biogeochemical Cycles*, 37(12). `https://doi.org/10.1029/2023GB007845`.

Villalobos, Y., Rayner, P., Thomas, S., and Silver, J. (2020). The potential of Orbiting Carbon Observatory-2 data to reduce the uncertainties in CO_2 surface fluxes over Australia using a variational assimilation scheme. *Atmospheric Chemistry and Physics*, 20(14):8473–8500. `https://doi.org/10.5194/acp-20-8473-2020`.

Villalobos, Y., Rayner, P. J., Silver, J. D., Thomas, S., Haverd, V., Knauer, J., Loh, Z. M., Deutscher, N. M., Griffith, D. W. T., and Pollard, D. F. (2022). Interannual variability in the Australian carbon cycle over 2015–2019, based on assimilation of OCO-2 satellite data. *Atmospheric Chemistry and Physics Discussions*, pages 1–57. `https://doi.org/10.5194/acp-2022-15`.

Vuichard, N., Messina, P., Luyssaert, S., Guenet, B., Zaehle, S., Ghattas, J., Bastrikov, V., and Peylin, P. (2019). Accounting for carbon and nitrogen interactions in the global terrestrial ecosystem model ORCHIDEE (trunk version, rev 4999): multi-scale evaluation of gross primary production. *Geoscientific Model Development*, 12(11):4751–4779. `https://doi.org/10.5194/gmd-12-4751-2019`.

Wang, K., Bastos, A., Ciais, P., Wang, X., Rödenbeck, C., Gentine, P., Chevallier, F., Humphrey, V. W., Huntingford, C., O'Sullivan, M., Seneviratne, S. I., Sitch, S., and Piao, S. (2022a). Regional and seasonal partitioning of water and temperature controls on global land carbon uptake variability. *Nature communications*, 13(1):3469. `https://doi.org/10.1038/s41467-022-31175-w`.

Wang, L., Jiao, W., MacBean, N., Rulli, M. C., Manzoni, S., Vico, G., and D'Odorico, P. (2022b). Dryland productivity under a changing climate. *Nature Climate Change*, 12(11):981–994. `https://doi.org/10.1038/s41558-022-01499-y`.

Way, D. A., Becklin, K., and Ward, J. (2021). Chapter 1 Leaf carbon flux responses to climate change: Challenges and opportunities. *Photosynthesis, Respiration, and Climate Change*, 48:3–13. `https://doi.org/10.1007/978-3-030-64926-5_1`.

Weir, B., Ott, L. E., Collatz, G. J., Kawa, S. R., Poulter, B., Chatterjee, A., Oda, T., and Pawson, S. (2020). Calibrating satellite-derived carbon fluxes for retrospective and near real-time assimilation systems. *Atmospheric Chemistry and Physics*, 2020:1–26. `https://doi.org/10.5194/acp-2020-496`.

Williams, C. A., Hanan, N. P., Baker, I., Collatz, G. J., Berry, J., and Denning, A. S. (2008). Interannual variability of photosynthesis across Africa and its attribution. *Journal of Geophysical Research: Atmospheres*, 113(G4). `https://doi.org/10.1029/2008JG000718`.

Williams, C. A., Hanan, N. P., Neff, J. C., Scholes, R. J., Berry, J. A., Denning, A. S., and Baker, D. F. (2007). Africa and the global carbon cycle. *Carbon balance and management*, 2:3. `https://doi.org/10.1186/1750-0680-2-3`.

Wunch, D., Toon, G. C., Blavier, J.-F. L., Washenfelder, R. A., Notholt, J., Connor, B. J., Griffith, D. W. T., Sherlock, V., and Wennberg, P. O. (2011). The total carbon column observing network. *Philosophical Transactions of the Royal Society A*, 369(1943):2087–2112. `https://doi.org/10.1098/rsta.2010.0240`.

Yadav, V. and Michalak, A. M. (2013). Improving computational efficiency in large linear inverse problems: an example from carbon dioxide flux estimation. *Geoscientific Model Development*, 6(3):583–590. `https://doi.org/10.5194/gmd-6-583-2013`.

Yue, X. and Unger, N. (2015). The Yale Interactive terrestrial Biosphere model version 1.0: description, evaluation and implementation into NASA GISS ModelE2. *Geoscientific Model Development*, 8(8):2399–2417. `https://doi.org/10.5194/gmd-8-2399-2015`.

Zaehle, S., Friend, A. D., Friedlingstein, P., Dentener, F., Peylin, P., and Schulz, M. (2010). Carbon and nitrogen cycle dynamics in the O-CN land surface model: 2. Role of the nitrogen cycle in the historical terrestrial carbon balance. *Global Biogeochemical Cycles*, 24(1). `https://doi.org/10.1029/2009GB003522`.

Zeng, N., Mariotti, A., and Wetzel, P. (2005). Terrestrial mechanisms of interannual CO_2 variability. *Global Biogeochemical Cycles*, 19(1). `https://doi.org/10.1029/2004gb002273`.

Zhang, Y., Guanter, L., Berry, J. A., van der Tol, C., Yang, X., Tang, J., and Zhang, F. (2016a). Model-based analysis of the relationship between sun-induced chlorophyll fluorescence and gross primary production for remote sensing applications. *Remote Sensing of Environment*, 187:145–155. `https://doi.org/10.1016/j.rse.2016.10.016`.

Zhang, Y., Xiao, X., Jin, C., Dong, J., Zhou, S., Wagle, P., Joiner, J., Guanter, L., Zhang, Y., Zhang, G., Qin, Y., Wang, J., and Moore, B. (2016b). Consistency between sun-induced chlorophyll fluorescence and gross primary production of vegetation in North America. *Remote Sensing of Environment*, 183:154–169. https://doi.org/10.1016/j.rse.2016.05.015.

Zomer, R. and Trabucco, A. (2019). Global aridity index and potential evapotranspiration (ET0) database: Version 3. figshare. Dataset. https://doi.org/10.6084/m9.figshare.7504448.v6.

Zomer, R. J., Xu, J., and Trabucco, A. (2022). Version 3 of the global aridity index and potential evapotranspiration database. *Scientific Data*, 9(1):409. https://doi.org/10.1038/s41597-022-01493-1.

Appendix

A. Lists

A.1. List of Abbreviations

Abbreviation	**Full name and *Description***
ACOS	NASA Atmospheric CO_2 Observations from Space - *retrieval to retrieve XCO_2 values from GOSAT measurement spectra*
AI	aridity index
CAMS	Copernicus Atmosphere Monitoring Service - *atmospheric inversion model*
CarbonTracker	*atmospheric inversion model*
CASA	Carnegie-Ames-Stanford-Approach biogeochemical model
COCCON	Collaborative Carbon Column Observing Network
CSIRO	Commonwealth Scientific and Industrial Research Organisation
DGVM	dynamic global vegetation model
FLUXCOM	*machine learning based approach to upscale fluxtower CO_2 fluxes globally*
FLUXNET	*global collection of fluxtower measurements*
GFED	Global Fire Emission Database
GOSAT	Greenhouse Gas Observing Satellite
GPP	gross primary productivity
IAV	interannual variability
ICOS	Integrated Carbon Observation System
in-situ-only inversions	*atmospheric inversions only assimilating in situ CO_2 measurements*
IPCC	Intergovernmental Panel on Climate Change
MIP/IS	*OCO-2 MIP ensemble assimilating in situ CO_2 measurements*

MIP/OCO-2+IS	*OCO-2 MIP ensemble assimilating in situ and OCO-2 CO_2 measurements*
MODIS	Moderate Resolution Imaging Spectroradiometer
NBP	net biome productivity
NEE	net ecosystem exchange
NEP	net ecosystem productivity
NOAA	National Oceanic and Atmospheric Administration
NPP	net primary productivity
ObsPack	Observation Package
OCO-2	Orbiting Carbon Observatory-2
OCO-2 cosamples	*modeled XCO_2 values at the location of the OCO-2 measurements*
OCO-2 MIP	OCO-2 Model Intercomparison Project - *Ensemble of atmospheric inversions assimilating in situ and OCO-2 CO_2 measurements*
OzFlux	*network of flux towers in Australia and New Zealand*
PAR	photosynthetically active radiation
PFT	plant functional type
Ra	autotrophic respiration
RemoTeC	*retrieval algorithm used to retrieve XCO_2 values from GOSAT measurement spectra*
Rh	heterotrophic respiration
SIF	Solar-Induced Fluorescence
TCCON	Total Carbon Column Observing Network
TER	total ecosystem respiration
TM5-4DVar	Transport Model version 5 four-dimensional variational inversion system (Basu et al., 2013)
TM5-4DVar/ACOS+IS	*TM5-4DVar global inversion assimilating in situ and GOSAT/ACOS CO_2 measurements*
TM5-4DVar/GOSAT+IS	*mean of TM5-4DVar/RemoTeC+IS and TM5-4DVar/ACOS+IS*
TM5-4DVar/IS	*TM5-4DVar global inversion only assimilating in situ CO_2 measurements*
TM5-4DVar/RemoTeC+IS	*TM5-4DVar global inversion assimilating in situ and GOSAT/RemoTeC CO_2 measurements*

TRENDY	trends and drivers of the regional-scale terrestrial sources and sinks of carbon dioxide - *Ensemble of DGVMs providing global CO_2 flux estimates*
XCO_2	column averaged dry air CO_2 mole fractions

A.2. List of Figures

A.3. List of Tables

B. Methods and Data

B.1. Land-Use Change and Lateral Carbon Fluxes

When subtracting fire emissions from the net fluxes of TM5-4DVar/GOSAT+IS to obtain a GOSAT-based NEE estimate, we neglect the 'other' disturbance fluxes in Equation 1.2. Hence, we assume that land-use change and lateral fluxes are of minor importance for the seasonal and interannual variability in the regional carbon cycle compared to GPP, Ra, and Rh. In the following the literature and data sources are described which show that the riverine and land-use change carbon fluxes are smaller than 1-2% of the vegetation gross fluxes (GPP, Ra and Rh) in the study regions.

Villalobos et al. (2023) show that riverine and land-use change carbon fluxes are smaller than 1% of the vegetation gross fluxes (GPP, Ra and Rh) in Australia (see Figure 2 in Villalobos et al., 2023). Liu et al. (2024b) derived a gridded dataset of riverine fluxes. It shows that the riverine carbon flux is significantly lower than 100 TgC/year for the South American Temperate region and southern Africa (see Figure 4 in Liu et al., 2024b). The yearly total respiration of the South American Temperate region is more than 10.000 TgC/year (see Figure 2 in Vardag et al., 2025) and more than 5000 TgC/year in southern Africa (see Figure A12 in Metz et al., 2025a), such that the effect is expected to be only about 1-2% of the total respiration signal. The carbon fluxes by land-use changes as estimated by TRENDY are also below 1% of the vegetation gross fluxes as shown in the reviewer response (Metz et al., 2024) to Metz et al. (2025a) for southern Africa. Using the same approach, the same can be shown for the TRENDY land-use change fluxes for the South American Temperate region.

B.2. Seasonal Amplitudes of TM5-4DVar Inversions

	MSC Amplitude [TgC/month]		
Inversion	**Australia**	**Southern Africa**	**South American Temperate**
TM5-4DVar/IS	105.14	226.65	359.45
TM5-4DVar/GOSAT+IS	144.83	377.89	380.39
TM5-4DVar prior	104.77	237.08	220.00
TM5-4DVar/GOSAT+IS - TM5-4DVar/IS	39.69	151.24	20.94
$\frac{TM5-4DVar/GOSAT+IS}{TM5-4DVar/IS}$	1.38	1.67	1.06

Table B.1.: Mean seasonal cycle amplitudes. Peak-to-peak amplitudes of the mean seasonal cycle (MSC) of the different TM5-4DVar inversion setups for Australia, southern Africa, and the South American Temperate region.

B.3. TRENDY PFTs and Timeseries of Fluxes

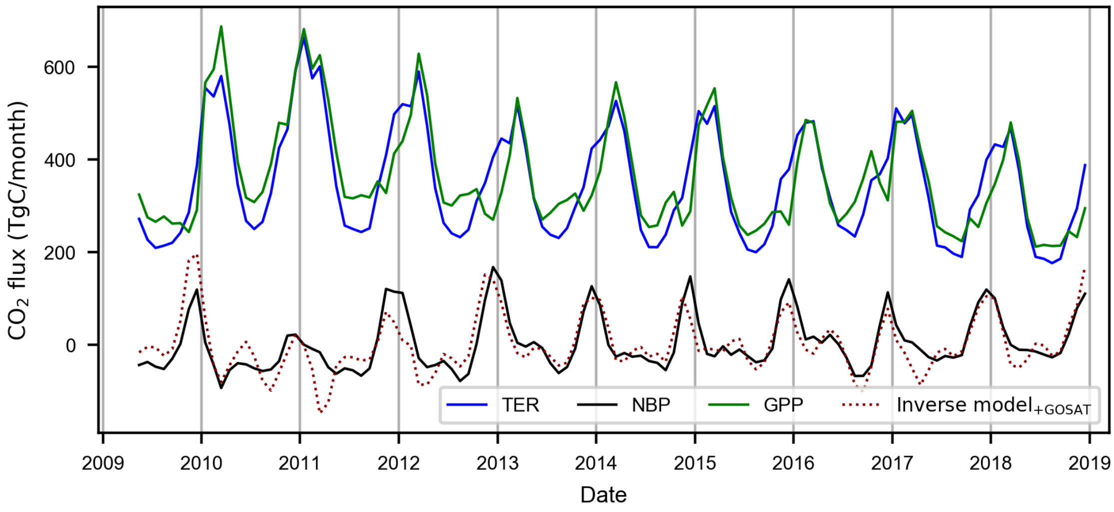

Figure B.1.: Australian carbon fluxes modeled by JSBACH. The carbon fluxes NBP, GPP and TER modeled by JSBACH are given in black, green and blue, respectively. Furthermore, the NBP fluxes of TM5-4DVar/GOSAT+IS are given in red dashed.

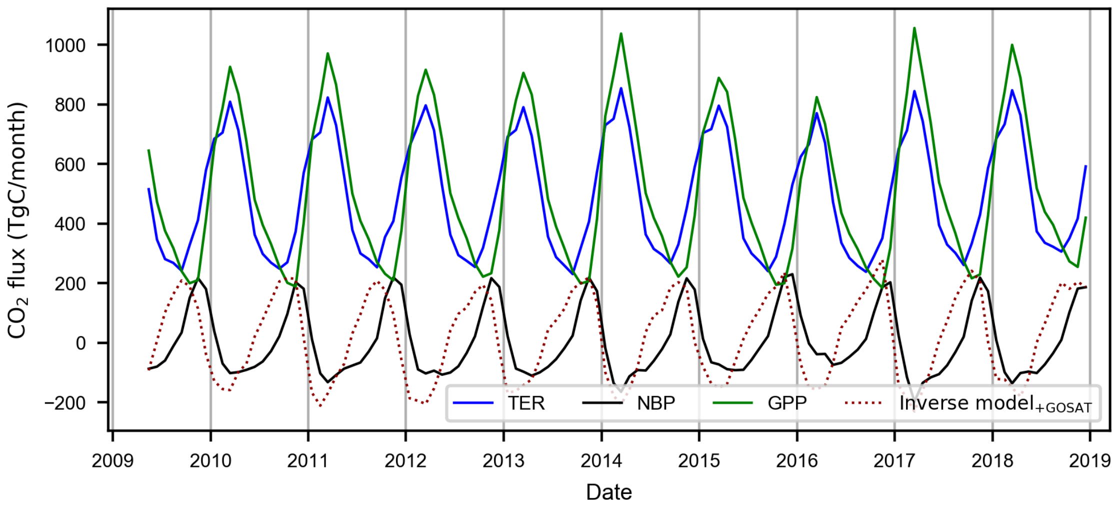

Figure B.2.: Southern African carbon fluxes modeled by JSBACH. The carbon fluxes NBP, GPP and TER modeled by JSBACH are given in black, green and blue, respectively. Furthermore, the NBP fluxes of TM5-4DVar/GOSAT+IS are given in red dashed.

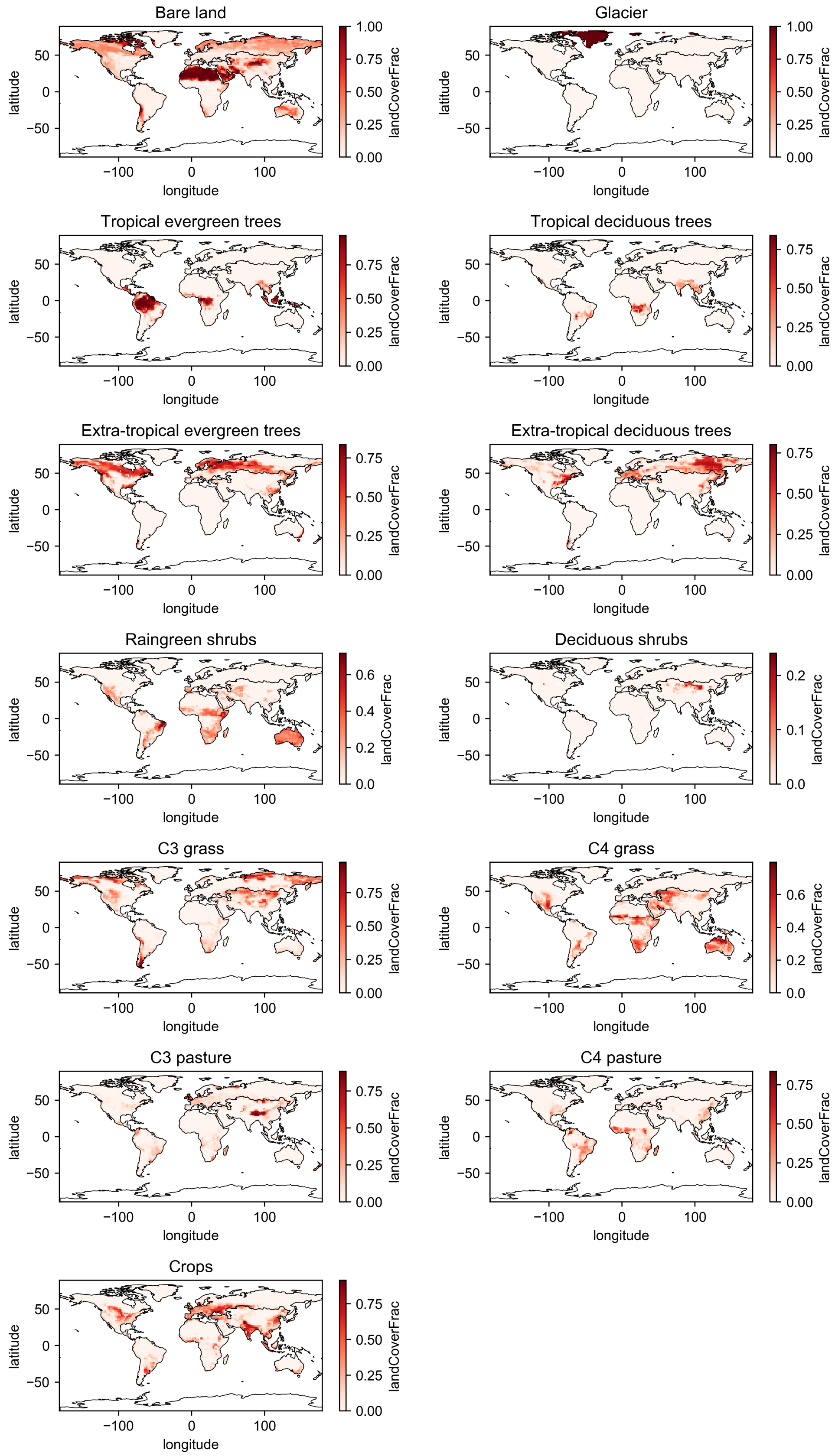

Figure B.3.: Distribution of plant functional types in JSBACH. The fraction of each PFT in the grid cells is shown.

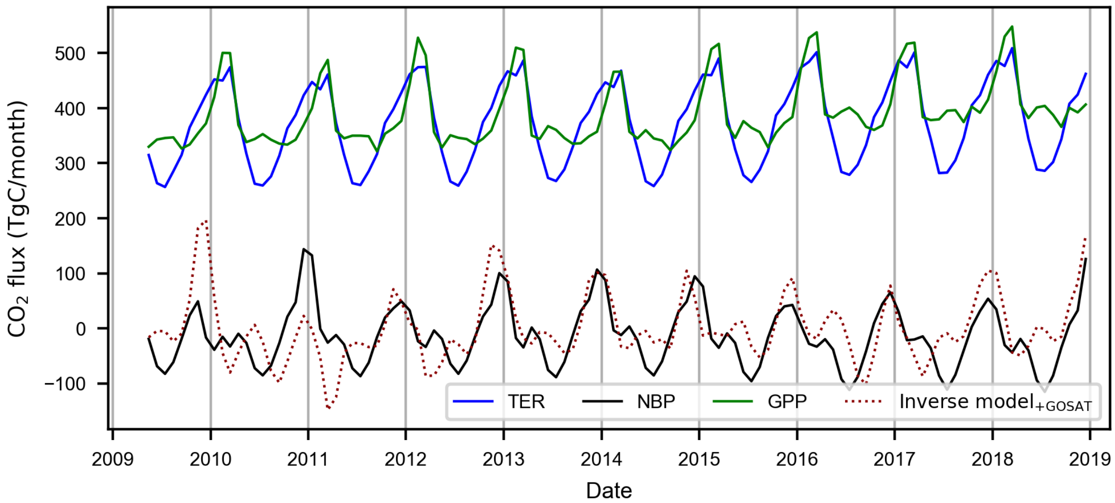

Figure B.4.: Australian carbon fluxes modeled by YIBs. The carbon fluxes NBP, GPP and TER modeled by YIBs are given in black, green and blue, respectively. Furthermore, the NBP fluxes of TM5-4DVar/GOSAT+IS are given in red dashed.

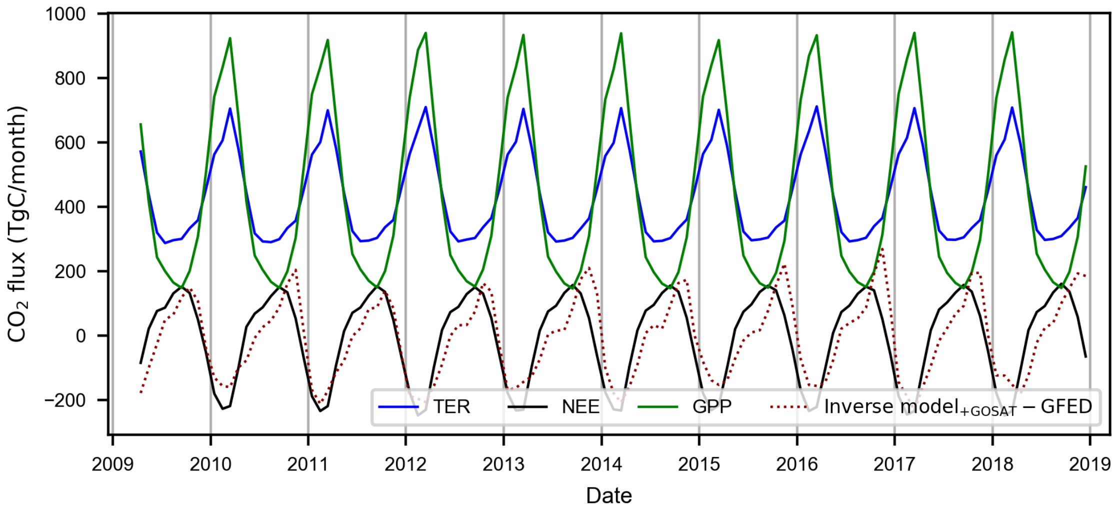

Figure B.5.: Southern African carbon fluxes modeled by YIBs. The carbon fluxes NEE, GPP and TER modeled by YIBs are given in black, green and blue, respectively. Furthermore, the NEE fluxes of TM5-4DVar/GOSAT+IS-GFED are given in red dashed. Please note, as the NBP fluxes of YIBs aligned well with TM5-4DVar/GOSAT+IS, the NEE fluxes are given in this figure to show why YIBs was not selected in southern Africa.

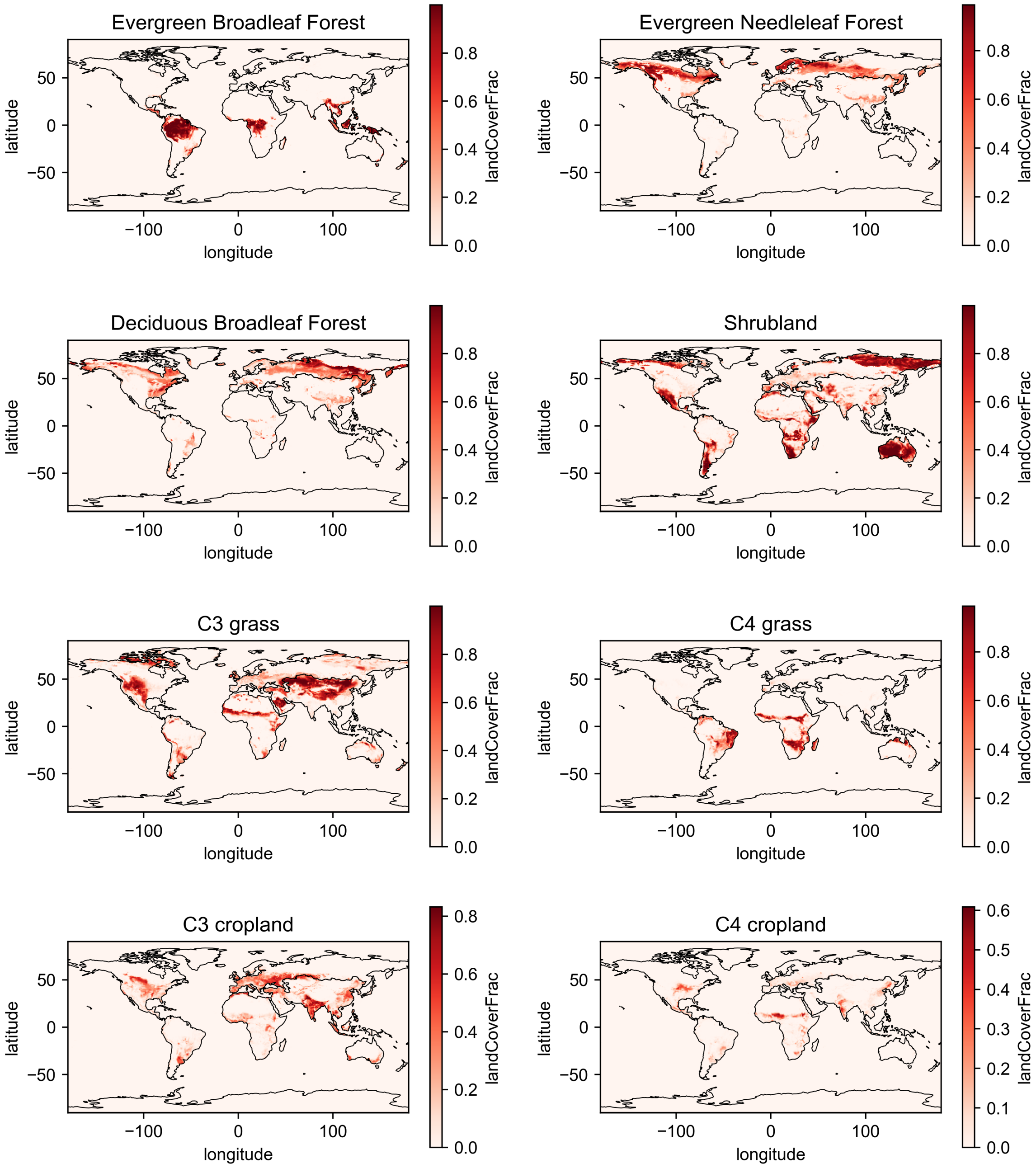

Figure B.6.: Distribution of plant functional types in YIBs. The fraction of each PFT in the grid cells is shown.

Acknowledgements

I would like to thank and acknowledge everyone who accompanied and supported me during my PhD time. Many thanks go to:

Prof. Dr. André Butz for giving me the opportunity to work in an exciting research area. For always taking time for constructive discussions and for giving me the freedom to work on my own, but providing guidance whenever I needed it.

Dr. Sanam Vardag for all the advices, her open ear at any time for big and small questions, the support for my scholarship application during her parental leave, and the support for my thesis.

The ATMO group. It was a pleasure to work in the constructive and supportive environment this group provided in group meetings, during lunchtime, during coffee breaks, or after work.

My office crew, Eva Rückert, Karolin Voss, Leon Kuhn, and Robert Maiwald for a great time together, for being proactive whenever things needed to be organized, for our shared passion for plants, and for all the conversations.

Sourish Basu for running and providing the TM5-4DVar inversions for my research and all the advice on atmospheric inversions.

Sourish Basu, Ben Poulter, and Andrew Feldman for giving me the opportunity to visit the NASA Goddard Spaceflight Center to work together with them.

Angelika Gassama, Rebekka Benetatos, and Karoline Thomas for their always kind and patient support in any administrative matters.

Tobias Schmitt, Benedikt Löw, Christopher Lüken-Winkels, Robert Maiwald, Karolin Voss, and my mum for proofreading my thesis.

The modelers of the TRENDY project for providing their model data.

The German Academic Scholarship Foundation for the financial support of my PhD.

My family and friends for always supporting me, especially my husband Timo.